이학박사 학위논문

Survey of Faint Quasars at High Redshifts: Contributions to the Cosmic Reionization and Growth of the First Supermassive Black Holes

고적색편이 어두운 퀘이사 연구: 우주적 재이온화에 대한 기여와 최초의 초거대질량 블랙홀의 성장

2019년 8월

서울대학교 대학원

물리·천문학부 천문학전공

김 용 정

Survey of Faint Quasars at High Redshifts: Contributions to the Cosmic Reionization and Growth of the First Supermassive Black Holes

by

Yongjung Kim
(yjkim@astro.snu.ac.kr)

A dissertation submitted in partial fulfillment of the requirements for the degree of

Doctor of Philosophy

in

Astronomy

in

Astronomy Program
Department of Physics and Astronomy
Seoul National University

Committee:

Professor	Myung Gyoon Lee
Professor	Myungshin Im
Professor	Jong-Hak Woo
Professor	Soojong Pak
Professor	Minjin Kim

ABSTRACT

Faint quasars occupy a large fraction of the quasar population at high redshifts ($z > 5$), but they are hidden owing to their brightness, and so related research has only been conducted rarely in recent years. In this thesis, faint high-redshift quasars with $M_{1450} > -24$ mag are studied in various ways.

First, the survey of faint quasars at $z \sim 6$ was performed with the near-infrared (NIR) imaging data from the Infrared Medium-deep Survey (IMS). Over an area of 86 deg^2, thirteen quasar candidates were selected by the color-selection technique, three of which were spectroscopically identified as quasars at $z \sim 6$, including IMS J2204+0112 that is newly discovered in this work. The $z = 6$ quasar luminosity functions (QLFs) were derived from the samples consisting of these three quasars and/or quasar candidates, resulting in the low ionizing photon density that is only $< 15\%$ of the amount required to fully ionize neutral hydrogen in the universe. This suggests the minor contribution of high-redshift quasars to the cosmic reionization.

Second, the black hole mass ($M_{\rm BH}$) of a supermassive black hole (SMBH) centered at IMS J2204+0112 was estimated through deep NIR spectroscopy. Assuming the virial motion of gas around the SMBH, its $M_{\rm BH}$ was measured from the redshifted C IV λ1549 emission line as $M_{\rm BH} = 1.2 \times 10^9\ M_\odot$, resulting in the Eddington ratio of $\lambda_{\rm Edd} \sim 0.1$. This is one of the lowest $\lambda_{\rm Edd}$ values of $z \gtrsim 6$ quasars discovered so far, which breaks the decadal belief on extremely growing SMBHs in the early universe. Such a low $\lambda_{\rm Edd}$ quasar can grow from a 100 $M_\odot$ seed black hole with episodic super-Eddington accretion or from a heavy black hole of $\sim 10^5 M_\odot$ with Eddington-limited accretion. Furthermore, the inclusion of IMS J2204+0112 gives the intrinsic $\lambda_{\rm Edd}$ distribution of $z \sim 6$ quasars that has slightly higher $\lambda_{\rm Edd}$ values by 0.35 dex than that of $z \sim 2$ quasars, giving a constraint to the SMBH growth in the early universe.

Third, based on the sub-mm observations of IMS J2204+0112 with the Atacama Large Millimeter/submillimeter Array (ALMA), its host galaxy is found to have a star formation rate (SFR) of 500–700 $M_\odot$ yr^{-1}, which is an order of magnitude higher than

those of the luminosity-matched $z \sim 6$ quasars with high $\lambda_{\rm Edd}$. Interestingly, all of the low $\lambda_{\rm Edd}$ quasars like IMS J2204+0112 known so far ($\lambda_{\rm Edd} < 0.2$) are also hosted by high SFR galaxies, corresponding to the recent simulation of the preceding SMBH growth and the subsequent formation of its host galaxy. Following this picture, such low $\lambda_{\rm Edd}$ quasars are in the end stage of SMBH evolution, while their host galaxies can afford to grow more.

Finally, the $z \sim 5$ faint quasar survey with IMS was conducted using the advanced selection method with medium-band observations, where the medium-band filters have a bandwidth of 500 Å. Through the optical spectroscopy of the selected candidates, ten quasars with $-25 < M_{1450} < -23$ are newly discovered at $z \sim 5$. The discoveries are also in agreement with the minor contribution of high-redshift quasars to keep the ionized state of hydrogen at $z \sim 5$. The medium-band-based approach allows to rule out many contaminants like dwarf stars, which account for $\gtrsim 20\%$ of the broad-band-selected candidates. Also, the inclusion of medium-band data improves the accuracy of the photometric redshift determination to $\langle|\Delta z|/(1+z)\rangle = 0.016$. Consequently, the medium-band-based approach is a cost-effective way to find high-redshift quasars even with their accurate redshifts.

Keywords: cosmology: observations – galaxies: active – galaxies: high-redshift – quasars: emission lines – quasars: supermassive black holes – surveys

Student Number: 2013-20389

Contents

List of Figures

List of Tables

Chapter 1

Introduction

1.1 Active Galactic Nucleus

Active Galactic Nucleus (AGN) is a compact and bright region at the center of its host galaxy, as can be inferred from its name. Nowadays, the AGN is commonly regarded as an extragalactic object that is observable at multi-wavelengths from γ-ray to radio. Interestingly, the multi-wavelength fluxes radiated by the AGN are extremely high with an AGN bolometric luminosity of $L_{\rm bol} \sim 10^{42}$–10^{48} erg s^{-1}, which is usually brighter than their host galaxies. Such an enormous amount of light is released from the central supermassive black hole (SMBH), which is known to weigh over millions or billions of solar mass, by accreting its surrounding gas-like materials. Figure 1.1 shows the unification model of the AGN structure (Urry & Padovani 1995) consisting of the central SMBH, accretion disk, broad and narrow line regions, dusty torus, and so on. The central SMBH is fueled by gas inflows via the accretion disk, while a huge amount of light is emitted in this process, which is expected to peak at ultraviolet (UV) and optical wavelengths. Also, there are cloud-like gas clumps that are rotating near the SMBH, called broad and narrow line regions because the broad and narrow emission lines, one of the observational characteristics of AGNs, are from these regions.

This unification model can explain the presence of various types of AGNs, which are classified according to their observational properties. For example, Seyfert 1 and 2

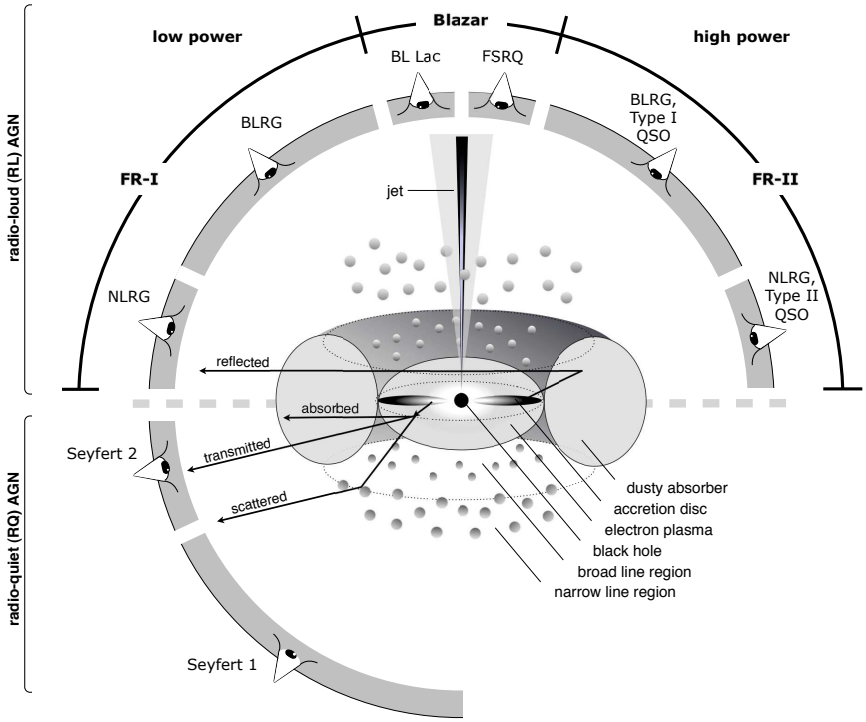

Figure 1.1. Schematic diagram of the AGN unification model suggested by Urry & Padovani (1995). There are a central SMBH that are surrounded by the accretion disk, broad and narrow line regions, and dusty torus. According to this feature, AGNs can be classified by the viewing angles of an observer, which is marked in the form surrounding the AGN structure. This figure is adapted from Beckmann, & Shrader (2012).

types are distinguished by the presence of broad emission lines. If the dusty torus is located along our line of sight, it is impossible to observe the light from the broad line region near the central SMBH, resulting in the absence of broad emission lines in the AGN spectrum, which is classified as a Type 2 AGN. Meanwhile, the presence of radio jets is a classifier of radio-loud AGNs like Blazars.

Quasar is also one of the AGN populations. When they were first discovered as radio sources around 1960, astronomers named them as quasi-stellar objects (or quasi-stellar radio sources) because they are stellar-like sources with extremely high luminosities. As an abbreviated form of the quasi-stellar radio source, "quasar" is also used for the simplification (Chiu 1964). Unlike their first discovery, however, more than 90% of the quasars have been known to radio-quiet ones these days (Bañados et al. (2015b) and references therein). But they have still named quasars, and the name is mainly used as a term to represent the unobscured AGN populations with extremely high luminosities ($L_{\rm bol} \gtrsim 10^{45}$ erg s^{-1}).

Through the investigation of quasars, we can understand the physical properties, accretion mechanism, and evolution history of their central SMBHs with their observational characteristics at multi-wavelengths. In fact, there are other ways to examine the SMBHs centered at galaxies (Kormendy & Ho (2013) and references therein). But for the high-redshift universe ($z \gtrsim 5$), quasars are practically a unique sample to investigate the SMBHs since they are too far away from Earth.

1.2 Discovery of Quasars in the Early Universe

To date, millions of quasars have been discovered at various redshifts from the large imaging surveys, which are well-cataloged in the Million Quasars Catalog (MILLIQUAS; Flesch 2015)*. In particular, the Sloan Digital Sky Survey (SDSS), the most popular imaging and spectroscopic survey using the Sloan Foundation 2.5 m Telescope at Apache Point Observatory (York et al. 2000; Gunn et al. 2006), was in the vanguard of the field of finding high-redshift quasars. Among the half millions of quasars discov-

*https://heasarc.gsfc.nasa.gov/w3browse/all/milliquas.html

ered so far in the SDSS survey (Pâris et al. 2018), there are 52 quasars at $5.7 < z \leq 6.4$ or just 1 Gyr after the Big Bang (Fan et al. 2000, 2001, 2003, 2004, 2006; Jiang et al. 2008, 2009, 2015, 2016), which are shown in Figure 1.4.

Following SDSS, there have been high-redshift quasar surveys with large imaging data last two decades: the Canada-France-Hawaii Telescope High-redshift Quasar Survey (CFHQS; Willott et al. 2005, 2007, 2009, 2010b), the United Kingdom Infrared Telescope (UKIRT) Infrared Deep Sky Survey (UKIDSS; Venemans et al. 2007; Mortlock et al. 2009, 2011), the Panoramic Survey Telescope & Rapid Response System 1 (Pan-STARRS1; Morganson et al. 2012; Bañados et al. 2014, 2016; Venemans et al. 2015a; Mazzucchelli et al. 2017; Tang et al. 2017), the Visible and Infrared Survey Telescope for Astronomy (VISTA) Kilo-Degree Infrared Galaxy Survey (VIKINGS; Venemans et al. 2013, 2015b), the Dark Energy Survey (DES; Reed et al. 2015, 2017), the Large Sky Area Multi-Object Fiber Spectroscopic Telescope (LAMOST) Quasar Survey (Wu et al. 2015), the Subaru High-z Exploration of Low-Luminosity Quasars (SHELLQS; Kashikawa et al. 2015; Matsuoka et al. 2016, 2018a,b, 2019), the Dark Energy Camera Legacy Survey (DECaLS; Wang et al. 2017, 2018a), and so on. From these surveys, by this time hundreds of quasars have been discovered at $z \gtrsim 5$, among which more than 150 quasars are at $z \gtrsim 6$ and 4 of them are even at $z \geq 7$ with a record holder named ULAS J1342+0928 at $z = 7.5$ (or 690 Myr after the Big Bang; Bañados et al. 2018).

Compared to the spectra of lower-redshift quasars, it has been reported that there is no significant evolution of spectral features of high-redshift quasars, such as broad emission lines and UV Fe II elements, along the redshifts (e.g., De Rosa et al. 2011; Shen et al. 2019), except the absence of fluxes at wavelengths shorter than that of the Lyα λ1216 emission line. Gunn & Peterson (1965) predicted such a deficit of UV electromagnetic emissions for high-redshift quasars, which would be due to neutral hydrogen in the early universe. This is referred to as the Gunn-Peterson trough that is observed in the high-redshift quasar spectra as a sharp break (see Figure 1.4). By calculating how the UV lights from high-redshift quasars are attenuated by the Intergalactic Medium

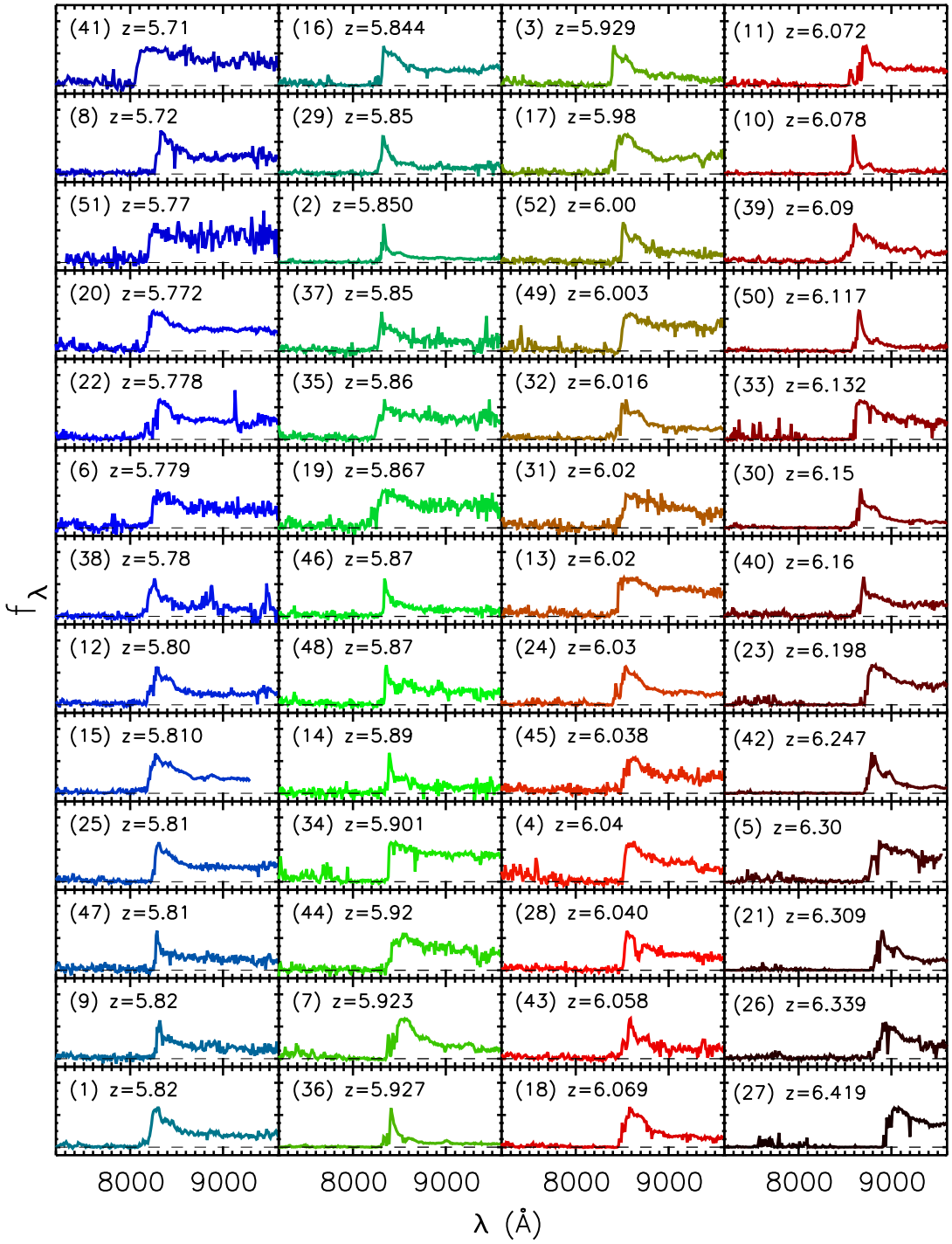

Figure 1.2. Spectra of 52 SDSS quasars at $5.7 < z \leq 6.4$. This figure is adapted from Jiang et al. (2016).

(IGM) in their spectra, several studies suggest that the fraction of neutral hydrogen decrease rapidly at $z \sim 6$–7 (Fan et al. 2006; Bañados et al. 2018), called the epoch of the cosmic reionization (see more details in Section 1.3).

Such a peculiar characteristic of high-redshift quasars results in their discriminating colors that are noticeably different from those of other stellar sources. For instance, the Lyα break of a $z = 6$ quasar would be located at $\sim$ 8500 Å, between the i' and z' bands, resulting in a very red $i' - z'$ color, while its longer wavelength colors (e.g., $z' - J$) would be relatively blue due to AGN continuum emission. This color distribution of high-redshift quasars is clearly distinguished from the red cool dwarf stars that have red colors even at near-infrared (NIR) wavelengths. Most of the surveys mentioned above found high-redshift quasars taking these characteristics into account, using the color selection criteria to select plausible candidates to be identified by spectroscopy (e.g., Fan et al. 2000; Willott et al. 2005; McGreer et al. 2013). Recent studies used the advanced method like Bayesian statistics (e.g., Matsuoka et al. 2016) or the likelihood methods (e.g., McGreer et al. 2018), but which are based on the unique colors of high-redshift quasars. As an alternative approach, it was also suggested to carry the follow-up imaging observations with the medium-band filters that have a bandwidth of 500 Å, which can effectively rule out the contaminants like cool dwarf stars (Jeon et al. 2016). Figure 1.3 shows the medium-band filter transmission curves with high-redshift quasar spectra. Note that the curves include the quantum efficiency of the detector of SED Camera for Quasars in EArly uNiverse (SQUEAN; Choi et al. 2015; Kim et al. 2016) on the 2.1 m Otto Struve Telescope at the McDonald Observatory.

Now many researchers in the field of seeking high-redshift quasars are preparing for the unprecedented data in the upcoming wide-field optical/NIR imaging surveys, carried out with the next generation telescopes, such as the Large Synoptic Survey Telescope (LSST), the Euclid space mission, and the Wide Field Infrared Survey Telescope (WFIRST). The limiting magnitudes of these surveys will reach 23–25 AB magnitudes, allowing us to discover the very first high-redshift quasars even at $z = 9$–10, or just $\sim$ 500 Myr after the Big Bang.

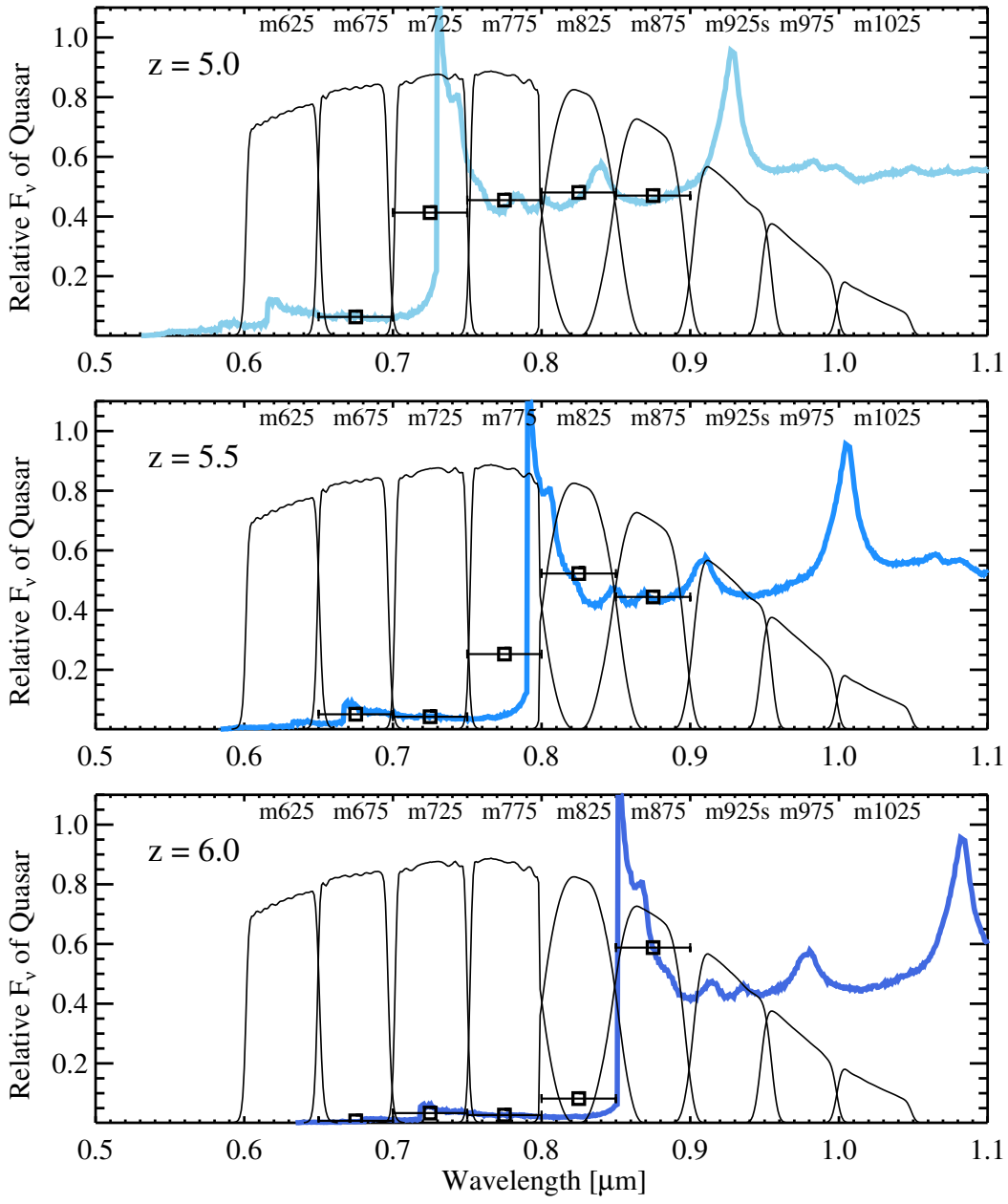

Figure 1.3. SQUEAN Medium-band filter transmission curves and high-redshift quasar spectra. This figure is adapted from Jeon et al. (2016).

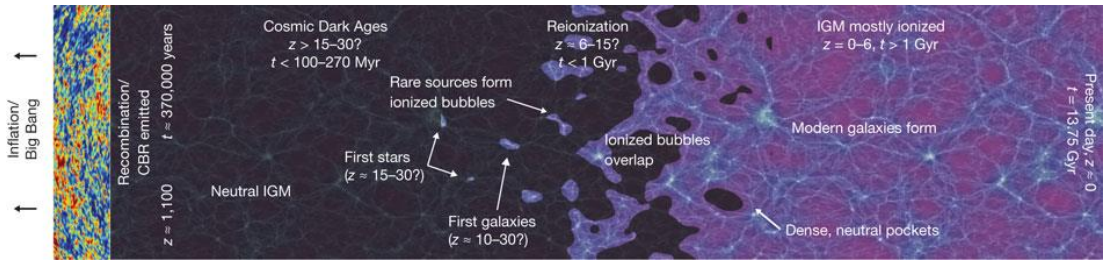

Figure 1.4. Transition of Intergalactic Medium along the cosmic time, from neutral hydrogen after the recombination ($z = 1,100$) to ionized hydrogen after the cosmic reionization ($z = 6$–15). This figure is adapted from Robertson et al. (2010).

1.3 Quasar Contributions to the Cosmic Reionization

Just after the recombination at $z \sim 1100$, neutral hydrogen atoms had formed through the combination of protons and electrons, which filled the space of the early universe. After hundreds of millions of years, the first stars started to form at the dense regions in gravitationally unstable areas. The first stars, classified as Pop III, emit a huge amount of UV photons that can ionize nearby neutral hydrogen atoms. The first galaxies, which formed after the first stars according to the Lambda cold dark matter (ΛCDM) cosmology, consist of young stars. They are much larger reservoirs of UV photons to ionize lots of neutral hydrogen in the early universe, making the ionized bubbles of the hydrogen around them. As time went by, the number of such UV-photon-emitting sources increased, and most of hydrogen became ionized, called as "cosmic reionization".

Interestingly, the epoch of the cosmic reionization turns out to be a very short period of time compared to the age of the universe. Recent work of Planck Collaboration et al. (2016) shows that the Thomson optical depth $\tau = 0.058$ from recent cosmic microwave background (CMB) observation corresponds to the significant reionization at $z \sim 7.8$–8.8. As regards to high-redshift quasars, their absorbed rest-UV spectra suggest that the reionization process is almost complete at $z \sim 5$–6 (Fan et al. 2006; McGreer et al. 2015). On the other hand, the neutral fraction of hydrogen ($\overline{x}_{\rm HI}$) derived from the NIR spectrum of the farthest quasar ULAS J1342+0928 at $z = 7.5$ is 0.56, implying that this quasar is at the height of the cosmic reionization. Likewise, from the detections/non-

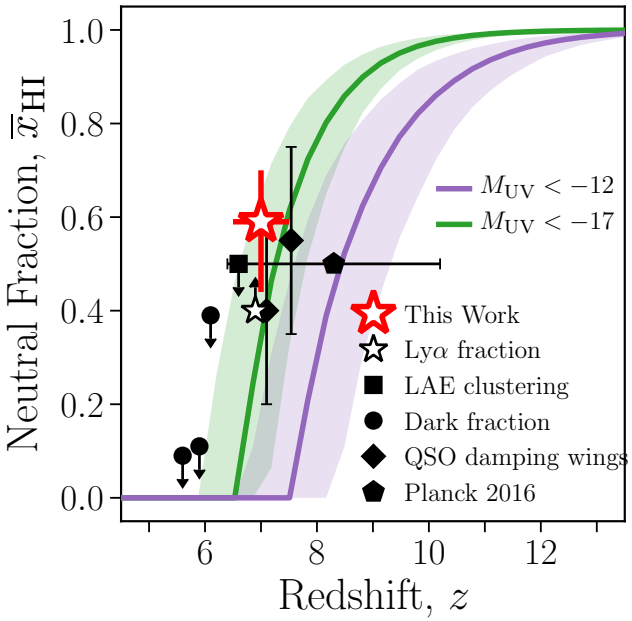

Figure 1.5. Redshift versus fraction of neutral hydrogen diagram. The $\overline{x}_{\rm HI}$ is expected to decrease rapidly at $6 \lesssim z \lesssim 8$. This figure is adapted from Mason et al. (2018).

detections of Lyα emission from Lyman Break galaxies (LBGs) at $z \sim 7$, Mason et al. (2018) also found that $\overline{x}_{\rm HI}$ is 0.59 at $z \sim 7$. Figure 1.5 summarizes these results, showing the rapid declination of $\overline{x}_{\rm HI}$ at $6 \lesssim z \lesssim 8$.

There is still debate over which objects radiate UV photons that can fully ionize whole neutral hydrogen in the early universe and keep the ionized state of them. High-redshift quasars, which radiate significant amounts of UV photons compared to normal galaxies, have been regarded as prospective contributors to the cosmic reionization. Figure 1.6 shows the quasar luminosity function at $z \sim 6$ from the literature. Including the sample of faint X-ray AGNs ($M_{1450} > -22$ mag; blue open circles), Giallongo et al. (2015) estimated ionizing emissivities and hydrogen photoionization rates, suggesting that the UV photons emitted by high-redshift AGNs occupy a large fraction enough to keep the ionized state of hydrogen in the universe (see also Madau & Haardt 2015). On the other hand, based on the bright optical/NIR quasars, many studies disagree with the suggestion (Willott et al. 2010b; Kashikawa et al. 2015; Kim et al. 2015a; Onoue et

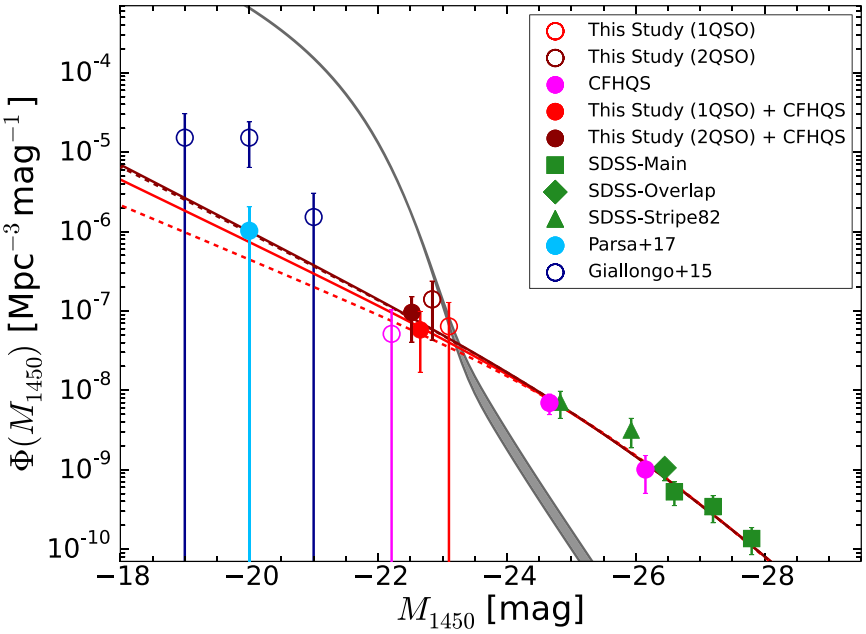

Figure 1.6. Quasar Luminosity Functions at $z \sim 6$. This figure is adapted from Onoue et al. (2017).

al. 2017). Using a handful number of faint quasars, they suggest that the faint end of the $z \sim 6$ quasar luminosity function is not steep but much lower than the estimation of Giallongo et al. (2015), implying the minor contribution of high-redshift quasars to the cosmic reionization.

The UV emissivity ionizing IGM of the universe is proportional to the number of quasars and their luminosity,

$$\epsilon \propto \Phi(L) \times L \tag{1.1}$$

where $\Phi(L)$ is the quasar luminosity function as a function of AGN luminosity L. Assuming a double power-law functional form for the quasar luminosity function, the ϵ value is maximum at $M_{1450} \approx -23.5$ mag. This means that faint quasars in the range of $-25 < M_{1450} < -22$ hold a key to the determination of the high-redshift quasars' contribution to the cosmic reionization. Unfortunately, the number of quasars in this magnitude range was quite small, thus finding out such faint quasars is important to

verify whether they are numerous enough to provide UV photons to neutral hydrogen in the epoch of the cosmic reionization.

1.4 Growth of the First Supermassive Black Holes

Under the assumption of the AGN unification model mentioned in Section 1.1, a quasar harbors an SMBH that makes dynamically moving environments around itself. Assuming that there are gas clouds in virial motions around an SMBH in the broad line region (BLR), the black hole mass ($M_{\rm BH}$) can be written as,

$$M_{\rm BH} \propto R_{\rm BLR} \cdot (v_{\rm BLR})^2. \tag{1.2}$$

where $R_{\rm BLR}$ is the size of BLR and $v_{\rm BLR}$ is the velocity of the gas clouds at $R_{\rm BLR}$ (Peterson 1993). Thanks to the $R_{\rm BLR}$-luminosity relation calibrated from the reverberation mapping studies for low redshift AGNs (Kaspi et al. 2000, 2005; Bentz et al. 2009), it is possible to estimate $R_{\rm BLR}$ from the luminosity at a specific wavelength (L_λ). If we assume that the Doppler broadening effect in a dominant factor of broad emission lines, the $v_{\rm BLR}$ can be estimated from the line width ($\Delta V_{\rm line}$; FWHM or line dispersion) of the broad emission lines from the BLR of a quasar. With the constant on accounts of inclination (e.g., $f = 5.1 \pm 1.3$; Woo et al. 2013), the Equation 1.2 can be converted to the function of L_λ and $\Delta V_{\rm line}$, described as follows:

$$\log\left(\frac{M_{\rm BH}}{M_\odot}\right) = \alpha + \beta \log\left(\frac{\lambda L_\lambda}{10^{44}\ {\rm erg\ s^{-1}}}\right) + \gamma \log\left(\frac{\Delta V_{\rm line}}{1000\ {\rm km\ s^{-1}}}\right), \tag{1.3}$$

where α, β, and γ are mainly determined from the reverberation-mapped sample of low-redshift AGNs (e.g., Vestergaard & Peterson 2006; Vestergaard & Osmer 2009; Park et al. 2013, 2017). This method is known as the single epoch method.

Since there is no significant evolution of quasar spectral features along with the redshift (e.g., De Rosa et al. 2011), we can measure the $M_{\rm BH}$ of high-redshift quasars using the single epoch method. For the quasars in the early universe, their UV emission lines such as C IV λ1549 and Mg II λ2798 are used for the $M_{\rm BH}$ measurements.

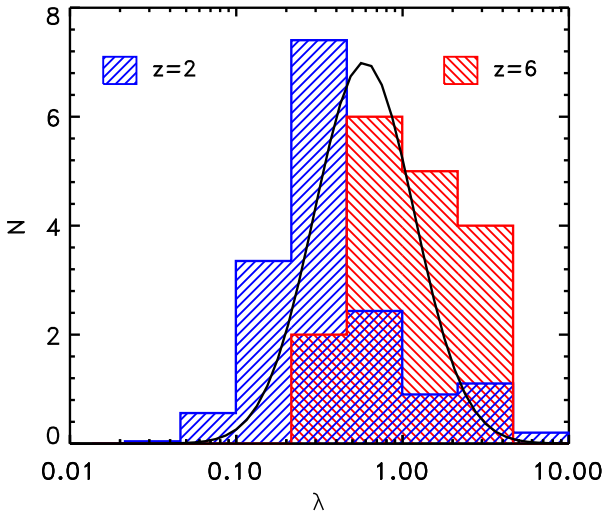

Figure 1.7. Eddington ratio ($\lambda_{\rm Edd}$) distribution of quasars at $z = 2$ and 6, shown as the blue and red histograms, respectively. The black line is the intrinsic $\lambda_{\rm Edd}$ distribution of $z \sim 6$ quasars. This figure is adapted from Willott et al. (2010a).

Although several studies suggest that the Hα and/or Hβ emission lines of quasars are significant and reliable $M_{\rm BH}$ estimators, the lines are redshifted to the mid-infrared (MIR) wavelengths without a high-sensitive spectrograph, thus using the UV lines is inevitable.

Many studies measured the $M_{\rm BH}$ of few tens of $z \gtrsim 6$ quasars from their NIR spectra (Jiang et al. 2007; Kurk et al. 2007, 2009; Willott et al. 2010a; De Rosa et al. 2011, 2014; Mortlock et al. 2011; Shen et al. 2011; Jun et al. 2015; Wu et al. 2015). The $M_{\rm BH}$ values are in the range of $10^8 \lesssim M_{\rm BH}/M_\odot \lesssim 10^{10}$, with accreting rates near the Eddington limit. Including the nine CFHQS quasars at $z \sim 6$, Willott et al. (2010a) estimated the $M_{\rm BH}$ of 17 high-redshift quasars, and also calculated their Eddington ratios ($\lambda_{\rm Edd}$),

$$\lambda_{\rm Edd} = \frac{L_{\rm bol}}{L_{\rm Edd}}, \tag{1.4}$$

where $L_{\rm bol}$ is the quasar bolometric luminosity derived from L_λ using a bolometric

correction factor (e.g., Runnoe et al. 2012) and $L_{\rm Edd}$ is the Eddington luminosity given as,

$$L_{\rm Edd} = \frac{4\pi G M_{\rm BH} m_{\rm p} c}{\sigma_{\rm T}} \cong 1.26 \times 10^{38} \left(\frac{M_{\rm BH}}{M_{\odot}} \right) \ {\rm erg\ s^{-1}}, \tag{1.5}$$

where G is the gravitational constant, $m_{\rm p}$ is the mass of a proton, c is the speed of light, and $\sigma_{\rm T}$ is the Thomson scattering cross-section for the electron. Figure 1.7 shows the $\lambda_{\rm Edd}$ distribution of the high-redshift quasars (red histogram). They have higher $\lambda_{\rm Edd}$ values than those of the $L_{\rm bol}$-matched quasars at $z = 2$, shown as the blue histogram, meaning that they are growing more rapidly than their low-redshift counterparts. Willott et al. (2010a) also derived the intrinsic $\lambda_{\rm Edd}$ distribution at $z = 6$ (black line) with a peak of $\lambda_{\rm Edd} = 0.6$, implying that most of the high-redshift quasars are great eaters.

Even with such high Eddington ratios, however, it is still a theoretical challenge to explain the existence of SMBHs weighing over $10^9\ M_{\odot}$ in the early universe. For a seed black hole (BH) of 100 $M_{\odot}$, it takes about 0.8 Gyr to grow to a $10^9\ M_{\odot}$ SMBH, even if we assume the Eddington accretion onto the seed during its whole lifetime. But the short time, less than 0.5 Gyr, is allowed for the first BHs, from the formation of the first stars and galaxies to $z \sim 6$. To solve this problem, various ideas have been suggested. There are simply two scenarios with respect to the initial mass of seed BH. First, 100 $M_{\odot}$ seed BH from Pop III stellar remnants can grow with super-Eddington accretion (e.g., Volonteri & Rees 2005; Wyithe & Loeb 2012; Madau et al. 2014). Second, $10^{4-6}\ M_{\odot}$ seed BH, which formed from dense clusters or the direct collapse, can grow to $10^9\ M_{\odot}$ under Eddington-limited accretion (e.g., Bromm & Loeb 2003; Begelman et al. 2006; Lodato & Natarajan 2006; Sijacki et al. 2009; Johnson et al. 2013).

To test which scenario is more reliable, it is required to understand the intrinsic Eddington ratio distribution of high-redshift quasars. But the intrinsic $\lambda_{\rm Edd}$ distribution of $z \sim 6$ quasars, derived by Willott et al. (2010a), could be a biased result from the sample consisting of high luminous and high accreting quasars. At low redshift, there is a potential correlation between the $L_{\rm bol}$ and $\lambda_{\rm Edd}$ of type 1 quasars (Shen et al.

2011). Therefore, extending the luminosity range and increasing the size of high-redshift SMBH sample is necessary to derive the intrinsic $\lambda_{\rm Edd}$ distribution at $z \sim 6$ accurately, and ultimately, to understand the formation and evolution of the first SMBHs in a short time scale. In fact, recently, some high-redshift quasars with moderate $L_{\rm bol}$ of $\lesssim 10^{47}$ erg s^{-1} are found to have low Eddington ratios (Mazzucchelli et al. 2017; Kim et al. 2018; Onoue et al. 2019), while it has been also suggested that there is no difference in $\lambda_{\rm Edd}$ of quasars at $z > 5.7$ and $z = 2$ (Shen et al. 2019). The existence of these low $\lambda_{\rm Edd}$ quasars breaks our belief on the extremely rapidly growing SMBHs in the early universe, and brought out more questions.

1.5 Black Hole-Galaxy Co-evolution at High Redshift

For the last few decades, a lot of research has been done on SMBHs and their host galaxies, suggesting that the properties of the both of them are correlated (e.g., $M_{\rm BH}$, spheroidal bulge mass, stellar velocity dispersion; Magorrian et al. 1998; Ferrarese, & Merritt 2000; Gebhardt et al. 2000; McLure & Dunlop 2002; Kormendy & Ho 2013 and references therein). This indicates that they co-evolve with each other, despite a vast difference in physical scale (pc versus kpc). Based on the ΛCDM cosmology, the hierarchical growth via mergers is a currently popular scenario for the SMBH-galaxy co-evolution (e.g., Di Matteo et al. 2005; Springel et al. 2005; Hopkins et al. 2008; Hickox et al. 2009; Lapi et al. 2014). The galaxy merger drives the gas inflow to the central region, triggering both the star formation and the SMBH growth. But the central BH is obscured until the covered gas and dust are expelled, called blowout phase observed as an obscured quasar; IR quasars (Zheng et al. 2002; Hao et al. 2005, 2008) or red quasars (Glikman et al. 2007; Georgakakis et al. 2009; Kim et al. 2015b; Kim & Im 2018). After most of the dust removed, the quasar shines without obscuration, an active phase radiating at UV-to-optical wavelengths, which can be identified as type 1 quasars with broad emission lines. Figure 1.8 shows the evolutionary scenario clearly.

At high redshift at $z \gtrsim 6$, quasar host galaxies are actively being studied as well as their central SMBHs. Since a huge amount of rest-UV/optical lights emitted from

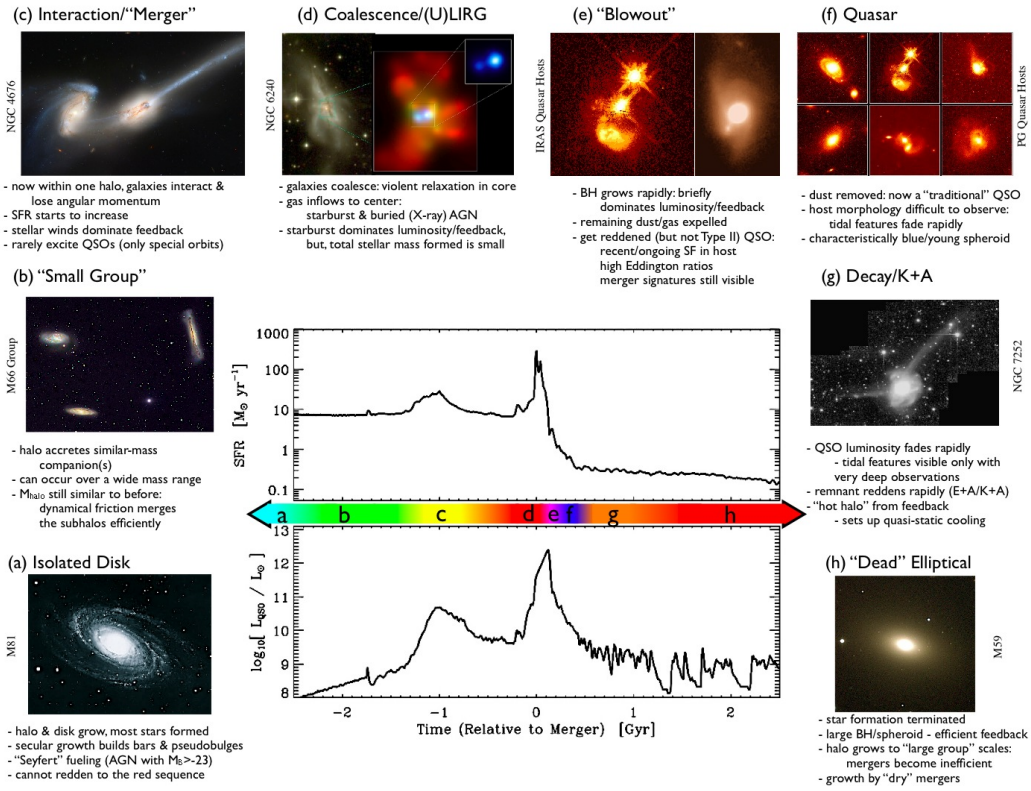

Figure 1.8. Pictorial outline of the galaxy-merging scenario, triggering both the star formation and SMBH growth. This figure is adapted from Hopkins et al. (2008).

the central engine, it is virtually impossible to observe their host galaxies at those wavelengths with current ground-based telescopes. Instead, the dust components that are observable at infrared (IR) wavelengths, where the quasar is not an absolutely dominant contributor to the fluxes, are mainly investigated to understand the host-galaxy properties. Jiang et al. (2010) reported the hot-dust-poor (dust temperature $T_d < 1500$ K) quasars at $z \sim 6$, which can be regarded as quasars too young for hot dust to form. Also, Jun et al. (2015) found that the fraction of hot-dust-poor quasars increases with redshift, which is consistent with the rapid SMBH growth in the early universe (Section 1.4).

For cool dust emission ($T_d < 60$ K), early observations in the sub-mm regions (or FIR in the rest frame) manifested that the host galaxies of bright high-redshift quasars are already metal-enriched at $z \gtrsim 6$ (Bertoldi et al. 2003a,b; Walter et al. 2003, 2009; Maiolino et al. 2005; Wang et al. 2008, 2011). The recent sub-mm observations of high-redshift quasars with the Atacama Large Millimeter/submillimeter Array (ALMA) have revealed that most of the high-redshift quasars are hosted by starburst galaxies with high FIR luminosities of $L_{\rm FIR} \gtrsim 10^{11}\ L_{\odot}$ (Wang et al. 2013; Willott et al. 2013, 2015, 2017; Bañados et al. 2015a; Venemans et al. 2016, 2018; Decarli et al. 2018; Izumi et al. 2018, 2019). The star formation rates (SFRs) that traced by the $L_{\rm FIR}$ of the host galaxies are widely spanned but mostly high (from 10 to 2000 $M_{\odot}$ yr^{-1}), implying that quasar host galaxies at high redshift are actively growing system like ultra-luminous infrared galaxies (ULIRGs) at low redshift.

Such a rapidly growing SMBH with its ULIRG-like host galaxy can form via galaxy and halo mergers in a short time scale of hundreds of millions of years, according to recent theoretical simulations (e.g., Li et al. 2007; Sijacki et al. 2009; Khandai et al. 2012; Pezzulli et al. 2016). As the SMBH grows, strong quasar outflows from the active central engine can suppress the star formation within its host galaxy (Khandai et al. 2012; DeGraf et al. 2017; Barai et al. 2018), which is consistent with the observations that a portion of high-redshift quasars has relatively low SFR values (Willott et al. 2013, 2015, 2017; Izumi et al. 2018, 2019). For the large sample of the most luminous

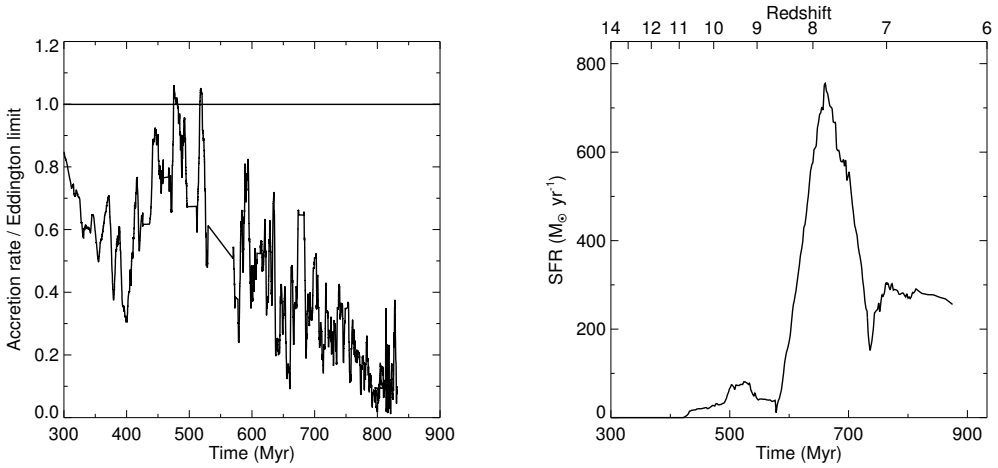

Figure 1.9. BH accretion rates (left) and SFRs (right) of a simulated quasar and its host galaxy. This figure is adapted from Smidt et al. (2018).

high-redshift quasars ($L_{\rm bol} \gtrsim 10^{13}\ L_{\odot}$), however, there is no significant correlation between $L_{\rm bol}$ and $L_{\rm FIR}$ (Venemans et al. 2018), although $L_{\rm bol}$ of a quasar is regarded as an indicator of its SMBH activity. On the other hand, it is also suggested that early growth of high-redshift quasars at $z > 7$ results in the low $\lambda_{\rm Edd}$ (~ 0.1) with high SFR values ($> 100\ M_{\odot}\ {\rm yr}^{-1}$) at $z \sim 6$, owing to the mature SMBH with metal enrichment in the host galaxy (Smidt et al. 2018; see Figure 1.9). Interestingly, it has been recently reported that there are high-redshift quasars with low $\lambda_{\rm Edd}$ (Mazzucchelli et al. 2017; Kim et al. 2018; Onoue et al. 2019; Shen et al. 2019), where $\lambda_{\rm Edd}$ is also an observable indicator of SMBH activity. Therefore, it is important to figure out the host galaxies of the low $\lambda_{\rm Edd}$ quasars at $z \gtrsim 6$, which will allows us to examine the co-evolution of the first SMBHs and their host galaxies.

1.6 Thesis Outline

The thesis is organized as follows. In the following chapters, we present the full details of the various studies undertaken to address the contents and questions covered in this chapter. In Chapter 2, we describe the survey of faint quasars at $z \sim 6$ with the discovery of a faint quasar IMS J2204+0112 $z \sim 6$, and its implications to the cosmic reionization. The $M_{\rm BH}$ and $\lambda_{\rm Edd}$ estimations of IMS J2204+0112 with deep NIR spectroscopy are presented in Chapter 3. The observational evidence for the co-evolution of low $\lambda_{\rm Edd}$ quasars and their host galaxies at $z \gtrsim 6$ are presented in Chapter 4. In Chapter 5, we describe the discovery of faint $z \sim 5$ quasars with the medium-band-based approach. The thesis conclusion is remarked in Chapter 6.

Chapter 2

Survey of Faint $z \sim 6$ Quasars in IMS and Implications for the Cosmic Reionization[†]

2.1 Introduction

Several dozens of quasars are now identified at $z \gtrsim 6$ (Fan et al. 2001, 2006; Wolf et al. 2003; Richards et al. 2006; Fontanot et al. 2007; Willott et al. 2010b; Mortlock et al. 2011; Venemans et al. 2013, 2015a,b; Bañados et al. 2014, 2016, 2018; Kashikawa et al. 2015; Kim et al. 2015a; Wu et al. 2015; Jiang et al. 2016; Matsuoka et al. 2016, 2018a,b, 2019; Wang et al. 2016; Reed et al. 2017). They are found to be powered by supermassive black holes (SMBHs) with masses of $10^8 - 10^{10}$ $M_\odot$ (Jiang et al. 2007; Willott et al. 2010a; Mortlock et al. 2011; Jun et al. 2015), shining at the Eddington limit, meaning that they are accreting mass at their maximal rates (Willott et al. 2010a; Jun et al. 2015), and some of them show paucity of hot dust emission (Jiang et al. 2010; Jun & Im 2013) in contrast to quasars at low redshift (Kim et al. 2015b). These results suggest that high-redshift quasars already harbor SMBHs at their centers just ~ 1 Gyr after

[†]This chapter is a revised version of the article published in *The Astrophysical Journal Letters* in November 2015 (Kim et al. 2015a).

the Big Bang, and these SMBHs are growing more vigorously than their counterparts at low redshift. Furthermore, strong Gunn-Peterson troughs (Gunn & Peterson 1965) in their spectra suggest that a significant fraction of the intergalactic medium (IGM) is reionized at $z \sim 6$ (Fan et al. 2006). However, two interesting questions still remain due to the lack of known faint quasars at $z \gtrsim 6$ ($M_{1450} > -24$ mag).

First, while the bright end of the $z \sim 6$ quasar luminosity function (QLF), which is not sufficient to reionize the IGM, is well constrained, the faint end of the function is still debated. Recently, Giallongo et al. (2015) found 22 faint active galactic nuclei (AGNs) candidates with X-ray detections at $z > 4$, indicating that there are more faint AGNs than previously expected, and the faint AGNs could be main contributors to the reionization of the universe (Glikman et al. 2011; Madau & Haardt 2015). Unfortunately, the number of spectroscopically confirmed $z \sim 6$ faint quasars is very small (only a few; Willott et al. 2009; Kashikawa et al. 2015). Consequently, the faint end of the QLF at $z \sim 6$ is still very uncertain, and the potential role of this population in the reionization of the early universe is yet unclear.

Second, most of the $z \sim 6$ quasars discovered so far are luminous, $M_{1450} < -24.5$ mag ($z' < 22$ mag), implying that the currently discovered sample of high-redshift quasars is biased to objects with high accretion rates. Such a bias hinders our understanding of the range of accretion rates of quasars in the early universe.

Recently, we have been performing the Infrared Medium-deep Survey (IMS), a moderately wide (120 deg^2), and moderately deep ($J \sim 22.5 - 23$ mag) near-infrared (NIR) imaging survey with the Wide Field Camera (WFCAM; Casali et al. 2007) on the United Kingdom InfraRed Telescope (UKIRT). One of the main scientific aims of the IMS is to discover faint quasars at $z \sim 6$ and beyond. We combined the NIR imaging data from the IMS with optical data from the Canada-France-Hawaii Telescope Legacy Survey (CFHTLS; Hudelot et al. 2012) and other Canada-France-Hawaii Telescope (CFHT) PI programs, and we employed multiple color selection criteria to identify $z \sim 6$ quasar candidates. Here, we present the discovery of the first IMS faint quasar at $z \sim 6$, and we discuss how this can constrain the sources responsible for the reionization

of the universe.

In this chapter, we assumed the cosmological parameters of $\Omega_m = 0.3$, $\Omega_\Lambda = 0.7$ (e.g., Im et al. 1997), and $H_0 = 70$ km s^{-1} Mpc^{-1}. All magnitudes are given in the AB system.

2.2 IMS and CFHTLS Data

The IMS includes seven extragalactic fields (M. Im et al. 2019, in preparation), among which four fields cover the survey area of the CFHTLS: XMM-Large Scale Structure survey region (XMM-LSS), CFHTLS Wide survey second region (CFHTLS-W2), Extended Groth Strip (EGS), and Small Selected Area 22h (SA22). Note that the XMM-LSS and SA22 fields are also covered by the the Deep eXtragalactic Survey (DXS; Lawrence et al. 2007) with WFCAM on the UKIRT, thus we used the NIR data of the survey together. For the sake of convenience, hereafter, we refer to the combined NIR dataset from the IMS and DXS surveys as "IMS". Each stacked CFHTLS image from the TERAPIX processing pipeline (Hudelot et al. 2012) covers the 1 deg^2 area, while each stacked IMS image covers a $13\farcm65 \times 13\farcm65$ area. We generated images that overlap the CFHTLS and IMS tiles for the forced photometry described below. Overall, the total survey area where CFHTLS and IMS overlap is ~ 86 deg^2.

The CFHTLS optical images of these four fields have almost uniform imaging qualities with homogeneous 5σ detection limits for a point source with an aperture that we used for following photometry (diameter of $2\times$FWHM$_{z'}$): $u' = 26.0$ mag, $g' = 26.4$ mag, $r' = 25.9$ mag, $i' = 25.6$ mag, and $z' = 24.6$ mag. Note that the i' filter here indicates the both i'_1 and i'_2 filters of MegaCam on CFHT, which were changed from i'_1 to i'_2 filters during the survey; about 18% of the total survey area was observed in i'_2 band. Adopting the transmission curves of the CFHTLS filters to the stellar templates of Pickles (1998), we found a relation of

$$i'_1 - i'_2 \approx -0.08(r' - i'_2). \tag{2.1}$$

This relation , however, is inappropriate to convert i'_2 to i'_1 for $z \sim 6$ quasars, because (1) the relation is from stellar spectra that is different from high-redshift quasar spectra and (2) the r'-band fluxes of $z \sim 6$ quasars are expected to be fainter than the detection limits of CFHTLS owing to the IGM attenuation by neutral hydrogen. In the following sections, we will use the same color selection criteria for both i'_1- and i'_2-band magnitudes (Section 2.3), while the magnitudes will be used separately to calculate the selection functions and QLFs at $z \sim 6$ (Section 2.5).

On the other hand, for the IMS data, the NIR images of the XMM-LSS and SA22 fields are about an magnitude deeper ($J = 23.8$ mag) than those of the other two fields (CFHTLS-W2 and EGS; $J = 22.8$ mag). Figure 2.1 shows the position and coverage of each field with the limiting magnitudes in 5σ level. In Table 2.1, we summarize information of the four fields.

For accurate photometry to find faint quasars at $z \sim 6$, we recalculated the zero-point (zp) values of the optical and NIR images. For the optical data, we used the unsaturated sources of which magnitudes are between 17.5 and 21.0 mag in the point source catalog of the first part of the Panoramic Survey Telescope and Rapid Response System (PS1; Chambers et al. 2016; Flewelling et al. 2016), which covers our survey area, as photometric standards. Since the PS1 photometric system is slightly different from that of CFHTLS, the PS1 magnitudes of the standard sources were converted to the CFHTLS system by following the conversion relations[1]:

- $u' - g_{\rm PS1} = 0.523 - 0.343X + 2.44X^2 - 0.998X^3$,
- $g' - g_{\rm PS1} = -0.001 - 0.004X - 0.0056X^2 + 0.00292X^3$,
- $r' - r_{\rm PS1} = 0.002 - 0.017X + 0.00554X^2 - 0.000692X^3$,
- $i'_1 - i_{\rm PS1} = 0.001 - 0.021X + 0.00398X^2 - 0.00369X^3$,
- $i'_2 - i_{\rm PS1} = -0.005 - 0.004X + 0.0124X^2 - 0.0048X^3$,
- $z' - z_{\rm PS1} = -0.009 - 0.029X + 0.012X^2 - 0.00367X^3$,

[1] http://www.cadc-ccda.hia-iha.nrc-cnrc.gc.ca/en/megapipe/docs/filt.html

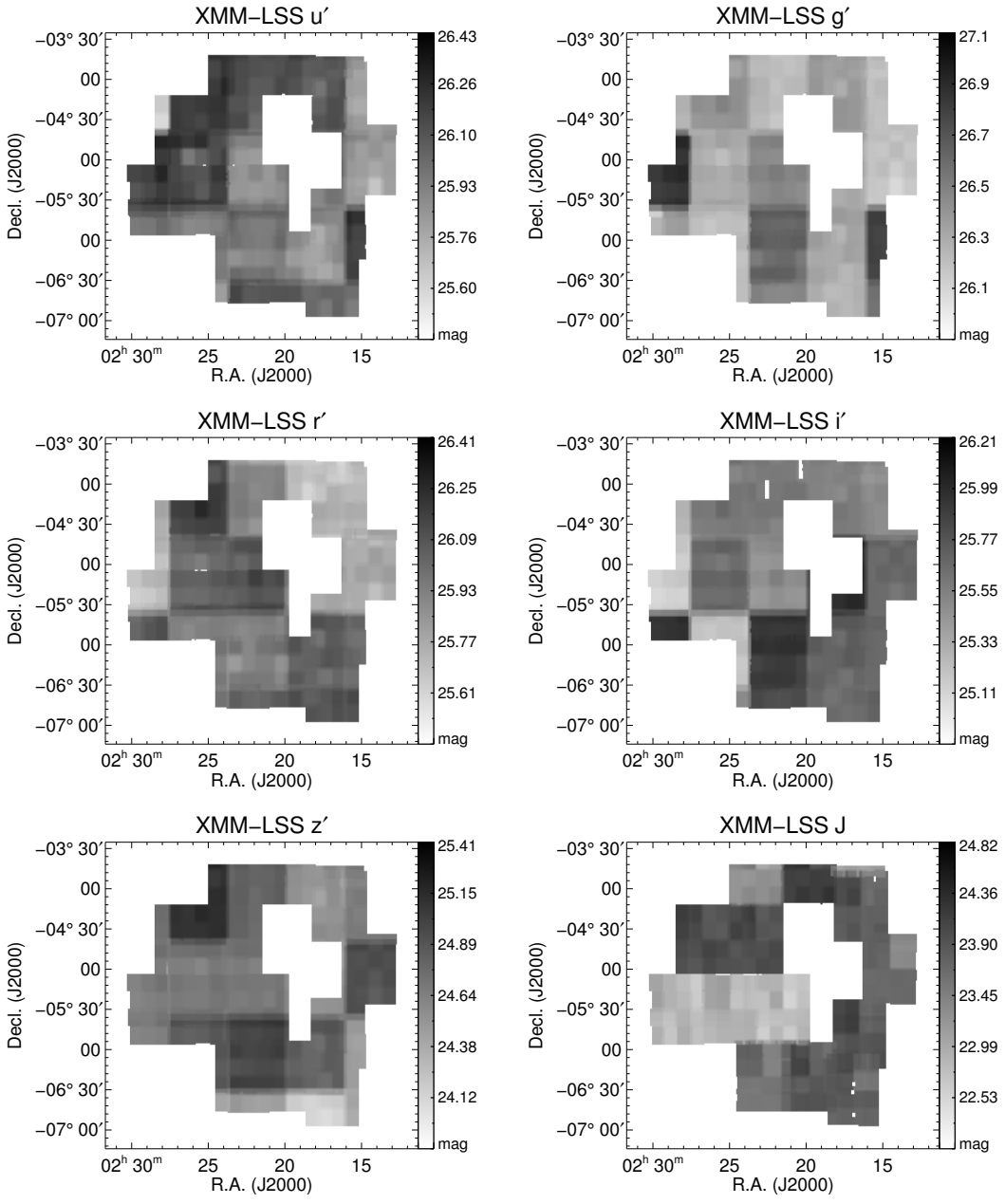

Figure 2.1. Image depth maps of CFHTLS and IMS. There are four extragalactic fields: XMM-LSS, CFHTLS-W2, EGS, and SA22. The total size of sky coverage is ~ 86 deg^2 area on the sky. The colorbars indicates the 5σ detection limits. Note that the maps in i'_1 and i'_2 bands are plotted simultaneously as the i'-band map.

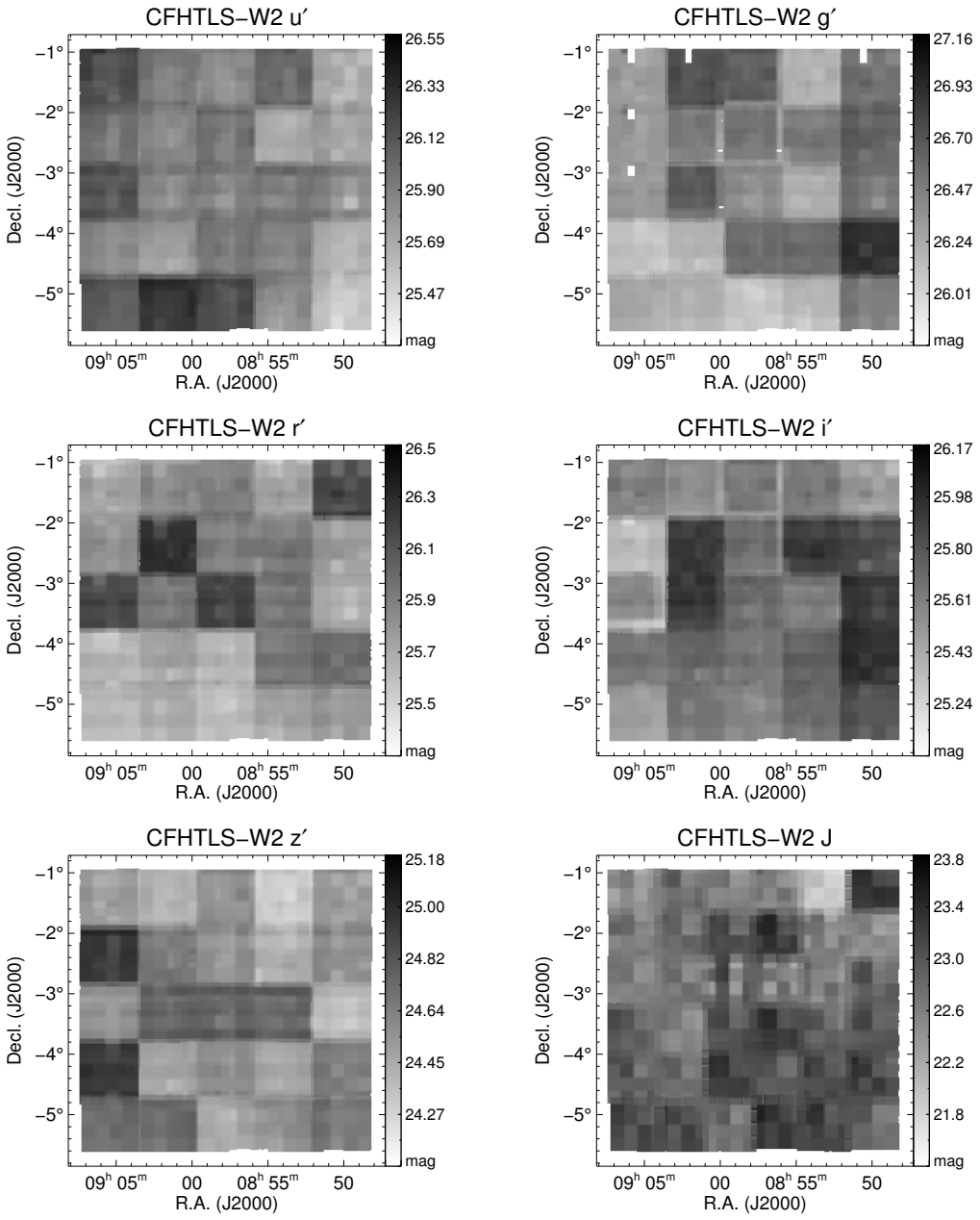

Figure 2.1. (cont'd)

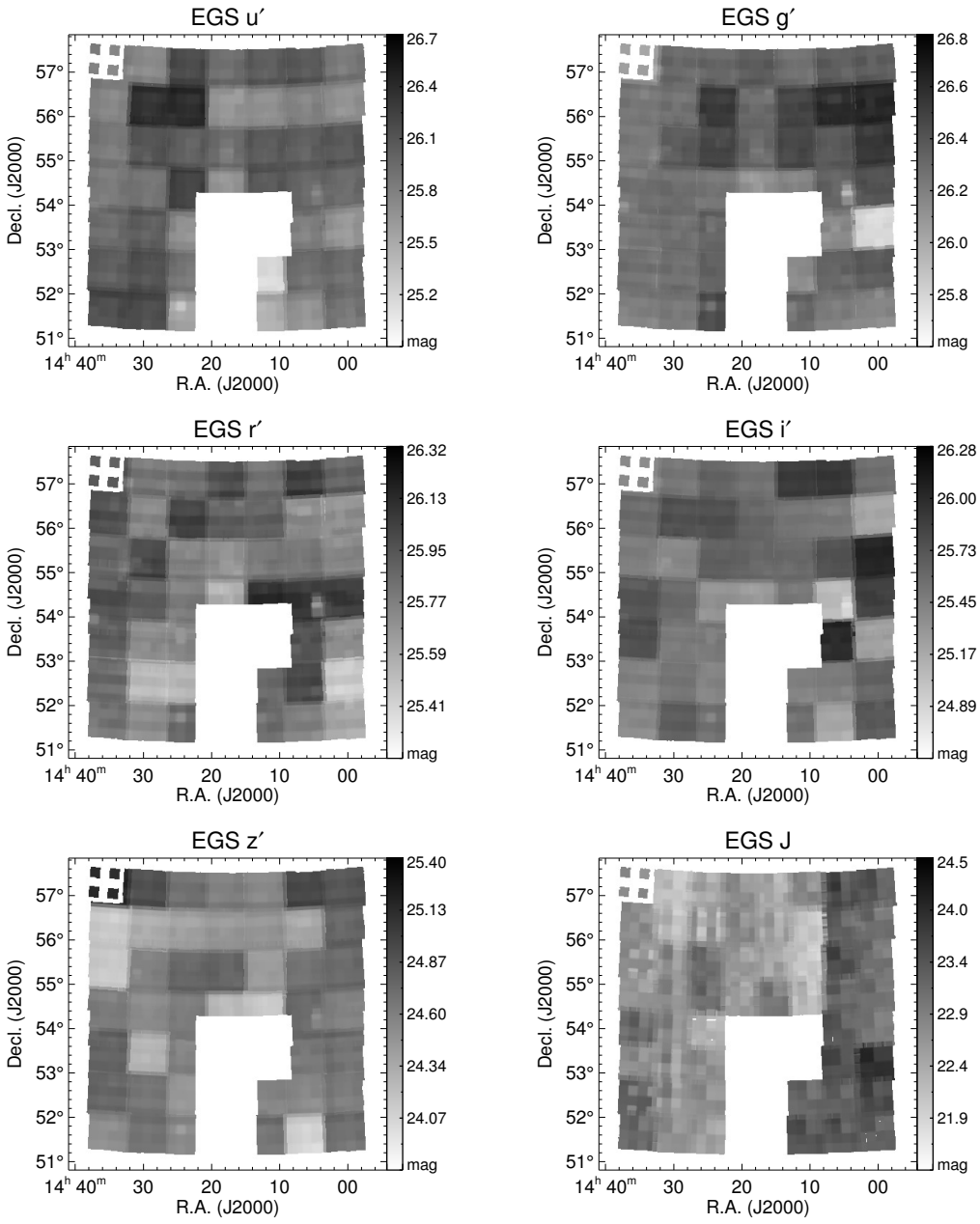

Figure 2.1. (cont'd)

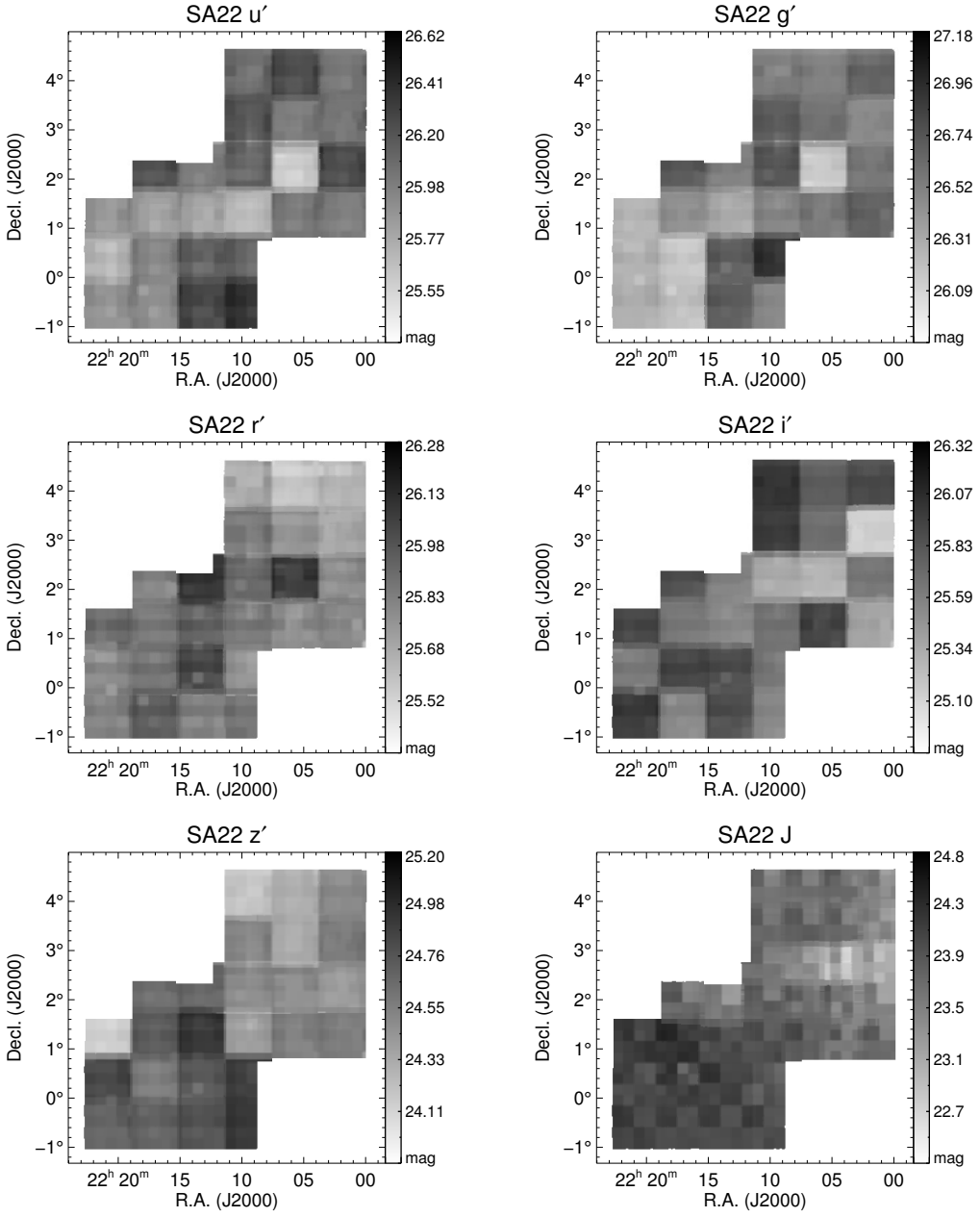

Figure 2.1. (cont'd)

where the PS1 magnitudes are addressed with a subscript of PS1, and $X = (g_{\rm PS1} - i_{\rm PS1})$.

In the case of the NIR data from IMS, we compared the bright point sources ($12 < J < 16$) with the coordinate-matched sources in the point source catalog of the Two Micron All Sky Survey (2MASS; Skrutskie et al. 2006). In order to convert 2MASS magnitudes into the UKIRT/WFCAM system, we used the relation of Hewett et al. (2006):

- $J - J_{\rm 2MASS} = -0.065(J_{\rm 2MASS} - H_{\rm 2MASS})$,

where magnitudes with a subscript of 2MASS are the 2MASS magnitudes. Figure 2.2 shows the color-color diagrams of point sources in the IMS extragalactic fields. After the *zp* recalculation, the point source distributions (gray contours) in color-color spaces are consistent with the synthetic stellar loci of SDSS/2MASS-detected stars (black solid lines; Covey et al. 2007). Just for the i'_2-band magnitudes of point sources in this figure, we adopted the Equation 2.1 to convert them to i'_1-band magnitudes.

Source detection was performed in z'-band images of CFHTLS using `SExtractor` (Bertin & Arnouts 1996). DETECT_THRESH and DETECT_MINAREA parameters were set as 1.3 and 9, respectively. Using the identified z'-band sources, we measured fluxes at bluer bands using the dual mode of the `SExtractor` software. Aperture magnitudes with $2\times$FWHM$_{z'}$ diameters (FWHM$_{z'} \sim 0\farcs7$) were used to measure fluxes, because the signal-to-noise ratio (S/N; FLUX/FLUXERR from `SExtractor`) of point source peaks for apertures with diameters of $\sim 2\times$FWHM$_{z'}$. The errors are based on pixel-to-pixel noise of our stacked images made of sub-pixel dithered frames. Note that this aperture photometry can underestimate the actual photometric error by ∼20–30% (e.g., Gawiser et al. 2006; Jeon et al. 2010; Kim et al. 2015a). The aperture fluxes were converted to total fluxes by applying aperture corrections derived using bright stars in each filter image.

Using the extinction map of Schlafly & Finkbeiner (2011), we corrected the galactic extinction with an assumption of $R_V = 3.1$ (Cardelli et al. 1989). Note that the extinction values of the four extragalactic fields are almost negligible ($\lesssim 0.05$ mag)

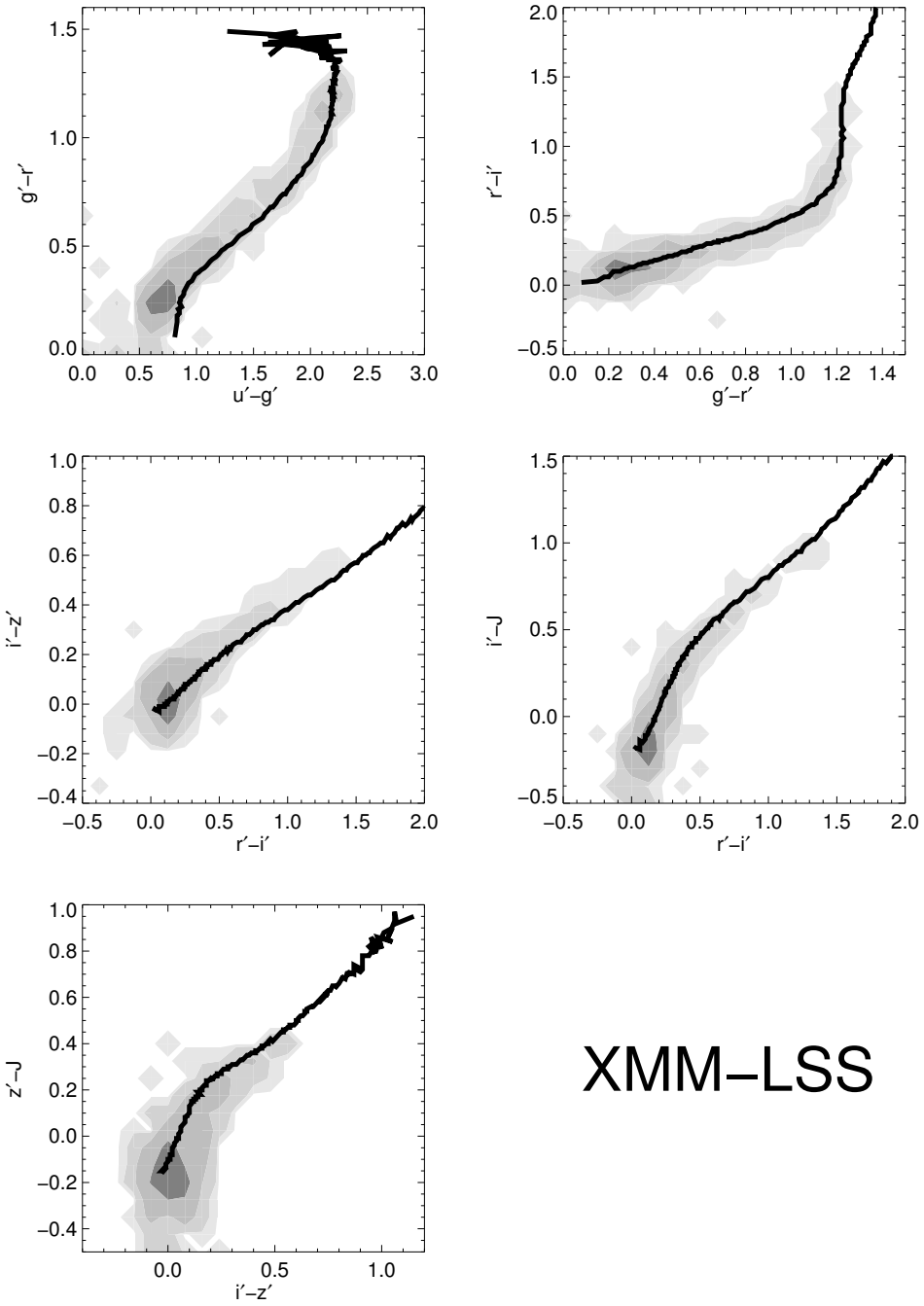

Figure 2.2. Stellar loci on color-color diagrams. The contours represent the bright point sources in the four extragalactic fields (XMM-LSS, CFHTLS-W2, EGS, and SA22), while the black solid lines are the stellar loci of Covey et al. (2007). Note that the i'_2-band magnitudes of the sources were converted to the i'_1-band magnitudes, following Equation 2.1.

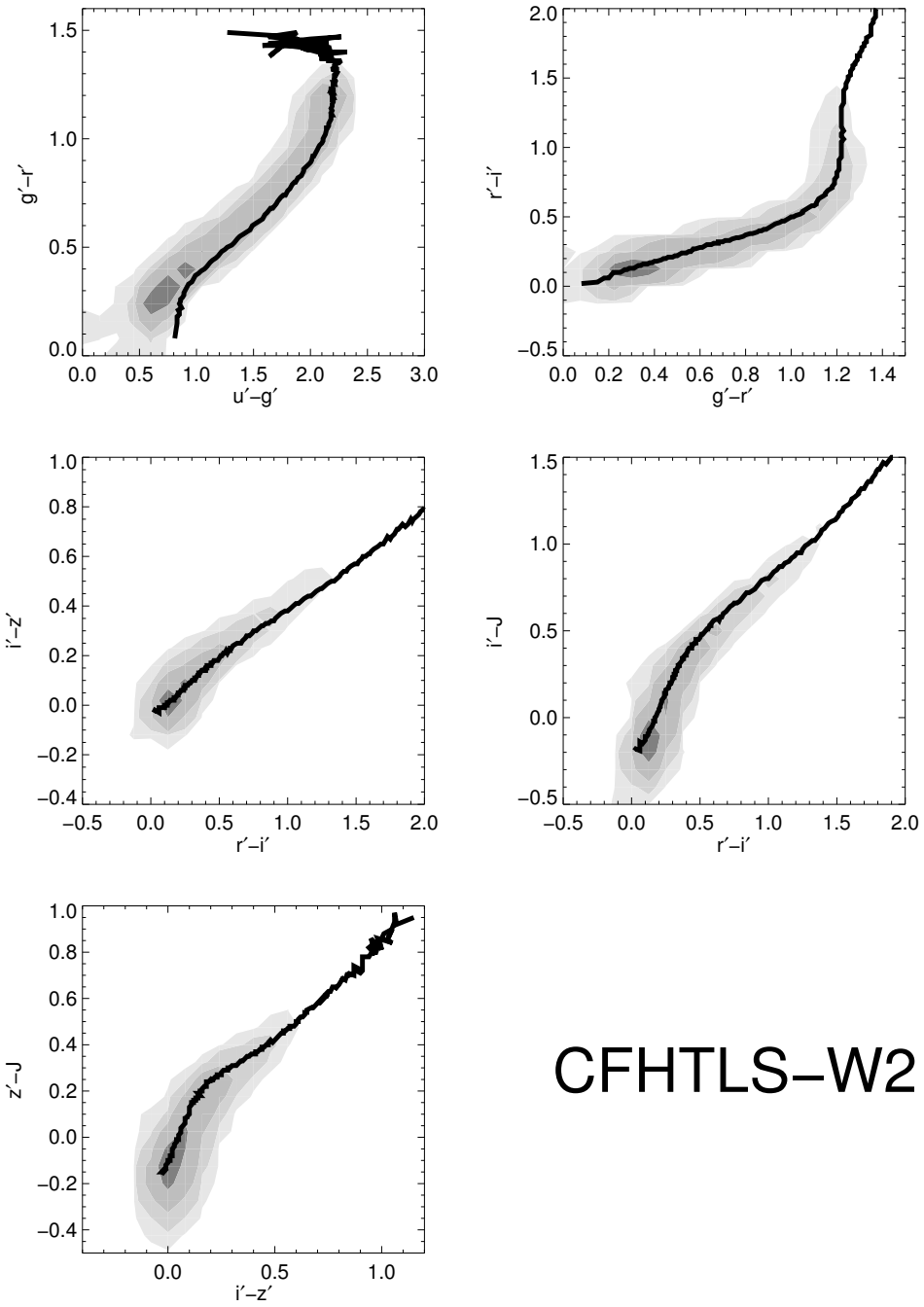

Figure 2.2. (cont'd)

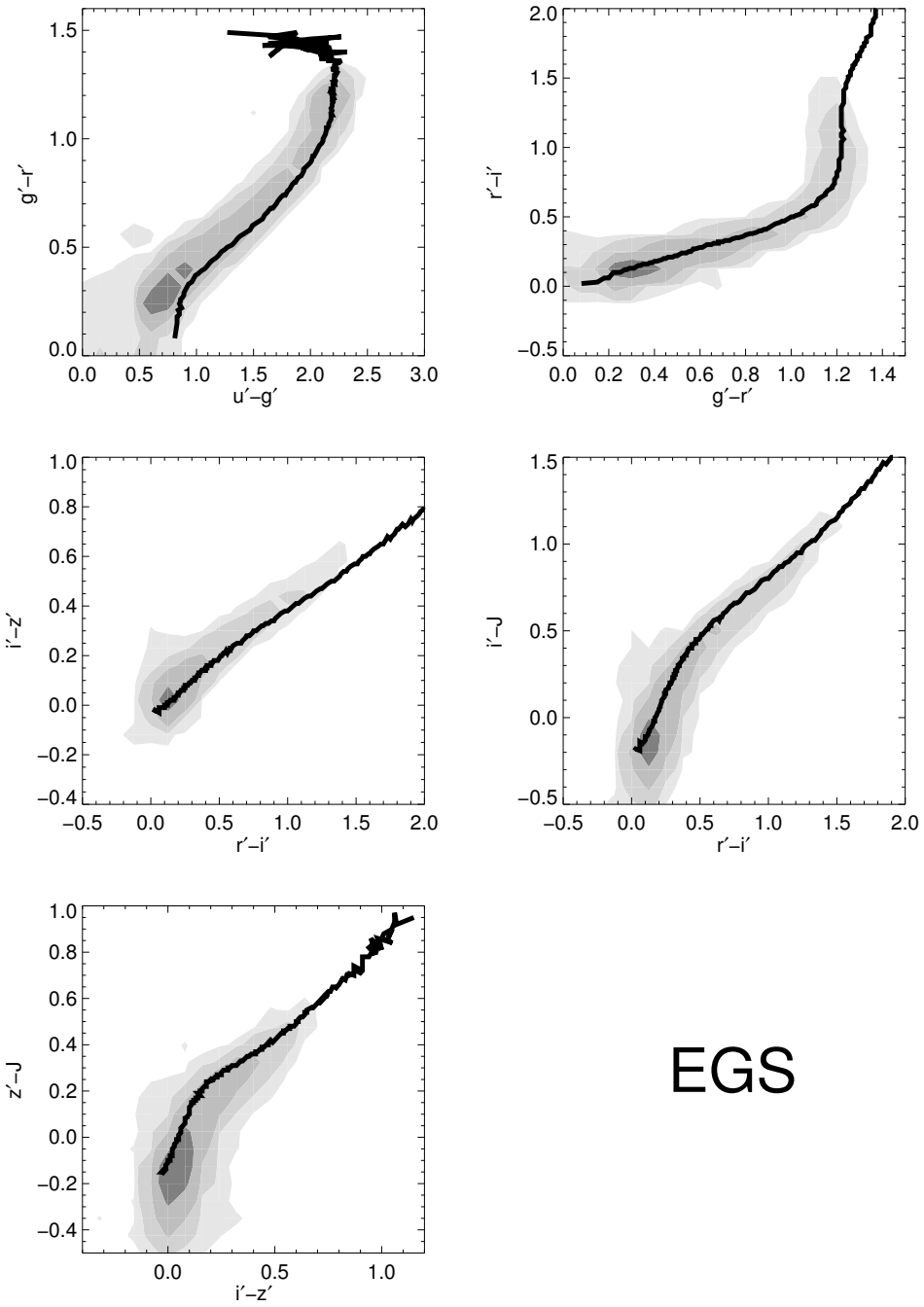

Figure 2.2. (cont'd)

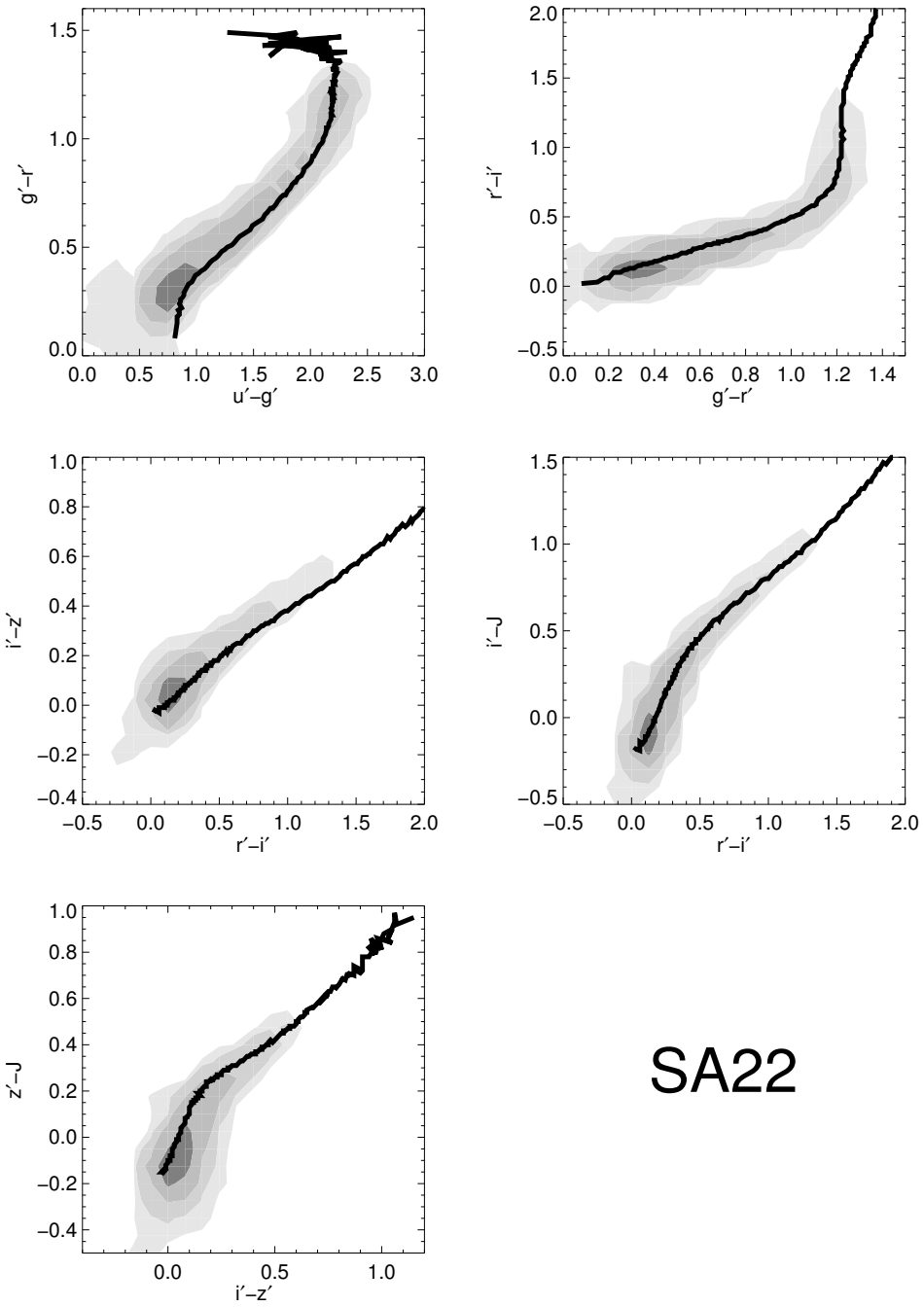

Figure 2.2. (cont'd)

For star/galaxy separation, we used the SPREAD_MODEL parameter, a star-galaxy classifier of `SExtractor`, which offers great performance to separate point sources from extended galaxies with the point spread function (PSF) model in each image[2]. Considering that a Lyα emission of a $z \sim 6$ quasar is expected to be located in z' band, we used the SPREAD_MODEL values in z' band (SPREAD_MODEL$_{z'}$) to select point sources. Figure 2.3 shows the z'-band magnitude versus SPREAD_MODEL$_{z'}$ of the sources in the four extragalactic fields. The point sources in the range of $-0.006 <$ SPREAD_MODEL$_{z'} < 0.006$ (dashed lines) are well separated from contaminants consisting of saturated and extended sources, thus we excluded objects outside this range. In addition to this, we reject objects that have FLAGS$\neq 0$ in the `SExtractor`-produced catalogs to avoid saturated/blended objects.

[2]https://sextractor.readthedocs.io/en/latest/Model.html

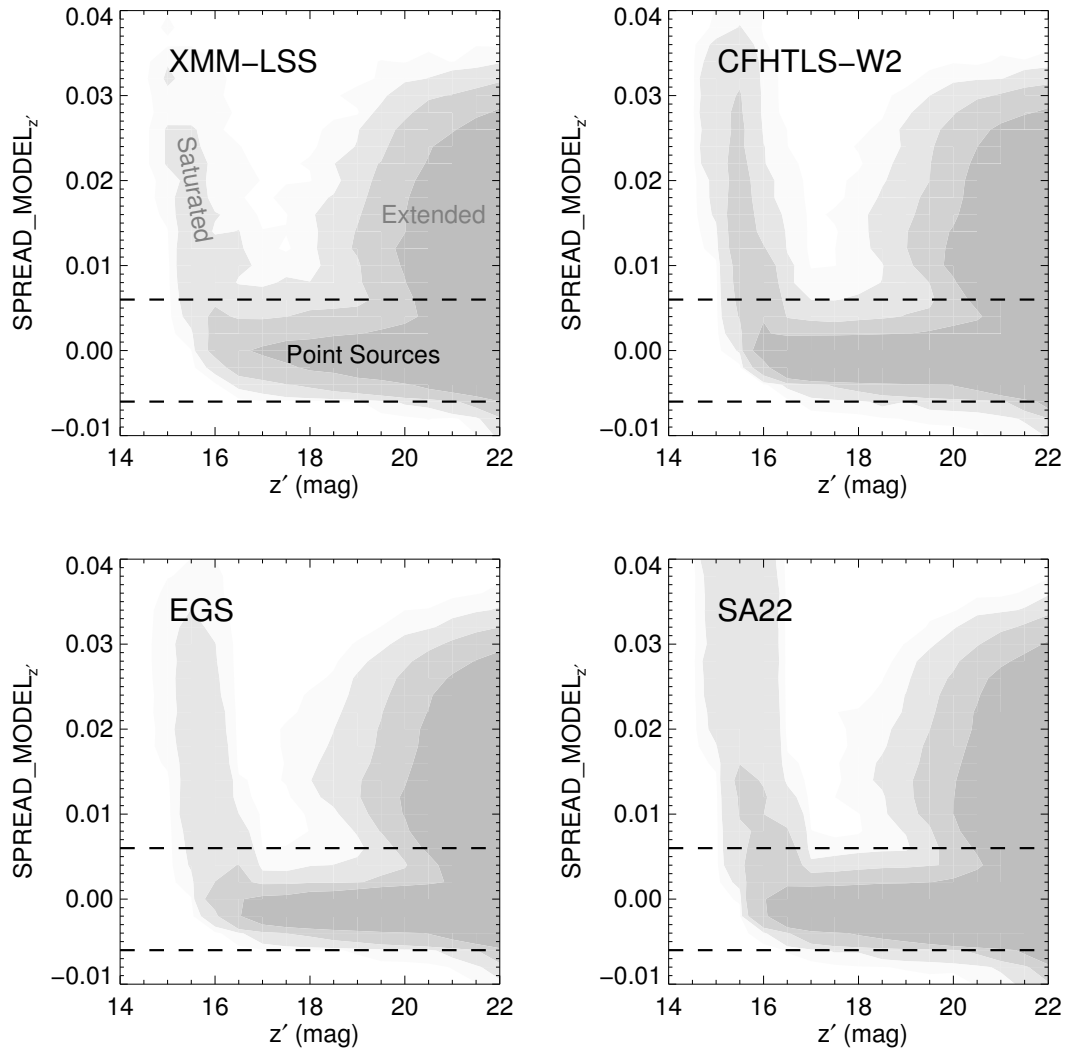

Figure 2.3. z'-band magnitudes versus SPREAD_MODEL$_{z'}$ diagrams of the four extragalactic fields. The gray contours show the detected sources in each field, while the black dashed lines represent the selection criteria for the point sources ($-0.006 <$ SPREAD_MODEL$_{z'} < 0.006$).

Table 2.1. Four Extragalactic Fields in CFHTLS and IMS

Field	R.A. (J2000)	Decl. (J2000)	Area[a] (deg^2)	5σ detection limit[b] (mag) / Seeing (arcsec)						
				u'	g'	r'	i'_1	i'_2	z'	J
XMM-LSS[c]	02:21:00	−05:00:00	8.7 (6.1/3.0)	26.0 / 0.92	26.4 / 0.86	26.0 / 0.71	25.6 / 0.74	25.7 / 0.65	24.7 / 0.71	23.7 / 0.85
CFHTLS-W2	08:58:00	−03:20:00	22.1 (20.7/2.0)	25.9 / 0.88	26.4 / 0.80	25.9 / 0.73	25.7 / 0.65	25.8 / 0.61	24.6 / 0.69	22.9 / 0.90
EGS	14:18:00	+54:30:00	34.5 (29.7/6.2)	25.9 / 0.85	26.3 / 0.82	25.8 / 0.73	25.5 / 0.67	25.9 / 0.54	24.6 / 0.64	22.8 / 0.88
SA22[c]	22:11:00	+01:50:00	21.1 (16.8/4.7)	26.0 / 0.82	26.5 / 0.76	25.8 / 0.605	25.7 / 0.64	25.9 / 0.56	24.6 / 0.64	23.8 / 0.82

[a]The size of an area where CFHTLS and IMS overlap, while the sizes of an area observed in i'_1 and i'_2 bands are also presented.

[b]Median values for a point source with an aperture size of $2\times\mathrm{FWHM}_{z'}$.

[c]These fields include the NIR data from DXS.

2.3 Quasar Candidate Selection

The spectral energy distributions (SEDs) of quasars at $z \sim 6$ show a sudden break blueward of Lyα (rest-frame 1216 Å) due to the Gunn-Peterson effect (Gunn & Peterson 1965). The break is located at $\lambda \sim 8500$ Å for a quasar at $z \sim 6$, which creates a very red $i' - z'$ color, but blue colors at longer wavelengths due to AGN continuum emissions. Therefore, we used following color selection criteria:

1. $i' - z' > 2.0$,
2. $z' - J < 0.625((i' - z') + 0.1)$,

where the 3σ detection limit in each band is marked with a subscript of 3σ. The first color cut samples objects with a strong break at $\lambda \sim 8500$ Å, and the second criterion removes red stars such as brown dwarfs. Figure 2.4 shows the color-color diagram for point sources in our survey data, and the color selection criteria. Considering the IGM attenuation by neutral hydrogen, we ruled out the sources detected in u'-, g'-, and r'-band images (3σ level). On the other hand, to narrow down the number of plausible candidates, we selected the sources of which J-band magnitudes are brighter than the 5σ detection limits, in addition to the magnitude cut of $z' < 23.5$ mag.

Spurious detections of image artifacts, such as diffraction spikes or hot pixels, could produce a number of false i'-dropout objects with very red $i' - z'$ colors that satisfy the color selection criteria. To remove spurious sources, we performed visual inspection in all filter images to finalize the quasar candidate selection. For the selected objects that are also covered by the Hyper Suprime-Cam Subaru Strategic Program (HSC SSP; Aihara et al. 2018a), Data Release 1 (Aihara et al. 2018b), we cross-checked whether their $i_{\rm HSC} - z_{\rm HSC}$ colors are also as red as $i_{\rm HSC} - z_{\rm HSC} > 1.5$. Through this process, we selected 13 quasar candidates at $z \sim 6$. We listed the photometry of these $z \sim 6$ quasar candidates in Table 2.2.

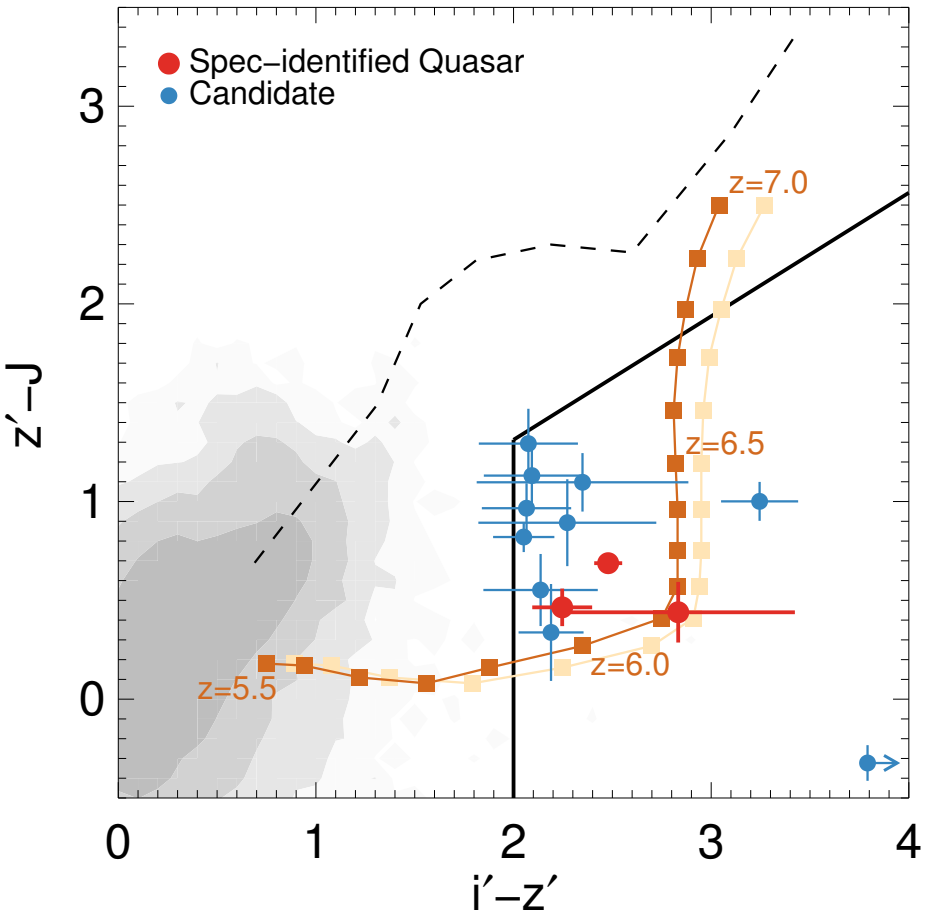

Figure 2.4. Color-color diagram to identify quasar candidates at $z \sim 6$. The spectroscopically identified $z \sim 6$ quasars are the red points, while the quasar candidates selected by our color selection criteria (black solid line) are shown as the blue points with error bars. Note that the arrows indicate the lower limit of color. The brown squares with a solid line represent a quasar evolution track at $5.5 < z < 7.0$ in bins of 0.1 based on i'_1-band magnitudes, while the light brown ones are that based on i'_2. The black dashed line is the mean color distribution of M/L/T dwarfs (Willott et al. 2005). The gray contours are sources classified as isolated point sources in our survey data.

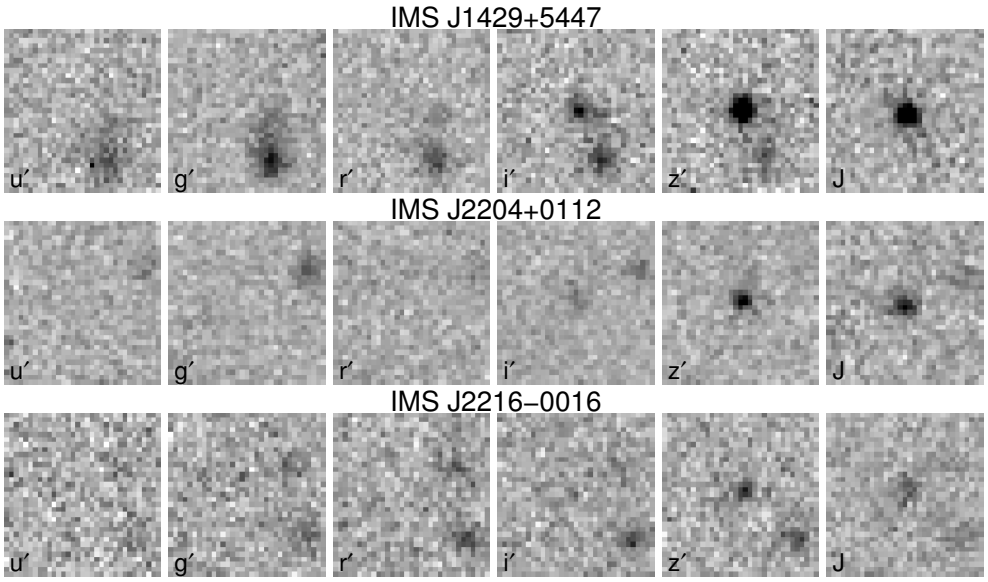

Figure 2.5. Postage stamp images of spectroscopically identified $z \sim 6$ quasars presented in $6'' \times 6''$ boxes. From left to right, u'-, g'-, r'-, i'-, z'-, and J-band images are shown.

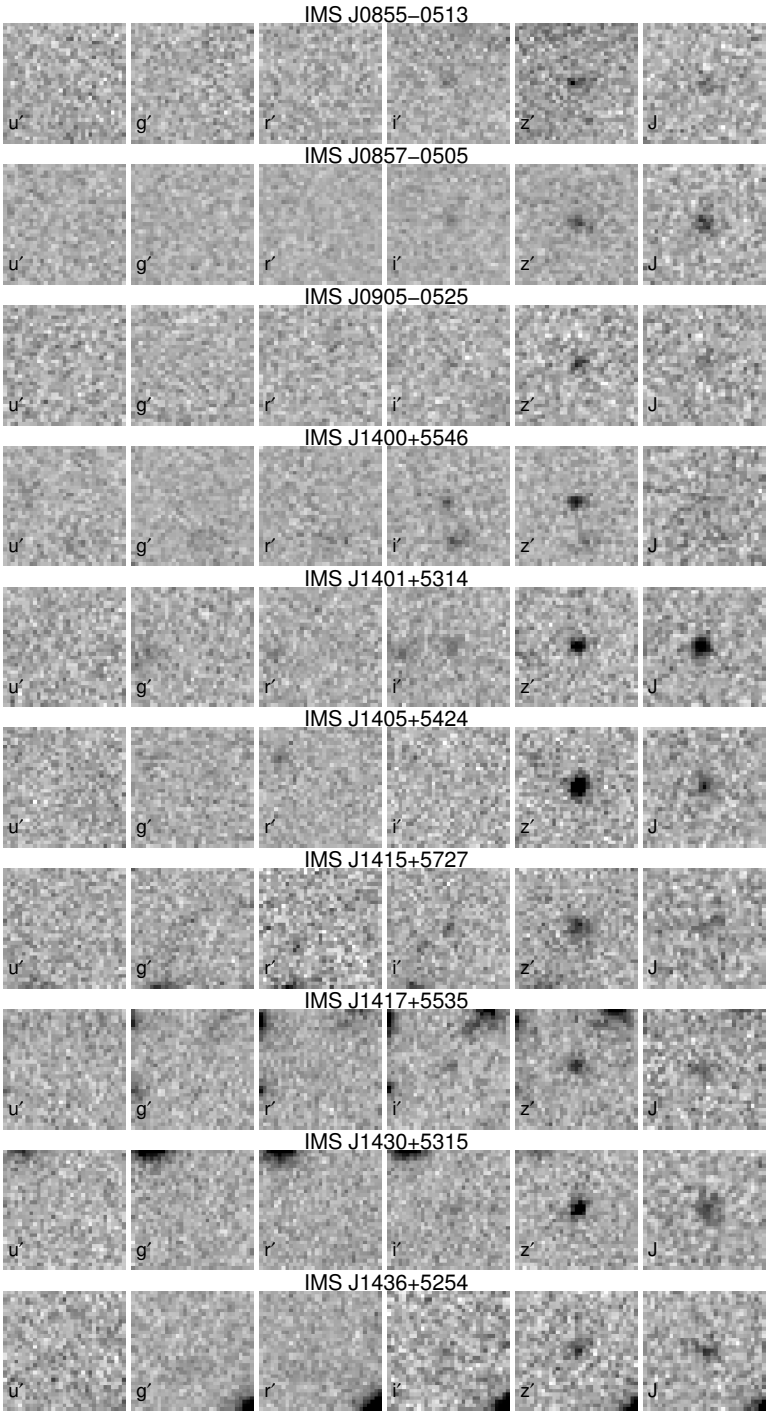

Figure 2.6. Postage stamp images of $z \sim 6$ quasar candidates presented in $6'' \times 6''$ boxes. From left to right, u'-, g'-, r'-, i'-, z'-, and J-band images are shown.

Table 2.2. Candidates for Quasars at $z \sim 6$

ID	R.A. (J2000)	Decl. (J2000)	i' (mag)	z' (mag)	J (mag)
IMS J0855−0513	08:55:50.30	−05:13:46.0	25.38 ± 0.27	23.25 ± 0.10	22.69 ± 0.15
IMS J0857−0505	08:57:55.94	−05:05:14.2	25.22 ± 0.21	23.16 ± 0.09	22.19 ± 0.09
IMS J0905−0525	09:05:53.65	−05:25:17.9	25.75 ± 0.43	23.48 ± 0.13	22.58 ± 0.18
IMS J1400+5546	14:00:01.31	+55:46:19.3	25.37 ± 0.15[d]	23.18 ± 0.07	22.85 ± 0.23
IMS J1401+5314	14:01:21.47	+53:14:33.5	24.94 ± 0.14	22.89 ± 0.06	22.07 ± 0.05
IMS J1405+5424	14:05:03.69	+54:24:35.0	> 25.70	21.91 ± 0.03	22.23 ± 0.09
IMS J1415+5727	14:15:56.03	+57:27:08.9	25.14 ± 0.23	23.05 ± 0.07	21.92 ± 0.15
IMS J1417+5535	14:17:51.61	+55:35:04.4	25.43 ± 0.24	23.35 ± 0.09	22.06 ± 0.15
IMS J1429+5447[a]	14:29:52.18	+54:47:17.7	23.97 ± 0.07	21.49 ± 0.02	20.81 ± 0.04
IMS J1430+5315	14:30:54.67	+53:15:20.3	25.44 ± 0.19	22.19 ± 0.05	21.19 ± 0.09
IMS J1436+5254	14:36:39.37	+52:54:51.7	25.74 ± 0.52	23.39 ± 0.11	22.29 ± 0.10
IMS J2204+0112[b]	22:04:17.93	+01:11:44.8	25.15 ± 0.14	22.90 ± 0.06	22.44 ± 0.07
IMS J2216−0016[c]	22:16:44.48	−00:16:50.1	26.06 ± 0.58	23.23 ± 0.09	22.79 ± 0.12

Note. — All magnitudes are aperture magnitudes with a diameter of $2\times\mathrm{FWHM}_{z'}$, given in the AB system.

[a]CFHQS J1429+5447 with $M_{1450} = -25.85$ mag at $z = 6.21$ (Willott et al. 2010b)

[b]A spectroscopically identified quasar with $M_{1450} = -23.99$ mag at $z = 5.926$ (Kim et al. 2015a, 2018)

[c]HSC 2216−0016 with $M_{1450} = -23.56$ mag at $z = 6.10$ (Matsuoka et al. 2016)

[d]These i'-band magnitudes are obtained with the i'_2 filter.

2.4 Spectroscopic Data

2.4.1 Gemini/GMOS Observation of IMS J2204+0112

Among the six high-priority quasar candidates at $z \sim 6$, IMS J2204+0112 was given the highest priority for follow-up spectroscopy due to small magnitude errors ($\Delta z' \sim 0.06$, $\Delta J \sim 0.07$; see Table 2.2), the location of the object in the selection box, and its point-like shape in z'- and J-band images (see Figure 2.6). We observed this target with the Gemini Multi-Object Spectrograph (GMOS; Hook et al. 2004) on the 8m Gemini-South Telescope in Chile, on 2015 July 21 and 23 (Program ID: GS-2015A-Q-201).

The observation was carried out using the Nod & Shuffle (N&S) longslit mode with the R150_G5326 grating to facilitate skyline subtraction. We set the central wavelength to 9000 Å to avoid hot columns and spurious charges in one of the CCD chips that had a technical problem. Since we wanted to cover the gap between each CCD chip, the observation was made with two configurations of the grating with central wavelengths of 8900 and 9000 Å. We adopted the N&S slit with $1\farcs0$ width and 4×4 pixel binning for maximal S/N, which gives a spectral resolution of 7.72 Å pixel^{-1} ($\sim$ 290 km s^{-1}). In addition, the RG610_G0331 filter was used to avoid the order-overlap. Each N&S sequence contained eight cycles of 60 s exposure and together with overheads, lasted 968 s. Although we observed 12 sequences for IMS J2204+0112, which gives a total exposure time of $\sim$ 3 hr, we opted to use only five frames that were taken during good weather conditions (seeing $\lesssim 1\farcs0$, gray night).

We followed the standard data reduction procedure with the IRAF/Gemini package: (1) bias subtraction and flat-fielding, (2) sky subtraction with shuffled spectra, (3) wavelength calibration with the CuAr arc lines, and (4) flux calibration with a spectrophotometric star (LTT 7987). After the flux calibration, we adjusted the overall flux scale using the photometric magnitude in the z'-band. Note that there is the most up-to-date z-band magnitude of this quasar from HSC SSP DR1 (Aihara et al. 2018a,b), thus we used the z-band magnitude of $z = 22.55$ mag instead (see details in Section 3.2 and Kim et al. 2018).

Figure 2.7 shows the spectrum of IMS J2204+0112. It shows a clear break at $\sim$ 8422 Å that can be identified as the redshifted Lyα line. We fit the spectrum with a composite spectrum of SDSS quasars (Vanden Berk et al. 2001), including the IGM attenuation (Madau et al. 1996), using the robust non-linear least square method with the IDL MPFIT package (Markwardt 2009). The fit with the composite spectrum matches the observed spectrum of IMS J2204+0112 well and gives a redshift of $z = 5.926 \pm 0.002$. We estimate the absolute magnitude at the rest-frame wavelength of 1450 Å from the quasar spectrum to be $M_{1450} = -23.99 \pm 0.11$ mag. IMS J2204+0112 shows strong Lyα and N V (rest-frame 1240 Å) emission lines at around 8600 Å, while a weak Si IV (1400 Å) line can be seen at $\sim$ 9700 Å. The absolute magnitude of $M_{1450} = -23.99$ mag ranked IMS J2204+0112 as the third or the fourth faintest quasar at $z \sim 6$ discovered until 2015 (Willott et al. 2009; Kashikawa et al. 2015), depending on whether we treat the faintest quasar in Kashikawa et al. (2015) as a quasar or a Lyman break galaxy.

If we assume that the quasar is accreting at the Eddington limit ($\lambda_{\rm Edd} = 1$), then the black hole mass of the quasar is $M_{\rm BH} \sim 10^8\ M_\odot$ (Vestergaard & Osmer 2009; Jun et al. 2015). We take this values as a lower limit of $M_{\rm BH}$ since this object could have $\lambda_{\rm Edd}$ lower than 1. For more details about its central SMBH, see Section 3.

2.4.2 Supplemental Data

Among the six high-priority candidates, IMS J1429+5447, also known as CFHQS J1420+5447, was identified as a high-redshift quasar at $z = 6.21$ by Willott et al. (2010b). Also, IMS J2216−0016 was identified as a faint quasar at $z = 6.10$ (HSC J2216−0016; Matsuoka et al. 2016). Their optical spectra are plotted in Figure 2.8, which are adapted from the literature, showing clear Lyα breaks with blue continuum emissions. They have M_{1450} of −25.85 and −23.56 mag, respectively, which correspond to their J-band magnitudes in this work.

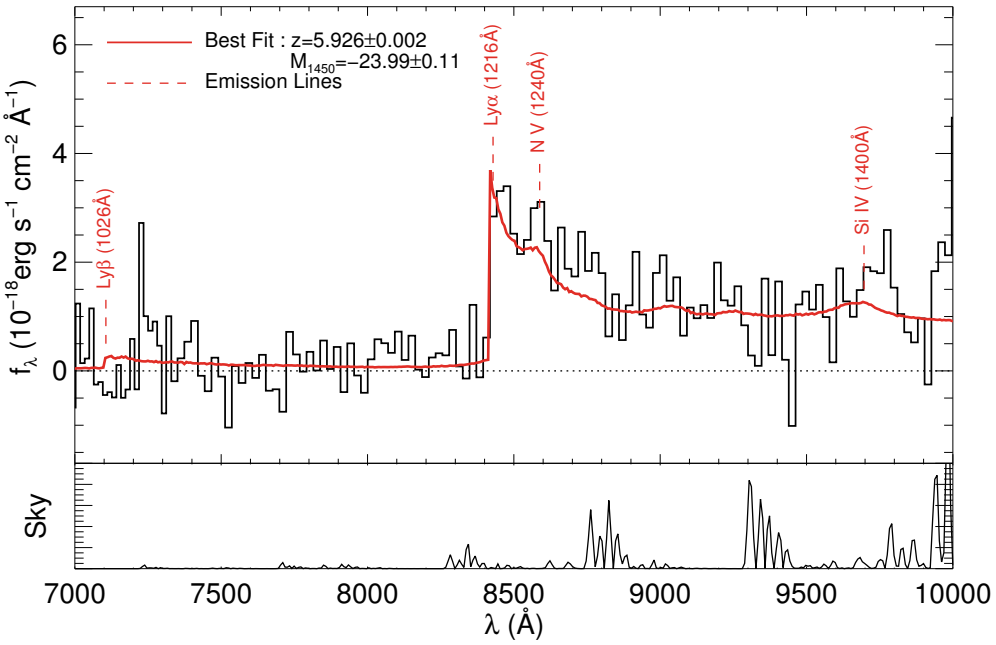

Figure 2.7. Optical spectrum of IMS J2204+0112 (black line). The red line represents an SDSS quasar composite spectrum (Vanden Berk et al. 2001) that is redshifted to $z = 5.926$ and adjusted for IGM attenuation (Madau et al. 1996). Quasar emission lines (red dashed) are also indicated. The bottom figure shows skylines.

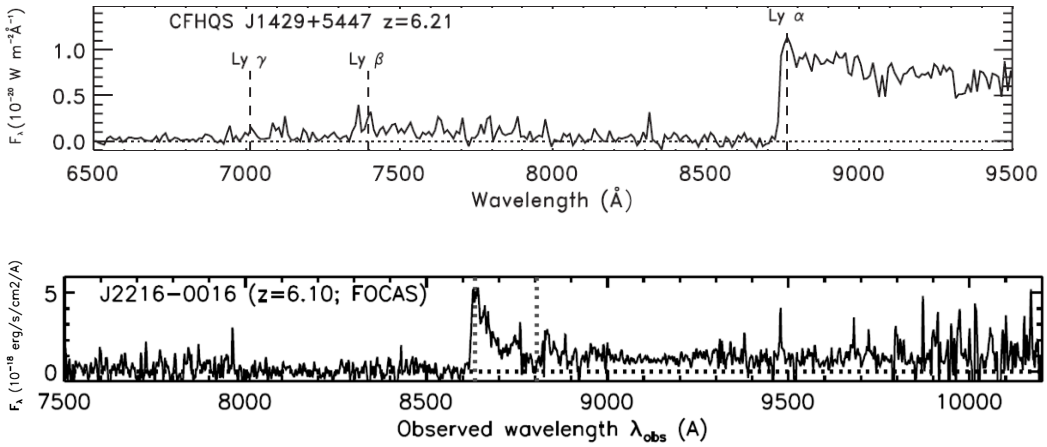

Figure 2.8. Optical spectra of IMS J1429+5447 (top) and IMS J2216−0016 (bottom). They are also known as CFHQS J1429+5447 at $z = 6.21$ (Willott et al. 2010b) and HSC J2216−0016 at $z = 6.10$ (Matsuoka et al. 2016), respectively, which are measured from their Lyα emission lines. Note that possible emission lines (Lyα, Lyβ, Lyγ, and N V) are also remarked with the vertical lines. This figure is adapted from Figure 2 of Willott et al. (2010b) and Figure 4 of Matsuoka et al. (2016).

2.5 Quasar Luminosity Function at $z \sim 6$

We can ask how the discovery of $z \sim 6$ quasars in IMS constrains the faint end of the QLF at $z \sim 6$, a question that is directly related to the reionization of the universe (Section 2.1). In the following sections, we describe the completeness of our high-redshift quasar survey and how we derive the QLF at $z \sim 6$ with IMS quasars.

2.5.1 Photometric Completeness

To measure the $z \sim 6$ QLF, we estimate the detection completeness in the z'-band images that we used for source detections. Hudelot et al. (2012) provided the 80% and 50% completeness magnitudes for the point sources in each CFHTLS z'-band tile. Using a simple minimum chi-square method with the MPFIT package (Markwardt 2009), we fit the completeness data (both 80% and 50% completeness data) with an analytic completeness function of the form f (Fleming et al. 1995):

$$f = \frac{1}{2}\left(1 - \frac{\alpha_f(z' - z'_*)}{\sqrt{(1 + \alpha_f^2(z' - z'_*)^2)}}\right) \tag{2.2}$$

where z'_* is the turnover magnitude at which f reaches 0.5 and α_f is the slope at z'_*.

Figure 2.9 shows the photometric completeness in z'-band images of the four IMS extragalactic fields. For the mean values of the completeness data, we obtained the best-fit completeness functions in the four fields (red lines), which are similar to each other. We also estimated the completeness function of all of the fields that we used (bottom panel), resulting in the best-fit values of $z'_* = 24.25$ mag and $\alpha_f = 2.25$. According to this function, our selection criterion in z'-band magnitude ($z' = 23.5$ mag; see Section 2.3) is complete to 93% for point sources.

2.5.2 Quasar Selection Function

We calculated the selection efficiency of our color selection criteria, which are described in Section 2.3, using our high-redshift quasar SED model (see Section 5.5.3 and also Kim et al. 2019). Here we briefly summarize the quasar model. The model is based on the

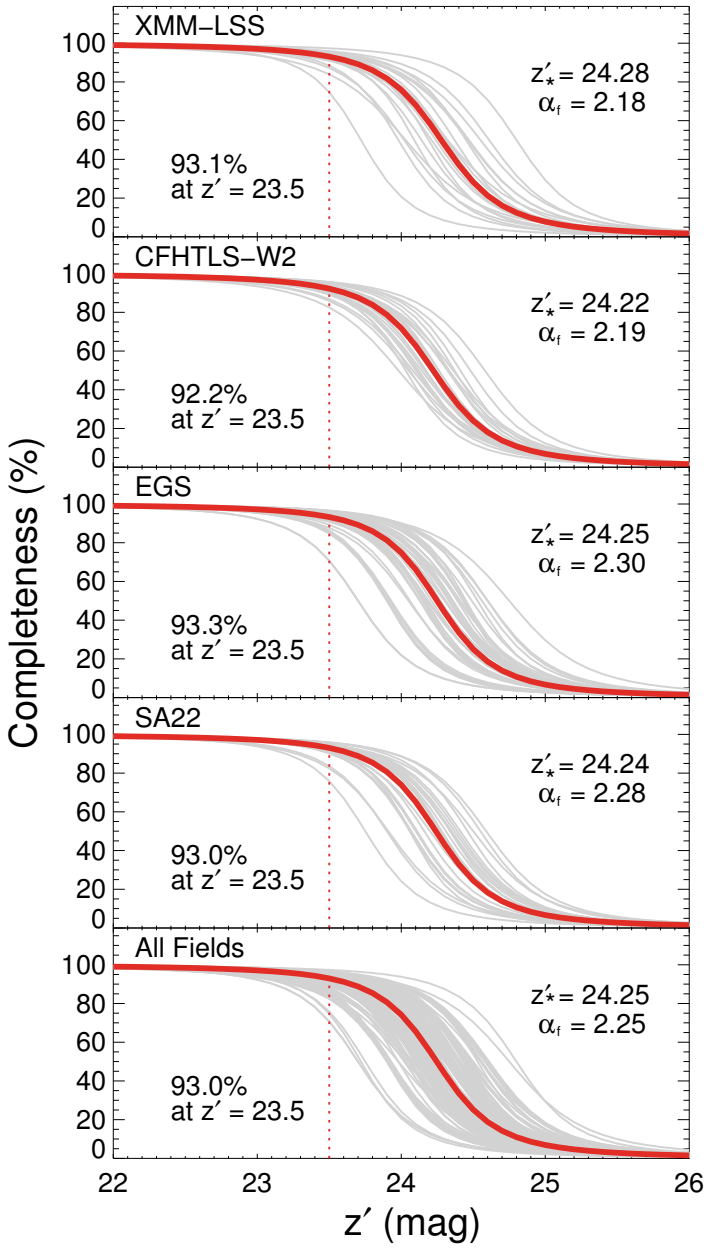

Figure 2.9. Photometric completeness in z'-band images of the IMS extragalactic fields, calculated in each CFHTLS tile (gray lines). The red solid lines indicate the best-fit completeness functions calculated with the mean values of the completeness data from Hudelot et al. (2012). The best-fit values of z'_* and α_f in each field are remarked in each panel, while the completeness percentages at $z = 23.5$ mag, corresponding to our z'-band magnitude cut (red dotted lines; see Section 2.3), are also presented.

composite spectrum of the SDSS quasars (Vanden Berk et al. 2001), including the IGM attenuation along the model redshift following the polynomial equations for the optical depth affected by neutral hydrogen (Madau et al. 1996). By multiplying exponential factors, we can change the AGN continuum slope (α_λ) and equivalent width of the combination of Lyα and N V emission lines (EW) of the model. Including a scaling factor of M_{1450}, the model has 4 parameters: z, M_{1450}, α_λ, and EW.

Using this model, we generated the spectra of 100,000 mock quasars of which z and M_{1450} are uniformly distributed (but generated from random numbers) in the ranges of $5.5 < z < 7.0$ and $-28 < M_{1450} < -22$, respectively. On the other hand, the other two parameters are randomly given in Gaussian distributions with mean and standard deviation values of $\alpha_\lambda = -1.6 \pm 1.0$ (Mazzucchelli et al. 2017) and $\log \mathrm{EW} = 1.542 \pm 0.391$ (Bañados et al. 2016). Consequently, there are ~ 100 quasars in each bin with sizes of $dz = 0.05$ and $dM_{1450} = 0.2$ mag. Integrating the mock quasar spectra with the filter transmission curves, we obtained their magnitudes in the bands that we used for our color selection. Considering that the imaging depths of the CFHTLS/IMS data varies from region to region, we used the depth maps that are resampled in a pixel scale of $1\farcs0$ to calculate the selection functions of every $1\farcs0 \times 1\farcs0$ area (or a pixel). According to the imaging depths of each area, we added Gaussian random noises to the magnitudes of the mock quasars. After then, for each bin, we calculated the ratio of the quasars satisfying our color selection criteria to all of the mock quasars, referred to as a selection completeness, resulting in the selection function in the z, M_{1450} parameter space. Note that we also consider the photometric completeness described in Section 2.5.1, which is adopted to the z'-band magnitudes of the mock quasars.

Figure 2.10 shows the selection functions averaged over each field. The functions of the four IMS fields are slightly different from each other, which are mainly affected by their J-band imaging depths; the 5σ detection limits of J-band images in the XMM-LSS and SA22 fields are a magnitude deeper than the other fields. We also derived the functions for i'_1 and i'_2 bands separately (the top and bottom panels in Figure 2.10, respectively), showing differences in completeness at $z \lesssim 5.9$. The three spectroscop-

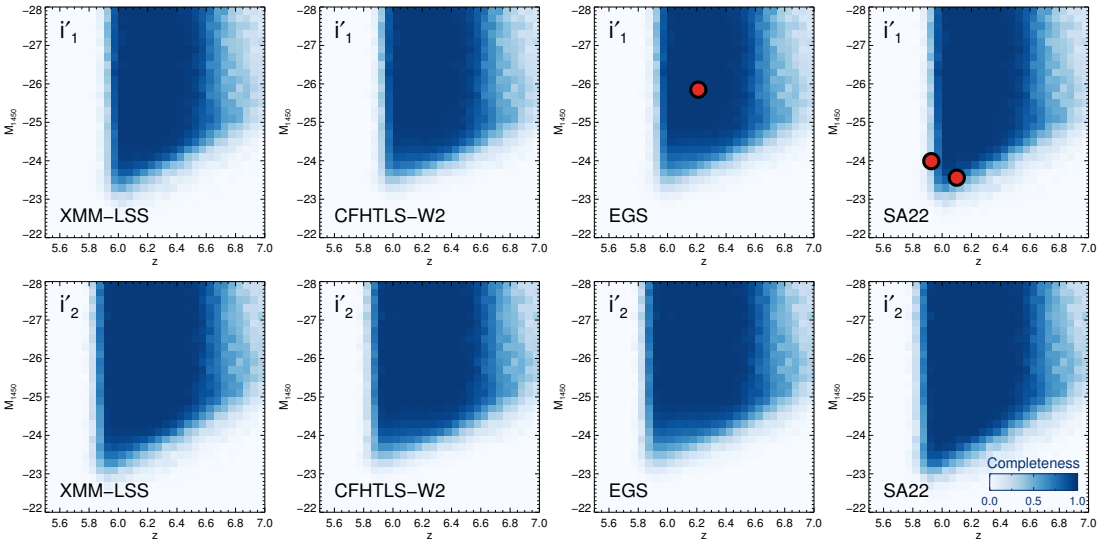

Figure 2.10. Selection functions for $z \sim 6$ quasars in the IMS extragalactic fields. The top and bottom panels are those derived for i'_1 and i'_2 bands, respectively. The colorbar show the scale of completeness. The red points highlighted with black outlines are the spectroscopically identified quasars.

ically identified quasars (IMS J1429+5447, IMS J2204+0112, and IMS J2216−0016; shown as red points), which are observed in i'_1 band, are located in the bins that have completeness values of 0.96, 0.31, and 0.73, respectively. This means that they deserve to be selected by our color selection criteria in the combination of the CFHTLS and IMS data.

In the following sections, we use these selection functions derived for i'_1 and i'_2 magnitudes in each field to estimate the QLF at $z \sim 6$ in our high-redshift quasar survey.

2.5.3 Binned Luminosity Function

To calculate the QLF at $z \sim 6$, we used the binned $1/V_a$ method (Avni & Bahcall 1980) which is based on the number of quasars in the specific co-moving volume of V_a. For a quasar in a bin of which sizes are ΔM_{1450} and Δz, the specific co-moving volume in an IMS k field is given as,

$$V_{a,k} = \frac{1}{\Delta M_{1450}} \int_{\Delta M_{1450}} \int_{\Delta z} p_k(z, M_{1450}) \frac{dV_k}{dz} \, dz \, dM_{1450}, \tag{2.3}$$

where $p_k(z, M_{1450})$ is the selection completeness described in Section 2.5.2 and dV_k/dz is the co-moving volume element of the area in the k field. Then, the binned QLF can be calculated as,

$$\Phi_k(M_{1450}) = \frac{1}{\Delta M_{1450}} \sum^{N_{\rm obj,k}} \frac{1}{V_{a,k}}, \tag{2.4}$$

of which uncertainty can be shown via error propagation to be

$$\Delta\Phi_k(M_{1450}) = \frac{1}{\Delta M_{1450}} \left[\sum^{N_{\rm obj,k}} \left(\frac{1}{V_{a,k}} \right)^2 \right]^{1/2}, \tag{2.5}$$

where $N_{\rm obj,k}$ is the number of sample in the magnitude bin in the k field.

The selection functions vary depending on the imaging depths and whether we use i'_1 or i'_2, while the sizes of the survey areas of the four IMS fields are also different from each other. Therefore, we use the weighted-mean of the $\Phi_k(M_{1450})$ values as the binned QLF of our total survey area, which can be written as,

$$\Phi(M_{1450}) = \frac{\sum_k^{N_{\rm field}} A_k(M_{1450}) \, \Phi_k(M_{1450})}{\sum_k^{N_{\rm field}} A_k(M_{1450})}, \tag{2.6}$$

where $A_k(M_{1450})$ is the weight component corresponding to the size of an area that can cover the magnitudes bin of M_{1450} (i.e., the size of an area with a J-band imaging depth deep enough to detect the objects in the magnitude bin at 5σ level), and $N_{\rm field}$ is the number of fields. The areas observed in i'_1 and i'_2 bands are regarded as different surveys, so there are totally eight fields with their own selection functions (i.e., $N_{\rm field} = 8$; see also

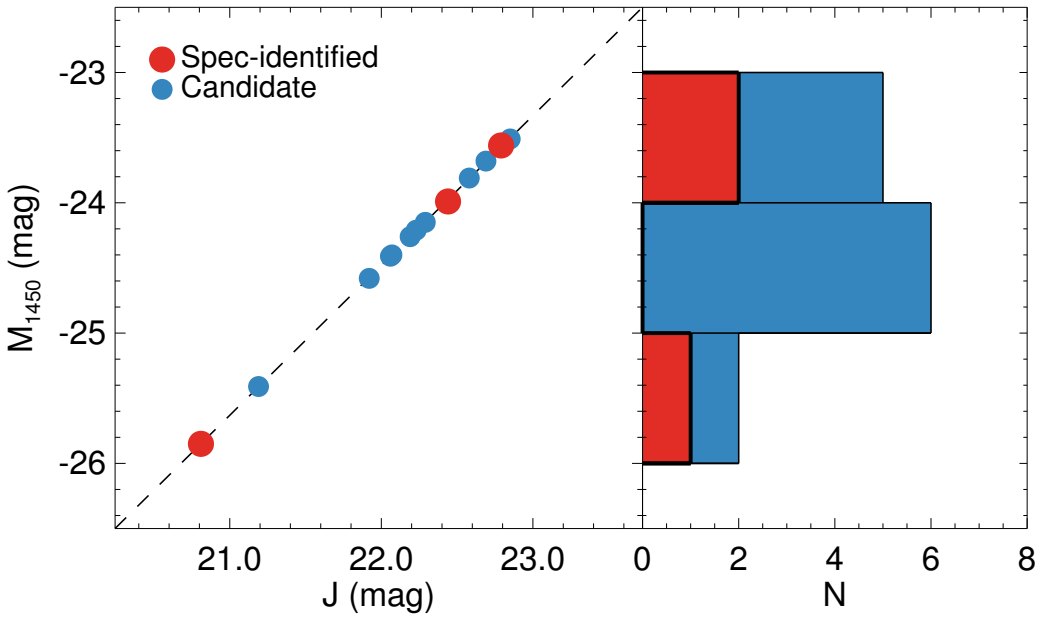

Figure 2.11. *Left*: J-band magnitudes versus M_{1450} of our sample consisting of spec-identified $z \sim 6$ quasars (red points) and $z \sim 6$ quasar candidates (blue points). The dashed line indicates a linear relation between the M_{1450} and J-band magnitudes of the spec-identified quasars. *Right*: histogram of the M_{1450} of our sample. The colors are consistent with the symbols in the left panel.

Figure 2.10). The uncertainties of $\Phi(M_{1450})$ are also calculated via error propagation including the weight component of A_k.

There are only three quasars identified by spectroscopy over the survey area of 86 deg^2, which are rather small. Therefore, we consider two samples: only the spec-identified quasars (Sample 1) and all of the quasars and candidates (Sample 2). Unlike the spec-identified ones, they have no information on M_{1450} and redshift. We found a linear relation between the M_{1450} and J-band magnitudes of the spec-identified quasars ($M_{1450} \approx 1.15\,J - 49.77$), shown as the dashed line in Figure 2.11. Using this relation, we roughly estimated the M_{1450} of the unidentified candidates with an assumption that all of them are $z = 6$ quasars. We divided the samples in three magnitude bins with a size of $\Delta M_{1450} = 1$ mag, corresponding to the magnitude bins shown in the histogram

Table 2.3. Binned Quasar Luminosity Function at $z \sim 6$

	Sample 1		Sample 2	
M_{1450} (mag)	$N_{\rm obj}$	$\Phi(M_{1450})$ (Gpc^{-3} mag^{-1})	$N_{\rm obj}$	$\Phi(M_{1450})$ (Gpc^{-3} mag^{-1})
-25.5	1	2.84 ± 2.84	2	5.67 ± 4.01
-24.5	0	...	6	18.63 ± 7.61
-23.5	2	12.51 ± 8.85	5	47.59 ± 22.10

Note. — M_{1450} is the center of a magnitude bin with a size of $\Delta M_{1450} = 1$ mag. $N_{\rm obj}$ is the number of sample in each magnitude bin.

of Figure 2.11. Also, we used a single redshift bin in the range of $5.8 < z < 6.4$ owing to the small number of our samples.

Figure 2.12 shows the $\Phi(M_{1450})$ values of our three samples, which are also listed in Table 2.3. The brightest magnitude bin at $M_{1450} = -25.5$ mag is consistent with the previous SDSS results (orange squares; Jiang et al. 2016) in Sample 1 and 2. As M_{1450} increases, the $\Phi(M_{1450})$ values of the two samples diverge. The $\Phi(M_{1450})$ values of Sample 2 continuously increase as the similar rate as those of SDSS quasars. On the other hand, the $\Phi(M_{1450})$ value of the faintest bin with $M_{1450} = -23.5$ mag in Sample 1 is 4 times lower than that of Sample 2.

We derived the parametric QLF by fitting the $\Phi(M_{1450})$ values including the bright SDSS sample (Jiang et al. 2016), using the IDL MPFIT package (Markwardt 2009). Considering the change of the slope of the $\Phi(M_{1450})$ values at $M_{1450} > -25$ mag, we used the double power-law function to fit the $\Phi(M_{1450})$ of Sample 1 and 2:

$$\Phi(M_{1450}) = \frac{\Phi^*}{10^{0.4(\alpha+1)(M_{1450}-M^*_{1450})} + 10^{0.4(\beta+1)(M_{1450}-M^*_{1450})}}, \tag{2.7}$$

where Φ^* is the normalization factor, M^*_{1450} is the break magnitude, α is the faint-end

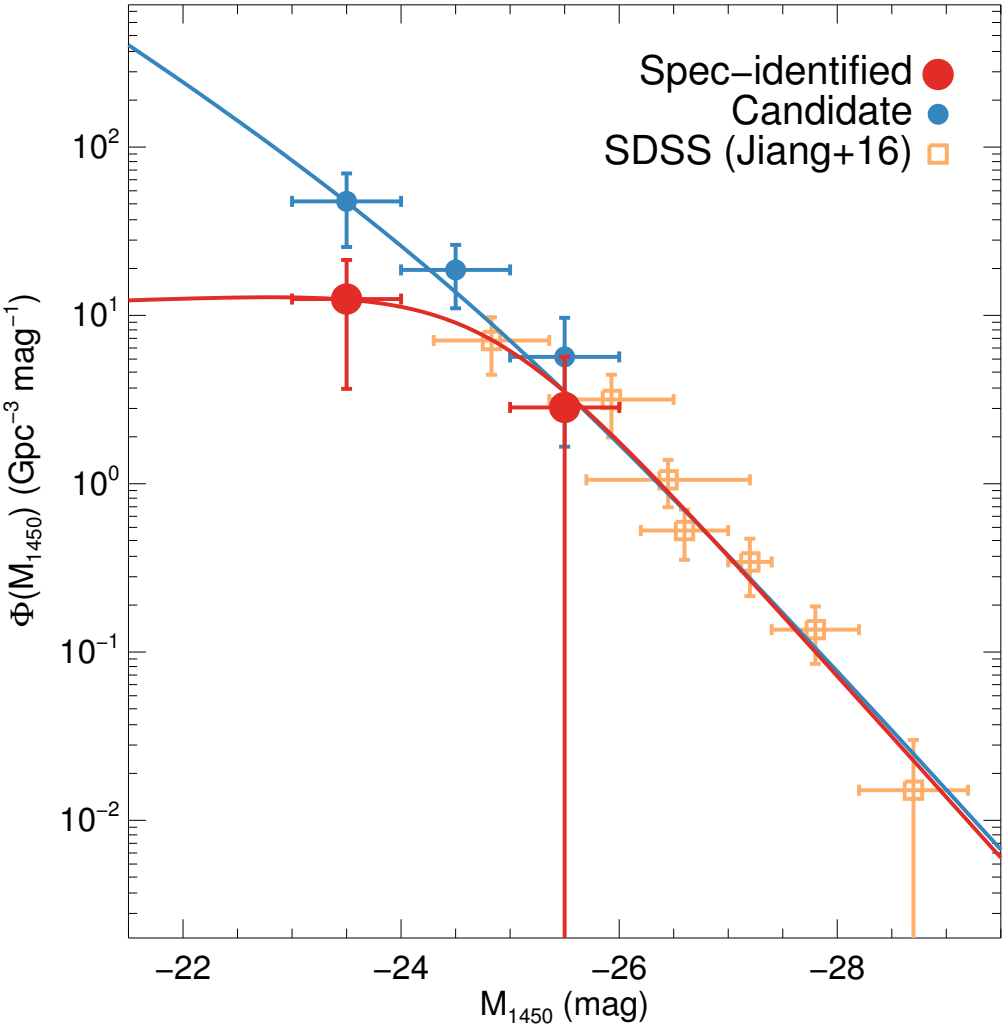

Figure 2.12. Derived QLFs at $z \sim 6$. The symbols of the three samples are the same as in Figure 2.11, while the orange squares represent the $\Phi(M_{1450})$ values of the SDSS quasars at $z \sim 6$ (Jiang et al. 2016). The solid lines are the fitted QLF of which colors correspond to the sample used for the fitting.

Table 2.4. Parameters of Quasar Luminosity Function at $z \sim 6$

Sample	Φ^* (Gpc^{-3} mag^{-1})	M^*_{1450} (mag)	α
Sample 1	14.78 ± 8.41	-24.79 ± 0.40	-0.94 ± 0.68
Sample 2	27.86 ± 54.63	-24.49 ± 1.42	-2.01 ± 0.72

Note. — The bright end slope β is fixed to $\beta = -2.8$ (Jiang et al. 2016).

slope, and β is the bright-end slope that is fixed to $\beta = -2.8$ (Jiang et al. 2016). The errors of the parameters are computed from the covariance matrix, also scaled by the reduced χ^2 values. The solid lines in Figure 2.12 shows the fitted QLFs, and we listed the best-fit parameters in Table 2.4. Note that the α value of the QLF of Sample 1 is higher than -1, a flatten slope, which may be due to the sample incompleteness.

2.6 Implication for the Cosmic Reionization

Figure 2.13 shows the $z = 6$ QLFs of this work and the literature. The orange (Jiang et al. 2016) and green (Matsuoka et al. 2018c) QLFs are derived from the optical/NIR detected quasars at $z \sim 6$. Meanwhile, the pink line of Giallongo et al. (2015) is derived from the faint X-ray AGNs (candidates), which is revised by Parsa et al. (2018), shown as the purple line. Note that Giallongo et al. (2015) and Parsa et al. (2018) presented their QLFs at $z = 5.75$. We scaled down these luminosity functions by a factor of $10^{-0.7(5.75-6.0)}$ to take into account the number density evolution (Jiang et al. 2016) between $z = 5.75$ and 6.0.

The QLF of Sample 1 is in line with that of Matsuoka et al. (2018c), which is the most up-to-date QLF that covers the M_{1450} range from -30 to -22 mag based on the quasar sample of the Subaru High-z Exploration of Low-Luminosity Quasars

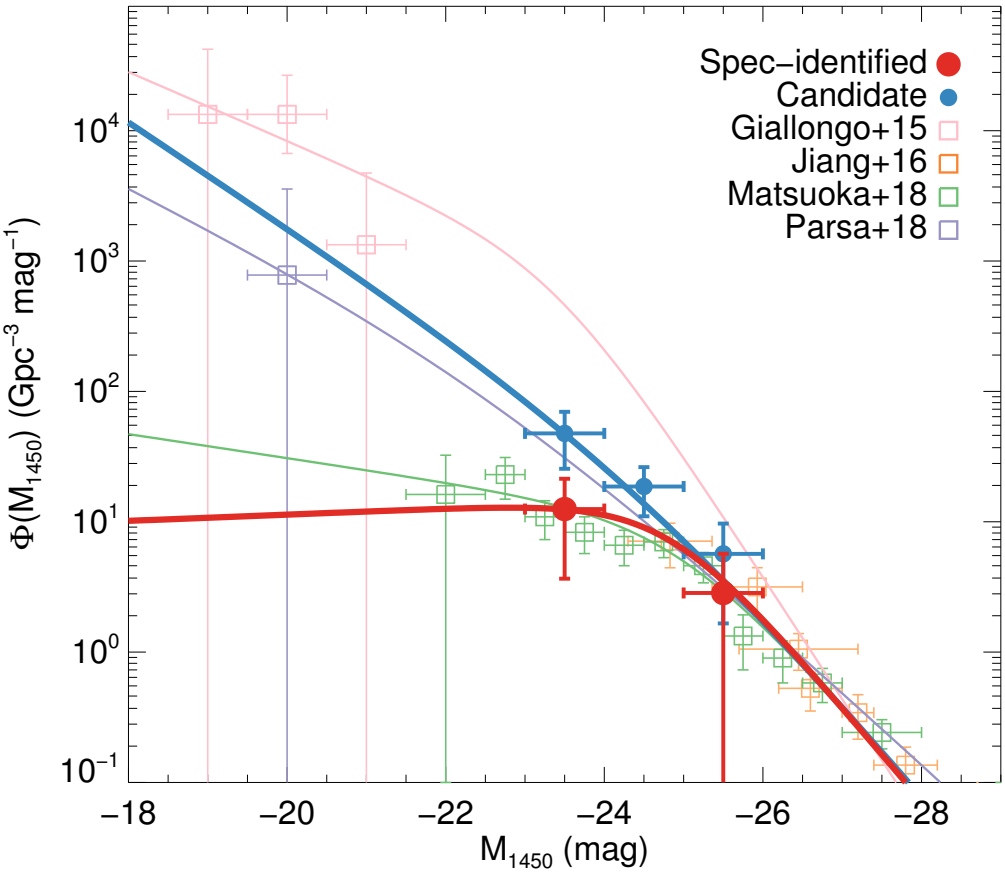

Figure 2.13. Comparison of $z \sim 6$ QLFs. The red and blue lines represent the QLFs of our samples, while the pink (Giallongo et al. 2015), orange (Jiang et al. 2016), green (Matsuoka et al. 2018c), and purple (Parsa et al. 2018) lines are the QLFs from the literature.

(SHELLQs) project (Matsuoka et al. 2016, 2018a,b, 2019). Note that Matsuoka et al. (2018c) used 28 quasars at $M_{1450} > -24$ mag, implying that the faint-end of QLF can be over-estimated with a small number of samples. Even in the case of Sample 2, the QLF at $M_{1450} \sim -23$ mag is an order of magnitude lower than that of Giallongo et al. (2015) of which sample contains faint X-ray AGNs (or candidates) in the magnitude range of $-19 < M_{1450} < -21$, but it is slightly higher than the QLF of Parsa et al. (2018).

Using the derived QLFs, we calculated the total ionizing photon density from quasars given by (Bolton & Haehnelt 2007)

$$\dot{n}_{\rm ion} = f_{\rm esc}\, \epsilon_{1450}\, \xi_{\rm ion} \ \left({\rm s}^{-1}\ {\rm Mpc}^{-3}\right), \tag{2.8}$$

where $f_{\rm esc}$ is the escape fraction of a photon from quasars, ϵ_{1450} is the UV monochromatic emissivity at 1450 Å (erg s^{-1} Hz^{-1} Mpc^{-3}), and $\xi_{\rm ion}$ is the number of the ionizing photons from a quasar with a normalized monochromatic luminosity (erg^{-1} Hz). We assume that most of UV photons can escape from the quasar ($f_{\rm ion} = 1$) and a high-redshift quasar has a power-law SED shapes following Lusso et al. (2015). Integrating from $M_{1450} = -30$ to -18, we find $\dot{n}_{\rm ion} = 0.5 \times 10^{49}$ and 2.5×10^{49} s^{-1} Mpc^{-3} for Sample 1 and 2, respectively. Compared to the required photon density to ionize neutral hydrogen at $z = 6$ ($\dot{n}_{\rm ion} = (1.8\text{–}4.5) \times 10^{50}$ s^{-1} Mpc^{-3} with a IGM clumping factor of 2–5; Madau et al. 1999), our results suggest the UV photons emitted by quasars are only 1–14% of the required UV photons for the cosmic reionization. In other words, high-redshift quasars are not the main contributor to the cosmic reionization. As with the suggestions of other studies, low-luminous star-forming galaxies could be the main contributors instead (e.g., Robertson et al. 2015; Matsuoka et al. 2018c)

2.7 Summary

Based on the optical and NIR imaging data from CFHTLS and IMS, respectively, we have performed the survey for the faint quasars at $z \sim 6$. Using the color-selection

method for high-redshift quasars, we found 25 quasar candidates, among which seven candidates are classified as high-priority ones. We spectroscopically identified that one of the high-priority candidates, IMS J2204+0112, is a faint quasar at $z \sim 6$, while other two of them were also identified with spectroscopy. Including these three quasars and the quasar candidates, we derived the QLFs at $z = 6$, which are consistent with the previous studies. The emitting photon density of high-redshift quasars was calculated from the QLFs, resulting in the minor contribution of high-redshift quasars to the cosmic reionization by emitting only $< 15\%$ of the required photons.

Chapter 3

Low Eddington Ratio of a Faint Quasar at $z \sim 6$: Not Every Supermassive Black Hole is Growing Fast in the Early Universe[†]

3.1 Introduction

Since the first discovery of a quasar in 1960s, more than 400,000 quasars have been discovered by numerous surveys (e.g., Schmidt & Green 1983; Hewett et al. 1995; Boyle et al. 2000; Im et al. 2007; Lee et al. 2008; Shen et al. 2008, 2011; Flesch 2015; Jeon et al. 2017; Pâris et al. 2017). Among them, about 100 quasars have been identified at $z \gtrsim 6$ (Fan et al. 2000, 2006; Goto 2006; Jiang et al. 2009, 2016; Willott et al. 2010b; Mortlock et al. 2011; Venemans et al. 2013, 2015a,b; Bañados et al. 2014, 2016,

[†]This chapter is a revised version of the article published in *The Astrophysical Journal* in March 2018 (Kim et al. 2018).

2018; Kashikawa et al. 2015; Kim et al. 2015a; Wu et al. 2015; Matsuoka et al. 2016, 2018a,b, 2019; Mazzucchelli et al. 2017). Compared to quasars at lower redshifts, these high-redshift quasars show no remarkable evolution in UV/optical spectral shapes (Fan et al. 2006; Jun et al. 2015), but a larger fraction of them is found to be dust-poor compared to their low-redshift counterparts, a possible indication that high-redshift quasars are rapidly evolving (Jiang et al. 2010; Jun & Im 2013).

Using a black hole (BH) mass estimator that assumes the Doppler broadening of virialized gas as the dominant cause for the broad emission lines of quasars (e.g, see Kim et al. 2010; Jun et al. 2015), the black hole masses ($M_{\rm BH}$) of few tens of high-redshift quasars are found to be $10^{8-10}\ M_{\odot}$ (Jiang et al. 2007; Kurk et al. 2007, 2009; Willott et al. 2010a; Mortlock et al. 2011; Shen et al. 2011; Jun et al. 2015; Venemans et al. 2015a; Wu et al. 2015). Interestingly, the existence of supermassive black holes (SMBHs) in such an early universe poses a theoretical challenge for the following reason.

The SMBH mass at a given time t ($M_{\rm BH}(t)$) can be expressed as,

$$M_{\rm BH}(t) = M_{\rm BH,0} \times \exp\left(\dot{m} f_{\rm Duty}(1-\epsilon)\frac{t-t_0}{t_{Edd}}\right), \tag{3.1}$$

where $\dot{m}$ is the mass accretion rate normalized by Eddington mass accretion (see Watarai et al. 2001; Volonteri et al. 2015), $t_{\rm Edd} = 450$ Myr, ϵ is the radiation efficiency, $f_{\rm Duty}$ is the duty cycle, $M_{\rm BH,0}$ is the seed BH mass, and t_0 is the time when the seed BH started to grow. For a standard disk model with Eddington-limited accretion, $\dot{m} = \lambda_{\rm Edd}/\epsilon = (L_{\rm bol}/L_{\rm Edd})/\epsilon$, where $\lambda_{\rm Edd}$ is the Eddington ratio, $L_{\rm bol}$ is the bolometric luminosity, and $L_{\rm Edd}$ is the Eddington luminosity ($L_{\rm Edd} = 1.26\times10^{38}\ (M_{\rm BH}/M_{\odot})$ in erg s^{-1}). Adopting a typical value of $\epsilon = 0.1$, even with a continuous maximal accretion at $\lambda_{\rm Edd} = 1$, it requires about ~ 0.8 Gyr for a stellar-mass BH with $M_{\rm BH,0} = 100\ M_{\odot}$ to grow into $10^9\ M_{\odot}$. The age of the universe is only 0.94 Gyr at $z = 6$ and 0.48 Gyr at $z = 10$ (a plausible redshift for a stellar-mass BH to form), so the creation of a $10^9\ M_{\odot}$ BH is nearly impossible especially when we also consider feedbacks from star formation and AGN activity that hinder the continuous Eddington-limited accretion (Pelupessy et al. 2007; Alvarez et al. 2009; Milosavljević et al. 2009; Jeon et al. 2012; Park & Ricotti 2012; Johnson et al. 2013). To solve this problem, super-Eddington

accretion ($\lambda_{\rm Edd} > 1$) of stellar-mass BHs (e.g., Volonteri & Rees 2005; Wyithe & Loeb 2012; Madau et al. 2014), and BH growth from massive seed BHs with $10^{4-6}\,M_{\odot}$ are introduced (e.g., Bromm & Loeb 2003; Begelman et al. 2006; Lodato & Natarajan 2006; Johnson et al. 2013).

Testing these different SMBH growth scenarios requires understanding Eddington ratios of high-redshift quasars. So far, the Eddington ratios are measured for about 20 luminous $z \sim 6$ quasars (bolometric luminosity, $L_{\rm bol} \gtrsim 10^{47}$ erg s^{-1}) and the values are found to be at $\lambda_{\rm Edd} \sim 1$ (e.g., see Willott et al. 2010a; Jun et al. 2015; Wu et al. 2015) in contrast to $\lambda_{\rm Edd} \sim 0.1$ of their counterparts at lower redshifts (Richards et al. 2006; Shen et al. 2011; Trakhtenbrot & Netzer 2012). The predominantly Eddington-limited accretion of SMBHs at high redshift might be in line with the rapid accretion scenario in the models that allow stellar-mass seed BHs (e.g., see Alexander & Hickox 2012; Volonteri 2012; Johnson et al. 2013 and references therein).

However, previous studies have been limited mostly to luminous quasars that are likely to be high $\lambda_{\rm Edd}$ objects. Therefore, the suggestion that high-redshift quasars are rapidly growing could be a result of this kind of bias. To avoid the bias, Willott et al. (2010a) tried to infer the intrinsic $\lambda_{\rm Edd}$ distribution from the observed $\lambda_{\rm Edd}$ distribution of 17 luminous quasars at $z \sim 6$ with an assumption that the distribution follows a lognormal form. According to their analysis, the peak of the intrinsic $\lambda_{\rm Edd}$ distribution of $z \sim 6$ quasars is $\log(\lambda_{\rm Edd}) = -0.22$, in comparison to the observed peak at $\log(\lambda_{\rm Edd}) \sim 0.03$. This result indicates that there should be more quasars with $\lambda_{\rm Edd} < 1$ if fainter luminosity quasars are explored, but it still implies nearly Eddington-limited accretion for most $z \sim 6$ quasars. However, recent studies of $z \sim 6.5$ quasars (De Rosa et al. 2014; Venemans et al. 2015a; Mazzucchelli et al. 2017) suggested that there are a few $10^{46.5-47}$ erg s^{-1} luminous quasars with $M_{\rm BH} > 10^{9.0}\,M_{\odot}$, and the average $\log(\lambda_{\rm Edd})$ of 15 $z \sim 6.5$ quasars is 0.39, which is comparable to their low-redshift counterparts (Mazzucchelli et al. 2017), implying that the derived intrinsic $\lambda_{\rm Edd}$ distribution of Willott et al. (2010a) is biased toward high $\lambda_{\rm Edd}$. Also, a possible positive correlation of $L_{\rm bol}$ and $\lambda_{\rm Edd}$ for low-redshift quasars (Shen et al. 2008, 2011;

Lusso et al. 2012) may lead to the same conclusion. Since the majority of quasars at high redshift are faint, as implied by the quasar luminosity function (Willott et al. 2010b; Giallongo et al. 2015; Kashikawa et al. 2015; Kim et al. 2015a), these limited quasar sample cannot truly represent the whole quasar population at $z \sim 6$, if $z \sim 6$ quasars have such a $L_{\rm bol}$-$\lambda_{\rm Edd}$ relation like their low-redshift counterparts.

Thanks to the recent wide-area deep surveys, new light can be shed on the accretion activities of high-redshift quasars. Now, dozens of faint $z \sim 6$ quasars are spectroscopically identified that have absolute magnitudes at a rest-frame 1450 Å of $M_{1450} > -24$ mag (Kashikawa et al. 2015; Kim et al. 2015a; Matsuoka et al. 2016, 2018a,b). These faint quasars can possibly represent the population of low $\lambda_{\rm Edd}$ SMBHs. Therefore, to really see how fast high-redshift quasars are growing, it is important to measure their $M_{\rm BH}$ and $\lambda_{\rm Edd}$ values. So far, little has been done to characterize these faint quasars at high redshift, but deep NIR spectroscopy with sensitive spectrographs should be able to reveal their $M_{\rm BH}$ and $\lambda_{\rm Edd}$ one by one.

In this chapter, we present the first NIR spectroscopic observation of IMS J2204+0112 (Kim et al. 2015a), one of the faintest $z \sim 6$ quasars discovered so far from the Infrared Medium-deep Survey (M. Im et al. 2019, in preparation). We describe the observation and the data analysis in Section 3.2. We present the quasar's spectral properties that are obtained through continuum/line-fitting in Section 3.3. We present the $M_{\rm BH}$ and $\lambda_{\rm Edd}$ values of IMS J2204+0112 in Section 3.4. The implications of our results about the growth SMBHs in the early universe are discussed in Section 3.5. We adopt $\Omega_m = 0.3$, $\Omega_\Lambda = 0.7$, and $H_0 = 70$ km s^{-1} Mpc^{-1} of a concordance cosmology that has been supported by observations in the past decades (e.g., Im et al. 1997).

3.2 Observation and Data Analysis

The NIR spectroscopic observation of IMS J2204+0112 was carried out with the Folded-port InfraRed Echellette (FIRE) mounted on the Magellan/Baade 6.5 m telescope at the Las Campanas Observatory in Chile. The observation aimed to detect the redshifted C IV line, a common $M_{\rm BH}$ estimator (Vestergaard & Peterson 2006; Jun et al. 2015).

Mg II is another, possibly better choice for $M_{\rm BH}$ measurement (Shen et al. 2011; Ho et al. 2012; Jun et al. 2015), but we opted for the C IV line due to the observational difficulty of detecting Mg II at longer wavelengths. We observed the target with the high-throughput prism mode (or long-slit mode) on 2015 September 12th and 13th. The data were taken with a $1\farcs0$ slit, which gives a spectral resolution in the J-band (R_J) of 500, corresponding to a resolution of ~ 600 km s^{-1}. The single exposure time for each frame was set at 908.8 s with the Sample-Up-The-Ramp (SUTR) readout mode, which reads out the detector continuously during exposure. This kind of long exposure in NIR observation makes the long-wavelength region ($\lambda > 12000$ Å) saturated, but enables us to obtain sufficient signals (S/N $\gtrsim 3$ over a resolution element) for continuum at short wavelength ($\lambda < 12000$ Å). We took 26 frames for IMS J2204+0112, but only 20 frames taken under good weather conditions (seeing $\lesssim 1\farcs0$) were used for the data analysis, giving a net exposure time of 5.05 hr.

Although the data were obtained through a nodding observation (i.e., ABBA offset), varying seeing conditions during the observing run with long exposures generated unstable sky-lines on the spectra. This made it difficult to eliminate the sky-lines directly by subtracting raw frames from each other. Thus, we processed the spectra one by one, using the IRAF package (Tody 1993). Saturated regions ($\lambda > 12000$ Å) were trimmed, and then we performed the bias subtraction and the flat-fielding. The wavelength solutions were derived from the NeAr arc frames. In order to eliminate sky-lines, we subtracted the median value of background pixels surrounding the target in the spatial direction from the wavelength-calibrated, reduced spectrum, giving us clear sky-subtracted images around the target. After combining the images, we extracted the spectrum with a $1\farcs0$ aperture. Telluric correction with a standard star (HD 216807) was applied to the extracted 1D spectrum. We adjusted the flux scale of the spectrum with the most recent photometric magnitude in the z-band from the Hyper Suprime-Cam Subaru Strategic Program (HSC SSP; Aihara et al. 2018a), Data Release 1 (Aihara et al. 2018b). IMS J2204+0112 has $z = 22.55 \pm 0.05$ AB mag[1] in the HSC data, giving

[1]The z'-band magnitude of IMS J2204+0112 was originally reported as 22.95±0.07 AB mag (Kim

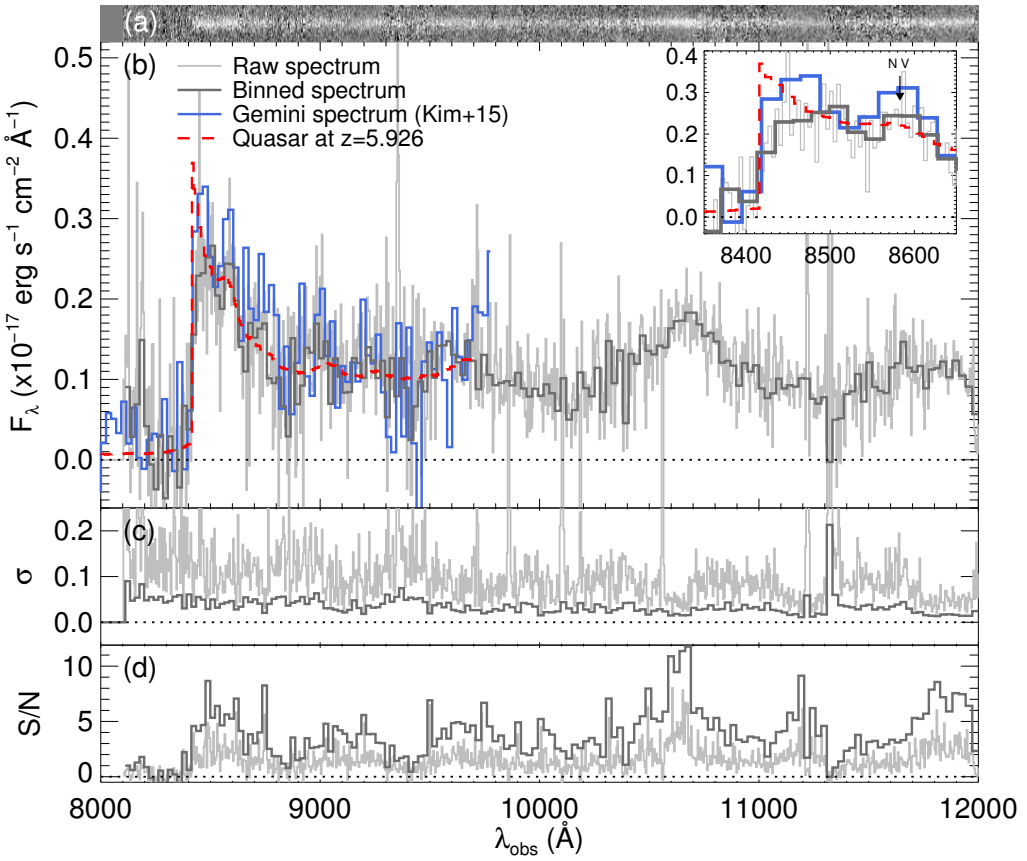

Figure 3.1. (a): NIR 2D spectrum of IMS J2204+0112. (b): NIR spectrum of IMS J2204+0112. The light gray lines represent the spectrum of IMS J2204+0112 taken with FIRE, and the dark gray lines show the spectrum binned at the spectral resolution of $R_J = 500$. The blue line represents the optical spectrum obtained with GMOS on Gemini (Kim et al. 2015a). The red dashed line shows the fitted quasar model of Kim et al. (2015a) with $z = 5.926$. The inset shows a zoomed-in spectrum around the Lyman-α break at ~ 8500 Å, and we marked the peak of the N V λ1240 emission line at $z = 5.926$. (c) and (d): the spectroscopic error and S/N of the NIR spectrum, respectively.

a flux scaling factor of 0.9. This value gives an updated M_{1450} of -23.99 ± 0.05 AB mag. The galactic extinction was corrected by the Cardelli et al. (1989) law with the extinction value A_V of ~ 0.127 (Schlafly & Finkbeiner 2011) assuming $R_V = 3.1$. Figure 3.1 shows the final spectrum of IMS J2204+0112. The uncertainty of the spectrum was derived during the aperture-extracting process.

3.3 Spectral Modeling

In this section, we show how we performed the spectral modeling for IMS J2204+0112 to estimate its continuum luminosity at a specific wavelength and FWHM of the C IV emission line. To use better S/N data for the spectral analysis, we binned the spectrum to match R_J (the dark gray line in Figure 3.1) without overlap between the pixels used for binning. Each bin contains 4-6 pixels, and we took the weighted-mean of the fluxes in each bin with the weight of $w_i = \sigma_i^{-2}$, where σ_i is the error of the ith pixel in each bin. The errors in each bin ($\sigma_{\rm bin}$) are estimated as $\sigma_{bin} = \left(\sum_{i=1}^{N_{\rm pix}} w_i\right)^{-1/2}$, where $N_{\rm pix}$ is the number of pixels in each bin. We updated the wavelength calibration of the Gemini spectrum (Kim et al. 2015a), and used the updated spectrum to derive redshifts, since the S/N near the Lyman break is about two times larger in the Gemini spectrum than the FIRE spectrum. Following the method described in Kim et al. (2015a), we find the updated redshift value of $z = 5.926 \pm 0.002$ by fitting a quasar spectrum model shown as a red dashed line in Figure 3.1. Note that this redshift value matches the location of the peak of N V λ1240 emission line well.

3.3.1 Continuum Components

It is crucial for a reliable $M_{\rm BH}$ measurement to have a well-defined continuum model for the quasar spectrum. To increase the S/N of the continuum part of the spectrum,

et al. 2015a), which is ~ 0.3 mag fainter than the value from the HSC data, considering the difference between z and z' filters. Note that this previous value is based on the images that were taken 9 years before the HSC data. If we use this value to normalize the spectrum, it will change $\lambda_{\rm Edd}$ by ~ 0.1 dex, which is negligible compared to other uncertainties in $\lambda_{\rm Edd}$ estimate.

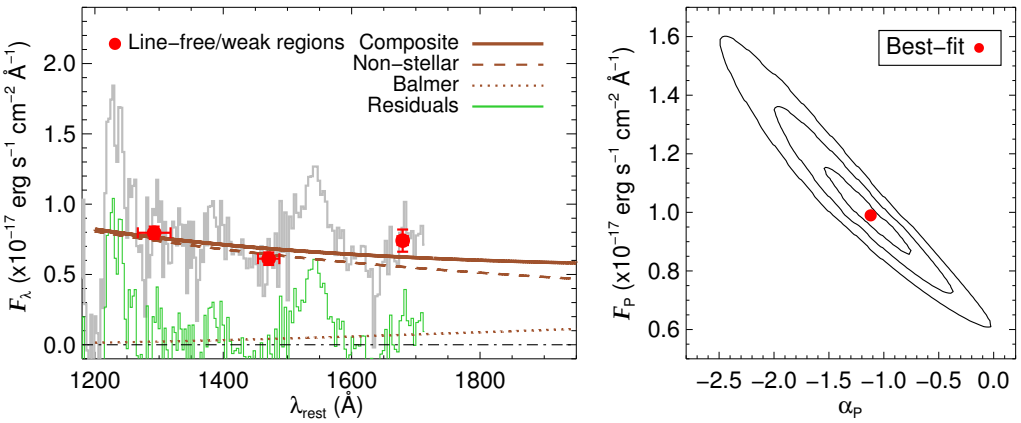

Figure 3.2. Left: Spectrum of IMS J2204+0112 in the rest-frame. The binned spectrum is shown as the gray line. The red circles represent the binned points of the spectrum at the line-free region. The best-fit model with the minimum $\chi^2_{\rm red}$ value is shown as the brown solid line. This model comprises of the non-stellar power-law model (the brown dashed line) and the Balmer pseudo-continuum model (the brown dotted line). The residual spectrum is shown as the green line. Right: Parameter space of $\alpha_{\rm P}$ and $F_{\rm P}$ (see Section 3.3.1). The red dot represents our best-fit values of $\alpha_{\rm P}$ and $F_{\rm P}$, and the contours show the confidence regions (1σ to 3σ from inner to outer).

we binned regions with no (or weak) emission lines (e.g., 1250-1335, 1445-1495, and 1670-1690 Å) and used them (the red circles in Figure 3.2) to fit the continuum. Each binned point represents the weighted mean value of the specific flux density in each wavelength range. We also ignored the Fe II and Fe III lines in the continuum fitting, since they are known to be weak at $\lambda_{\rm rest} \lesssim 2,000$ Å (e.g., quasar spectra in Jiang et al. 2007; De Rosa et al. 2014).

We modeled the quasar continuum spectrum as the sum of the non-stellar power-law continuum from the accretion disk and the Balmer pseudo-continuum from gas clouds surrounding the black hole as

$$F_\lambda = F_{\rm P} \left(\frac{\lambda}{1000\text{Å}} \right)^{\alpha_{\rm P}} + F_{\rm B} B_\lambda(T_e) \left(1 - e^{-\tau_{\rm BE}(\lambda/\lambda_{\rm BE})^3} \right), \ \lambda < \lambda_{\rm BE}, \qquad (3.2)$$

where $F_{\rm P}$ is the normalized flux density for the non-stellar power-law continuum at 1000 Å, $\alpha_{\rm P}$ is the slope of the power-law continuum, $F_{\rm B}$ is the normalized flux density for the Balmer continuum, $B_\lambda(T_e)$ is the Planck function at an electron temperature T_e, and $\tau_{\rm BE}$ is the optical depth at the Balmer edge ($\lambda_{\rm BE} = 3646$ Å in the rest-frame; Grandi 1982). Since both high- and low-redshift quasars have the slope of $\alpha_{\rm P} = -1.5 \pm 1.2$ (Decarli et al. 2010; De Rosa et al. 2011; Shen et al. 2011), we adopted the fitting range of $-3.0 \leq \alpha_{\rm P} \leq 1.0$, which covers 1σ dispersion of $\alpha_{\rm P}$. The second term is for the Balmer pseudo-continuum from Dietrich et al. (2003). The basic assumption is that there are gas clouds with uniform $T_e = 15,000$ K (Dietrich et al. 2003) in a partially optically thick condition ($\tau_{\rm BE} = 1.0$; Kurk et al. 2007). We also tested models with $10,000 \leq T_e \leq 20,000$ K and $0.1 \leq \tau_{\rm BE} \leq 2.0$, the range that previous studies used (e.g., De Rosa et al. 2014), but there are no significant differences between the models due to the small contribution of the Balmer continuum to the composite continuum at $\lambda_{rest} < 2000$ Å. Since our NIR spectrum does not cover the wavelength ($\lambda_{rest} = 3675$ Å) where the normalization of the model is usually done (Dietrich et al. 2003; Kurk et al. 2007; Jiang et al. 2009; De Rosa et al. 2011, 2014), we normalized the Balmer continuum with assumptions that (i) the power-law continuum is dominant at our fitting range of $1200 < \lambda_{rest} < 1800$ Å, and (ii) the flux density of the Balmer continuum can be

normalized to a fraction of the power-law continuum flux density at $\lambda_{rest} = 3675$ Å that is extrapolated from our NIR data: $F_{\rm B} = f_{\rm B} \cdot F_{\rm P} \cdot (3675\ \text{Å})^{\alpha_{\rm P}}$, where $f_{\rm B}$ is the fraction of the Balmer continuum at 3675 Å. Since $f_{\rm B}$ is less than 1.0 and typically ~ 0.3 (Dietrich et al. 2003; De Rosa et al. 2011), the fitting range of $f_{\rm B}$ is set to $0.1 \leq f_B \leq 1.0$.

We calculated $\chi^2_{\rm red}$ values with a grid-based parameter set of ($F_{\rm P}$, $\alpha_{\rm P}$, $f_{\rm B}$), and found the best-fit result that has the minimum $\chi^2_{\rm red}$ value, given in Table 3.1. The errors were computed by finding marginal points of $\chi^2_{\rm red} < \chi^2_{\rm red,min} + 1$ (1σ confidence level) in the parameter space. Figure 3.2 shows the best-fit continuum model plotted on the NIR spectrum of IMS J2204+0112. The best-fit non-stellar power-law model has a slope of $\alpha_{\rm P} = -1.12^{+0.38}_{-0.40}$, consistent with that of other high-redshift quasars. For the Balmer pseudo-continuum model, the best-fit model results in $f_{\rm B} = 1.0$ due to the significant flux at ~ 1680 Å.

The flux density of the best-fit continuum model and its 1σ error are generated from the χ^2 distribution of α and $F_{\rm P}$ (Figure 3.2), while the other parameters ($f_{\rm B}$, T_e, and $\tau_{\rm BE}$) are fixed. From the flux density of the best-fit continuum model in the rest-frame system, we calculated the monochromatic continuum luminosity at $\lambda_{rest} =$ 1350 Å and 1450 Å (L_{1350} and L_{1450}, respectively), assuming isotropic radiation at the luminosity distance of IMS J2204+0112. We also computed the bolometric luminosity $L_{\rm bol}$ from L_{1450}, using the quasar bolometric correction from Runnoe et al. (2012): $L_{\rm bol} = 4.20 \times L_{1450}$. The estimated values with the errors at the 1σ confidence level are given in Table 3.2. The $\log(L_{\rm bol})$ of IMS J2204+0112 is only $46.21^{+0.12}_{-0.16}$ erg s^{-1}. Note that the errors from both the flux density and the best-fit continuum model are included in the uncertainty.

Table 3.1. Continuum Fitting Results

Continuum Fitting Parameters	Best-fit Value with 1σ error
$F_{\rm P}$ ($\times 10^{-18}$ erg s^{-1} cm^{-2} Å^{-1})	$9.90^{+1.67}_{-1.37}$
$\alpha_{\rm P}$	$-1.12^{+0.38}_{-0.42}$
$f_{\rm B}$	1.0^{a}
T_e (K)	$15{,}000^{b}$
$\tau_{\rm BE}$	1.0^{b}

[a]Marginal value in the fitting range. Full details are in Section 3.3.1.

[b]Fixed values. Full details are in Section 3.3.1.

3.3.2 C IV Line Measurement

After subtracting the best-fit continuum model obtained from Section 3.3.1, we fitted the C IV emission line and measured its spectral properties. It is well-known that the C IV emission line of quasars often shows asymmetric line shapes that cannot be well modeled by a single Gaussian function (Shen et al. 2011; Tang et al. 2012; Park et al. 2013, 2017; Runnoe et al. 2013; De Rosa et al. 2014; Karouzos et al. 2015; Coatman et al. 2016). While this asymmetric line shape of C IV can be seen in high S/N spectra (S/N $\gtrsim$ 10 for continuum), it is not discernible in the spectrum with low S/N of $\lesssim$ 10 (De Rosa et al. 2014), like our case. Hence, the C IV emission of IMS J2204+0112 was fitted with a single Gaussian function. For the error analysis, we adjusted the parameters of the non-stellar power-law continuum ($F_{\rm P}$ and $\alpha_{\rm P}$) using random pairs of $\alpha_{\rm P}$ and $F_{\rm P}$ following the χ^2 distribution in parameter space. This process enables us to determine the error of the continuum flux density per binned pixel. We took the quadratic sum of errors of the continuum model and of the NIR spectrum as the uncertainties of the continuum-subtracted spectrum for each pixel.

We used the MPFIT package (Markwardt 2009), a robust nonlinear least squares curve fitting with the Levenberg-Marquardt technique, for the C IV line-fitting. The fitting range was set to 1400 Å $\leq \lambda_{\rm rest} \leq$ 1650 Å. The fitting provides the central peak wavelength $\lambda_{\rm CIV}$, and the Gaussian standard deviation $\sigma_{\rm G}$ that is converted to the C IV line FWHM (FWHM$_{\rm CIV}$) with a relation of FWHM$\simeq 2.355 \times \sigma_{\rm G}$. Note that the instrumental resolution of FWHM$_{ins}$ = 600 km s^{-1} is subtracted from the measured FWHM$_{\rm obs}$ as FWHM$_{\rm CIV} = \sqrt{({\rm FWHM_{obs}})^2 - ({\rm FWHM_{ins}})^2}$.

Figure 3.3 shows the radial velocity profile of the C IV line. The red solid line indicates the best-fit model for the C IV emission line with $\lambda_{\rm CIV} = 1540.32^{+3.14}_{-3.20}$ Å and FWHM$_{\rm CIV} = 9046^{+1499}_{-1305}$ km s^{-1} (or $\sigma_{\rm G} = 3841^{+636}_{-554}$ km s^{-1}). To derive the errors, we generated 100,000 mock radial profiles by adding appropriate random Gaussian noises to the best-fit model. After re-fitting the mock spectra, we took the 68% ranges of the distributions of $\lambda_{\rm CIV}$ and FWHM$_{\rm CIV}$ as their 1σ errors.

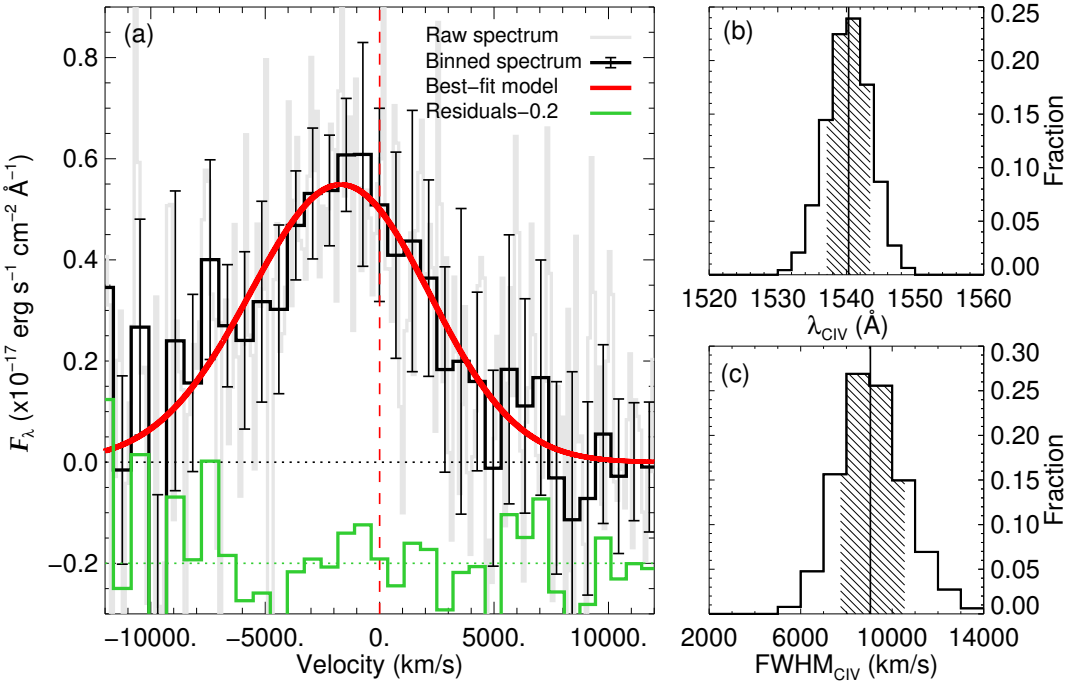

Figure 3.3. (a) The specific flux density of C IV emission line of IMS J2204+0112 in rest-frame after subtracting the best-fit continuum model. While the raw spectrum is shown as the gray line, the binned spectrum with flux error is shown as the black line. The red solid line represents the best-fit model for the C IV emission line, and the green line shows the residual spectrum. (b) and (c): Distributions of $\lambda_{\rm CIV}$ (left) and FWHM$_{\rm CIV}$ (right) in 100,000 trials, respectively. While the vertical line in each panel indicates the best-fit result, the shaded region corresponds to the 68% range (or 1σ confidence level) of the distribution.

Table 3.2. Spectral Properties of IMS J2204+0112

Estimated Properties	Best-fit Value with 1σ error
z^a	5.926 ± 0.002
$\log L_{1350}$ (erg s^{-1})	$45.59^{+0.08}_{-0.10}$
$\log L_{1450}$ (erg s^{-1})	$45.59^{+0.12}_{-0.16}$
$\log L_{\rm bol}$ (erg s^{-1})	$46.21^{+0.12}_{-0.16}$
$\lambda_{\rm CIV}$ (Å)	$1540.32^{+3.14}_{-3.20}$
FWHM$_{\rm CIV}$ (km s^{-1})	9046^{+1499}_{-1305}
$\sigma_{\rm G}$ (km s^{-1})	3841^{+636}_{-554}

Note. — The uncertainties of luminosity are lower limits with constraining the contribution of the Balmer pseudo-continuum and elimination of iron lines for fitting.

[a]Derived from Gemini spectrum (Kim et al. 2015a).

3.4 Results

3.4.1 Black Hole Mass

The BH mass, $M_{\rm BH,CIV}$ of IMS J2204+0112 is estimated using scaling relations that utilize L_{1350} and $\rm FWHM_{CIV}$ as follows:

$$\log\left(\frac{M_{\rm BH,CIV}}{M_\odot}\right) = A + \log\left\{\left(\frac{L_{1350}}{10^{44}\ {\rm erg\ s^{-1}}}\right)^{\beta}\left(\frac{\rm FWHM_{CIV}}{1000\ {\rm km\ s^{-1}}}\right)^{\gamma}\right\}. \quad (3.3)$$

Many groups have suggested that one needs to be cautious about $M_{\rm BH,CIV}$. The $M_{\rm BH,CIV}$ values are found to have a large scatter of ~ 0.4 dex against Hβ or Mg II-based $M_{\rm BH}$ values (Vestergaard & Peterson 2006; Shen et al. 2011; Ho et al. 2012; Jun et al. 2015, 2017). Also, the C IV line often shows an asymmetric shape possibly due to non-virial motion of gas and/or blending with other neighboring lines, suggesting that virial motions may not be the dominant component that determines the C IV line width. The unusual line shape is often associated with the blueshift of the C IV line, which is thought to be one of the main uncertainties in the C IV-based estimator. Several new $M_{\rm BH}$ estimators are derived to use blueshift as a way to improve $M_{\rm BH}$ measurements (Coatman et al. 2016; Jun et al. 2017). Considering these various ways of obtaining $M_{\rm BH}$ from the C IV line, we derived $M_{\rm BH,CIV}$ using several representative estimators. Note that the virial factor of $\log f = 0.71$ (Woo et al. 2013) was used.

First, we used the estimators consistent with the idea that the exponent of the velocity term reflects the virial motion of the broad line region gas, i.e., $\gamma \sim 2$. For this, we adopted the $M_{\rm BH,CIV}$ estimator of Vestergaard & Peterson (2006), Jun et al. (2015), and Park et al. (2017), where the parameter set values (A, β, γ) are (6.66, 0.53, 2.0), (6.707, 0.547, 2.11), and (6.84, 0.33, 2.00), respectively. The intrinsic scatters in the derived $M_{\rm BH}$ are of the order of ± 0.3 dex in these estimators (see Table 3.3). Using the line luminosity and FWHM values we obtained in Section 3.3, we find that the $M_{\rm BH,CIV}$ values of IMS J2204+0112 are $\log(M_{\rm BH,CIV}/M_\odot) = 9.38^{+0.13}_{-0.15}$ (Vestergaard & Peterson 2006), $9.55^{+0.24}_{-0.24}$ (Jun et al. 2015), and $9.27^{+0.19}_{-0.20}$ (Park et al. 2017). The 1σ uncertainty of $M_{\rm BH,CIV}$ is estimated by inserting the rms uncertainties of L_{1350} and $\rm FWHM_{CIV}$

in the $M_{\rm BH}$ estimators. All the three estimators give values that are consistent within error, with $\log(M_{\rm BH,CIV}/M_{\odot}) \sim 9.4$.

Second, we used the estimator with a very small γ value of ~ 0.5, which is not consistent with the virial motion assumption. This kind of estimator is put forward to minimize the scatter in $M_{\rm BH}$ between this method and the reverberation mapping result. Using the relation that adopts a parameter set of (7.54, 0.45, 0.5) from Park et al. (2017), we find $\log(M_{\rm BH,CIV}/M_{\odot}) = 8.72^{+0.60}_{-0.59}$ with an intrinsic scatter of 0.16 dex. This is about 0.6 dex smaller than the nominal $M_{\rm BH}$ estimates above, but showing very large uncertainty due to a γ of $0.50^{+0.55}_{-0.53}$. However, the adoption of the low γ value may not be physically plausible (Denney et al. 2013), and Jun et al. (2015) have shown that such a relation is likely to underestimate/overestimate $M_{\rm BH}$ at the high ($\log(M_{\rm BH}/M_{\odot}) > 9.5$) and low mass ends ($\log(M_{\rm BH}/M_{\odot}) < 8$).

Third, we used the estimators that correct the blueshift effect of the C IV line, since the blueshift of the C IV line ($v_{bs,\rm CIV} \equiv c \times (1549.48 - \lambda_{\rm CIV})/1549.48$) can be a signal to correct possible bias in $M_{\rm BH,CIV}$ (Coatman et al. 2016, 2017; Jun et al. 2017). Using the $\lambda_{\rm CIV}$ value from Section 3.3.2 and the systemic redshift of $z = 5.926$, we estimate the C IV blueshift as $v_{bs,\rm CIV} = 1685^{+608}_{-620}$ km s^{-1}. Using either the parameter set of (6.71, 0.53, 2) in Eq. (6) of Coatman et al. (2017) or $M_{\rm BH,CIV}$ with the blueshift correction term of Jun et al. (2017), we get $\log(M_{\rm BH,CIV}/M_{\odot}) = 9.05^{+0.26}_{-0.29}$, and $\log(M_{\rm BH,CIV}/M_{\odot}) = 9.27^{+0.27}_{-0.28}$, respectively. These values are consistent within the error. Note that the systemic redshift of IMS J2204+0112 is derived from the continuum break and the location of the N V line; we assume that this is identical to the redshift derived from a narrow high ionization line (e.g., [O III]), or host galaxy emission (e.g., Far-infrared [C II]). If this assumption is wrong, the derived $M_{\rm BH}$ with this method could be biased. Furthermore, the Mg II line of a few high-redshift quasars is statistically blueshifted compared to CO and [C II] emission lines, while that of low-redshift ones is not (Venemans et al. 2016; Mazzucchelli et al. 2017). These imply that the application of the blueshift correction factor from the $z < 4$ quasars may be inappropriate for high redshift quasars.

An alternative way to derive $M_{\rm BH,CIV}$ is to use the line dispersion of the C IV line ($\sigma_{\rm CIV}$; Denney et al. 2013; Park et al. 2013, 2017). The second moment line dispersion $\sigma_{\rm CIV}$ is $\sim 3900 \pm 700$ km s^{-1}, which is calculated within $\pm$10000 km s^{-1} around $\lambda_{\rm CIV}$. With the best-fit parameter set from Park et al. (2017), this $\sigma_{\rm CIV}$ and the $\sigma_{\rm G}$ (estimated in Section 3.3.2) give $\log(M_{\rm BH,CIV}/M_\odot) = 8.59^{+0.19}_{-0.21}$ and $8.58^{+0.18}_{-0.19}$, respectively. But the $\sigma_{\rm CIV}$ value varies significantly with the fitting range due to the low S/N of the continuum, as also noticed in previous studies (Denney et al. 2013; Coatman et al. 2016). Furthermore, $M_{\rm BH,CIV}$ with $\sigma_{\rm G}$ being possibly underestimated considering the common shape of the C IV line (Denney et al. 2013; Park et al. 2013, 2017).

In Table 3.3, we list these $M_{\rm BH,CIV}$ values of IMS 2204+0112. As a representative $M_{\rm BH}$ value, we use the weighted mean of the $M_{\rm BH}$ value ($\log(M_{\rm BH,CIV}/M_\odot) = 9.09 \pm 0.41$) from different methods: $\gamma = 2$ (Vestergaard & Peterson 2006), $\gamma = 0.5$ (Park et al. 2017), $v_{bs,\rm CIV}$ (Coatman et al. 2017), and $\sigma_{\rm CIV}$ (Park et al. 2017). Note that the weight is the inverse variance of the $M_{\rm BH}$ estimation in each method. Not surprisingly, this value matches closely with the $M_{\rm BH}$ value from Mg II of lower-redshift quasars with spectral characteristics similar to IMS J2204+0112[2].

3.4.2 Eddington Ratio

Using the $M_{\rm BH,CIV}$ and $L_{\rm bol}$ values from previous sections, we calculate $\lambda_{\rm Edd} = L_{\rm bol}/L_{\rm Edd}$. The calculated $\lambda_{\rm Edd}$ values are listed in Table 3.3, indicating that $\lambda_{\rm Edd}$ is 0.10, one of the lowest values among quasars at $z \sim 6$.

Figure 3.4 shows $L_{\rm bol}$ versus the $M_{\rm BH}$ of IMS J2204+0112 (the red diamond; weighted mean $M_{\rm BH,CIV}$ value), quasars at $z \sim 6$ (the navy diamonds), and at $z < 3$ (the gray dots and contours). In the left panel, we show the values that are based on $M_{\rm BH,CIV}$ from the Vestergaard & Peterson (2006) relation, and in the right panel, the Mg II-based $M_{\rm BH}$ values, $M_{\rm BH,MgII}$ (Vestergaard & Osmer 2009), are given. The

[2]One can also adopt the $M_{\rm BH}$ derived from Mg II estimators of quasars that have spectral properties similar to IMS J2204+0112. For this, we selected quasars with $7500 < {\rm FWHM_{CIV}}$ (km s^{-1}) < 10500 and $45 < \log L_{1350}$ (erg s^{-1}) < 46 from Shen et al. (2011) and obtained their mean $M_{\rm BH}$ from Mg II. We obtain $\log(M_{\rm BH,MgII}/M_\odot) = 9.08 \pm 0.40$.

Table 3.3. $M_{\rm BH}$ and $\lambda_{\rm Edd}$ of IMS J2204+0112

Reference	Method	$\log(M_{\rm BH,CIV}/M_\odot)$	σ_{int}	$\log \lambda_{\rm Edd}$
(1)	(2)	(3)	(4)	(5)
Vestergaard & Peterson (2006)[a]	$\gamma = 2$	$9.38^{+0.13}_{-0.15}$	0.36	-1.27
Jun et al. (2015)	$\gamma = 2$	$9.55^{+0.24}_{-0.24}$	0.40	-1.43
Park et al. (2017)	$\gamma = 2$	$9.27^{+0.19}_{-0.20}$	0.22	-1.16
Park et al. (2017)[a]	$\gamma = 0.50$	$8.72^{+0.60}_{-0.59}$	0.16	-0.61
Coatman et al. (2017)[a]	$v_{bs,\rm CIV}$[b]	$9.05^{+0.26}_{-0.29}$	$\sim$0.5	-0.93
Jun et al. (2017)	$v_{bs,\rm CIV}$[b]	$9.27^{+0.27}_{-0.28}$	$\sim$0.35	-1.15
Park et al. (2017)[a]	$\sigma_{\rm CIV}$	$8.59^{+0.19}_{-0.21}$	0.12	-0.48
Park et al. (2017)	$\sigma_{\rm G}$	$8.58^{+0.18}_{-0.19}$	0.12	-0.47
Weighted mean	-	9.09 ± 0.41	-	-0.97

Note. — The results of $M_{\rm BH,CIV}$ and $\lambda_{\rm Edd}$ measurements from several methods. (1) References. (2) Methods for $M_{\rm BH,CIV}$ estimation. (3) $M_{\rm BH,CIV}$ with 1σ errors. The intrinsic scatter of each method is not included in the error. (4) Intrinsic scatter of the $M_{\rm BH}$ estimator. (5) $\lambda_{\rm Edd}$.

[a]The methods used for calculating the weighted mean $M_{\rm BH}$ value with the weight of the inverse variance of the $M_{\rm BH}$ estimates.

[b]The $v_{bs,\rm CIV}$ value used in this method is derived from the continuum break and the N V line, and this procedure could bias the result.

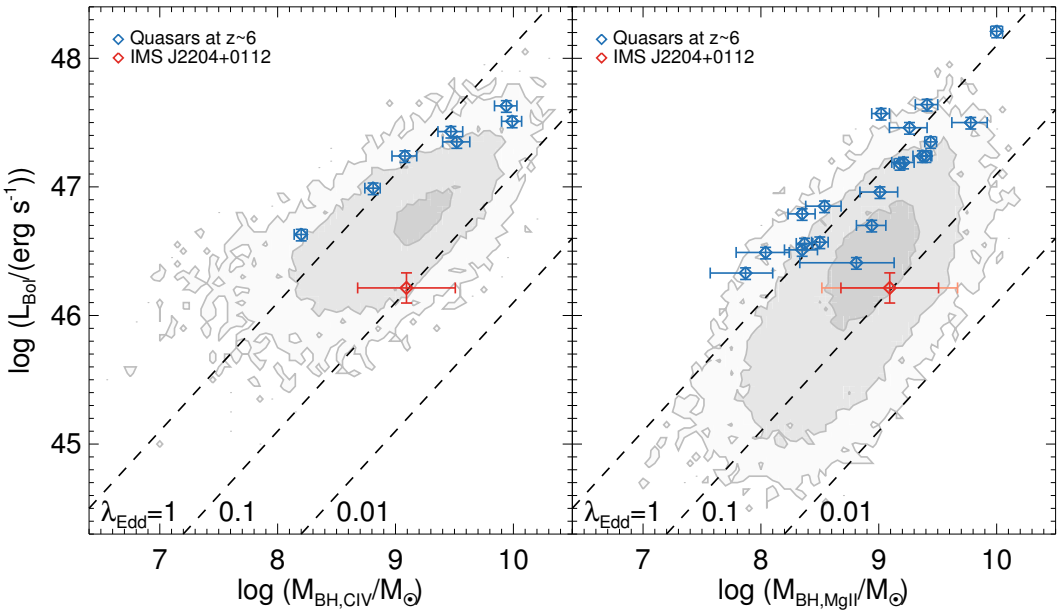

Figure 3.4. $M_{\rm BH}$-$L_{\rm bol}$ distributions of quasars. The left and the right panels show the results based on $M_{\rm BH,CIV}$ and $M_{\rm BH,MgII}$, respectively. While the gray dots and the contours represent the low-redshift quasars from SDSS DR7 Quasar catalog (Shen et al. 2011), the blue diamonds indicate quasars at $z \sim 6$ (Jiang et al. 2007; Kurk et al. 2007, 2009; Willott et al. 2010a; De Rosa et al. 2011; Wu et al. 2015). IMS J2204+0112 is shown as the red diamond, which seems to be isolated from other high-redshift quasars. Note that the red error bar of IMS J2204+0112 in the right panel includes the error of $M_{\rm BH}$ measurements and the dispersion of $M_{\rm BH,MgII}$ compared to $M_{\rm BH,CIV}$. This figure indicates that IMS J2204+0112 is a quasar with an exceptionally low $\lambda_{\rm Edd}$ among $z = 6$ quasars.

$L_{\rm bol}$ and $M_{\rm BH}$ values of $z \sim 6$ quasars are derived in the same manner as done for IMS J2204+0112 using the literature values of L_{1350} and $\rm FWHM_{CIV}$ (Jiang et al. 2007; Kurk et al. 2007) or L_{3000} and $\rm FWHM_{MgII}$ (Willott et al. 2003, 2010a; Kurk et al. 2007, 2009; De Rosa et al. 2011; Wu et al. 2015), and the derived values are listed in Table 3.4. For quasars at $z < 3$, we take the values from Shen et al. (2011), where the $M_{\rm BH,CIV}$ values are based on the Vestergaard & Peterson (2006) relation and the $M_{\rm BH,MgII}$ values are derived using the Vestergaard & Osmer (2009) relation.

The striking feature in the figure is that IMS J2204+0112 occupies a unique parameter space, the parameter space that has not been populated by other $z = 6$ luminous quasars, but is a rather common among $z \sim 2$ quasars. This prompts a question: have we only been seeing only a limited population of high $\lambda_{\rm Edd}$ quasars in previous studies? Figure 3.5 shows the intrinsic $\lambda_{\rm Edd}$ distribution derived by Willott et al. (2010a). If we impose the survey depth of IMS of $J_{\rm AB} < 22.5 - 23.0$ mag (Kim et al. 2015a) for the intrinsic $\lambda_{\rm Edd}$ distribution from Willott et al. (2010a), the $\lambda_{\rm Edd}$ distribution for such a magnitude-limited survey has a peak value at $\log \lambda_{\rm Edd} = -0.10$ and a dispersion of 0.26 dex (dotted line). In such a case, there is only a chance of $\sim 0.03\%$ (or 3.5σ away from the peak) of finding a quasar with a $\lambda_{\rm Edd}$ lower than IMS J2204+0112. Even if we consider the 1σ error of $\lambda_{\rm Edd}$ of IMS J2204+0112 ($\log \lambda_{\rm Edd} = -0.56$), the probability is only 3.84%, which is still low. That is to say, the probability of finding such a quasar in IMS is quite low for the intrinsic $\lambda_{\rm Edd}$ distribution of Willott et al. (2010a).

Table 3.4. Derived Parameters of $z \sim 6$ Quasars from Literature

Quasar	z	M_{1450} (mag)	$\mathrm{FWHM_{line}}$ (km $\mathrm{s^{-1}}$)	$\log L_{\mathrm{UV}}$ (erg $\mathrm{s^{-1}}$)	$\log L_{\mathrm{bol}}$ (erg $\mathrm{s^{-1}}$)	$\log M_{\mathrm{BH}}$ ($M_\odot$)	$\log \lambda_{\mathrm{Edd}}$	Reference
(1)	(2)	(3)	(4)	(5)	(6)	(7)	(8)	(9)
				Mg II-based Quasars				
SDSS J0005−0006	5.85	−25.86	2100	46.14	46.85	8.54	0.21	Kurk et al. (2007)
CFHQS J0050+3445	6.25	−26.62	4360	46.53	47.24	9.37	−0.23	Willott et al. (2010a)
CFHQS J0055+0146	5.98	−24.53	2040	45.80	46.51	8.35	0.07	Willott et al. (2010a)
SDSS J0100+2802	6.30	−29.26	5130	47.50	48.21	10.00	0.11	Wu et al. (2015)
CFHQS J0210−0456	6.44	−24.28	1300	45.62	46.33	7.87	0.37	Willott et al. (2010a)
CFHQS J0221−0802	6.16	−24.45	3680	45.70	46.41	8.81	−0.50	Willott et al. (2010a)
SDSS J0303−0019	6.08	−25.31	2340	45.86	46.57	8.50	−0.02	Kurk et al. (2009)
SDSS J0836+0054	5.82	−27.86	3600	46.93	47.64	9.41	0.14	Kurk et al. (2007)
SDSS J1030+0524	6.28	−27.53	3600	46.47	47.18	9.18	−0.09	Kurk et al. (2007)
SDSS J1048+4637	6.23	−27.55	3366	46.75	47.46	9.26	0.11	De Rosa et al. (2011)
SDSS J1148+5252	6.41	−27.80	6000	46.79	47.50	9.78	−0.38	Willott et al. (2003)
SDSS J1306+0356	5.99	−27.32	4500	46.53	47.24	9.40	−0.26	Kurk et al. (2007)
SDSS J1411+1217	5.95	−26.75	2400	46.86	47.57	9.02	0.45	Kurk et al. (2007)
CFHQS J1509−1749	6.12	−26.78	4420	46.64	47.35	9.44	−0.19	Willott et al. (2010a)
SDSS J1623+3112	6.25	−27.04	3700	46.48	47.19	9.21	−0.11	Jiang et al. (2007)
SDSS J1630+4012	6.05	−26.11	3366	46.25	46.96	9.01	−0.14	De Rosa et al. (2011)

Table 3.4 (cont'd)

Quasar	z	M_{1450} (mag)	$\mathrm{FWHM_{line}}$ (km s^{-1})	$\log L_{\mathrm{UV}}$ (erg s^{-1})	$\log L_{\mathrm{bol}}$ (erg s^{-1})	$\log M_{\mathrm{BH}}$ ($M_{\odot}$)	$\log \lambda_{\mathrm{Edd}}$	Reference
(1)	(2)	(3)	(4)	(5)	(6)	(7)	(8)	(9)
CFHQS J1641+3755	6.05	−25.19	1740	46.08	46.79	8.35	0.34	Willott et al. (2010a)
CFHQS J2100−1715	6.09	−25.03	3610	45.99	46.70	8.94	−0.34	Willott et al. (2010a)
CFHQS J2229+1457	6.15	−24.52	1440	45.78	46.49	8.04	0.36	Willott et al. (2010a)
CFHQS J2329−0301	6.42	−25.00	2020	45.85	46.56	8.37	0.10	Willott et al. (2010a)
C IV-based Quasars								
SDSS J0005−0006	5.85	−25.86	2900	46.37	46.99	8.81	0.08	Kurk et al. (2007)
SDSS J0130+0524	6.31	−27.53	5286	46.73	47.35	9.52	−0.27	Jiang et al. (2007)
SDSS J0303−0019	6.08	−25.31	1780	46.01	46.63	8.20	0.34	Kurk et al. (2007)
SDSS J0836+0054	5.81	−27.86	7183	47.01	47.63	9.94	−0.40	Jiang et al. (2007)
SDSS J1044−0125	5.78	−27.61	8171	46.89	47.51	9.99	−0.57	Jiang et al. (2007)
SDSS J1306+0356	6.02	−26.75	4744	46.81	47.43	9.47	−0.14	Jiang et al. (2007)
SDSS J1411+1217	5.93	−26.75	3388	46.62	47.24	9.08	0.06	Jiang et al. (2007)

Note. — (1) Quasar name. (2) Redshift based on Mg II or C IV. (3) Absolute magnitude at 1450 Å in the rest-frame. (4) FWHM of Mg II or C IV. (5) Rest-frame UV luminosity at 3000 and 1350 Å for Mg II and C IV, respectively. (6) AGN bolometric luminosity derived from L_{UV}. (7) Black hole mass derived from $\mathrm{FWHM_{line}}$ and L_{UV}. (8) Eddington ratio. (9) References.

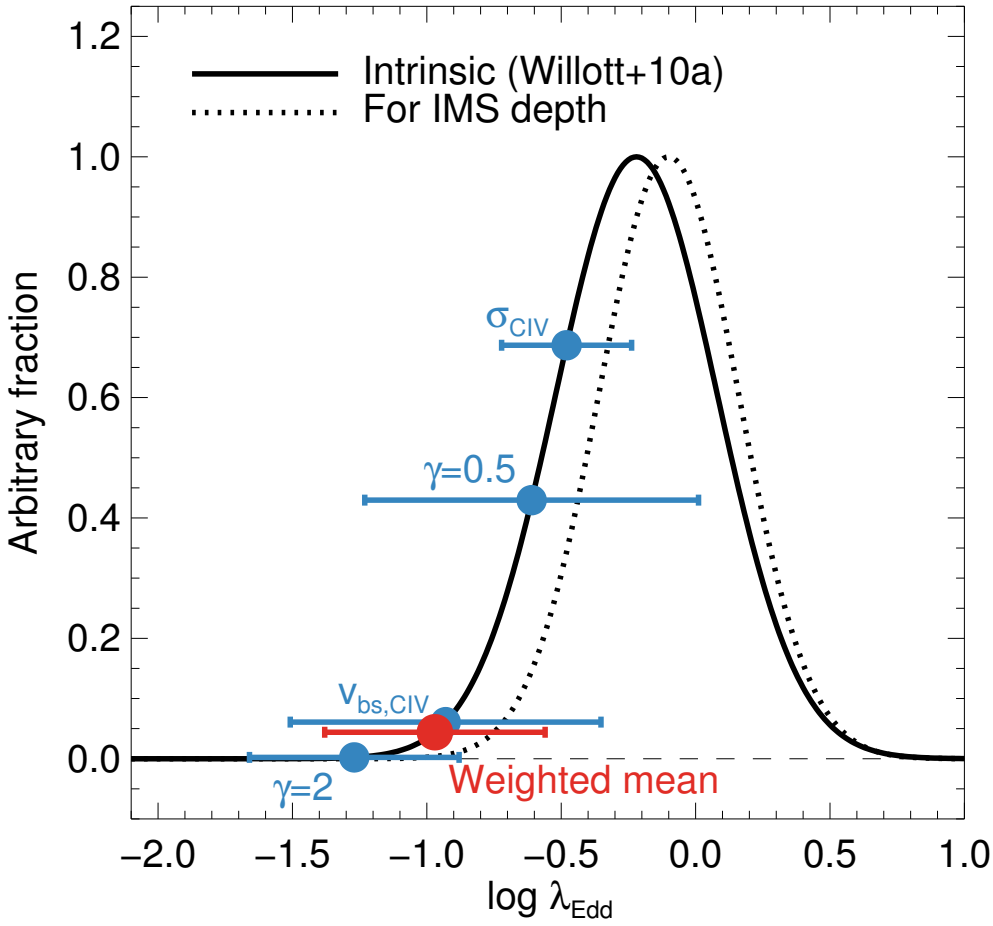

Figure 3.5. Intrinsic $\lambda_{\rm Edd}$ distribution of high-redshift quasars (solid line; Willott et al. 2010a), while the dotted line represent the case limited by the survey depth of IMS. The weighted mean of $\lambda_{\rm Edd}$ value is shown as a red circle, while the $\lambda_{\rm Edd}$ values derived from different methods are shown as blue circles: $\gamma = 2$ (Vestergaard & Peterson 2006), $\gamma = 0.5$ (Park et al. 2017), $v_{bs,\rm CIV}$ (Coatman et al. 2017), and $\sigma_{\rm CIV}$ (Park et al. 2017)

3.5 Discussion

3.5.1 Growth of IMS J2204+0112

It is remarkable that there is a faint quasar with only $\lambda_{\rm Edd} = 0.10$ at $z \sim 6$, though its mass determination is quite uncertain due to the characteristics of the C IV line. Recently, it was suggested that the average $\lambda_{\rm Edd}$ of high-redshift quasars is similar to that of their luminosity-matched counterparts at low redshift (Mazzucchelli et al. 2017). The existence of IMS J2204+0112 reinforces that suggestion even at a lower $L_{\rm bol}$ of $\sim 10^{46}$ erg s^{-1}.

As we mentioned in the introduction, the growth of a 100 $M_\odot$ seed BH to a $\sim 10^9 M_\odot$ SMBH at $z = 6$ is already very challenging due to the short time available between the creation of the BH seed and the epoch of $z = 6$. The situation gets significantly worse if $\lambda_{\rm Edd} = 0.10$. At $\lambda_{\rm Edd} = 0.10$, Eq. (3.1) shows that it takes 8 Gyr to obtain a $10^9\,M_\odot$ BH from a stellar-mass seed. Therefore, in such a case, it is impossible to grow stellar-mass BHs into SMBHs in quasars at $z \sim 6$. Thus, alternative scenarios must be sought if the $\lambda_{\rm Edd}$ value is around 0.10 for IMS J2204+0112 at $z \sim 6$.

Recent studies promote super-Eddington accretion as a way to create 10^9 $M_\odot$ BHs by $z = 6$. In that scenario, episodes of short-duration or steady super-Eddington accretion are shown to create SMBHs by $z = 6$, with a duty cycle of 0.5 or less (Li 2012; Madau et al. 2014; Smole et al. 2015; Volonteri et al. 2015; Pezzulli et al. 2016; Sakurai et al. 2016; DeGraf et al. 2017). In the case of super-Eddington accretion with a slim disk (Watarai et al. 2001; Wang & Netzer 2003; Ohsuga et al. 2005; Volonteri et al. 2015), $\dot{m}$ in Eq. (3.1) is given by

$$\dot{m} \sim \frac{2}{\epsilon} \exp\left(\frac{\lambda_{\rm Edd}}{2} - 1\right), \tag{3.4}$$

for $\lambda_{\rm Edd} \geq 2$. For example, if we have a super-Eddington accretion with $\lambda_{\rm Edd} = 3$, adopting $\epsilon \sim 0.04$ (Mineshige et al. 2000) with a duty cycle of $f_{\rm Duty} = 0.5$, only about 180 Myr is needed to create a 10^9 $M_\odot$ BH from a 10^2 $M_\odot$ seed BH, while the SMBH can have a low $\lambda_{\rm Edd}$ (~ 0.1 or less) for the remaining time (see also Trakhtenbrot et al. 2017b). Under the episodic super-Eddington accretion scenario with a stellar mass

seed BH, our result of $\lambda_{\rm Edd} = 0.1$ implies that IMS J2204+0112 underwent bursts of super-Eddington accretion before, and is relatively quiescent at $z \sim 6$.

Another possible BH growth scenario is to have very heavy seed BHs with $M_{\rm BH,0} \sim 10^4$–10^6 $M_\odot$ (Volonteri et al. 2008; Johnson et al. 2013; DeGraf et al. 2012; Di Matteo et al. 2012; Johnson et al. 2013; Ferrara et al. 2014; Pacucci et al. 2015; Gallerani et al. 2017; Regan et al. 2017; Smidt et al. 2018 and references therein). Using Eq. (3.1) with the final BH mass of $M_{\rm BH} = 10^9 M_\odot$, and $M_{\rm BH,0} = 10^5$ $M_{\rm BH}$ for the seed BH, we get the accretion time scale of ~ 4.6 Gyr if the accretion continues at $\lambda_{\rm Edd} = 0.10$ and ~ 0.46 Gyr at $\lambda_{\rm Edd} = 1$. Therefore, a 10^5 $M_\odot$ seed BH can become a 10^9 $M_\odot$ BH if the BH growth can last about a few hundred Myr at the Eddington limit before subsiding to $\lambda_{\rm Edd} \sim 0.1$ at $z = 6$. Simulations show that cold gas flows can feed massive BH seeds (DeGraf et al. 2012; Di Matteo et al. 2012; Smidt et al. 2018). In the simulation, the BH growth proceeds nearly at Eddington-limited accretion for an extended period until $z \sim 7$ or so and then reduces to $\lambda_{\rm Edd} \sim 0.1$ or less (e.g, Di Matteo et al. 2012; Smidt et al. 2018). This is consistent with our findings.

Figure 3.6 is the schematic diagram of these two possible scenarios for the growth of IMS J2204+0112 within a Gyr.

3.5.2 Intrinsic Eddington Ratio Distribution of $z \sim 6$ Quasars

As described above, the probability of finding a high-redshift quasar with a low $\lambda_{\rm Edd}$ like IMS J2204+0112 is significantly low, according to the $\lambda_{\rm Edd}$ distribution of Willott et al. (2010a). We address this issue by constructing the intrinsic $\lambda_{\rm Edd}$ distribution.

Since the $z \sim 6$ quasars in Table 3.4 come from various surveys that have different depths, area coverages, and completeness limits in quasar identification, we scaled the number of each quasar using M_{1450} and QLF at $z \sim 6$ (Willott et al. 2010b) as a weight to construct the $\lambda_{\rm Edd}$ distribution of a luminosity-limited unbiased sample of quasars. For the QLF, their best-fit parameters of the break magnitude $M^*_{1450} = -25.13$ mag, the bright end slope $\beta_{\rm QLF} = -2.81$, with the faint end slope of $\alpha_{\rm QLF} = -1.5$ are used. For example, the weight of IMS J2204+0112 with $M_{1450} = -23.99$ mag is given as

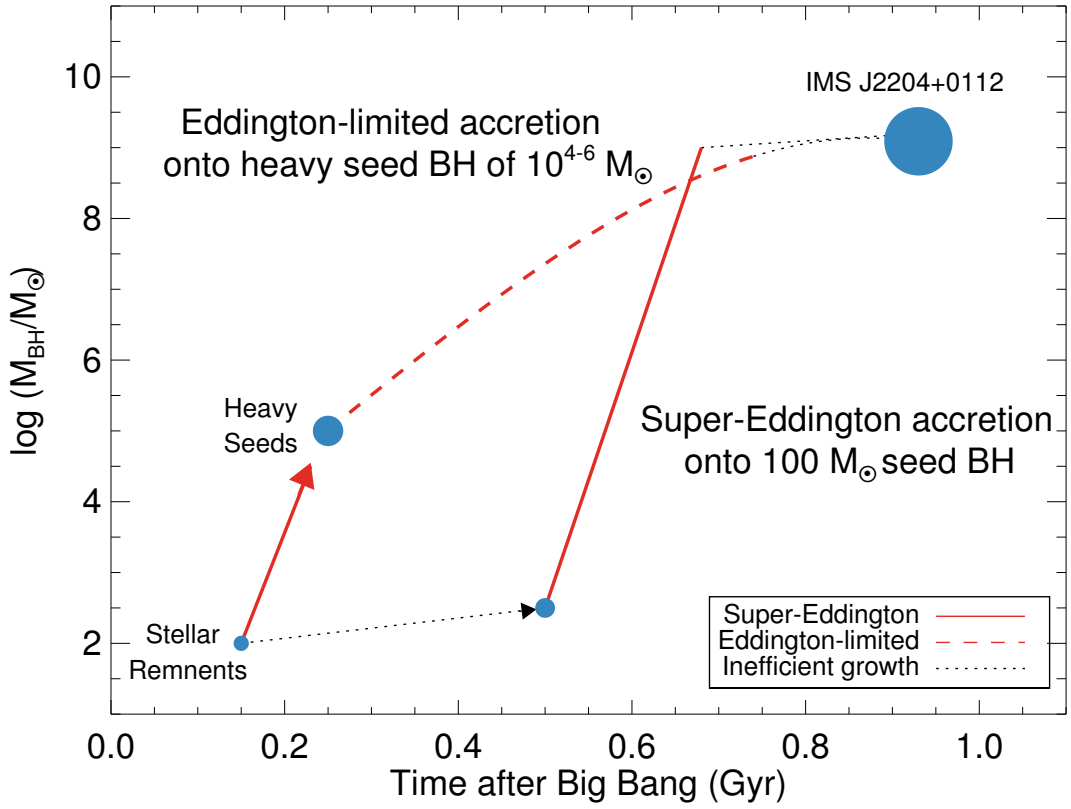

Figure 3.6. Schematic diagram for the growth of IMS J2204+0112. This figure is adapted from the Figure 2 of Smith et al. (2017).

2.96 (common quasars in nature, but rarely discovered so far at $z \sim 6$), while that of SDSS 1509−1749 with $M_{1450} = -26.78$ mag is 0.10 (many luminous quasars have been discovered but they are rare in nature).Note that we give an additional dispersion of 0.40 dex for the $\lambda_{\rm Edd}$ of IMS J2204+0112 to compare with the $\lambda_{\rm Edd}$ derived with Mg II line of $z \sim 6$ quasars, considering the dispersion of $M_{\rm BH,MgII}$ of a SDSS quasar sample (Shen et al. 2011) which has spectral properties comparable to IMS J2204+0112. Figure 3.7 shows the luminosity-limited $\lambda_{\rm Edd}$ distributions, after we summed the weighted number of quasars at a given $\lambda_{\rm Edd}$ bin. The luminosity limit is chosen as that of IMS J2204+0112, i.e., $M_{1450} \lesssim -24$ mag. As a comparison, we also constructed a similar luminosity-limited $\lambda_{\rm Edd}$ distribution of quasars at $1.9 < z < 2.1$ by randomly sampling 10,000 sets of 7 (C IV) or 21 (Mg II) $z \sim 2$ quasars from Shen et al. (2011), which are matched to the 7 (C IV) or 21 (Mg II and IMS J2204+0112) $z \sim 6$ quasars in $L_{\rm bol}$, respectively. We used the same approach of introducing the QLF-based weight at $z \sim 2$ (Schulze et al. 2015). The error bars reflect the standard deviation from the 10,000 trials. The error bars reflects the Poisson noise of the actual number of quasars that are included in each bin. The mean and the standard deviation of the luminosity-limited $\lambda_{\rm Edd}$ distributions at $z \sim 2$ and $z \sim 6$ are $\log(\lambda_{\rm Edd}) = -0.58 \pm 0.23$ dex (C IV) or -0.59 ± 0.43 dex (Mg II) and $\log(\lambda_{\rm Edd}) = -0.58 \pm 0.55$ dex (C IV) or -0.17 ± 0.53 dex (Mg II), respectively. We take the average of the mean values and standard deviations from the 10,000 sets. Note that this procedure includes the usage of QLF, and the faint end of QLF can be steeper than what we assumed here (e.g., Giallongo et al. 2015). However, the adoption of steeper faint end ($\alpha_{\rm QLF}$ of −2.0 from Onoue et al. 2017 or QLF from Giallongo et al. 2015) only reduces the mean $\log(\lambda_{\rm Edd})$ value by $\lesssim 0.1$ dex, while a flatter $\alpha_{\rm QLF}$ of −1.0 increases the value by $\lesssim 0.1$ dex. The mean $\lambda_{\rm Edd}$ of the luminosity-limited $z = 6$ sample is either comparable to (C IV), or larger by 0.42 dex (Mg II) with respect to the $z = 2$ sample, depending on which line we use for $M_{\rm BH}$ measurements. The main reason for the difference is possibly the combination of (1) the small number of objects used in the C IV-based result (7 for C IV versus 21 for Mg II) and (2) the larger (smaller) $M_{\rm BH}$ ($\lambda_{\rm Edd}$) value of IMS J2204+0112 in the C IV-based

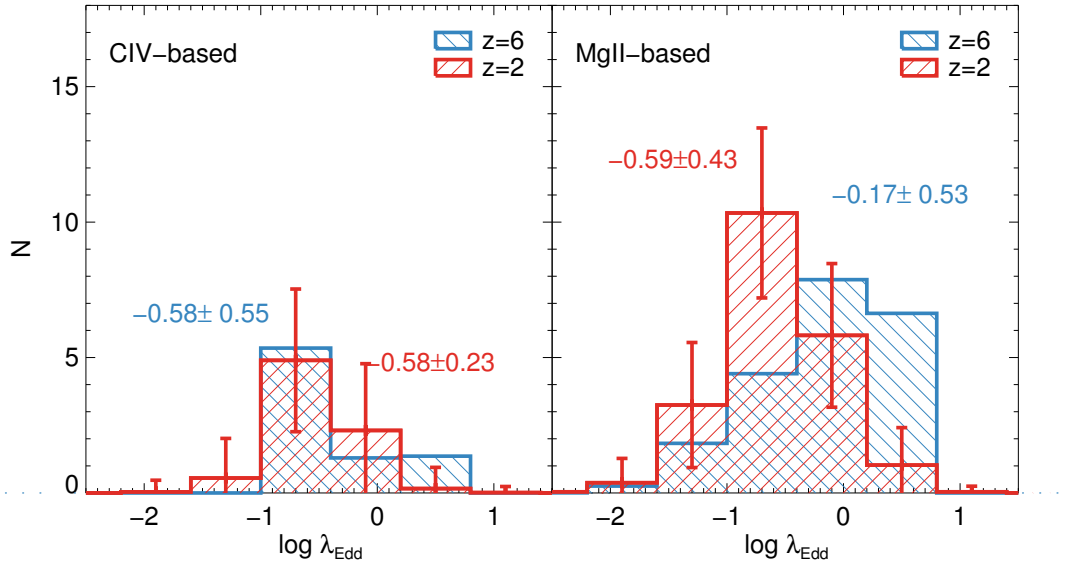

Figure 3.7. $\lambda_{\rm Edd}$ distributions of quasars derived from $M_{\rm BH,CIV}$ (left) and $M_{\rm BH,MgII}$ (right). The red and the blue histograms represent the the $\lambda_{\rm Edd}$ distributions of observed quasars at $z \sim 2$ and at $z \sim 6$, respectively. These histograms are scaled with QLFs from Schulze et al. (2015) and Willott et al. (2010b), respectively, to correct for the difference in the area coverage and the incompleteness from various surveys. Note that the error bars are typical uncertainty in each bin that is derived from 10,000 simulations. The mean and standard deviation values of the distributions are shown with same color as the histograms.

result. The smaller number statistics makes the C IV-based result less reliable than the Mg II-based result. Hence we will concentrate on the Mg II-based sample for further discussion, keeping in mind that the C IV result can give a somewhat different result.

The $\lambda_{\rm Edd}$ distribution at $z \sim 6$ with the high $\lambda_{\rm Edd}$ mean value does not necessarily reflect the true, intrinsic $\lambda_{\rm Edd}$ distribution of quasars since low $\lambda_{\rm Edd}$ quasars are likely to be missed in the luminosity-limited sample due to their faint luminosities. To derive the intrinsic $\lambda_{\rm Edd}$ distribution, we introduced the 2-dimensional fitting for density map on the $M_{\rm BH}$-$L_{\rm bol}$ plane. First, We generated the density map of the observed $z \sim 6$ quasars (panel (a) in Figure 3.8). We reproduced the mock quasars by scaling the

number of each observed quasar using QLF at $z \sim 6$ (Willott et al. 2010b) with adding the Gaussian random noises according to the errors of $M_{\rm BH}$ (but intrinsic scatters are excluded) and $L_{\rm bol}$ of each observed quasar. For this, we used the $M_{\rm BH}$ values based on Mg II only (for IMS J2204+0112, the weighted mean $M_{\rm BH,CIV}$) since the number of quasars with C IV $M_{\rm BH}$ estimates is only 7. The bin size was set to 0.01 in log scale, for both $M_{\rm BH}$ and $L_{\rm bol}$ parameters. Second, we generated various sets of 10^6 black holes which follow the black hole mass function at $z \sim 6$ (Willott et al. 2010b) in the range of 10^{7-10} $M_{\odot}$ and the $\lambda_{\rm Edd}$ distribution in a log-normal distribution with various sets of peak $\lambda_{\rm Edd}$ and dispersion values. For each set, we computed

$$\chi^2_{red} = \frac{1}{\nu} \sum \frac{(D_{\rm obs,i} - D_{\rm mock,i})^2}{D_{\rm obs,i}}, \tag{3.5}$$

where $D_{\rm obs,i}$ and $D_{\rm mock,i}$ are the normalized densities of the observed quasars and the mock quasars of each set in i-th bin, respectively, and ν is the degree of freedom. Note that we adopted the $L_{\rm bol}$ limit for fitting (red dashed lines in Figure 3.8), which is consistent with the $M_{1450} = -24$ mag at $z \sim 6$. The panel (c) in Figure 3.8 shows the χ^2_{red} distribution of the peak and the dispersion values of $\log(\lambda_{\rm Edd})$ from the various sets, after smoothed with the bin size of 0.05. We determined the best-fit parameters with the minimum χ^2_{red} as an intrinsic $\lambda_{\rm Edd}$ distribution; a peak of $\log(\lambda_{\rm Edd}) = -0.70^{+0.40}_{-0.90}$ with a dispersion of $0.35^{+0.25}_{-0.15}$ dex. Basically, the inclusion of IMS J2204+0112 with QLF-weighting reduces the peak $\lambda_{\rm Edd}$ by ~ 0.5 dex[3] in comparison to the intrinsic $\lambda_{\rm Edd}$ distribution from 17 bright quasar sample of Willott et al. (2010a), meaning that IMS J2204+0112 with $\log(\lambda_{\rm Edd}) = -0.97$ may not be an outlier but an average quasar at $z \sim 6$. For the intrinsic $\lambda_{\rm Edd}$ distribution of the luminosity matched $z \sim 2$ quasars, we also generated the density map of them (panel (d) in Figure 3.8) and computed χ^2_{red} again. The result shows that a peak value of the distribution is $-1.05^{+0.30}_{-0.35}$ with a dispersion of $0.40^{+0.15}_{-0.10}$ dex, which is still lower than that of $z \sim 6$ quasars by ~ 0.35

[3]If we change the $L_{\rm bol}$ limit ($M_{1450} = -25$ mag at $z \sim 6$), a peak of $\log(\lambda_{\rm Edd})$ is -0.20 with a dispersion of 0.15 dex, which is similar to the intrinsic $\lambda_{\rm Edd}$ distribution of Willott et al. (2010a) in the same M_{1450} limit.

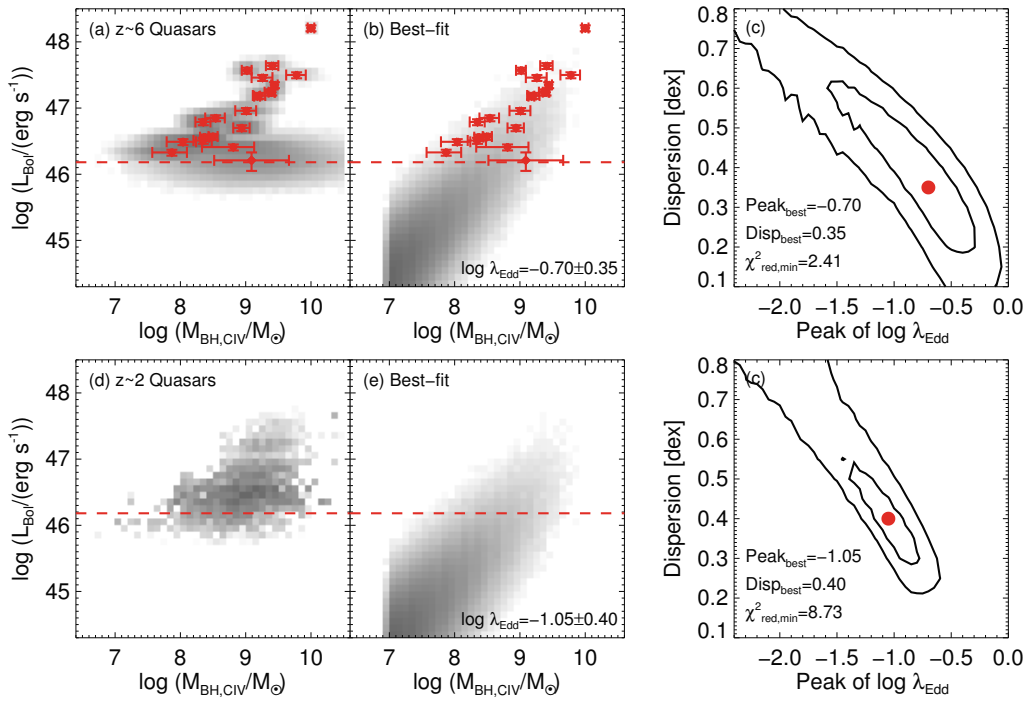

Figure 3.8. (a) The normalized density map of the $z \sim 6$ quasars (gray-scale color map), generated from the $M_{\rm BH}$-$L_{\rm bol}$ distribution of 21 quasars (red diamonds) considering the QLF (Willott et al. 2010b). The red dashed line indicates the $L_{\rm bol}$ limit corresponding to $M_{1450} = -24$ mag at $z \sim 6$. (b) The normalized density map of the best-fit set of an intrinsic $\lambda_{\rm Edd}$ distribution (gray-scale color map) for $z \sim 6$ quasars; a peak of $\log \lambda_{\rm Edd,int} = -0.70$ with a dispersion of 0.35 dex. (c) The parameter space of the peak and the dispersion of $\log(\lambda_{\rm Edd})$ for $z \sim 6$ quasars. The red dot represents our best-fit value, and the contours show the 1σ (inner) and 2σ (outer) confidence regions. (d) The normalized density map of the $z \sim 2$ quasars, generated from the 10,000 sets of randomly selected 21 quasars from Shen et al. (2011), which are luminosity-matched to 21 observed quasars at $z \sim 6$. (e) The normalized density map of the best-fit set of an intrinsic $\lambda_{\rm Edd}$ distribution (gray-scale color map) for $z \sim 2$ quasars; a peak of $\log(\lambda_{\rm Edd}) = -1.05$ with a dispersion of 0.40 dex. (f) The parameter space of the peak and the dispersion of $\log(\lambda_{\rm Edd})$ for $z \sim 2$ quasars. See details of the fitting in Section 3.5.2.

dex. Even we change the $L_{\rm bol}$ limit corresponding to $M_{1450} = -25$ mag at $z \sim 6$, the peak value of the intrinsic $\lambda_{\rm Edd}$ distribution for $z \sim 2$ quasars slightly increases to $-0.90^{+0.20}_{-0.10}$ with a dispersion of $0.35^{+0.05}_{-0.05}$ dex.

Our result shows that the peak $\lambda_{\rm Edd}$ of $z \sim 6$ quasars is larger than that of $z \sim 2$ ones (the Mg II-based result) or is nearly identical to that at $z \sim 2$ (the C IV-based result). Recently, several studies have revealed previously hidden population of quasars with low $\lambda_{\rm Edd}$ as quasar survey limits go fainter, suggesting that the $\lambda_{\rm Edd}$ distribution of $z \gtrsim 6$ quasars is not so much different from that of $z \sim 2$ quasars (Mazzucchelli et al. 2017; Shen et al. 2019), which is consistent with our findings. From $z = 2$ to $z = 6$, the scale factor of $(1 + z)^3$ gives an increase in $\lambda_{\rm Edd}$ by factor of 12.7 or 1.1 dex. The amount of the predicted $\lambda_{\rm Edd}$ evolution is somewhat stronger than the observed one (a factor of 2.2 or 0.35 dex), but can be in a broad agreement considering the uncertainty due to the small number statistics. Or, the $\lambda_{\rm Edd}$ scaling with $(1 + z)^3$ is probably too simplistic and should be limited to $z > 4.75$ or so (DeGraf et al. 2012). If we take the C IV-based result seriously, there should be no evolution of $\lambda_{\rm Edd}$ between $z = 2$ to $z = 6$, in which case it is difficult to understand with the models.

3.6 Conclusion

Through deep NIR spectroscopic observations using FIRE on the Magellan telescope, we measured the $M_{\rm BH}$ and $\lambda_{\rm Edd}$ of one of the faintest quasars at $z \sim 6$. Our result shows that IMS J2204+0112 has $M_{\rm BH} \sim 10^9 M_\odot$ and a relatively low Eddington ratio of $\lambda_{\rm Edd} = 0.1$ in comparison to other $z = 6$ quasars, implying that IMS J2204+0112 is a mature SMBH at high redshift with two possible growth scenarios: the BH growth from a massive seed BH ($\sim 10^5\, M_\odot$), or the BH growth through short, episodic super-Eddington accretion of stellar-mass BHs. Our intrinsic $\lambda_{\rm Edd}$ distribution derived from the high-redshift quasar sample including IMS J2204+0112 is in line with the recent report that the average $\lambda_{\rm Edd}$ of high-redshift quasars could be similar to that of lower-redshift quasars (Mazzucchelli et al. 2017; Shen et al. 2019). The reliability of the $M_{\rm BH}$ measurements can be improved by observing the Mg II line or the Balmer lines,

and the $\lambda_{\rm Edd}$ measurements can be improved with multi-wavelength observations that include longer wavelengths (e.g., sub-mm). Upcoming extremely large telescopes, such as the Giant Magellan Telescope and the *James-Webb Space Telescope*, will allow us to routinely observe faint quasars to measure $M_{\rm BH}$ reliably, giving a vivid perspective on SMBH evolution in the early universe.

Chapter 4

High Star Formation Rates of Low Eddington Ratio Quasars at $z \gtrsim 6$[†]

4.1 Introduction

High-redshift quasars have continued to shed light on our understanding of the early universe. To date, quasars are identified even when the universe was much less than 1 Gyr old, with the currently known highest redshift quasar ULAS J1342+0928 at $z = 7.54$ (Bañados et al. 2018) and hundreds of quasars discovered in the epoch of reionization from the optical/near-infrared (NIR) surveys (Fan et al. 2000, 2006; Goto 2006; Jiang et al. 2009, 2016; Willott et al. 2010b; Mortlock et al. 2011; Venemans et al. 2013, 2015a,b; Bañados et al. 2014, 2016, 2018; Kashikawa et al. 2015; Kim et al. 2015a; Wu et al. 2015; Matsuoka et al. 2016, 2018a,b, 2019; Wang et al. 2016, 2017, 2018b; Mazzucchelli et al. 2017; Yang et al. 2018). Mass estimates of supermassive black holes (SMBHs) residing at centers of these high-redshift quasars suggest that there are SMBHs as massive as 10^8–10^{10} $M_\odot$ just hundreds of millions of years after the Big

[†]This chapter is originally based on the article published in *The Astrophysical Journal* in July 2019 (Kim & Im 2019).

Bang (Kurk et al. 2007, 2009; Jiang et al. 2009; Willott et al. 2010a; De Rosa et al. 2011; Mortlock et al. 2011; Jun et al. 2015; Wu et al. 2015; Mazzucchelli et al. 2017; Bañados et al. 2018; Kim et al. 2018; Shen et al. 2019). Their accretion rates are found to reach the Eddington limit for most of $z \gtrsim 6$ bright quasars, meaning that they are in a rapidly growing phase (Willott et al. 2010a; De Rosa et al. 2011, 2014; Trakhtenbrot 2014; Jun et al. 2015). However, as quasar survey limits go fainter, recent studies have revealed previously hidden population of quasars with low Eddington ratios ($\lambda_{\rm Edd}$), raising a possibility that the $\lambda_{\rm Edd}$ distribution of $z \gtrsim 6$ quasars is not so much different from that of lower redshift quasars (Mazzucchelli et al. 2017; Kim et al. 2018; Shen et al. 2019; Matsuoka et al. 2019).

Not only the central black holes (BHs) but also the dust components of their host galaxies have also been examined, which are observable at from infrared (IR) to sub-mm wavelengths. The fraction of quasars without hot dust emission (dust temperature of $T_d < 1,500$ K) is found to increase with redshift (Jiang et al. 2010; Jun & Im 2013), indicating the expeditious SMBH growth prior to the star formation at high redshift. In the case of cool dust emission ($T_d < 60$ K), the recent sub-mm observations of high-redshift quasars have revealed that their rest-frame Far-infrared (FIR) luminosities ($L_{\rm FIR}$) are found to span a large range (Petric et al. 2003; Wang et al. 2008, 2010, 2013, 2016b; Venemans et al. 2012, 2016, 2017c, 2018; Omont et al. 2013; Willott et al. 2013, 2015, 2017; Bañados et al. 2015a; Mazzucchelli et al. 2017; Decarli et al. 2018; Izumi et al. 2018), inferring that their star-formation rates (SFRs) are between 10 and 2000 $M_\odot$ yr^{-1}. These high SFR values imply that high-redshift quasar host galaxies are also growing vigorously, like ultra-luminous infrared galaxies (ULIRGs) at low redshift.

In order to grow to a SMBH weighing over 10^9 $M_\odot$ hosted by a ULIRG-like galaxy in a short time of sub-Gyr, the BH accretion rate must be kept high until $z \sim 6$, despite of negative feedbacks from starbursts. Recent simulations describe this process in detail (e.g., Li et al. 2007; Sijacki et al. 2009; Pezzulli et al. 2016; Smidt et al. 2018). For example, Smidt et al. (2018) find that the 10^5 $M_\odot$ seed BH grows with cold gas inflow and mergers to 10^{10} $M_\odot$ at $\lambda_{\rm Edd} \lesssim 1$, in succession with starburst activities in the

host. At $M_{\rm BH} \sim 10^9\ M_\odot$, the BH growth slows down due to feedback mechanisms, but the starburst activities are maintained a few Myrs more at several hundred $M_\odot\ {\rm yr}^{-1}$ due to the efficient cooling of the gas with newly synthsized metals and continued cold gas inflow. At this later stage of the extended star-forming period, one expects to see quasars to have high $M_{\rm BH}$, high SFR, but low $\lambda_{\rm Edd}$. Overall, the expected evolutionary track of this simulated quasar is to start from low $M_{\rm BH}$, low SFR, high $\lambda_{\rm Edd}$ to become a high $M_{\rm BH}$, high SFR, and low $\lambda_{\rm Edd}$ quasar. This is somewhat of a contrast to the popular evolutionary scenario of Active Galactic Nuclei (AGN) where galaxies grow in obscured starburst via mergers, SMBHs grow rapidly at $\lambda_{\rm Edd} \sim 1$ and blow away the obscuring gas, and become type 1 quasars that we find in low redshift (e.g., Di Matteo et al. 2005; Springel et al. 2005; Hopkins et al. 2008; Hickox et al. 2009; Lapi et al. 2014).

For the high-redshift quasar evolutionary picture to be true, one must find low $\lambda_{\rm Edd}$ quasars with high SFR and $M_{\rm BH}$. However, it is only recently that different groups started to report the discovery of low $\lambda_{\rm Edd}$ quasars at $z \gtrsim 6$. IMS J2204+0112 is a quasar with a low bolometric luminosity of $L_{\rm bol} = 4.24 \times 10^{12}\ L_\odot$ (Kim et al. 2015a, 2018) identified from the Infrared Medium-deep Survey (IMS; M. Im et al, in preparation). This quasar has $M_{\rm BH} = 1.23 \times 10^9\ M_\odot$, and $\lambda_{\rm Edd} = 0.11$, making it one of the lowest $\lambda_{\rm Edd}$ quasars among $z \gtrsim 6$ quasars identified so far. We have obtained sub-mm data of IMS J2204+0112, using the Atacama Large Millimeter/submillimeter Array (ALMA) and the Submillimetre Common-User Bolometer Array 2 (SCUBA-2) on the James Clerk Maxwell Telescope (JCMT) operated by the East Asian Observatory (EAO), in order to measure SFR of its host galaxy. Together with 5 other sub-mm-detected low $\lambda_{\rm Edd}$ quasars in the literature, we examine if their FIR property is consistent with the evolutionary scenarios of high-redshift quasars that have been put forward lately.

This chapter is organized as follows. We describe the sub-mm observations of IMS J2204+0112 in Section 4.2, and present the sub-mm continuum maps of IMS J2204+0112 and its $L_{\rm FIR}$ measurements in Section 4.3. In Section 4.4, we describe the FIR excess of IMS J2204+0112 and the evolution of such low-$\lambda_{\rm Edd}$ quasars at high

redshift, inferred from their observed characteristics. Throughout this paper, we used the cosmological parameters of $\Omega_m = 0.3$, $\Omega_\Lambda = 0.7$, and $H_0 = 70$ km s^{-1} Mpc^{-1}, which are supported by observations in the past decades (e.g., Im et al. 1997)

4.2 Observations and Data

4.2.1 ALMA

The ALMA observations of IMS J2204+0112 were carried out in band 6 and 7. The band 6 data were obtained on 2016 December 13 and 2017 April 25 in the ALMA Cycle 4 project 2016.1.01311.S, and the band 7 data were obtained on 2018 May 17 in the ALMA Cycle 5 project 2017.1.00125.S. In both cases, 38 to 46 of the 12 m antennae were used and the baseline lengths were between 15 and 460 m, giving an angular resolution of 0.″6-0.″7. The sources for the flux/bandpass/pointing calibration were J2148+0657 and J2253+1608, while J2156-0037 was observed as a phase calibrator.

Four basebands, each with a bandwidth of 1875.00 MHz and a resolution of 15.625 MHz, were used for estimating the continuum flux density integrated over a continuum bandwidth of 7.5 GHz. The central frequencies of the bands 6 and 7 were set to 250 and 343.5 GHz, respectively. The on-source integration times were 57.46 (band 6) and 47.88 minutes (band 7).

We used the reduced data that were provided by the ALMA Science Pipeline. These data were processed through the standard reduction procedure of the Common Astronomy Software Application package (CASA; McMullin et al. 2007). Note that the data were provided as integrated continuum maps at 250 and 343.5 GHz over the entire bandwidths and continuum maps at 4 spectral windows (corresponding to basebands) in each band; 241, 243, 257, and 259 GHz for the band 6 and 336.5, 338.4, 348.5, and 350.5 GHz for the band 7. Figure 4.1 shows the ALMA integrated continuum maps of IMS J2204+0112. Note that the synthesized beam sizes of the bands 6 and 7 are $0.''80 \times 0.''57$ and $0.''81 \times 0.''67$, respectively, shown as the red-hatched ellipses in the middle panels of the figure. The rms noise values are 0.021 (band 6) and 0.026 mJy (band 7)

over the 7.5 GHz bandwidth.

4.2.2 SCUBA-2

The SCUBA-2 observations (PID: M18AP016) were carried out on 2018 June and July (5 nights) under the dry weather conditions; $0.03 \leq \tau_{225\mathrm{GHz}} \leq 0.09$ and the average seeing of $\sim 1\farcs0$. We used the CV Daisy mode that is designed for observing small and compact sources such as isolated point sources. Furthermore, a dichroic beam splitter was used to take fluxes at 450 and 850 μm simultaneously. In order to improve the signal-to-noise ratio (S/N), we applied the beam filter sizes of 8 (450 μm) and 5 (850 μm) as recommended by JCMT. The on-source integration time was 4.17 hours. For the calibrations, Uranus, Mars, and also secondary calibrators listed in Dempsey et al. (2013) were observed before/after the quasar observations.

All of the raw data were processed using the Observatory Reduction and Acquisition Control Data Reduction pipeline (ORAC-DR; Cavanagh et al. 2008; Jenness & Economou 2015). The adopted Flux Conversion Factors (FCFs) were 491 and 537 Jy pW^{-1} beam^{-1} for the 450 μm and 850 μm data, respectively (Dempsey et al. 2013). We used the PIpeline for Combining and Analyzing Reduced Data (PICARD) package for post-processing works. We mosaicked all of the data obtained at each wavelength (`MOSAIC_JCMT_IMAGES`), and then applied a beam-matched filter to the mosaicked maps with a 15$''$ Gaussian kernel (`SCUBA2_MATCHED_FILTER`). The maps were cropped to a circle centered at IMS J2204+0112 with a radius of 60$''$, an area of almost a constant integration time and rms noise values (`CROP_SCUBA2_IMAGES`). Figure 4.2 shows the SCUBA-2 continuum maps of IMS J2204+0112. The rms sensitivities measured from the median values of the cropped variance maps are 20.16 and 0.95 mJy beam^{-1} for 450 μm and 850 μm data, respectively.

4.2.3 Ancillary Data

There are imaging datasets from several surveys covering IMS J2204+0112 over a wide wavelength range: the Canada-France-Hawaii Telescope Legacy Survey (CFHTLS;

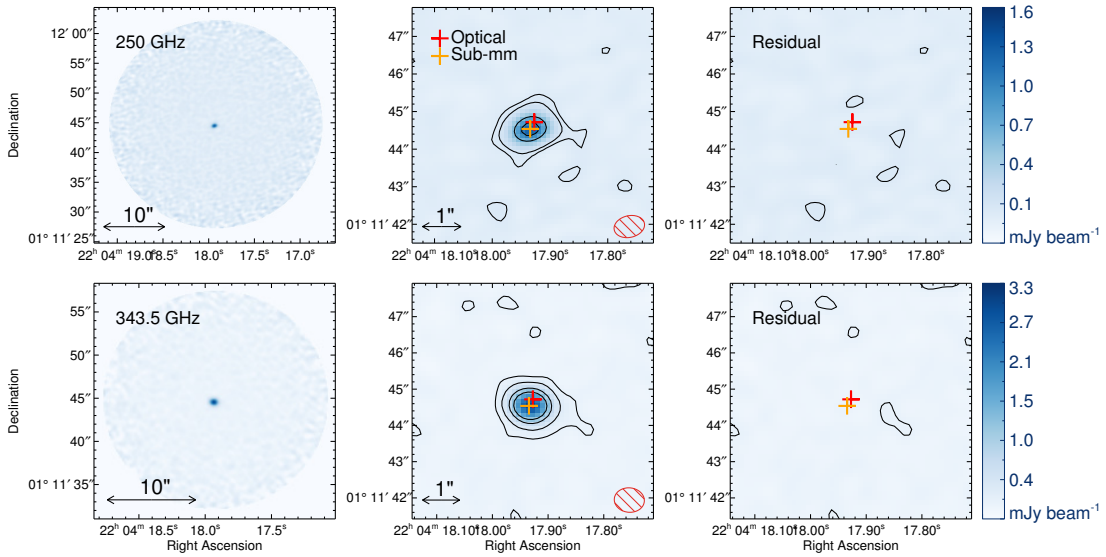

Figure 4.1. From left to right, ALMA integrated continuum maps covering the ALMA FOV, maps covering the central region around IMS J2204+0112, and residual maps after the 2D Gaussian model subtraction. Top and bottom panels represent maps at 250 (band 6) and 343.5 GHz (band 7), respectively. In both frequency maps, IMS J2204+0112 is detected as a point source without any significant neighbors. The red and orange crosses show the positions of IMS J2204+0112 in optical (HSC-SSP z-band) and sub-mm (ALMA band 6), respectively, showing the positional offset of only $\sim 0\farcs21$. The synthetic beam sizes are given in the red ellipses in the corner. The 1σ rms noises of the maps at 250 and 343.5 GHz are 21 and 26 μJy, respectively, meanwhile the black contours indicate 2, 10, 30, and 50σ significance levels.

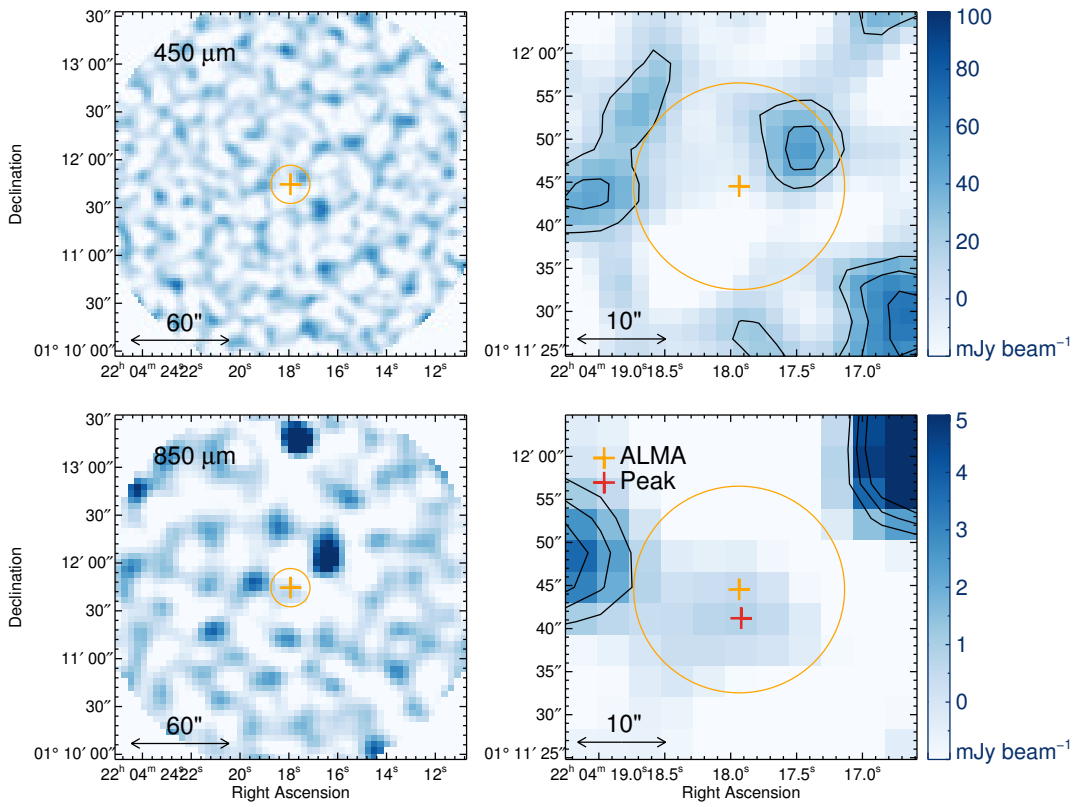

Figure 4.2. SCUBA-2 continuum maps of IMS J2204+0112 at 450 (top) and 850 μm (bottom). The right panels are enlarged portions of the center of the left panels. The 1σ rms sensitivities of the maps are 20.06 and 0.95 mJy beam^{-1}, respectively, meanwhile the black contours represent 1, 2, and 3σ significance levels. The orange cross and circle are the central position of IMS J2204+0112 and ALMA FOV with a radius of 12.″, respectively, from the ALMA band 6 data. The red cross indicates the peak of a faint object near the center, regarded as a weak signal of IMS J2204+0112 in the SCUBA-2 data.

Hudelot et al. 2012), IMS, the Data Release 1 of the Hyper Suprime-Cam Subaru Strategic Program (HSC-SSP DR1; Aihara et al. 2018a,b), the VIPERS Multi-Lambda Survey (VIPERS-MLS; Moutard et al. 2016), the Wide-field Infrared Survey Explorer (WISE; Wright et al. 2010), and the Faint Images of the Radio Sky at Twenty Centimeters Survey (FIRST; Becker et al. 1995). Among the photometric data taken at multiple epochs over the past decades, we use the most up-to-date photometric data considering the potential variability of IMS J2204+0112 (Kim et al. 2018). For example, we used the i-, z-, and y-band data of HSC-SSP instead of the i-, z- and Y-band data of CFHTLS and IMS that were taken a few years before the HSC-SSP data. We measured the fluxes of IMS J2204+0112 with SExtractor (Bertin & Arnouts 1996) as described in Kim et al. (2015a, 2019). Table 4.1 lists the multi-wavelength datasets and the measured flux densities. If not detected, we used 5σ detection limits for point sources.

4.3 Results

4.3.1 Sub-mm Continuum Maps of IMS J2204+0112

As shown in Figure 4.1, IMS J2204+0112 was clearly detected in the 250 and 343.5 GHz continuum maps obtained with ALMA (S/N $\sim$ 60 and 110, respectively). There are no noteworthy objects adjacent to IMS J2204+0112, and we found no spectral features with respect to the velocity as one can expect from its redshift $z = 5.926$. Using the IMFIT task of the CASA package, we fitted the source on each continuum map with a simple 2D Gaussian model, resulting in the integrated flux densities at 250 and 343.5 GHz are $f_{250\mathrm{GHz}} = 1.474 \pm 0.023$ and $f_{343.5\mathrm{GHz}} = 3.132 \pm 0.028$ mJy, respectively. Note that the peak flux densities are 1.289 ± 0.020 and 2.966 ± 0.027 mJy beam^{-1}, respectively. These flux densities are higher than the value expected from the relation between L_{bol} and L_{FIR} of other high-redshift quasars (equation (2) in Venemans et al. 2016; see details in Section 4.4.1) by a factor of 6, although there has been a recent suggestion that there is no correlation between L_{bol} and L_{FIR} (Venemans et al. 2018). Assuming that the FIR flux is dominated by a host galaxy, no features in the residual

Table 4.1. Flux Densities of IMS J2204+0112 from Archival Data

Data	Band	$\lambda_{\rm obs}$ (μm)	f_ν (mJy)
(1)	(2)	(3)	(4)
CFHTLS	u'	0.35	$< 1.3 \times 10^{-4}$
CFHTLS	g'	0.48	$< 0.8 \times 10^{-4}$
CFHTLS	r'	0.62	$< 1.6 \times 10^{-4}$
HSC-SSP	i	0.77	$(1.4 \pm 0.5) \times 10^{-4}$
HSC-SSP	z	0.89	$(3.4 \pm 0.2) \times 10^{-3}$
HSC-SSP	y	0.98	$(3.6 \pm 0.4) \times 10^{-3}$
IMS	J	1.25	$(3.8 \pm 0.4) \times 10^{-3}$
VIPERS-MLS	K_s	2.15	$(4.0 \pm 1.5) \times 10^{-3}$
WISE	$W1$	3.4	< 0.068
WISE	$W2$	4.6	< 0.098
WISE	$W3$	12	< 0.86
WISE	$W4$	22	< 5.4
FIRST	1.4 GHz	2.1×10^5	< 0.95

Note. — (1) The name of the survey from which the data was acquired. (2) The name of the band. (3) Observed wavelength given in units of μm. (4) Flux density in units of mJy, except for the FIRST catalog detection limit given in units of mJy beam^{-1}.

maps after the point source model subtraction (right panels of Figure 4.1) is consistent with its host galaxy being as compact as $\lesssim 0\farcs7$ (or about 4 kpc in physical scale at $z \sim 6$), like those of other high-redshift quasars (Wang et al. 2013; Willott et al. 2015, 2017; Venemans et al. 2016, 2017a; Mazzucchelli et al. 2017; Decarli et al. 2018). The central positions of the ALMA detection are offset by only about $0\farcs2$ from the z-band position (see crosses in Figure 4.1). These small offsets between the optical and sub-mm detections are in agreement with the previously reported uncertainties of ALMA astrometry (Capak et al. 2015; Willott et al. 2015; Pentericci et al. 2016), disfavoring the possibility that the sub-mm flux comes from a neighboring or foreground galaxy.

On the other hand, IMS J2204+0112 is not detected in the SCUBA-2 continuum maps. Figure 4.2 shows the SCUBA-2 continuum maps at 450 (top) and 850 μm (bottom). The non-detection at 450 μm is anticipated from the low sensitivity at that wavelength, and we give an upper limit on the flux density at 450 μm as the 5σ detection limit ($f_{450\mu\mathrm{m}} < 100.8$ mJy). At 850 μm, there is a possible indistinct source of which peak value is 0.83 mJy beam^{-1}, marked with a red cross. The weak signal can be regarded as IMS J2204+0112 considering the absence of other nearby objects within the ALMA FOV (orange circle) and the SCUBA-2 pointing accuracy of $2\farcs1$[1]. But this low signal (or non-detection) contradicts the flux density of 3.132 mJy in ALMA band 7 (873 μm) data. Note that the flux ratio of the ALMA (band 7) to the SCUBA-2 (850 μm) is known to be unity (Simpson et al. 2015a,b; Stach et al. 2018). Sub-mm flux variability is expected to be negligible since (i) the time interval is short between the ALMA band 7 and SCUBA-2 observations and (ii) the sub-mm flux of a high-redshift quasar is mainly from the dust in its host galaxy, not the central BH. Quasar radio fluxes may affect adjacent sub-mm wavelengths since they are known to vary significantly on a short time-scale. However, no sources are found within $30''$ area centered at IMS J2204+0112 in the FIRST survey of which detection limit is as low as 0.95 mJy beam^{-1} at 1.4 GHz (Becker et al. 1995), implying that the radio contribution to the sub-mm variability is negligible.

[1] https://www.eaobservatory.org/jcmt/observing/pointing/

Table 4.2. Sub-mm Flux Densities of IMS J2204+0112

Instrument	Band/Filter	$\lambda_{\rm obs}$ (μm)	f_ν (mJy)	$f_{\nu,\rm peak}$ (mJy beam^{-1})
(1)	(2)	(3)	(4)	(5)
ALMA	band 6 (250 GHz)	1199	1.474 ± 0.023	1.289 ± 0.020
	band 7 (343.5 GHz)	873	3.132 ± 0.028	2.966 ± 0.027
SCUBA-2	450 μm	450	...	...
	850 μm	850	...	0.83 ± 0.95

Note. — (1) Instrument (ALMA/SCUBA-2). (2) Band of ALMA or filter of SCUBA-2. (3) Observed wavelength given in units of μm. (4) Integrated flux density estimated from 2D Gaussian model using IMFIT task of the CASA package. (5) Peak flux density.

In Table 4.2, we present the sub-mm flux densities of IMS J2204+0112. Figure 4.3 shows the spectral energy distribution (SED) of IMS J2204+0112 in the observed frame. The black filled circles represent the flux densities of IMS J2204+0112 from Kim et al. (2015a, 2018) and the values derived from the archival data (see Section 4.2.3), while the red and blue filled circles are from our ALMA and SCUBA-2 observations, respectively. Also plotted are the composite quasar spectrum (gray line; Selsing et al. 2016), the intrinsic SED of type 1 quasar (green line; Lyu & Rieke 2017) and the empirical SED of ULIRGs hosting AGN at $z \sim 2$ (purple line; AGN4 of Kirkpatrick et al. 2015). The ULIRG AGN template is consistent with the sub-mm data, which suggests that the host of IMS J2204+0112 is ULIRG-like, similar to the hosts of other high-redshift quasars (Wang et al. 2013; Willott et al. 2013, 2015, 2017; Venemans et al. 2016; Decarli et al. 2018; Izumi et al. 2018). Note that the templates were redshifted to the observed frame using $z = 5.926$ (Kim et al. 2018), including the Intergalactic Medium (IGM) attenuation effect (Madau et al. 1996), and were scaled to our data points at adequate wavelengths.

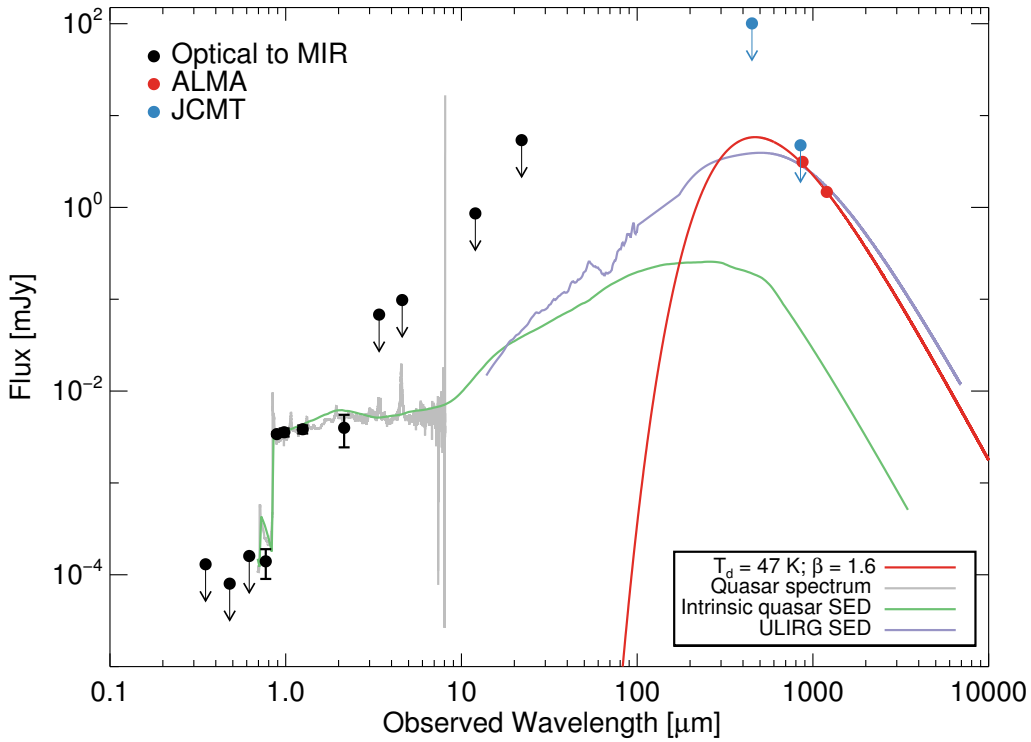

Figure 4.3. SED of IMS J2204+0112 in the observed frame. The red and blue filled circles represent the flux densities obtained by our ALMA and JCMT observations, respectively, while the black ones are the data points from Kim et al. (2015a) and the archival data (see Section 4.2.3 and Table 4.1). Note that the arrows indicate the 5σ detection limits for the undetected fluxes. The gray, green, and purple solid lines are the SED templates of the composite quasar spectrum (Selsing et al. 2016), the intrinsic SED of type 1 quasar (Lyu & Rieke 2017), and the empirical SED of ULIRGs hosting AGNs at $z \sim 2$ (AGN4 of Kirkpatrick et al. 2015), respectively. The templates are redshifted to $z = 5.926$ (Kim et al. 2018). The modified blackbody model fitted for the single $f_{250\mathrm{GHz}}$ with the fixed values of $T_d = 47$ K and $\beta = 1.6$ is shown as the red solid line (see details in Section 4.3.2).

4.3.2 FIR Luminosity and Star-formation Rate

Dunne et al. (2000) and Beelen et al. (2006) suggest that the dust emission in high-redshift quasar host galaxies can be characterized by a modified blackbody model as

$$f_\nu \propto \nu^\beta B_\nu(T_d), \tag{4.1}$$

where β is the dust emissivity power-law spectral index and B_ν is the Planck function with a given T_d. Following their papers, we define the $L_{\rm FIR}$ as the integrated luminosity over the wavelength range from 42.5 to 122.5 μm in the rest frame. We derive $L_{\rm FIR}$ using several methods. First we estimate $L_{\rm FIR}$ from a single point of $f_{250\rm GHz}$ adopting a model with fixed values of $T_d = 47$ K and $\beta = 1.6$ (Beelen et al. 2006). The best-fit model using the MPFIT package (Markwardt 2009) is shown as the black solid line in Figure 4.4, resulting in $L_{\rm FIR} = (3.30^{+0.05}_{-0.05}) \times 10^{12}\ L_\odot$. Note that the uncertainty of $L_{\rm FIR}$ is determined by Monte Carlo method[2].

Despite being widely used for high-redshift quasar host galaxies (e.g., Decarli et al. 2018), the method using a single $f_{250\rm GHz}$ with the fixed T_d and β values for the $L_{\rm FIR}$ estimation can be quite uncertain considering the wide variance of T_d from 30 to 60 K for high-redshift quasars (Beelen et al. 2006; Leipski et al. 2014; Venemans et al. 2016; Trakhtenbrot et al. 2017a). Here we have several sub-mm data points, as many as 8 continuum flux densities from the spectral windows ($f_{\nu,\rm spw}$) in the bands 6 and 7, allowing us to figure out the FIR SED of IMS J2204+0112 more accurately. In Figure 4.4, the best-fit model for two data points of $f_{250\rm GHz}$ and $f_{343.5\rm GHz}$ (red circles) with the fixed T_d and β is shown as the black dotted line, giving $L_{\rm FIR}$ of $(3.43^{+0.03}_{-0.03}) \times 10^{12}\ L_\odot$. Under the same conditions, we found $L_{\rm FIR}$ of $(3.46^{+0.03}_{-0.03}) \times 10^{12}\ L_\odot$ for the eight $f_{\nu,\rm spw}$ values (blue circles). These results are only 5% larger than $L_{\rm FIR}$ from the single point of $f_{250\rm GHz}$.

On the other hand, given T_d and β as free parameters, we found a bimodal bivariate

[2]We generated 10,000 mock sets of flux densities by adding Gaussian random noises scaled by the flux measurement uncertainties, and found a best-fit model for each set. We took a median $L_{\rm FIR}$ value, and the 68% range of the inferred $L_{\rm FIR}$ distribution were taken as 1σ error.

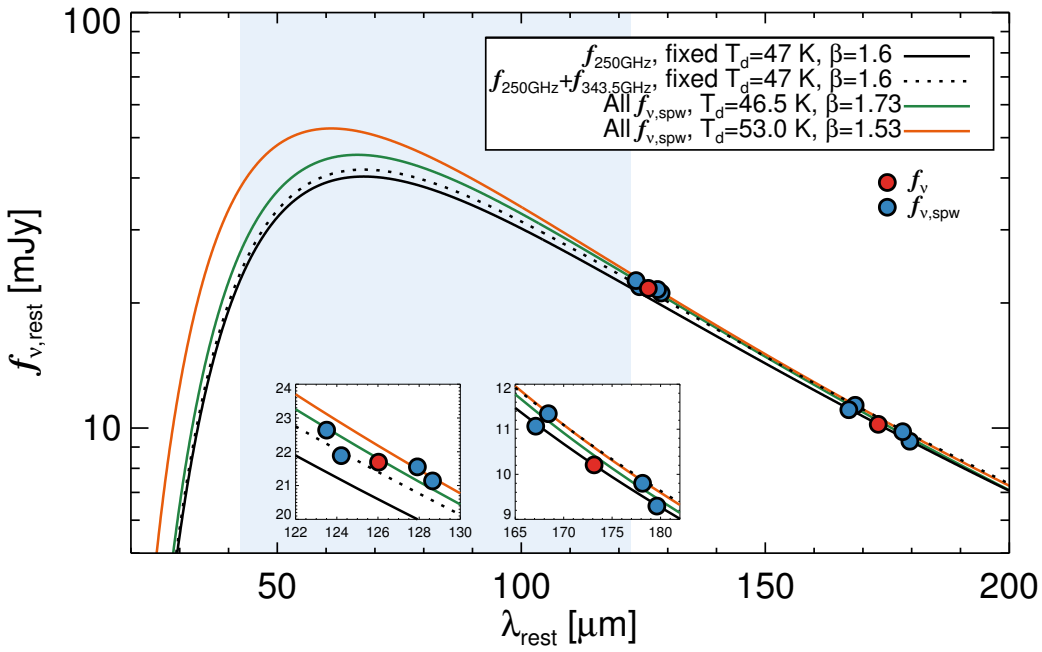

Figure 4.4. FIR SED of the cool dust components of IMS J2204+0112 in the rest frame. The red and blue filled circles are the f_ν and $f_{\nu,\mathrm{spw}}$ values, respectively. The best-fit modified blackbody models for the $f_{250\mathrm{GHz}}$ and $f_{250\mathrm{GHz}}+f_{343.5\mathrm{GHz}}$ with $T_d = 47$ K and $\beta = 1.6$ are shown as the black solid and dotted lines, respectively. The green and orange lines represent the best-fit models for the $f_{\nu,\mathrm{spw}}$ values with the two sets of T_d and β, which are from a bimodal bivariate distribution in the T_d-β parameter space. The shaded region indicates the wavelength range to determine L_{FIR} (from 42.5 to 122.5 μm). The insets are enlarged diagrams in band 6 and 7.

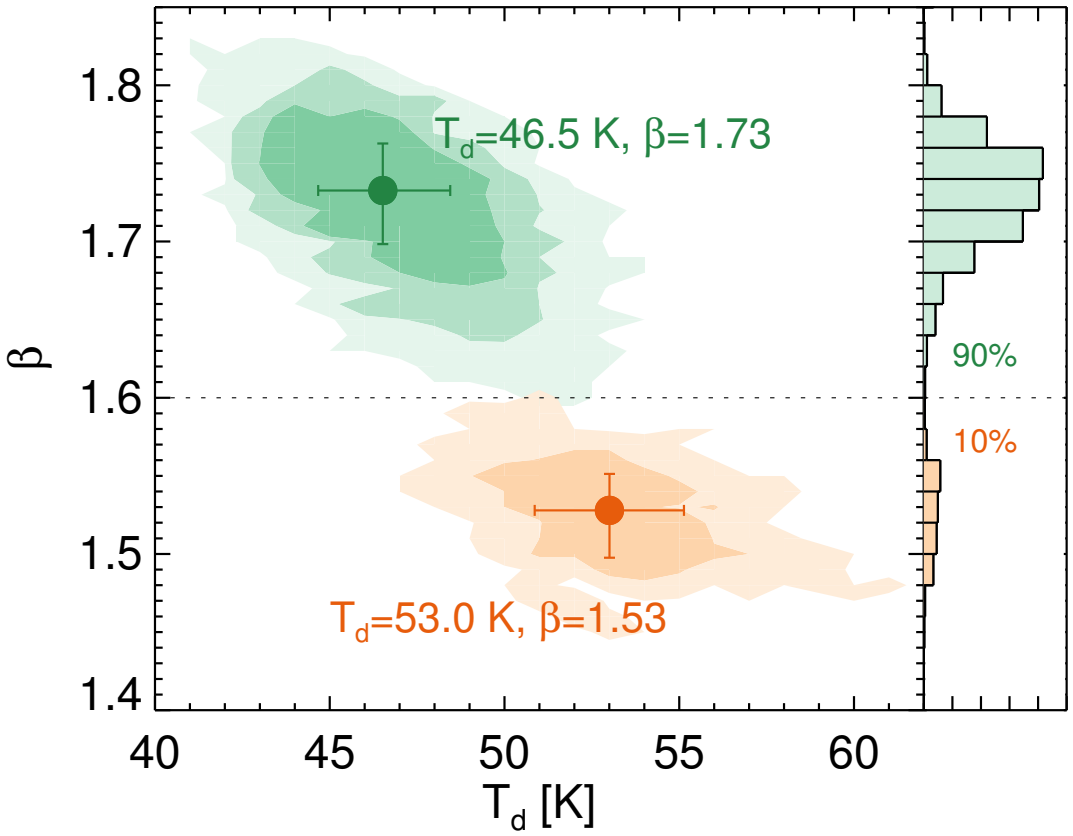

Figure 4.5. Posterior distribution of T_d and β from 10,000 trials of the Monte Carlo method described in Section 4.3.2. We divide the distribution by two at $\beta = 1.6$ (dotted line). The best-fit values are remarked with 1σ errors in the panel, and also listed in Table 4.3. The contour levels represent the number of trials; 1, 10, and 50 from outer to inner. The histograms of the divided distributions are also shown with their fractions.

Table 4.3. $L_{\rm FIR}$ and SFR of IMS J2204+0112

Band(s)	T_d (K)	β	$L_{\rm FIR}$ (10^{12} $L_\odot$)	SFR ($M_\odot$ yr^{-1})	Note
(1)	(2)	(3)	(4)	(5)	(6)
			Using f_ν		
Band 6	47	1.6	$\mathbf{3.30^{+0.05}_{-0.05}}$	$\mathbf{560^{+8}_{-8}}$	fixed T_d, β
Band 6, 7	47	1.6	$3.43^{+0.03}_{-0.03}$	583^{+4}_{-4}	fixed T_d, β
			Using $f_{\nu,\rm spw}$		
Band 6, 7	47	1.6	$3.46^{+0.03}_{-0.03}$	587^{+4}_{-4}	fixed T_d, β
Band 6, 7	$46.5^{+1.9}_{-1.8}$	$1.73^{+0.03}_{-0.03}$	$3.71^{+0.31}_{-0.33}$	631^{+55}_{-51}	$\beta > 1.6$
Band 6, 7	$53.0^{+2.1}_{-2.1}$	$1.53^{+0.02}_{-0.03}$	$4.30^{+0.35}_{-0.37}$	731^{+60}_{-62}	$\beta < 1.6$

Note. — (1) the band(s) where the f_ν ($f_{\nu,\rm spw}$) used for fitting came from. (2) Dust temperature in unit of K. (3) Dust emissivity power-law spectral index. (4) FIR luminosity determined by integrating fitted modified blackbody model from 42.5 to 122.5 μm in the rest frame. (5) Star-formation rates estimated from FIR luminosities. The values in bold were used for comparison with those of other quasars. For the case with non-fixed T_d and β, the Monte Carlo method gives a bimodal distribution of them in their parameter space, and we present the results of them in the bottom two rows (see details in Section 4.3.2). The reason for the small uncertainties of the cases for the fixed parameters is that the only flux measurement uncertainties are included.

distribution in the T_d-β parameter space (Figure 4.5). We obtained $L_{\rm FIR} = (3.71^{+0.33}_{-0.31}) \times 10^{12}\ L_\odot$ from the generated sample with $\beta > 1.6$ (green contours). In the case of $\beta < 1.6$ (orange contours), we obtained $L_{\rm FIR} = (4.30^{+0.35}_{-0.37}) \times 10^{12}\ L_\odot$ that is 30% higher than the $L_{\rm FIR}$ estimated from the single $f_{\rm 250GHz}$. But the latter case accounts for only 10% of the sample generated for the error estimation, and could be regarded as an exceptional case.

Overall, the inclusion of flux densities from more wavelengths than just a single 250 GHz results in a modest increase (5–10%, but up to 30% in rare cases) in the $L_{\rm FIR}$ value. The derived T_d values also agree with previously reported T_d of $z \gtrsim 5$ quasars (Beelen et al. 2006; Leipski et al. 2014; Trakhtenbrot et al. 2017a). This implies that the assumption of $T_d = 47$ K and $\beta = 1.6$ is reasonable for IMS J2204+0112 for estimating $L_{\rm FIR}$ to an accuracy of 5%−30%. We listed the fitted values from the various methods in Table 4.3.

Under the assumption that the FIR flux of IMS J2204+0112 mainly arises due to star formation, we estimate the SFR following the relation of

$$\frac{\rm SFR}{M_\odot\ {\rm yr}^{-1}} \sim 1.7 \times 10^{-10}\ \frac{L_{\rm FIR}}{L_\odot}, \tag{4.2}$$

described in Willott et al. (2017) for the Chabrier initial mass function (Carilli & Walter 2013). The SFRs estimated from the above $L_{\rm FIR}$ values are in the range of 560-731 $M_\odot$ yr^{-1}, and they are also listed in Table 4.3.

In the following sections, we used the $L_{\rm FIR}$ value derived from $f_{\rm 250GHz}$ as a representative value of IMS J2204+0112, for the sake of comparison with other $z \gtrsim 6$ quasars for which $L_{\rm FIR}$ are derived from single data points at ~ 250 GHz.

4.4 Discussion

4.4.1 FIR Excess of IMS J2204+0112

IMS J2204+0112 is a relatively low luminosity quasar with $L_{\rm bol} = 4.24 \times 10^{12}\ L_\odot$ (Kim et al. 2018). However, the observed $L_{\rm FIR}$ of IMS J2204+0112 is comparable to

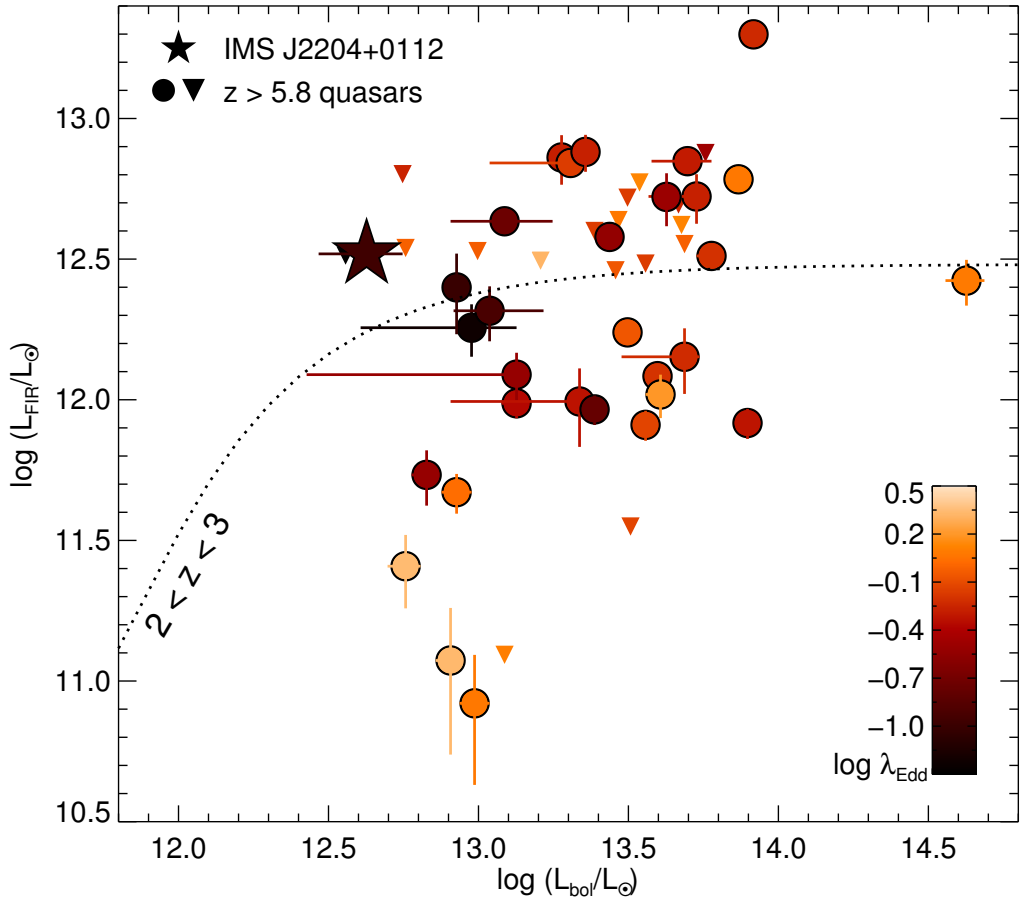

Figure 4.6. $L_{\rm bol}$-$L_{\rm FIR}$ distributions of quasars. The star symbol indicates IMS J2204+0112. The filled circles with error bars represent the $z > 5.8$ quasars which have both UV and FIR measurements in the literature, while the upside-down triangles are the upper limits on $L_{\rm FIR}$ of FIR-undetected sources (see details in Section 4.4.1). The colors of the symbols indicate the $\lambda_{\rm Edd}$ of the quasars. The dotted line shows the relation for quasars at $2 < z < 3$ (Harris et al. 2016).

the average $L_{\rm FIR}$ value of other high-redshift quasars with $L_{\rm bol} > 10^{13}$ $L_{\odot}$ ($L_{\rm FIR} \sim 3 \times 10^{12}$ $L_{\odot}$; Venemans et al. 2018). High $L_{\rm FIR}$ of IMS J2204+0112 is inconsistent with the previous suggestion that low-luminosity quasars are hosted by low-$L_{\rm FIR}$ galaxies (Willott et al. 2013, 2017; Izumi et al. 2018).

For comparison, we plot in Figure 4.6 the $L_{\rm FIR}$ versus $L_{\rm bol}$ values of IMS J2204+0112 (star) and other $z > 5.8$ quasars (circles) that have both the rest-UV spectral properties and the rest-FIR continuum properties in the literature. For the other quasars, The $L_{\rm bol}$ values were derived from L_{3000} (a luminosity at 3000 Å in the rest frame) with a bolometric correction factor of 5.18 (Runnoe et al. 2012). Meanwhile, the $L_{\rm FIR}$ values were derived in the same manner as IMS J2204+0112 using the FIR continuum flux densities at $\sim$ 250 GHz in the literature (i.e. a single FIR flux density is used for each quasar). For FIR-undetected quasars, we used 3σ detection limits on FIR flux densities, shown as the upside-down triangles in Figure 4.6. In addition, we estimated the $M_{\rm BH}$ of the quasars from their L_{3000} and FWHM values of Mg II emission line following Vestergaard & Osmer (2009) under the assumption of the virial motions of Mg II emitting gas, giving their $\lambda_{\rm Edd}$ values as well. The derived values are given in Table 4.4.

It is remarkable that the $L_{\rm FIR}$ value of IMS J2204+0112 is an order of magnitude higher than that of its $L_{\rm bol}$-matched quasar (CFHQS J0210−0456; Willott et al. 2010a, 2013), which has $\lambda_{\rm Edd} \sim 2$. Likewise, the recently discovered $z \gtrsim 6.5$ quasars with low $\lambda_{\rm Edd}$ (Mazzucchelli et al. 2017; Shen et al. 2019) also have higher $L_{\rm FIR}$ values than those of their $L_{\rm bol}$-matched sample with high $\lambda_{\rm Edd}$. This trend is more prominent in Figure 4.7 which shows a negative correlation between $L_{\rm FIR}/L_{\rm bol}$ and $\lambda_{\rm Edd}$ of the high-redshift quasars ($L_{\rm FIR}/L_{\rm bol} \propto {\lambda_{\rm Edd}}^{-1}$), although these quasars are not a complete sample. Note that we cannot find such a negative correlation for the Palomar-Green (type 1) Quasars (Lani et al. 2017; Lyu et al. 2017). In particular, IMS J2204+0112 has the highest $L_{\rm FIR}/L_{\rm bol}$ value of 0.8 among the sources with sub-mm detection in Figure 4.7. If it were at a low redshift, this quasar can be classified as an obscured quasar that is in the evolving stage before the optically bright type 1 quasar phase

($L_{\rm FIR}/L_{\rm bol} > 0.3$; Hao et al. 2005; Lapi et al. 2014; Mancuso et al. 2017).

Since the $L_{\rm bol}$ of IMS J2204+0112 is derived from its UV continuum luminosity, one may argue that the large $L_{\rm FIR}/L_{\rm bol}$ ratio is a result of absorption/scattering of the UV flux by the dust in its host galaxy. We examine if the dust absorption is the reason for its low luminosity and $\lambda_{\rm Edd}$. Under the assumption that its host galaxy is a starburst galaxy, we estimated the UV extinction of the host galaxy ($A_{\rm UV}$ at 0.16 μm) of IMS J2204+0112 from the ratio of the host galaxy's FIR and UV luminosities (equation (7) in Calzetti et al. 2000):

$$A_{\rm UV} \simeq 2.5 \log \left[\frac{1}{0.9} \frac{L_{\rm FIR}}{f_{\rm host} L_{\rm UV}} + 1 \right], \tag{4.3}$$

where $L_{\rm UV}$ is the UV luminosity at 0.16 μm following the prescription of Runnoe et al. (2012), and $f_{\rm host}$ is the fractional contribution of the host galaxy to $L_{\rm UV}$. Here, we also assume that $L_{\rm FIR}$ is dominated by the host galaxy.

In the right panel of Figure 4.7, we show the change of $A_{\rm UV}$ in terms of $L_{\rm FIR}/L_{\rm bol}$. The lower limit of the UV extinction of IMS J2204+0112 would be $A_{\rm UV} > 1.7$ or $E(B-V) > 0.4$, which is achieved when $f_{\rm host} = 1$ (solid line). Application of the $A_{\rm UV} > 1.7$ correction would increase the intrinsic $L_{\rm bol}$ of IMS J2204+0112 by > 0.7 dex, which in turn gives $L_{\rm FIR}/L_{\rm bol} < 0.1$, in agreement with the $L_{\rm FIR}/L_{\rm bol}$ values of type 1 quasars (Lapi et al. 2014; Lani et al. 2017; Lyu et al. 2017; Stanley et al. 2017) and the $L_{\rm bol}$-$L_{\rm FIR}$ relation of $z \gtrsim 6$ quasars (Figure 7 and equation (2) in Venemans et al. 2016). However, the suggestion that IMS J2204+0112 is an obscured quasar can be rejected due to the following reasons. First, IMS J2204+0112 has evident Lyα λ1216 and C IV λ1549 emission lines (Kim et al. 2018). Given such a large $E(B-V)$ value, the UV emission lines are expected to be weak or undetectable even in luminous quasars ($L_{\rm bol} > 3 \times 10^{12}$ $L_{\odot}$; Wethers et al. 2018). Second, the spectrum of IMS J2204+0112 shows a moderate UV power-law slope of $\alpha_{\lambda} = -1.12$ (Kim et al. 2018), inconsistent with the expectation for an obscured quasar. For the large $A_{\rm UV}$ value, the intrinsic α_{λ} should be much steeper than $\alpha_{\lambda} < -3.5$ that is a rare case for quasars. Finally, the above situations become worse if $f_{\rm host} < 1$. For example, $A_{\rm UV}$ increases to 6.4 if we

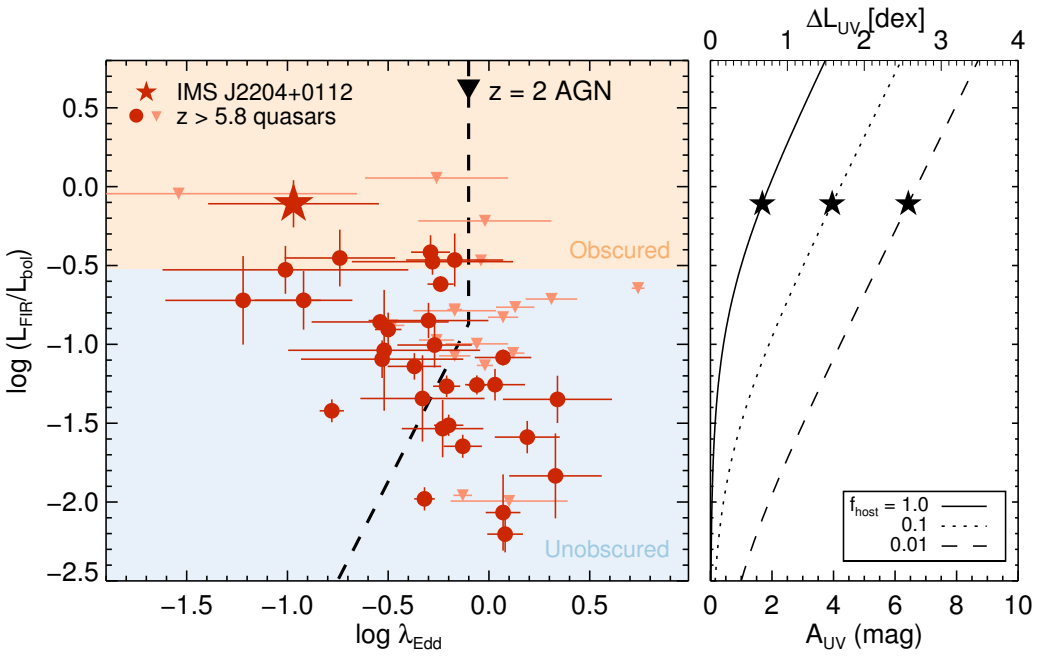

Figure 4.7. *Left*: $L_{\rm FIR}/L_{\rm bol}$ of high-redshift quasars with respect to $\lambda_{\rm Edd}$. The symbols are the same as in Figure 4.6, while their colors are given red and orange depending on whether they were detected or not. The dashed line with an arrow shows the simple evolutionary track of AGN at $z = 2$ (Lapi et al. 2014), while the arrow indicates the direction of evolution. The orange/blue shaded regions for obscured/unobscured quasars are robustly divided at $L_{\rm FIR}/L_{\rm bol} = 0.3$ following Lapi et al. (2014). *Right*: $L_{\rm FIR}/L_{\rm bol}$ as a function of UV extinction. The solid, dotted, and dashed lines represent the cases of $f_{\rm host} = 1.0$, 0.1, and 0.01, respectively. The star symbols indicate the cases of IMS J2204+0112.

assume that 1 % of the UV photons are from its host galaxy ($f_{\rm host} = 0.01$; dashed line). In fact, the host-to-AGN UV flux ratio of quasars with $L_{\rm bol} > 10^{12}\ L_{\odot}$ is almost zero (Shen et al. 2011), and $A_{\rm UV}$ becomes extremely high ($\gg 6.4$) in such a case.

One possibility is that dust is not along our line of sight, allowing us to see its central engine. It may happen under the assumption of the spaciously distributed dust components (Lyu & Rieke 2018), while dust along the polar direction (or the line of sight) was blown out by strong outflows from the central BH. For example, there are optically selected $0.5 < z < 4$ quasars that are also FIR detected with high $L_{\rm FIR}/L_{\rm bol}$ values, although they occupy only a few percents of the whole sample of optically selected quasars (Pitchford et al. 2016).

Like IMS J2204+0112, the spectral features of other $z > 5.8$ quasar sample we used also show a little possibility of being obscured by the dust in their host galaxies. Therefore, in the following discussions, we regard the estimated $\lambda_{\rm Edd}$ values of them as intrinsic ones without any UV extinction.

Table 4.4. Derived Rest-UV and FIR Properties of $z \gtrsim 6$ Quasars from the Literature

ID	z	$L_{\rm bol}$ (10^{12} $L_\odot$)	$M_{\rm BH}$ (10^8 $M_\odot$)	$\lambda_{\rm Edd}$	$L_{\rm FIR}$ (10^{12} $L_\odot$)	SFR ($M_\odot$ yr^{-1})	References
(1)	(2)	(3)	(4)	(5)	(6)	(7)	(8)
J0005−0006	5.844	$14.4^{+0.3}_{-0.3}$	$0.8^{+0.1}_{-0.1}$	5.50	< 3.26	< 553	1, 2
J0028+0457	5.99	$27.4^{+0.2}_{-0.2}$	$28.8^{+26.1}_{-17.4}$	0.29	$3.79^{+0.07}_{-0.07}$	644 ± 12	3, 4
J0033−0125	6.02	$8.5^{+0.1}_{-0.1}$	$26.3^{+80.8}_{-19.8}$	0.10	$2.51^{+0.80}_{-0.80}$	426 ± 135	3, 5
J0050+3445	6.253	$46.5^{+4.5}_{-5.1}$	$25.7^{+4.5}_{-4.3}$	0.55	< 4.95	< 840	6, 7
J0055+0146	5.983	$8.5^{+1.0}_{-0.9}$	$2.4^{+0.8}_{-0.7}$	1.07	$0.47^{+0.08}_{-0.08}$	79 ± 12	6, 8
J0100+2802	6.30	$423.7^{+62.8}_{-63.1}$	$107.2^{+15.9}_{-13.8}$	1.20	$2.65^{+0.49}_{-0.49}$	450 ± 83	9, 10
J0109−3047	6.763	$13.4^{+1.3}_{-10.7}$	$13.5^{+4.7}_{-8.9}$	0.30	$1.23^{+0.24}_{-0.24}$	208 ± 41	11, 12
J0136+0226	6.21	$5.6^{+0.1}_{-0.1}$	$3.1^{+2.9}_{-1.9}$	0.55	< 6.34	< 1077	3, 7
J0210−0456	6.438	$5.7^{+0.7}_{-0.7}$	$0.8^{+0.6}_{-0.4}$	2.19	$0.26^{+0.07}_{-0.07}$	43 ± 12	6, 13
J0221−0802	6.161	$6.7^{+0.6}_{-0.7}$	$6.9^{+7.5}_{-4.6}$	0.30	$0.54^{+0.12}_{-0.12}$	91 ± 20	6, 14
J036.5078+03.0498	6.533	$53.3^{+5.1}_{-16.4}$	$30.2^{+11.5}_{-9.8}$	0.54	$5.28^{+1.06}_{-1.06}$	897 ± 179	11, 15
J0227−0605	6.21	$5.7^{+0.1}_{-0.1}$	$1.8^{+1.6}_{-1.1}$	0.95	< 3.46	< 588	3, 7
J0303−0019	6.079	$9.9^{+0.2}_{-0.2}$	$3.3^{+0.2}_{-0.2}$	0.91	< 3.38	< 574	1, 2
J0305−3150	6.61	$20.3^{+2.5}_{-9.4}$	$9.1^{+3.5}_{-3.6}$	0.68	$6.95^{+0.21}_{-0.21}$	1180 ± 35	11, 12
J0353+0104	6.072	$36.1^{+1.7}_{-1.6}$	$15.8^{+2.8}_{-2.7}$	0.68	< 3.05	< 518	1, 2
J0836+0054	5.81	$18.9^{+1.4}_{-1.7}$	$11.0^{+2.5}_{-2.1}$	0.51	$7.27^{+1.45}_{-1.45}$	1235 ± 247	16, 17
J0841+2905	5.95	$28.6^{+0.1}_{-0.1}$	$10.0^{+3.8}_{-3.2}$	0.87	< 2.89	< 490	3, 5
J0842+1218	6.069	$39.5^{+1.9}_{-1.8}$	$19.1^{+3.3}_{-2.8}$	0.63	$1.21^{+0.11}_{-0.11}$	206 ± 19	1, 4
J1030+0524	6.302	$32.1^{+0.7}_{-0.7}$	$13.2^{+1.3}_{-1.4}$	0.74	< 0.35	< 60	1, 4
J1048+4637	6.198	$73.6^{+1.7}_{-1.7}$	$19.1^{+6.6}_{-5.6}$	1.17	$6.08^{+0.14}_{-0.14}$	1033 ± 24	1, 4
J167.6415−13.4960	6.505	$12.2^{+3.9}_{-5.5}$	$3.0^{+1.2}_{-1.4}$	1.26	< 0.12	< 21	11, 4
J1120+0641	7.087	$48.6^{+5.9}_{-18.7}$	$25.1^{+8.0}_{-8.9}$	0.59	$1.42^{+0.37}_{-0.37}$	241 ± 63	11, 18
J1137+3549	6.01	$57.2^{+0.3}_{-0.3}$	$52.5^{+7.8}_{-6.8}$	0.33	< 7.54	< 1281	3, 19
J1148+5251	6.407	$78.9^{+1.8}_{-1.8}$	$50.1^{+6.1}_{-5.5}$	0.48	$0.83^{+0.10}_{-0.10}$	140 ± 17	1, 4
J1148+0702	6.34	$36.1^{+0.2}_{-0.2}$	$14.8^{+3.4}_{-3.0}$	0.74	$0.81^{+0.10}_{-0.10}$	138 ± 16	3, 4
J1205−0000	6.73	$9.5^{+3.9}_{-5.4}$	$47.9^{+61.8}_{-18.4}$	0.06	$1.80^{+0.38}_{-0.38}$	306 ± 64	11, 11
J1207+0630	6.03	$24.4^{+0.2}_{-0.2}$	$44.7^{+6.6}_{-5.8}$	0.17	$0.92^{+0.11}_{-0.11}$	157 ± 18	3, 4
J1250+3130	6.14	$34.4^{+0.2}_{-0.2}$	$7.8^{+1.8}_{-1.6}$	1.35	< 5.92	< 1006	3, 19
J1306+0356	6.017	$31.4^{+0.7}_{-0.7}$	$11.0^{+1.1}_{-1.2}$	0.87	$1.74^{+0.13}_{-0.13}$	295 ± 21	1, 4
J1335+3533	5.90	$42.4^{+1.0}_{-1.0}$	$40.7^{+6.0}_{-6.1}$	0.32	$5.26^{+1.12}_{-1.12}$	894 ± 191	20, 19
J1342+0928	7.527	$40.5^{+3.9}_{-4.4}$	$7.8^{+3.7}_{-2.1}$	1.55	$1.04^{+0.18}_{-0.18}$	177 ± 31	21, 22
J1411+1217	5.903	$47.5^{+1.1}_{-1.1}$	$10.7^{+1.3}_{-1.4}$	1.32	< 4.18	< 710	1, 19

Table 4.4 (cont'd)

ID	z	$L_{\rm bol}$ ($10^{12}\ L_\odot$)	$M_{\rm BH}$ ($10^8\ M_\odot$)	$\lambda_{\rm Edd}$	$L_{\rm FIR}$ ($10^{12}\ L_\odot$)	SFR ($M_\odot\ {\rm yr}^{-1}$)	References
(1)	(2)	(3)	(4)	(5)	(6)	(7)	(8)
J1427+3312	6.12	$29.3^{+0.2}_{-0.2}$	$7.6^{+1.3}_{-1.3}$	1.17	< 4.35	< 739	3, 5
J1429+5447	6.12	$22.8^{+0.2}_{-0.2}$	$13.2^{+13.7}_{-8.9}$	0.52	$7.61^{+1.14}_{-1.14}$	1292 ± 194	3, 7
J1509−1749	6.121	$59.8^{+5.8}_{-6.5}$	$29.5^{+3.6}_{-3.2}$	0.62	$3.25^{+0.09}_{-0.09}$	551 ± 16	6, 4
J231.6576−20.8335	6.587	$49.8^{+10.1}_{-12.0}$	$30.9^{+6.3}_{-20.7}$	0.50	$7.05^{+0.10}_{-0.10}$	1198 ± 17	11, 4
J1602+4228	6.08	$48.6^{+0.2}_{-0.2}$	$15.5^{+1.5}_{-1.4}$	0.95	< 3.58	< 607	3, 5
J1623+3112	6.211	$31.4^{+0.7}_{-0.7}$	$14.1^{+1.0}_{-1.2}$	0.68	< 5.23	< 888	1, 19
J1630+4012	6.058	$24.4^{+4.9}_{-5.0}$	$11.0^{+5.3}_{-4.0}$	0.68	< 3.98	< 676	1, 2
J1641+3755	6.047	$16.1^{+1.6}_{-1.8}$	$2.4^{+0.7}_{-0.6}$	2.04	< 3.12	< 530	6, 7
J2100−1715	6.087	$13.4^{+1.3}_{-1.5}$	$9.3^{+3.0}_{-2.4}$	0.43	$0.97^{+0.11}_{-0.11}$	165 ± 19	6, 4
J323.1382+12.2986	6.592	$21.7^{+1.6}_{-13.7}$	$14.1^{+4.1}_{-7.0}$	0.47	$0.99^{+0.31}_{-0.31}$	167 ± 52	11, 11
J2229+1457	6.152	$8.1^{+0.8}_{-0.9}$	$1.2^{+0.7}_{-0.5}$	2.14	$0.12^{+0.06}_{-0.06}$	20 ± 10	6, 8
J338.2298+29.5089	6.66	$10.9^{+5.6}_{-2.6}$	$27.5^{+12.3}_{-10.9}$	0.12	$2.07^{+0.46}_{-0.46}$	352 ± 77	11, 11
J2310+1855	5.96	$82.6^{+0.2}_{-0.2}$	$43.7^{+6.5}_{-6.5}$	0.58	$19.91^{+0.18}_{-0.18}$	3384 ± 30	3, 23
J2329−0301	6.417	$9.7^{+1.2}_{-1.1}$	$2.5^{+0.4}_{-0.4}$	1.17	$0.08^{+0.04}_{-0.04}$	14 ± 6	6, 14
J2348−3054	6.902	$12.2^{+5.4}_{-4.1}$	$20.4^{+8.4}_{-9.7}$	0.18	$4.31^{+0.31}_{-0.31}$	732 ± 53	11, 12
J2356+0023	6.05	$3.6^{+0.1}_{-0.1}$	$38.9^{+84.1}_{-36.8}$	0.03	< 3.25	< 553	3, 2

Note. — (1) ID of quasars. (2) Redshift from UV spectra (e.g., Mg II). (3) Bolometric luminosity. (4) Black hole mass. (5) Eddington ratio ($L_{\rm bol}/L_{\rm Edd}$). (6) FIR luminosity. (7) Star-formation rate. (8) References for rest-UV and rest-FIR, respectively: 1—De Rosa et al. (2011); 2—Wang et al. (2011); 3—Shen et al. (2019); 4—Decarli et al. (2018); 5—Wang et al. (2008); 6—Willott et al. (2010a); 7—Omont et al. (2013); 8—Willott et al. (2015); 9—Wu et al. (2015); 10—Wang et al. (2016b); 11—Mazzucchelli et al. (2017); 12—Venemans et al. (2016); 13—Willott et al. (2013); 14—Willott et al. (2017); 15—Bañados et al. (2015b); 16—Kurk et al. (2007); 17—Petric et al. (2003); 18—Venemans et al. (2012); 19—Wang et al. (2007); 20—Eilers et al. (2018); 21—Bañados et al. (2018); 22—Venemans et al. (2017c); 23—Wang et al. (2013).

4.4.2 SMBH Activity and Star Formation

In the previous section, we found a negative correlation between the $\lambda_{\rm Edd}$ and $L_{\rm FIR}/L_{\rm bol}$ of high-redshift quasars. This correlation is mainly because of the FIR excesses of low-$\lambda_{\rm Edd}$ quasars ($\lambda_{\rm Edd} < 0.2$, hereafter referred to as LEQ), including IMS J2204+0112. A mere conjecture for the FIR excesses is that their relatively weak SMBH activities are not enough to efficiently quench the star formation within their host galaxies. But such a simple picture is inadequate to explain the widely spanned $L_{\rm FIR}$ of high-$\lambda_{\rm Edd}$ quasars.

A currently popular scenario for the co-evolution of quasars and host galaxies is that obscured star-formation occurs first (possibly triggered by galaxy merger), followed by a blowout phase, and then to type 1 quasar and finally normal galaxies after the type 1 quasar activity subsides (e.g., Di Matteo et al. 2005; Springel et al. 2005; Hopkins et al. 2008; Hickox et al. 2009; Netzer 2009; Lapi et al. 2014). According to this scenario, quasars start to be identified in the blowout phase as somewhat obscured quasars with high $\lambda_{\rm Edd}$ and SFRs (Hao et al. 2005; Glikman et al. 2007; Georgakakis et al. 2009; Kim et al. 2015b; Kim & Im 2018). Then, later they become low to moderate $\lambda_{\rm Edd}$ quasars in low SFR hosts. Following this, we expect LEQs at $z \gtrsim 6$ to have low SFR hosts, but on contrary, they are found to be in high SFR hosts (see the blue-outlined symbols in Figure 4.8), and yet its dust obscuration is minimal.

This unexpected property of LEQs can be explained as the end stage of quasar evolution in the early universe as put forward recent in simulation works. In Figure 4.8, we plot the evolutionary track of a BH in the simulation of Smidt et al. (2018), shown as the navy solid lines with arrows indicating the direction of evolution. Note that we binned the track into 100 Myr for simplification. This track shows the growth of a direct collapse BH ($10^5\ M_\odot$) fed by cold and dense streams to an SMBH as massive as $10^{10}\ M_\odot$ at $z \sim 6$, while the star formation within its host galaxy is boosted by mergers and metal enrichments at an epoch coeval to or later than the time when a rapid BH growth occurred. At the end phase, the accretion rate subsides to $\lambda_{\rm Edd} \sim 0.1$, while the SFR is maintained at a few hundreds of $M_\odot\ {\rm yr}^{-1}$. This end stage of quasars in the

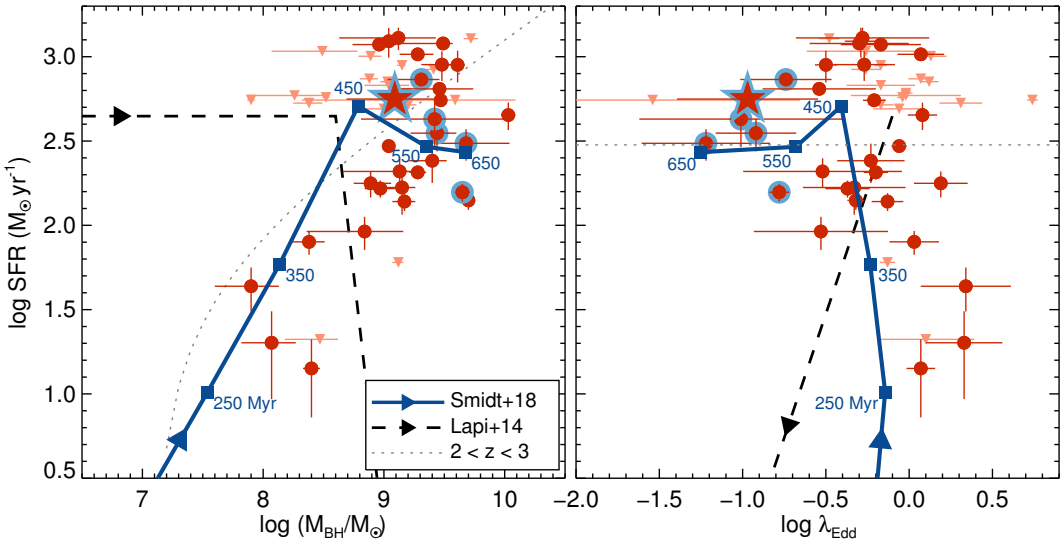

Figure 4.8. SFRs of high-redshift quasars along $M_{\rm BH}$ (left) and $\lambda_{\rm Edd}$ (right). The symbols are same as Figure 4.7, while the LEQs ($\lambda_{\rm Edd} < 0.2$) are highlighted with blue outlines. The evolutionary track of high-redshift quasars by Smidt et al. (2018) is shown as the navy solid lines with arrows indicating the direction of evolution, while the denoted numbers are the time since a 10^5 $M_\odot$ seed BH began to grow. The dashed lines with arrows show the simple evolutionary track of AGN at $z = 2$ (Lapi et al. 2014). The dotted line in the left panel is a power-law model matched to quasars at $2 < z < 3$ (Harris et al. 2016). Note that in the right panel, the mean SFR value of 300 $M_\odot$ yr^{-1} is plotted for quasars at $2 < z < 3$ since there was no obvious correlation between their $\lambda_{\rm Edd}$ and SFRs.

simulation result is consistent with the characteristics of the LEQs, suggesting that the central engines of these LEQs could be in the end game, while their host galaxies are expected to grow further.

It is also noteworthy in Figure 4.8 that the evolutionary track of Smidt et al. (2018) is in line with the distributions of not only the LEQs but also the other high-redshift quasars on the diagrams. In this view, the low SFR of some high $\lambda_{\rm Edd}$ quasars (e.g., J0210−0456, J2229+1457, and J2329−0301) are because they are too young to start the intense starbursts with metal enrichments. This suggestion of their young ages is also supported by their sizes of proximity zone, which are smaller than the sizes expected from their M_{1450} (Eilers et al. 2017). If this overall picture of the quasar evolution applies to the majority of $z \sim 6$ quasars, which have moderate $\lambda_{\rm Edd}$ like low-redshift type 1 quasars, we expect that there will be very few $\lambda_{\rm Edd} \sim 0.1$ quasars with low SFRs at $z \gtrsim 6$. Future deep sub-mm observation of more $\lambda_{\rm Edd} \sim 0.1$ quasars at $z \gtrsim 6$ should teach us if this is the case.

Finally, we caution that the $M_{\rm BH}$-SFR distribution of $z \sim 6$ quasars is in line with that of $2 < z < 3$ quasars (dotted line; Harris et al. 2016). The high-$\lambda_{\rm Edd}$ quasars with low SFRs can also be explained by the episodic super-Eddington accretion that suppresses the star formation in host galaxies (DeGraf et al. 2017), leaving a possibility that high-redshift quasar evolution is much more diverse than the simple picture we discussed earlier.

4.5 Summary

In this paper, we present the sub-mm observations of IMS J2204+0112, a faint $z \sim 6$ quasar with $M_{1450} = -24$ mag, using ALMA and SCUBA-2 on JCMT. We also examine if the observed sub-mm property of this and other high-redshift quasars agrees with recent simulation results. Followings are what we find in this work.

1. We obtained the 250 and 343.5 GHz (band 6 and 7, respectively) continuum maps of IMS J2204+0112 by ALMA, which show significant detections of IMS

J2204+0112. We find that IMS J2204+0112 has flux densities of $f_{250\mathrm{GHz}} = 1.474 \pm 0.023$ mJy and $f_{343.5\mathrm{GHz}} = 3.132 \pm 0.028$ mJy. On the other hand, the object was not detected in the 450 and 850 μm continuum maps obtained by SCUBA-2 on JCMT.

2. Assuming the modified blackbody model for cool dust, we estimate the L_{FIR} of (3.30–4.30)$\times 10^{12}$ $L_\odot$ for IMS J2204+0112, or the SFR of 560–731 $M_\odot$ yr^{-1}. The inclusion of the band 7 data slightly increases the L_{FIR} by 10% with $T_d = 46.5$ K and $\beta = 1.73$ (but up to 30% in rarely extreme situations). This implies that the widely used cool-dust model for high-redshift quasars with $T_d = 47$ K and $\beta = 1.6$ using a single $f_{250\mathrm{GHz}}$ is a suitable assumption for IMS J2204+0112.

3. We find that the derived L_{FIR} of IMS J2204+0112 is high in comparison to that of quasars with similar L_{bol} ($L_{\mathrm{FIR}}/L_{\mathrm{bol}} = 0.8$ versus < 0.1). At low redshift such high $L_{\mathrm{FIR}}/L_{\mathrm{bol}}$ quasars are mostly dust-obscured quasars. However the spectral features of IMS J2204+0112 rule out the possibility of this quasar being highly obscured.

4. The FIR excesses are also found for other five low-λ_{Edd} quasars ($\lambda_{\mathrm{Edd}} < 0.2$) in the literature. Combined with other quasars with higher λ_{Edd} and sub-mm detection, the overall distribution of the high-redshift quasars in the M_{BH}, λ_{Edd}, and SFR (L_{FIR}) space is consistent with simulation results of quasars in the early universe, where low λ_{Edd} and high SFR quasars are expected near at the end of the SMBH growth.

Since the number of low-λ_{Edd} quasars used in the discussion is small, enlarging the sample is necessary to see the validity of our suggestion. The recently reported low λ_{Edd} quasars at $z \gtrsim 5.7$ (Shen et al. 2019) can be good candidates for deep sub-mm observations with ALMA, allowing us to judge whether quasars with low λ_{Edd} and SFRs exist or not. Also, there are a handful number of high-redshift quasars with extremely large $L_{\mathrm{FIR}}/L_{\mathrm{bol}}$ ratios (> 0.3 or beyond; Venemans et al. 2018 and references therein), but without M_{BH} and λ_{Edd} measurements. Deep NIR spectroscopy of such

objects, possibly with upcoming future facilities such as Giant Magellan Telescope and/or James-Webb Space Telescope, should shed light on the general properties of high $L_{\rm FIR}$ quasars.

Chapter 5

Discovery of Faint Quasars at $z \sim 5$ with a Medium-band-based Approach[†]

5.1 Introduction

Based on wide-field surveys, half a million quasars have hitherto been discovered (e.g., Pâris et al. 2017), hundreds of them being at a high redshift of $z \gtrsim 5$ (Fan et al. 2001, 2006; Wolf et al. 2003; Richards et al. 2006; Fontanot et al. 2007; Willott et al. 2010b; Mortlock et al. 2011; Ikeda et al. 2012, 2017; McGreer et al. 2013, 2018; Venemans et al. 2013, 2015a,b; Bañados et al. 2014, 2016, 2018; Kashikawa et al. 2015; Kim et al. 2015a; Jun et al. 2015; Wu et al. 2015; Jiang et al. 2016; Matsuoka et al. 2016, 2018a,b, 2019; Wang et al. 2016; Yang et al. 2016, 2017; Jeon et al. 2017; Reed et al. 2017). With the identification of high-redshift quasars, we are now broadening our horizon of knowledge deep into the very early universe, especially on the cosmic reionization epoch.

Recent results from the Planck Collaboration suggest an instantaneous reionization

[†]This chapter is originally published in *The Astrophysical Journal* in January 2019 (Kim et al. 2019).

of the intergalactic medium (IGM) at $z \sim 8.8$ (Planck Collaboration et al. 2016), which is complete by $z \sim 5$. At $z \sim 2$, we know that active galactic nuclei (AGNs) are the main IGM ionizing sources (e.g., Haardt & Madau 2012), but at higher redshifts, stellar light from low-mass star-forming galaxies has been suggested to be the main reionization source (Fontanot et al. 2012, 2014; Robertson et al. 2013, 2015; Japelj et al. 2017; Hassan et al. 2018). However, such a scenario has met difficulties: it requires an exceptionally large escape fraction of Lyman continuum photons (> 20 % as opposed to a few percent for Lyman break galaxies at $z \sim 3$; Fontanot et al. 2012; Grazian et al. 2017; Japelj et al. 2017; Matthee et al. 2017; Dayal et al. 2018) and/or a very steep faint-end slope for the galaxy luminosity function (LF; Bouwens et al. 2017; Japelj et al. 2017). Alternatively, Giallongo et al. (2015) and Madau & Haardt (2015) suggest that AGNs are the main IGM ionizing sources at $4 < z < 6.5$. However, at $z \sim 6$, results are emerging suggesting that the contribution of faint quasars to the IGM ionization is not significant (e.g., Kim et al. 2015a; Onoue et al. 2017). At $z \sim 5$, it is not yet clear whether quasars or galaxies produce more ultraviolet (UV) ionizing photons. The derivation of the LF by Giallongo et al. (2015) relies on the interpolation between a photometric redshift sample of very faint quasar candidates ($M_{1450} > -22$ mag) and spectroscopically identified luminous quasars ($M_{1450} < -26$ mag). With their LF, the major contributor of the UV luminosity density is quasars with $M_{1450} \sim -23.5$ mag.

To date, various groups have performed surveys for $z \sim 5$ quasars with optical and/or infrared data (Ikeda et al. 2012, 2017; McGreer et al. 2013, 2018; Jeon et al. 2016, 2017; Yang et al. 2016, 2017). While most of the spectroscopically identified $z \sim 5$ quasars are bright with $M_{1450} < -24$ mag, the most recent study of McGreer et al. (2018, hereafter M18) focused on the dearth of quasars at $M_{1450} \sim -23$ mag. They found 104 candidates in the Canada-France-Hawaii Telescope Legacy Survey (CFHTLS) stacked images (Gwyn 2012) by using the broadband color selection method and/or the likelihood method, and 8 of which are spectroscopically identified as faint quasars ($M_{1450} > -24$ mag) at $4.7 < z < 5.4$. The faint end of the quasar luminosity function (QLF) derived from these quasars shows a lower number density

than the result from Giallongo et al. (2015) by an order of magnitude, implying low ionizing emissivity of $z \sim 5$ AGNs and their minor contribution to the cosmic reionization. Recent X-ray studies also suggested that the QLF of Giallongo et al. (2015) could be overestimated and high-redshift AGNs might not be main contributors to the cosmic reionization (Ricci et al. 2017; Parsa et al. 2018). At the faint end, however, the QLFs from the X-ray AGNs are still higher than those from the UV/optical survey by M18. The selection methods of M18 (both optical color selection and a likelihood method) might miss quasars, or conversely, their candidates could be contaminated by brown dwarfs or galaxies with peculiar colors, considering the lack of near-infrared (NIR) data and the low spectral resolution for using the likelihood method.

Recently, we performed an NIR imaging survey named the Infrared Medium-deep Survey (IMS; M. Im et al. 2019, in preparation), where NIR imaging data were obtained by the United Kingdom Infrared Telescope (UKIRT) in Hawaii. The data reache 5σ depths of $J \sim 23$ mag, over 100 deg^2 areas in the sky, which overlap with the ancillary optical data from CFHTLS, of which 5σ depths reach $\gtrsim 25$ mag in $u'g'r'i'z'$ bands. The combination of these optical and NIR data enables us to sample quasars as faint as $M_{1450} \sim -23$ mag at $z \sim 5$.

In addition to this, we developed the SED Camera for Quasars in EArly uNiverse (SQUEAN; Choi et al. 2015; Kim et al. 2016), as an upgraded instrument of the Camera for Quasars in EArly uNiverse (CQUEAN; Kim et al. 2011; Park et al. 2012; Lim et al. 2013), on the 2.1 m Otto Struve Telescope of McDonald Observatory. This new instrument works with 20 filters consisting of broadband filters (e.g., *griz*) and 50 nm medium bandwidth filters of which the central wavelengths are in the range of 675–1025 nm ($m675$–$m1025$[1]). Through observations of bright quasars at $z \sim 5$, Jeon et al. (2016) verified its effectiveness in distinguishing high-redshift quasars ($4.7 < z < 6.0$) from brown dwarfs, which are regarded as the main contaminator in high-redshift quasar selection. Furthermore, the redshift determination through the photometric redshift

[1]The medium band filters are named as m (initial of the medium-band) + the central wavelength of the filter in nm.

($z_{\rm phot}$) derived from broad- and medium-band data shows an accuracy of 1-2 % when compared to the spectroscopic redshift ($z_{\rm spec}$). Besides, the other surveys with medium-band observations such as COMBO-17 (Wolf et al. 2003), ALHAMBRA (Moles et al. 2008; Matute et al. 2012), and the NEWFIRM Medium-band Survey (van Dokkum et al. 2009) also obtained the redshifts of quasars or galaxies at $1 \lesssim z \lesssim 4$ successfully with few percent uncertainties. In addition, Matute et al. (2013) discovered a faint quasar with $M_{1450} = -24.07$ mag at $z = 5.41$ from the ~ 1 deg^2 area of the ALHAMBRA survey by adopting a spectral energy distribution (SED) fitting method (Matute et al. 2012). These results testify the effectiveness of using medium-band observations for the redshift determination of high-redshift quasars.

Based on the optical data of CFHTLS and the NIR data of IMS, we are now performing a $z \sim 5$ quasar survey with a medium-band-based approach to increase the size of the faint quasar sample at $z \sim 5$ and better determine their number density. In this chapter, we present the initial results of the $z \sim 5$ quasar survey with the medium-band observations, reporting 10 newly discovered quasars at $z \sim 5$ that are in the magnitude range of $-25 < M_{1450}$ (mag) < -23. We describe the data we used and the quasar selection method with broadband color criteria in Section 5.2, while the medium-band-based selection method with imaging follow-up with SQUEAN is described in Section 5.3. In Section 5.4, the spectroscopy data we used are characterized, consisting of our spectroscopic observations and supplemental samples from the literature. We present our main results in Section 5.5: the newly discovered quasars at $z \sim 5$ and the effectiveness of the medium-band observations at finding faint quasars at $z \sim 5$ and measuring their redshift accurately. Finally, we present the implication of the newly discovered quasars to the faint-end slope of the QLF at $z \sim 5$ in Section 5.6. Throughout the paper, we adopt the cosmological parameters of $\Omega_m = 0.3$, $\Omega_\Lambda = 0.7$, and $H_0 = 70$ km s^{-1} Mpc^{-1}, which are supported by previous observations (e.g., Im et al. 1997). All magnitudes in this paper are given in the AB system. Note that Vega-based J-band magnitudes from IMS were converted to the AB system by following Hewett et al. (2006).

5.2 Initial Sample Selection

5.2.1 CFHTLS and IMS Imaging Data

Here we describe the imaging data from which quasar candidates are selected based on the broadband colors. This selection is the initial step of the high-redshift quasar selection, which will be refined later through medium-band imaging follow-up observations (Section 5.3). The sample selection was first carried out on the optical data from the CFHTLS Wide Survey (Hudelot et al. 2012) and the NIR data from the IMS (M. Im et al. 2019, in preparation) and the Deep eXtragalactic Survey (DXS; Lawrence et al. 2007). There are four extragalactic fields covered by these surveys: XMM-Large Scale Structure survey region (XMM-LSS), CFHTLS Wide survey second region (CFHTLS-W2), Extended Groth Strip (EGS), and Small Selected Area 22h (SA22). Figure 5.1 shows the positions and layouts of tiles in CFHTLS (black squares), IMS (blue squares), and DXS (purple squares). Hereafter, for convenience, we refer to the combination of NIR data from IMS and DXS as "IMS".

For CFHTLS, we used stacked images from the TERAPIX processing pipeline (see Hudelot et al. 2012 and the T0007 documentation file[2]), which are given for each CFHTLS tile in each CFHTLS field. Note that "CFHTLS tile" here denotes the $1^\circ \times 1^\circ$ area named from the position of each MegaCam field of view of the Wide survey (e.g., W1+0+0), while "CFHTLS field" indicates the four extragalactic fields of the Wide survey (e.g., W1, W2, W3, and W4). The zero-point (zp) of each tile was reestimated by comparing the point sources in CFHTLS with those in Sloan Digital Sky Survey Data Release 12 (SDSS DR12). Through the SQL service of SDSS, we selected point sources, classified as star-like sources, within the appropriate magnitude range of $17 < r < 18.5$, considering the saturation level of CFHTLS and the photometric accuracy (magnitude errors < 0.1 mag) of SDSS data in all the bands. For the position-matched sources with reliable photometry (i.e. spatially isolated point sources without saturation), we compared their auto-magnitudes (MAG_AUTO in `SExtractor`; Bertin & Arnouts 1996)

[2]http://terapix.iap.fr/cplt/T0007/doc/T0007-doc.html

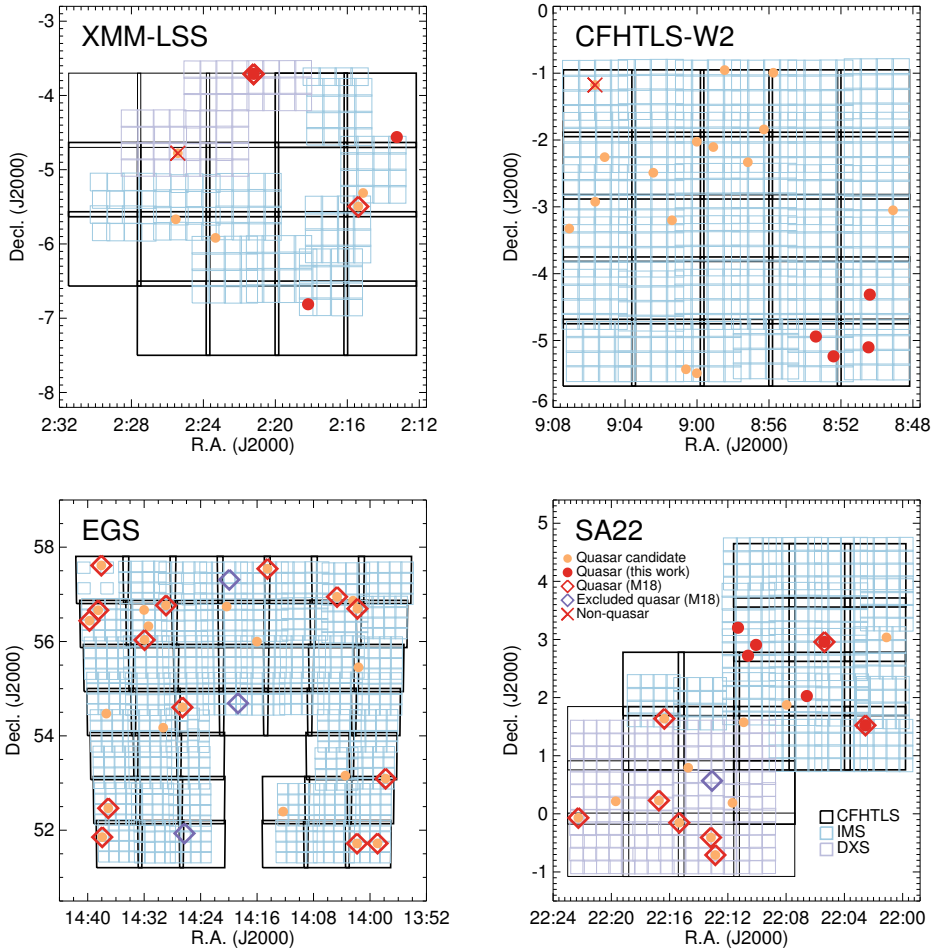

Figure 5.1. Coverage layout of the high-redshift quasar survey with IMS. The four panels show the different extragalactic fields: XMM-LSS, CFHTLS-W2, EGS, and SA22. The black squares represent the tiles of CFHTLS ($1^\circ \times 1^\circ$ for each), and the blue and purple squares are the tiles of IMS and DXS ($13\farcm65 \times 13\farcm65$ for each), respectively. The total survey areas of CFHTLS, IMS, and DXS in this figure are 103, 73, and 12 deg^2, respectively. The orange filled circles represent our $z \sim 5$ quasar candidates selected by broadband color criteria, while the spectroscopically identified quasars are additionally marked with the red filled circles (this work) and the red open diamonds (M18). Note that some of the spectroscopically identified quasars with $i < 23$ mag (M18), which are located in our survey area but excluded by our selection owing to their broadband colors, are shown as the purple open diamonds, for easy distinction. The red crosses show the candidates spectroscopically identified as nonquasar objects.

from CFHTLS with their point-spread function (PSF) magnitudes from SDSS and determined a reliable zp for each tile. In this process, we converted the auto-magnitudes in optical bands ($u'g'r'i'z'$) into SDSS photometric systems ($ugriz$), following the transformations from MegaCam to SDSS[3]. For the tiles, which do not overlap with the SDSS area, we used the overlapped stars in adjacent CFHTLS fields. The average and standard deviation of the zp value offsets in u, g, r, i, and z bands are 0.14 ± 0.04 mag, -0.06 ± 0.02 mag, -0.05 ± 0.02 mag, -0.06 ± 0.02 mag, and -0.09 ± 0.03 mag, respectively.

On the other hand, for IMS, we stacked the images of each detector covering the area of $13\farcm65 \times 13\farcm65$ instead of stacking the images of each IMS tile covering the 0.75×0.75 deg^2 area, in order to determine a reliable zp for each image. The zp of each stacked image was scaled to 28.0 in the Vega system by comparing the J-band auto-magnitudes of point sources in IMS and those from the Two Micron All Sky Survey (2MASS) catalog (Skrutskie et al. 2006). The average 5σ point-source detection limits of the optical/NIR images are $u = 26.1$, $g = 26.4$ mag, $r = 25.9$ mag, $i = 25.6$ mag, $z = 24.6$ mag, and $J = 22.9$ mag[4], enabling us to select $z \sim 5$ quasars with $i \lesssim 23$ mag or those as faint as $M_{1450} \lesssim -23$ mag. For photometry, we detected sources in the i'-band images and estimated fluxes in each band within $2\times$FWHM$_{i'}$ diameters, using the dual-image mode of the SExtractor software, with DETECT_THRESH of 1.3 and DETECT_MINAREA of 9, corresponding to a $\sim 4\sigma$ detection limit. By applying aperture correction factors derived from bright stars in each filter image, we converted the aperture magnitudes to total magnitudes. Note that the total magnitudes were also converted to the SDSS photometric system.

Although we adjusted the zp values of the optical/NIR images with point sources in the SDSS/2MASS catalogs, respectively, there are small inconsistencies of stellar loci

[3]http://www.cadc-ccda.hia-iha.nrc-cnrc.gc.ca/en/megapipe/docs/filtold.html

[4]Unlike the homogeneous optical data, the J-band data including IMS and DXS are inhomogeneous. The average depths of four extragalactic fields of IMS (XMM-LSS, CFHTLS-W2, EGS, and SA22) are 23.2, 22.7, 22.7, and 23.2 mag, respectively, and those of DXS (XMM-LSS and SA22) are 23.7 and 23.9 mag, respectively.

on the order of $\lesssim 0.1$ mag on color-color diagrams from tile to tile. Compared to the stellar libraries of Pickles (1998), these offsets were already reported by the TERAPIX team as one can see in their color-color diagrams (see footnote 2). Since the color offset can affect the quasar candidate selection substantially, we calculated the color offsets of stellar loci in each CFHTLS tile to correct the inconsistencies and improve the color selection for quasar candidates.

We used the median stellar loci of 0.3 million SDSS–2MASS stars of Covey et al. (2007) as a reference. Though their colors are not corrected for the Galactic extinction, the shape of the loci is consistent with the recent loci based on the 1 million SDSS–2MASS–WISE stars with a low extinction of $A_r < 0.125$ (Davenport et al. 2014). Furthermore, the loci of Covey et al. (2007) are also in line with those of Gwyn (2012) based on the point sources in CFHTLS data. Note that we used the loci of Covey et al. (2007), instead of those of Davenport et al. (2014), which used larger color bins in extreme cases (e.g., $r - i > 2$). For the objects classified as stars (CLASS_STAR > 0.95 from `SExtractor`) within the magnitude range of $17 < r < 21$ in each CFHTLS tile, we estimated the color offsets $C_k^{\rm offset}$ (where the index k indicates the color: $g-r$, $r-i$, $i-z$, and $i-J$), which minimize the color distance factor $D_{\rm color}$, given as

$$(D_{\rm color})^2 = \sum_i \sum_k \frac{(X_{i,k}^{\rm obj} - X_{i,k}^{\rm locus} + C_k^{\rm offset})^2}{(\sigma_{i,k}^{\rm obj})^2 + (\sigma_{i,k}^{\rm locus})^2}, \tag{5.1}$$

where $X_{i,k}^{\rm obj}$ is the k color value of the ith object, $X_{i,k}^{\rm locus}$ is the k color value of the nearest stellar locus of Covey et al. (2007) to $X_{i,k}^{\rm obj}$, $\sigma_{i,k}^{\rm locus}$ is the quadratic sum of magnitude errors consisting of the k color of the ith object, and $\sigma_{i,k}^{\rm locus}$ is the given error of $X_{i,k}^{\rm locus}$ by Covey et al. (2007). For the whole survey area, the mean values of $C_k^{\rm offset}$ are less than 0.2 mag with small standard deviations of ~ 0.05 mag: $C_{g-r}^{\rm offset} = -0.02 \pm 0.05$, $C_{r-i}^{\rm offset} = -0.01 \pm 0.05$, $C_{i-z}^{\rm offset} = -0.07 \pm 0.06$, and $C_{i-J}^{\rm offset} = 0.18 \pm 0.04$. The $C_{i-J}^{\rm offset}$ are much larger than the other $C_k^{\rm offset}$ on average, indicating that the J-band magnitudes might be slightly over-estimated when we introduce the bright 2MASS stars for the zp estimation of IMS data. We list the $C_k^{\rm offset}$ values of our candidates with spectroscopy data in Table 5.1. Note that the color offsets are not adjusted for

the apparent magnitudes of the quasars in this paper, but are used only for the color selection of quasar candidates in Section 5.2.2.

For the Galactic extinction correction, we used the extinction map of Schlafly & Finkbeiner (2011) with the Cardelli et al. (1989) law assuming $R_V = 3.1$. To account for the pixel-to-pixel correlation from the image-combining process, we scaled magnitude errors accordingly, using the noise properties (σ_N) of an effective aperture size N in each image (Gawiser et al. 2006; Jeon et al. 2010; Kim et al. 2015a).

Table 5.1. Color Offsets of Spectroscopically Identified Candidates for $z \sim 5$ Quasars

ID	$C_{g-r}^{\rm offset}$ (mag)	$C_{r-i}^{\rm offset}$ (mag)	$C_{i-z}^{\rm offset}$ (mag)	$C_{i-J}^{\rm offset}$ (mag)
Spectroscopically Identified Quasars				
IMS J021315−043341	−0.05	−0.01	−0.08	0.20
IMS J021523−052946	−0.02	0.02	−0.06	0.21
IMS J021811−064843	−0.04	−0.01	−0.15	0.12
IMS J022112−034232	−0.04	−0.01	−0.09	0.21
IMS J022113−034252	−0.04	−0.01	−0.09	0.21
IMS J085024−041850	−0.03	0.03	−0.05	0.13
IMS J085028−050607	−0.02	0.04	0.02	0.11
IMS J085225−051413	0.00	0.03	0.02	0.11
IMS J085324−045626	0.00	0.03	0.02	0.11
IMS J135747+530543	0.03	−0.04	−0.02	0.19
IMS J135856+514317	−0.04	0.06	−0.06	0.23
IMS J140147+564145	−0.01	0.06	−0.10	0.16
IMS J140150+514310	−0.04	0.06	−0.06	0.23
IMS J140440+565651	−0.02	0.07	−0.03	0.17
IMS J141432+573234	0.04	0.02	−0.04	0.21
IMS J142635+543623	0.01	0.01	−0.10	0.12
IMS J142854+564602	−0.01	0.00	−0.08	0.23
IMS J143156+560201	−0.01	0.00	−0.08	0.23
IMS J143705+522801	0.00	0.01	−0.08	0.23
IMS J143757+515115	−0.03	−0.03	−0.04	0.20
IMS J143804+573646	0.00	0.01	−0.01	0.26
IMS J143831+563946	0.02	−0.07	−0.02	0.27
IMS J143945+562627	0.02	−0.07	−0.02	0.27
IMS J220233+013120	−0.05	−0.03	−0.09	0.18
IMS J220522+025730	−0.05	−0.04	−0.12	0.09
IMS J220635+020136	0.02	−0.01	−0.13	0.12
IMS J221004+025424	−0.02	0.03	0.03	0.13
IMS J221037+024314	−0.02	0.03	0.03	0.13
IMS J221118+031207	−0.02	0.03	0.03	0.13
IMS J221251−004231	−0.10	−0.01	−0.09	0.16
IMS J221310−002428	−0.10	−0.01	−0.09	0.16
IMS J221520−000908	−0.04	−0.15	0.04	0.17

Table 5.1 (cont'd)

ID	$C_{g-r}^{\rm offset}$ (mag)	$C_{r-i}^{\rm offset}$ (mag)	$C_{i-z}^{\rm offset}$ (mag)	$C_{i-J}^{\rm offset}$ (mag)
IMS J221622+013815	−0.04	−0.01	−0.09	0.14
IMS J221644+001348	−0.04	−0.07	−0.10	0.12
IMS J222216−000406	−0.04	−0.05	−0.11	0.12
Spectroscopically Identified Non-quasars				
IMS J022525−044642	0.00	0.05	−0.10	0.22
IMS J090540−011038	0.00	−0.02	−0.10	0.15

5.2.2 Broadband Color Selection

The broadband color selection follows the criteria of McGreer et al. (2013), where they defined the color selection by simulating the color tracks using low-redshift SDSS quasar spectra that are redshifted to $z \sim 5$. Considering the deeper depths of CFHTLS and IMS, we made a minor change to the i-magnitude limit. The following shows the selection criteria that we used:

1. $i < 23$,
2. S/N $(u) < 2.5$,
3. $g - r > 1.8$ or S/N $(g) < 3.0$,
4. $r - i > 1.2$,
5. $i - z < 0.625\ ((r - i) - 1.0)$,
6. $i - z < 0.55$,
7. $i - J < ((r - i) - 1.0) + 0.56$,

where the signal-to-noise ratio (S/N) values are directly estimated from the fluxes and flux errors in the aperture mentioned above. The candidates satisfying the criteria were visually inspected to exclude spurious objects such as cross-talks, diffraction spikes, etc.,

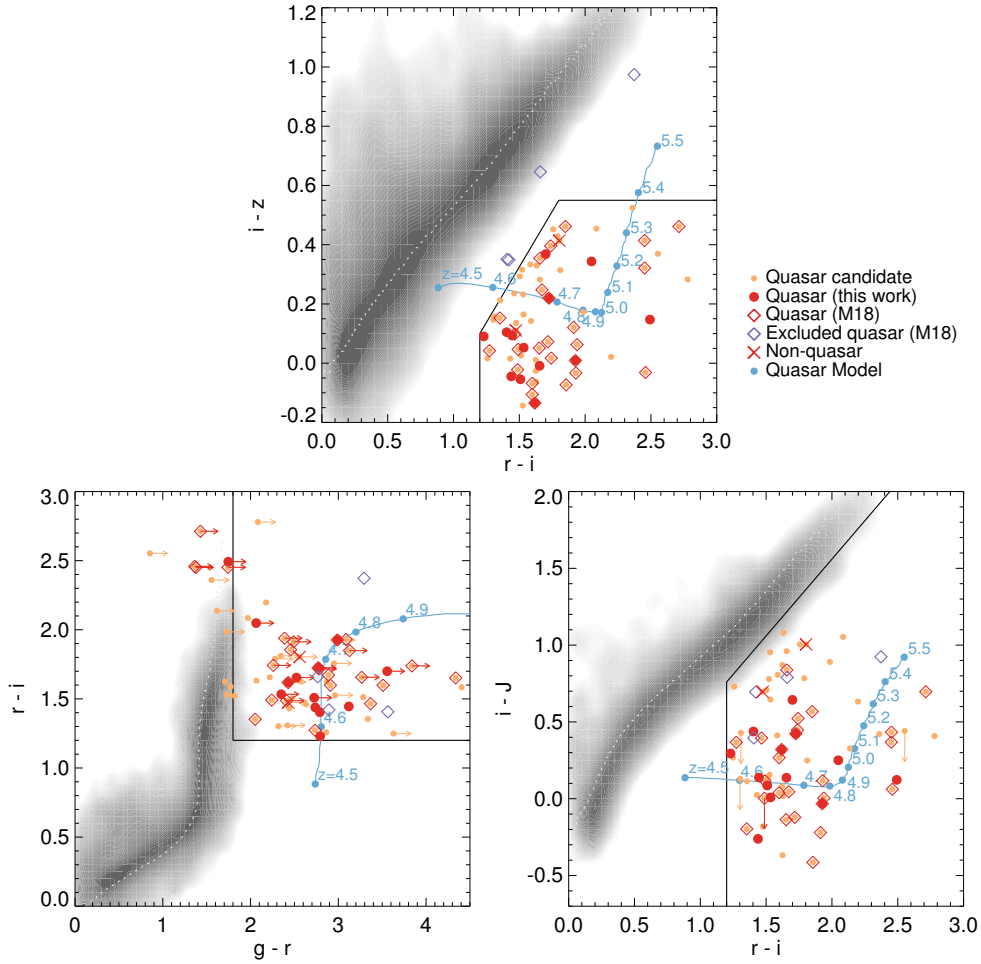

Figure 5.2. Broadband color-color diagrams for quasar selection. The gray contours represent the point sources from one of the tiles of CFHTLS (and IMS), while the dotted lines on the contours indicate the stellar loci of Covey et al. (2007). The black solid lines indicate our selection criteria, and the blue filled circles with lines show the redshift evolution of our quasar SED model described in Section 5.5.3 on the color-color spaces. The other symbols of candidates, quasars, and nonquasars are the same as in Figure 5.1. Note that the arrows indicate the upper/lower limit of colors.

resulting in 70 $z \sim 5$ quasar candidates. The positions of the candidates (orange circles) are plotted on the layouts in Figure 5.1. Figure 5.2 shows the color-color diagrams ($g-r$ vs. $r-i$, $r-i$ vs. $i-z$, and $r-i$ vs. $i-J$) of objects in the multiband catalog and the broadband color selection criteria (the black solid lines). The broadband photometries of our candidates are listed in Table 5.2. In this paper, we only include the candidates that are spectroscopically observed in this work or previous works (e.g., M18) and also observed in medium bands, instead of the full sample of our candidates (see details of the spectroscopic sample in Section 5.4).

Table 5.2. Broadband Photometry of Spectroscopically Observed Quasar Candidates

ID	R.A. (J2000)	Decl. (J2000)	u (mag)	g (mag)	r (mag)	i (mag)	z (mag)	J (mag)
Spectroscopically Identified Quasars								
IMS J021315−043341[a,b]	02:13:15.00	−04:33:40.5	> 26.70	> 26.59	24.01 ± 0.09	22.35 ± 0.02	22.28 ± 0.06	22.41 ± 0.12
IMS J021523−052946	02:15:23.29	−05:29:45.9	> 26.46	> 26.57	22.71 ± 0.02	20.99 ± 0.01	20.53 ± 0.01	20.75 ± 0.02
IMS J021811−064843[a,b]	02:18:10.80	−06:48:42.6	> 26.73	25.70 ± 0.13	22.87 ± 0.02	21.46 ± 0.01	21.20 ± 0.04	21.14 ± 0.04
IMS J022112−034232[a]	02:21:12.32	−03:42:31.8	> 26.80	26.44 ± 0.32	23.41 ± 0.09	21.48 ± 0.01	21.38 ± 0.03	21.72 ± 0.10
IMS J022113−034252	02:21:12.62	−03:42:52.3	> 26.80	24.57 ± 0.06	21.02 ± 0.01	19.41 ± 0.00	19.43 ± 0.01	19.58 ± 0.03
IMS J085024−041850[a,b]	08:50:23.81	−04:18:49.6	> 26.31	26.07 ± 0.13	23.31 ± 0.03	21.90 ± 0.01	21.89 ± 0.04	22.29 ± 0.17
IMS J085028−050607[a,b]	08:50:28.16	−05:06:06.9	> 26.21	> 26.75	24.67 ± 0.14	22.66 ± 0.02	22.34 ± 0.06	22.52 ± 0.28
IMS J085225−051413[a,b]	08:52:24.73	−05:14:13.4	> 26.59	> 26.50	24.15 ± 0.09	22.64 ± 0.02	22.61 ± 0.06	22.75 ± 0.26
IMS J085324−045626[a,b]	08:53:23.68	−04:56:25.6	> 26.53	> 26.48	23.75 ± 0.08	22.27 ± 0.02	22.35 ± 0.06	22.30 ± 0.11
IMS J135747+530543	13:57:47.34	+53:05:42.6	> 26.31	> 26.19	23.09 ± 0.04	21.21 ± 0.01	20.72 ± 0.02	20.83 ± 0.03
IMS J135856+514317	13:58:55.96	+51:43:17.0	> 26.66	26.37 ± 0.19	21.99 ± 0.02	20.40 ± 0.00	20.29 ± 0.01	20.77 ± 0.03
IMS J140147+564145	14:01:46.97	+56:41:44.8	> 26.50	26.63 ± 0.20	23.54 ± 0.05	21.67 ± 0.01	21.60 ± 0.04	21.71 ± 0.07
IMS J140150+514310	14:01:49.96	+51:43:10.4	> 26.72	> 26.73	25.33 ± 0.13	22.93 ± 0.03	22.90 ± 0.07	23.10 ± 0.22
IMS J140440+565651	14:04:40.29	+56:56:50.7	> 26.89	24.62 ± 0.05	22.36 ± 0.01	20.94 ± 0.00	20.86 ± 0.01	20.99 ± 0.03
IMS J141432+573234	14:14:31.56	+57:32:34.4	> 26.85	> 26.67	23.45 ± 0.05	21.81 ± 0.01	21.42 ± 0.03	21.18 ± 0.11
IMS J142635+543623	14:26:34.86	+54:36:22.7	> 26.86	24.41 ± 0.04	21.51 ± 0.01	19.92 ± 0.00	19.89 ± 0.01	19.78 ± 0.02
IMS J142854+564602	14:28:53.85	+56:46:02.0	> 27.13	26.64 ± 0.30	23.75 ± 0.05	22.07 ± 0.01	21.75 ± 0.04	22.26 ± 0.15
IMS J143156+560201	14:31:56.36	+56:02:00.9	> 27.16	24.76 ± 0.06	22.01 ± 0.01	20.74 ± 0.00	20.62 ± 0.02	20.60 ± 0.04
IMS J143705+522801	14:37:05.17	+52:28:00.8	> 26.75	> 26.69	24.20 ± 0.08	22.30 ± 0.02	22.10 ± 0.04	22.75 ± 0.16
IMS J143757+515115	14:37:56.54	+51:51:15.1	> 26.90	> 26.68	24.91 ± 0.07	22.43 ± 0.03	22.07 ± 0.05	22.20 ± 0.12
IMS J143804+573646	14:38:04.05	+57:36:46.4	> 26.56	> 26.49	24.08 ± 0.07	22.60 ± 0.02	22.61 ± 0.04	> 22.86

Table 5.2 (cont'd)

ID	R.A. (J2000)	Decl. (J2000)	u (mag)	g (mag)	r (mag)	i (mag)	z (mag)	J (mag)
IMS J143831+563946	14:38:30.83	+56:39:46.4	> 26.49	25.01 ± 0.09	22.98 ± 0.03	21.56 ± 0.01	21.39 ± 0.04	22.03 ± 0.15
IMS J143945+562627	14:39:44.88	+56:26:26.6	> 26.60	> 26.72	24.48 ± 0.09	22.67 ± 0.03	22.63 ± 0.10	22.42 ± 0.23
IMS J220233+013120[a]	22:02:33.20	+01:31:20.3	> 26.53	> 26.84	24.02 ± 0.07	22.26 ± 0.03	21.95 ± 0.04	22.02 ± 0.08
IMS J220522+025730[a]	22:05:22.15	+02:57:30.0	> 26.47	25.80 ± 0.13	23.32 ± 0.05	21.66 ± 0.01	21.68 ± 0.05	21.43 ± 0.08
IMS J220635+020136[a,b]	22:06:34.81	+02:01:36.3	> 26.06	> 26.31	24.58 ± 0.04	22.08 ± 0.02	21.81 ± 0.05	22.08 ± 0.10
IMS J221004+025424[a,b]	22:10:03.90	+02:54:24.4	> 26.65	26.37 ± 0.15	23.56 ± 0.06	22.36 ± 0.01	22.30 ± 0.05	22.19 ± 0.08
IMS J221037+024314[a,b]	22:10:36.99	+02:43:13.7	> 26.60	> 26.71	23.13 ± 0.04	21.46 ± 0.00	21.12 ± 0.02	20.95 ± 0.03
IMS J221118+031207[a,b]	22:11:18.37	+03:12:07.4	> 26.71	25.91 ± 0.09	22.77 ± 0.02	21.36 ± 0.00	21.29 ± 0.02	21.35 ± 0.04
IMS J221251−004231	22:12:51.49	−00:42:30.7	> 26.78	24.33 ± 0.04	21.77 ± 0.01	19.91 ± 0.00	19.89 ± 0.00	20.48 ± 0.04
IMS J221310−002428	22:13:09.67	−00:24:28.1	> 26.88	> 27.08	24.59 ± 0.15	22.65 ± 0.02	22.49 ± 0.05	22.80 ± 0.21
IMS J221520−000908	22:15:20.22	−00:09:08.4	> 26.54	> 26.52	25.05 ± 0.09	22.19 ± 0.03	21.77 ± 0.05	21.67 ± 0.07
IMS J221622+013815	22:16:21.85	+01:38:14.7	> 26.42	> 26.73	25.32 ± 0.11	22.85 ± 0.03	22.35 ± 0.05	22.63 ± 0.12
IMS J221644+001348	22:16:44.02	+00:13:48.2	> 26.40	25.48 ± 0.16	22.07 ± 0.01	20.54 ± 0.00	20.34 ± 0.01	20.26 ± 0.04
IMS J222216−000406	22:22:16.02	−00:04:05.7	> 26.28	> 26.60	23.78 ± 0.06	22.02 ± 0.01	21.83 ± 0.04	22.26 ± 0.11
Spectroscopically Identified Nonquasars								
IMS J022525−044642	02:25:25.18	−04:46:41.5	> 26.85	> 26.70	24.27 ± 0.12	22.85 ± 0.04	22.64 ± 0.10	22.37 ± 0.17
IMS J090540−011038	09:05:40.10	−01:10:38.4	> 26.80	> 26.58	24.02 ± 0.07	22.20 ± 0.02	21.68 ± 0.04	21.34 ± 0.10

Note. — All magnitudes are given in the AB system, and their errors are scaled with σ_N, the noise properties of an effective aperture size N (see also Section 5.2.1). Note that all the magnitudes are not corrected with $C_k^{\rm offset}$ (also see Section 5.2.1).

[a]These quasars are spectroscopically observed in this work.

[b]These quasars are newly discovered in this work, while others are discovered by previous studies (McGreer et al. 2013; M18; Ikeda et al. 2017).

5.3 Medium-Band Selection

5.3.1 Medium-band Observation

To further exclude interlopers and better determine redshifts photometrically, we observed our candidates in medium bands with SQUEAN from 2015 December to 2018 April. Since the Lyman-α (Lyα; 1216 Å) break of a $z \sim 5$ quasar is expected to be located at $\lambda_{\rm obs} \sim 7300$ Å, the medium-band observations were performed mainly with the $m725$ and $m775$ filters. If the two medium-band data were not enough to identify the object as a $z > 5.1$ quasar (i.e. $m725 - m775 < 1$; see Section 5.3.2), additional imaging data in the $m675$ band were also obtained. For the spectroscopically identified quasars, if needed, observations in the $m675$ and/or $m825$ bands were also carried out to check the accuracy of the $z_{\rm phot}$ from medium-band data. For each band, we took 3-70 frames with exposure times of 1-3 minutes, which gives the total integration time of 0.05-1.75 hr per band per filter. Note that brighter candidates ($i < 22$ mag) were observed as high-priority targets, when the observing condition was unstable with a seeing size of $> 1\farcs2$. Among the 70 quasar candidates, 58 candidates were observed in the $m725$ and $m775$ bands and 45 of them were further observed in the $m675$ band.

We reduced the medium-band data, following the procedure in Jeon et al. (2016). After subtracting the bias and dark frames, we divided the science frames by the normalized flat frames, which were produced from the twilight sky. Excluding the images taken under bad weather conditions (e.g. low signals due to heavy clouds), the science images after the reduction were combined. We first detected the sources in the combined images with a detection threshold of $\sim 2.7\sigma$ (DETECT_THRESH of 1.2 and DETECT_MINAREA of 5). The zp of each medium-band image was determined by fitting the stellar templates to the broadband photometry (riz) of stars in each field (see details in Jeon et al. 2016). Note that we regarded auto-magnitudes of the stars in each medium band as total magnitudes for the zp determination. The uncertainty in the zp determination is found to be ~ 0.03 mag, by taking the standard deviation of the zp values from the stars in the same field. For each quasar candidate, we estimated the

aperture magnitude (size of $2 \times \mathrm{FWHM_{mb}}$ is used, where $\mathrm{FWHM_{mb}}$ is FWHM of point sources in each medium-band image) with forced photometry on the target position determined in the i-band image. We applied the aperture correction factor determined from the stars in each field. Like the broadband photometry, the Galactic extinction was corrected by following the Cardelli et al. (1989) law assuming $R_V = 3.1$ with the extinction map of Schlafly & Finkbeiner (2011), and we also scaled the SExtractor-derived magnitude errors to account for the correlated noise in the stacked image (σ_N). We gave the upper limit, which is defined as the magnitude limit for the 2.7σ detection, to the objects with no detection or magnitudes less than the upper limit. The observing runs and the medium-band photometry are given in Table 5.3. As with Table 5.2, only the spectroscopically examined candidates are listed.

5.3.2 Medium-band Selection of $z \sim 5$ Quasar Candidates

Figure 5.3 shows the color-color diagrams for the medium bands only ($m675 - m725$ vs. $m725 - m775$) and for the combinations of broad- and medium-band colors ($r - i$ vs. $m675 - m725$ and $r - i$ vs. $m725 - m775$, respectively). The gray filled circles represent the colors of the 175 star templates covering various spectral types and luminosity classes (Gunn & Stryker 1983) and the 41 L/T dwarf star models (Burrows et al. 2006). The other symbols are identical to those in Figure 5.2. We followed the color selection criteria with medium bands suggested by Jeon et al. (2016):

1. $m675 - m725 > 1$ and $m675 - m725 > m725 - m775 + 1.5$ $(4.7 < z < 5.1)$,

2. $m725 - m775 > 1$ $(5.1 < z < 5.5)$,

which are plotted as dotted lines in Figure 5.3. The $m675 - m725$ versus $m725 - m775$ diagram in Figure 5.3 shows the above criteria at a glance. Among 45 candidates observed in the $m675$, $m725$, and $m775$ bands, 33 candidates satisfy the above color selection criteria. The medium-band color criteria ($m675 - m725 > 1$ and $m725 - m775 > 1$) could be roughly adopted to the combination of broad- and medium-band

colors (dashed lines). Note that the former criterion is limited by $r - i$ color: $m675 - m725 > 0.5\ (r - i) - 0.25$.

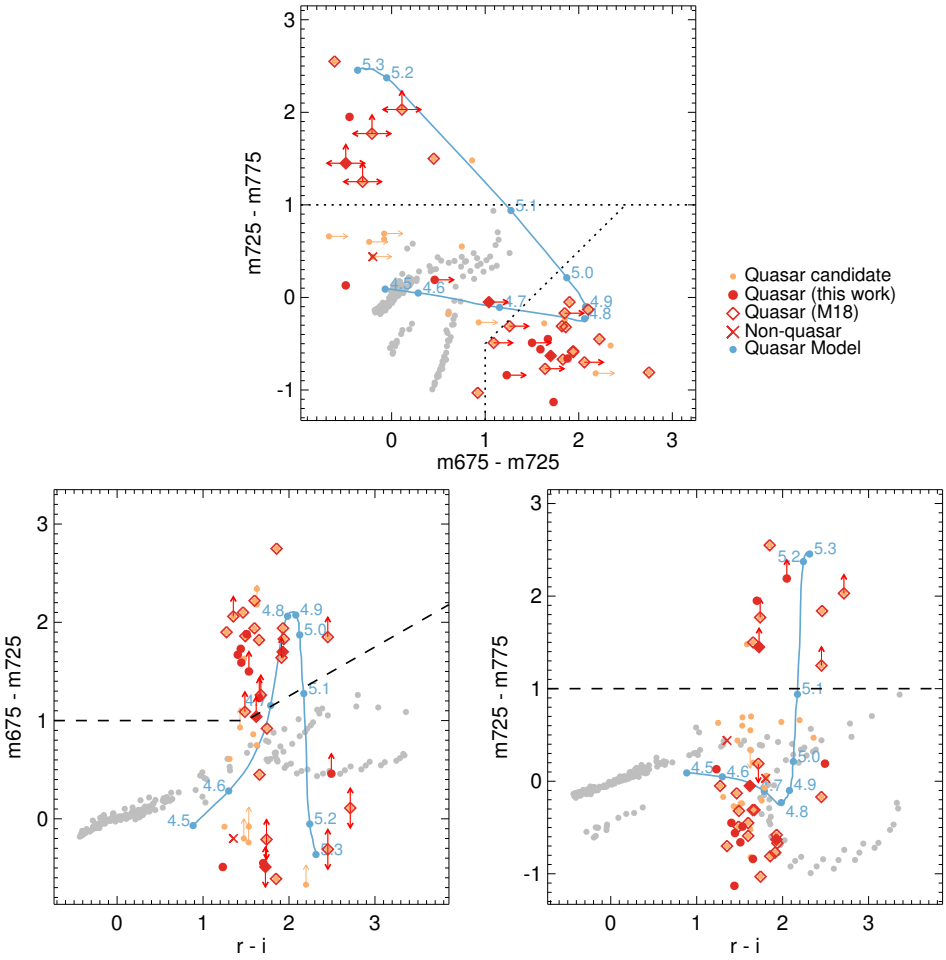

Figure 5.3. Medium-band color-color diagrams for quasar selection. The symbols of candidates, quasars, nonquasars, and the quasar model are the same as in Figure 5.2. The gray filled circles represent the colors of typical stars from stellar templates of main sequence (Gunn & Stryker 1983) and dwarf (Burrows et al. 2006). The dotted lines are the medium-band selection criteria provided by Jeon et al. (2016), while the dashed lines are the additional criteria presented in this work.

Table 5.3. Medium-band Photometry of Spectroscopically Observed Quasar Candidates

ID	Observing Runs, exposure times (s), and magnitudes (mag)											
	$m675$			$m725$			$m775$			$m825$		
Spectroscopically Identified Quasars												
IMS J021315−043341	Oct 17	3600	> 23.82	Oct 15	1800	22.59 ± 0.17	Oct 15	4140	23.43 ± 0.80	Oct 17	2700	22.86 ± 0.26
IMS J021523−052946	Dec 17	1800	> 22.33	Dec 17	1800	> 22.54	Dec 17	1260	20.77 ± 0.23	-	-	-
IMS J021811−064843	Oct 17	1800	22.92 ± 0.17	Feb 16	900	21.25 ± 0.13	Feb 16	900	21.70 ± 0.27	Oct 17	1800	21.57 ± 0.07
IMS J022112−034232	Sep 17	1800	22.97 ± 0.54	Feb 16	900	21.27 ± 0.08	Feb 16	900	21.90 ± 0.28	Sep 17	1800	21.79 ± 0.22
IMS J022113−034252	Dec 17	600	21.27 ± 0.17	Dec 17	300	19.33 ± 0.04	Dec 17	300	19.92 ± 0.06	-	-	-
IMS J085024−041850	Dec 17	2700	23.67 ± 0.73	Dec 17	1800	21.94 ± 0.11	Dec 17	1800	23.07 ± 0.34	-	-	-
IMS J085028−050607	-	-	-	Apr 17	3600	> 23.97	Apr 17	3600	21.78 ± 0.10	Apr 18	3600	22.63 ± 0.16
IMS J085225−051413	Apr 18	3600	> 24.03	Apr 17	3600	22.53 ± 0.10	Apr 17	3600	23.02 ± 0.26	-	-	-
IMS J085324−045626	Dec 17	3240	24.25 ± 0.60	Feb 16	1800	22.37 ± 0.15	Feb 16	1800	23.03 ± 0.40	-	-	-
IMS J135747+530543	Jan 18	2700	22.47 ± 0.34	Apr 17	3600	23.08 ± 0.20	Apr 17	3600	20.53 ± 0.08	Dec 17	900	21.22 ± 0.12
IMS J135856+514317	Feb 17	900	22.37 ± 0.12	Feb 16	900	20.55 ± 0.05	Feb 16	900	20.86 ± 0.09	-	-	-
IMS J140147+564145	Feb 17	1800	22.82 ± 0.19	Feb 16	900	20.88 ± 0.04	Feb 16	960	21.46 ± 0.08	-	-	-
IMS J140150+514310	-	-	-	Apr 17	3600	24.12 ± 0.35	Apr 17	3600	22.28 ± 0.15	Apr 18	3600	23.19 ± 0.22
IMS J140440+565651	Dec 17	3540	23.24 ± 0.40	Apr 17	900	21.38 ± 0.06	Apr 17	1440	21.70 ± 0.09	Apr 16	900	21.61 ± 0.09
IMS J141432+573234	Feb 17	3600	23.20 ± 0.18	Feb 16	900	22.75 ± 0.23	Feb 16	900	21.25 ± 0.10	Dec 17	1620	22.12 ± 0.20
IMS J142635+543623	Dec 17	300	21.86 ± 0.19	Dec 17	180	19.64 ± 0.04	Dec 17	180	20.09 ± 0.06	Dec 17	180	20.06 ± 0.07
IMS J142854+564602	Dec 17	2700	> 23.89	Apr 17	4140	22.63 ± 0.15	Apr 17	1800	22.94 ± 0.36	-	-	-
IMS J143156+560201	Feb 17	900	22.99 ± 0.30	Apr 17	1800	21.09 ± 0.11	Apr 17	2340	21.14 ± 0.20	Apr 16	900	21.04 ± 0.06
IMS J143705+522801	Dec 17	2700	> 23.78	Dec 17	900	22.14 ± 0.12	Dec 17	1800	22.91 ± 0.28	-	-	-
IMS J143757+515115	Feb 18	2700	> 23.57	Apr 17	3600	> 23.88	Apr 17	1800	22.63 ± 0.34	Feb 18	1980	22.97 ± 0.42
IMS J143804+573646	Dec 17	2700	> 23.70	Apr 17	4140	22.61 ± 0.17	Apr 17	5400	23.10 ± 0.61	Apr 18	2040	22.86 ± 0.33

Table 5.3 (cont'd)

ID	Observing Runs, exposure times (s), and magnitudes (mag)											
	$m675$			$m725$			$m775$			$m825$		
IMS J143831+563946	Feb 17	6300	> 23.39	Jun 16	900	21.33 ± 0.14	Jun 16	900	22.03 ± 0.22	Apr 18	1260	22.04 ± 0.22
IMS J143945+562627	Dec 17	2700	23.51 ± 0.30	Apr 17	4500	22.59 ± 0.15	Apr 17	1800	23.62 ± 0.97	-	-	-
IMS J220233+013120	Dec 16	3060	> 23.18	Oct 15	2160	> 23.67	Oct 15	2160	22.22 ± 0.11	Dec 16	1800	> 22.17
IMS J220522+025730	Jul 16	900	> 22.73	Oct 15	1260	21.69 ± 0.07	Oct 15	1260	21.74 ± 0.09	Dec 16	900	22.32 ± 0.31
IMS J220635+020136	Dec 16	1620	> 22.53	Jun 16	1980	22.07 ± 0.17	Jun 16	1800	21.88 ± 0.18	Oct 17	1800	22.04 ± 0.11
IMS J221004+025424	Dec 16	4200	22.36 ± 0.27	Oct 15	1800	22.85 ± 0.20	Oct 15	1800	22.72 ± 0.19	Dec 16	1800	23.33 ± 0.56
IMS J221037+024314	Dec 16	1860	22.67 ± 0.49	Oct 15	2520	23.12 ± 0.41	Oct 15	1620	21.17 ± 0.08	Oct 17	2520	21.36 ± 0.06
IMS J221118+031207	Jul 16	900	23.10 ± 0.38	Oct 15	1800	21.51 ± 0.11	Oct 15	1800	22.07 ± 0.20	Dec 16	1440	21.77 ± 0.18
IMS J221251−004231	Dec 17	600	22.48 ± 0.37	Dec 17	300	19.73 ± 0.06	Dec 17	600	20.54 ± 0.12	-	-	-
IMS J221310−002428	Oct 17	5400	24.07 ± 0.37	Jun 16	3600	22.24 ± 0.14	Jun 16	3600	22.91 ± 0.35	Oct 17	4320	22.94 ± 0.22
IMS J221520−000908	Oct 17	5040	> 23.51	Oct 15	1800	> 23.40	Oct 15	1800	21.37 ± 0.10	Oct 17	2700	21.94 ± 0.14
IMS J221622+013815	Oct 17	5400	> 24.57	Oct 15	3780	22.72 ± 0.13	Oct 15	3600	22.89 ± 0.22	Oct 17	3600	22.89 ± 0.18
IMS J221644+001348	Dec 17	1560	22.37 ± 0.37	Dec 17	540	20.27 ± 0.07	Dec 17	600	20.40 ± 0.12	-	-	-
IMS J222216−000406	-	-	-	Dec 17	1080	21.65 ± 0.23	Jan 18	900	> 21.46	-	-	-
Spectroscopically Identified Nonquasars												
IMS J022525−044642	Oct 17	3600	> 23.46	Oct 15	3600	23.66 ± 0.31	Oct 15	3420	23.22 ± 0.30	-	-	-
IMS J090540−011038	-	-	-	Apr 17	3600	21.93 ± 0.20	Apr 17	3600	21.90 ± 0.33	-	-	-

Note. — All magnitudes are given in the AB system, and their errors are scaled with σ_N.

5.4 Spectroscopy Data

We performed spectroscopic observations of 15 candidates from the broadband selection method, among which 10 satisfy the medium-band selection. The medium-band-selected candidates were spectroscopically observed prior to other candidates. Here "other candidates" mean the objects that are outside the medium-band selection boxes but could be included considering their large magnitude uncertainties (or upper limits of flux at short wavelength). These observations are reported below in Table 5.4 and Figure 5.4. Additionally, we took spectra of seven candidates from the broadband photometry, *before* we improved the photometry as described in Section 5.2.1. After improving the photometry as described in Section 5.2.1, they turned out not to satisfy the broadband quasar selection criteria, and they are all found to be nonquasars from spectroscopy. For completeness, we present these nonquasar spectra in 5.4.4, but we will exclude them in our analysis in Section 5.5 and 5.6. Additionally, we used published redshifts for some of the medium-band observed objects, as described in Section 5.4.3.

5.4.1 Gemini/GMOS Observation

Spectroscopic observations of 13 candidates were carried out with Gemini Multi-Object Spectrographs (GMOS; Hook et al. 2004) on Gemini-North and Gemini-South 8 m Telescopes at Maunakea, Hawaii, and Cerro Pachon, Chile, respectively, on 2016 September 3-8 (PID: GS-2016B-Q-46), 2018 March 20 and June 18 (PID: GS-2018A-Q-220), and 2018 May 18 (PID: GN-2018A-Q-315). The sky was almost clear, with average seeings of $\sim 1\farcs0$. To ease the sky subtraction for the faint targets, the Nod & Shuffle (N&S) observing mode was adopted with a $1\farcs0$ width N&S slit. The spectra were obtained by using the R150+_G5326 grating, which has a resolution of $R \sim 315$ at 717 nm for a slit width of $1\farcs0$, and the GG455_G0329 or OG515_G0330 filters to avoid the zeroth-order order overlap. This setup gives the wavelength range of 4550 or 5150–10300 Å. In order to cover the gaps between the chips on the Hamamatsu CCD, the central wavelengths were set to 7100 and 7250 Å. This setting allows the detection of the redshifted Lyα break, which is expected to be located at ~ 7200 Å for $z \sim 5$ quasars. For the observing

Table 5.4. Spectroscopic Observations of $z \sim 5$ Quasar Candidates

ID	Telescope/Instrument	Date	Exposure Time (s)	Seeing (arcsec)
		Spectroscopically Identified Quasars		
IMS J021315−043341	Magellan/IMACS	2016 Dec 4-5	4500	0.5-0.8
IMS J021811−064843	Gemini/GMOS-S	2016 Sep 6	480	1.0-1.1
IMS J022112−034232	Gemini/GMOS-S	2016 Sep 3	960	1.2-1.3
IMS J085024−041840	Gemini/GMOS-N	2018 May 18	1440	0.7
IMS J085028−050607	Gemini/GMOS-S	2018 Mar 20	3000	1.1
IMS J085225−051413	Gemini/GMOS-S	2018 Mar 20	3000	1.1
IMS J085324−045626	Magellan/IMACS	2016 Dec 6	3600	0.6-0.9
IMS J220233+013120	Gemini/GMOS-S	2016 Sep 4-6	2880	1.1-1.3
IMS J220522+025730	Gemini/GMOS-S	2016 Sep 6	1440	1.1
IMS J220635+020136	Gemini/GMOS-S	2018 Jun 18	1440	0.8
IMS J221004+025424	Gemini/GMOS-S	2016 Sep 8	2880	0.5
IMS J221037+024314	Gemini/GMOS-S[a]	2016 Sep 8	9600	0.8
IMS J221118+031207	Gemini/GMOS-S	2016 Sep 4	960	1.2-1.3
		Spectroscopically Identified Nonquasars		
IMS J022525−044642	Gemini/GMOS-S	2016 Sep 4-8	5760	1.0
IMS J090540−011038	Gemini/GMOS-N	2018 May 18	1440	0.7

[a]MOS observation with our candidate for a faint quasar at $z \sim 6$ (see details in Section 5.4.1)

run in the 2018A semester, we set the central wavelengths to 4300 and 4600 Å for the Gemini-South, in order to avoid the bad columns on the CCD, and 6350 and 6650 Å for the Gemini-North. Note that we adopted a 4×4 binning in spatial/spectral pixels to maximize the S/N.

For one target, IMS J221046+024313, we obtained its spectrum through the MOS observing mode of GMOS-S (PID: GS-2016B-Q-11), during which we observed other targets of interest for another program. For the MOS observation with the N&S mode, we used the same R150+_G5326 grating with the RG610_G0331 filter, and the central wavelengths were set to 8900 and 9000 Å. To increase the S/N, the spectrum was also binned with 4×4.

For data reduction, the spectra were processed by using the Gemini IRAF package. After the bias subtraction and flat-fielding, sky lines were subtracted with the shuffled spectra. The wavelength calibration was done with CuAr arc lines, and the flux calibration was done with standard stars (LTT 7379, CD 329927, and Wolf 1346). For IMS J221036+024313 with the MOS observation, the wavelength calibration preceded the sky subtraction owing to the alignments of sky lines in the spatial direction. The aperture size for the spectral extraction was set at $1\farcs0$ in diameter for all cases. Note that the overall flux scale of each spectrum was adjusted using the i-magnitude of each target. In order to increase the S/N, we binned the spectra along the spectral direction by a factor of 2-5 (pixels) by using the inverse-variance weighting method (e.g., Kim et al. 2018). This binning gives the spectral resolution of ~ 300.

5.4.2 Magellan/IMACS Observation

The optical spectra of the other two candidates were obtained by the Inamori-Magellan Areal Camera and Spectrograph (IMACS; Dressler et al. 2011) on the Magellan Baade 6.5 m Telescope in Las Campanas Observatory, Chile, on 2016 December 3-5. Unlike the Gemini observations, the Magellan spectra were obtained with a standard long-slit mode (not N&S). We used the $f/4$ camera of IMACS with a grating of 150 lines/mm, giving a spectral resolution of ~ 600 at 7200 Å for a $0\farcs9$ slit, and used the OG570 filter

to avoid the overlap. This setup gives a wavelength coverage of 5700–9740 Å. Note that we used chips 5 and 8 of the $f/4$ camera, which have the highest sensitivities among the IMACS CCD chips. To maximize the S/N, each spectrum was binned by 2×2 during the observation.

For data reduction, we followed general reduction processes: bias subtraction and flat-fielding. After the wavelength calibration with HeNeAr lines, we generated 2D maps of sky lines, by performing a polynomial fitting for pixel values along the spatial direction. We combined the processed 2D spectra from different chips with the astronomical software SWarp (Bertin 2010). Note that there are CCD gaps along the spectral direction, which are located at $\lambda_{\rm obs}$ = 6530-6630 Å and $>$ 9700 Å. Identical to the Gemini spectra, the fluxes within a $1\farcs0$ diameter aperture were extracted and flux-calibrated using both the spectra of A0V standard stars (HD 18225, HD 85589) and the i-magnitude of each target. The binning was also performed for these spectra in a similar way to that for the Gemini spectra, but the binned spectra have a spectral resolution of ~ 600.

5.4.3 Supplemental Spectroscopic Redshift Sample

For some of the medium-band observed objects, we adopted their spectral parameters such as $z_{\rm spec}$ and M_{1450} from the literature. They mainly come from the catalog of $z \sim 5$ quasar candidates by M18, which also used the optical data from CFHTLS to select quasar candidates. Of the 38 quasars they identified with spectroscopy, we used spectral parameters of 18 quasars; they are located in our survey area (IMS) and satisfy our broadband color criteria with the magnitude limit ($i \lesssim 23$ mag). Two quasars among them, IMS J221520−000908 and IMS J222216−000406, are also identified by Ikeda et al. (2017), but we took their spectral parameters from M18. Note that we revise the $z_{\rm spec}$ of IMS J140150+514310 from 4.20 in M18 to 5.17 since the Lyα and Lyβ lines are located at 7500 and 6320 Å, respectively, along with other possible emission lines at the same redshift (see Figure 9 of M18). The M_{1450} value of the quasar is also revised with the $z_{\rm spec}$. Additionally, we used the spectral parameters of four quasars, which

are not included in the final catalog of M18 but spectroscopically identified by them. Consequently, we used the $z_{\rm spec}$ and M_{1450} values of 22 quasars from M18, which are listed in Table 5.6. Note that there are no M_{1450} values for the four quasars excluded in the final catalog of M18. Including our spectroscopically identified quasars, the total number of spectroscopically identified quasars we used for our study is 35.

5.4.4 Spectra of Nonquasar Objects

As we described above, spectroscopic data were obtained for some of the broadband-selected quasar candidates before we improved our photometry. Later, these were excluded from quasar candidates based on the improved broadband photometry. Not surprisingly, these objects were spectroscopically identified as nonquasars. This section provides spectra of these nonquasar objects. The spectroscopic observations of these objects were carried out with GMOS on the Gemini-North/South 8 m Telescopes (PID:GS-2016B-Q-46, GS-2017A-Q-19, and GN-2018A-Q-315) and IMACS on the Magellan Baade 6.5 m Telescope. The information of the observing runs and their i-band magnitudes are listed in Table 5.5, and Figure 5.5 shows their optical spectra. These candidates are identified as nonquasar objects without any break or line feature at $\gtrsim$ 7000Å as we saw for our newly discovered quasars. The spectra obtained with IMACS show increased fluxes at $\sim$ 6600 Å since it is close to the CCD gap. However, there is a significant continuum emission at $\lambda_{\rm obs} < 6500$ Å with no emission-line features in both the 1D and the 2D spectra. Therefore, these objects are regarded as nonquasar objects.

Table 5.5. Spectroscopic Observations of Nonquasar objects

ID	Telescope/Instrument	Date	Exposure Time (s)	i (mag)
IMS J022356−053408	Gemini/GMOS-S	2016 Sep 3-4	5760	22.79
IMS J022404−061947	Magellan/IMACS	2016 Dec 5	3600	22.41
IMS J022405−055946	Magellan/IMACS	2016 Dec 6	1800	22.09
IMS J022409−054147	Magellan/IMACS	2016 Dec 6	1800	22.05
IMS J022409−061951	Gemini/GMOS-S	2016 Sep 3	960	21.56
IMS J084904−022740	Gemini/GMOS-S	2017 Feb 22	4800	22.71
IMS J085414−023613	Gemini/GMOS-S	2017 Feb 22	4800	22.76
IMS J090126−024544	Magellan/IMACS	2016 Dec 6	2100	21.91
IMS J220831+032710	Gemini/GMOS-S	2018 Jun 22	3000	22.84

Note. — These objects were selected before the improved photometry described in Section 5.2.1.

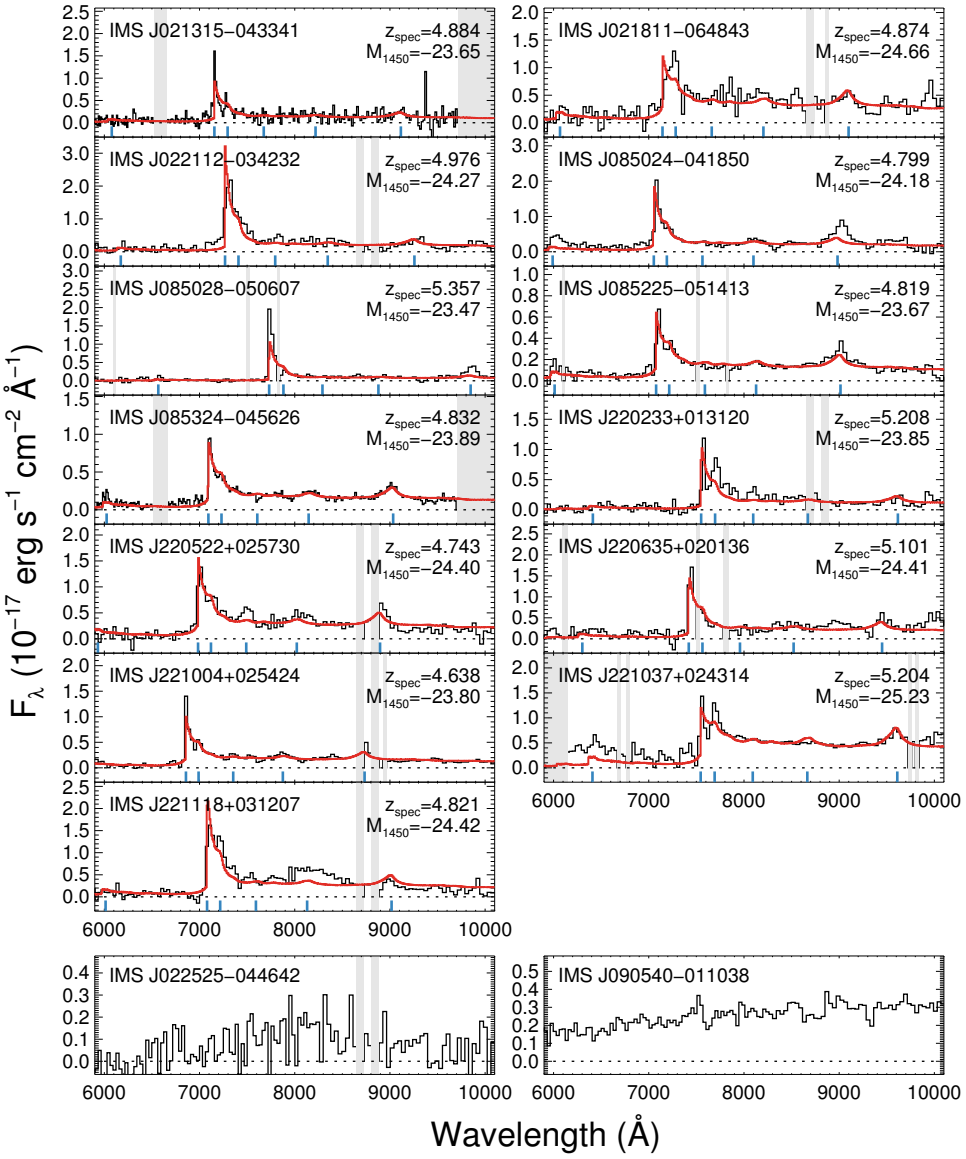

Figure 5.4. Optical spectra of the identified candidates; the first 13 spectra show the $z \sim 5$ quasars, while the last 2 are identified as nonquasar objects, despite of being broadband-selected. The binned spectra are shown as the black solid lines, while the red solid lines are the best-fit models for each quasar. The blue marks indicate the wavelengths of possible emission lines of each quasar (Lyβ, Lyα, N V, O I, Si IV, and C IV, from short to long wavelengths). The dotted lines indicate $F_\lambda = 0$ and the shaded regions represent the bad columns (e.g., hot pixels or gap) on CCD or the wavelength range not covered by the observational configuration.

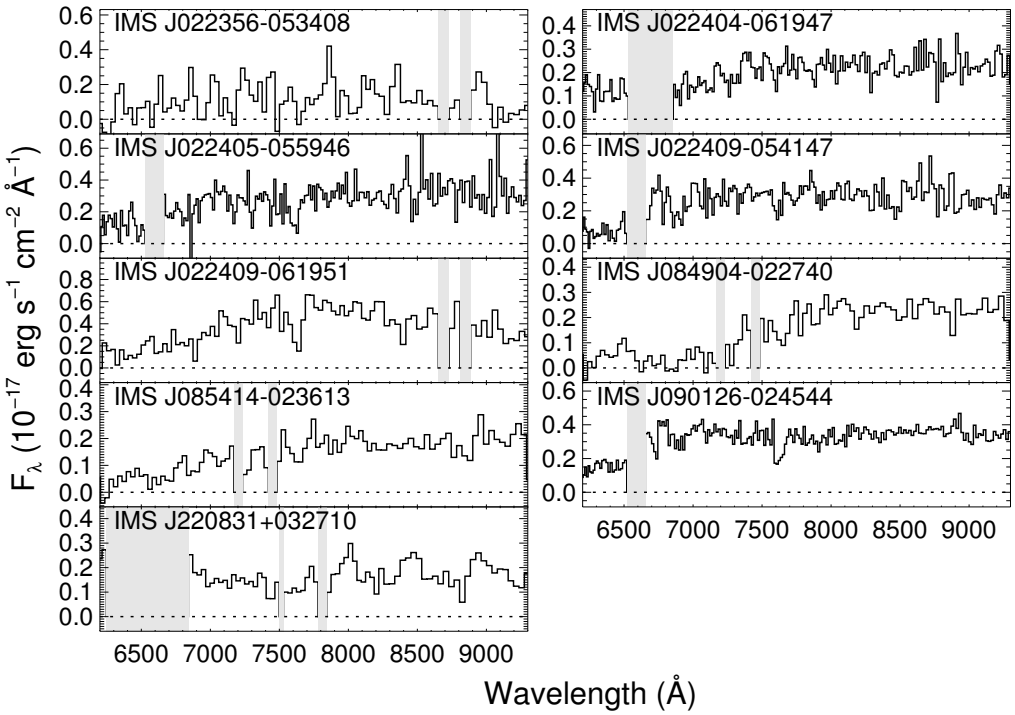

Figure 5.5. Optical spectra of nonquasar objects, which are excluded after the improved photometry described in Section 5.2.1. The binned spectra are shown as black solid lines. The dotted lines indicate $F_\lambda = 0$ and the shaded regions represent the bad column area on the CCD.

5.5 Results

5.5.1 Spectroscopic Identification of Quasars

We present the optical spectra of the 15 broadband-selected quasar candidates in Figure 5.4. Thirteen of them have clear Lyα breaks at 7000-7500 Å in their spectra, showing that they are high-redshift quasars. Most of the quasars also have strong Lyα emission line (S/N $\geq$ 5), while IMS J021811−064843 does not. In addition, some spectra show broad emission lines such as C IV (e.g., IMS J085024−041850, IMS J085324−045626, IMS J221037+024314). The quasar spectra we obtained show no significantly unusual feature, except for IMS J221118+031207, which has a seemingly broadened Fe complex at $\sim$ 8000 Å. Out of the 15 candidates we observed, 10 quasars (marked with b in Table 5.2) are newly discovered ones, and three were independently identified by M18. On the other hand, the other 2 candidates selected by broadband color criteria are identified as nonquasar objects (Figure 5.4), considering that they have no significant break or emission-line feature.

5.5.2 Medium-band Color Selection and Its Efficiency

In this section, we examine the effectiveness of using medium-band data obtained by SQUEAN for finding $z \sim 5$ quasars. Figure 5.6 summarizes the numbers of our candidates along the i-band magnitude at various selection or observation stages. There are 70 broadband-selected candidates (gray histogram), 45 of them were observed in three medium bands ($m675$, $m725$, and $m775$; green histogram), and 33 of the 45 candidates satisfy the color criteria (orange histogram) given by Jeon et al. (2016). Among the 33 medium-band-selected candidates, 28 of them have spectroscopic data, and all of them are identified as high-redshift quasars (red histogram). We suggest that the other 5 medium-band-selected candidates are also high-redshift quasars that they are bright ($i < 22$ mag) and have high-S/N medium-band data, and yet their SED shape is very much in agreement with the other confirmed quasars. On the other hand, 27% (12 out of 45) of the broadband-selected candidates were removed by the

medium-band color criteria. Out of the 12 excluded candidates, 4 turned out to be quasars. IMS J143945+562627 and IMS J221004+025424 are excluded owing to their redshift ($z \leq 4.7$), so their exclusion is under special circumstances. The other two, IMS J220522+025730 and IMS J220635+020136, are not selected since they have shallow depth images in the $m675$ band, which gives only a lower limit on the $m675 - m725$ color. Excluding these two quasars, we estimate that the contaminants occupy 23% (10 out of 43) of the broadband-selected sample. Note that we assumed that the 10 candidates are all nonquasars or quasars that are out of the explored redshift range. Figure 5.6 shows the histogram of our candidates for $z \sim 5$ quasars along the i-band magnitude. The medium-band selection becomes more important if we concentrate on faint objects. At $22 < i < 23$, in comparison to $i < 23$, the contamination rate increases to 47% (9 out of 19, except IMS J220635+020136), for the broadband-selected candidates that are rejected after the medium-band observation. This is due to the increase of faint red stars that can act as interlopers, and without the medium-band approach, the exclusion of such objects becomes more challenging as we go to fainter magnitudes. Consequently, this medium-band-approach is an effective way to narrow down the number of plausible candidates for $z \sim 5$ quasars.

However, our method is limited by the broadband selection and photometry. As one can see in Figure 5.2, there are four quasars at $z \sim 5$ reported by M18 that were excluded from our broadband-selected candidates (purple open diamonds). Except for a quasar with a red $i - z$ color of 1.0, not included in the final catalog of M18, the other three quasars were not selected by our selection criteria because there are small differences in broadband magnitudes (~ 0.1 mag) between M18 and this work. In other words, we may have missed 10% (4 out of 39) of quasars (or candidates) during our broadband selection. We checked whether the photometric accuracy is the main reason for missing 10% of quasars during the broadband selection by using our SED model described in 5.5.3. We randomly generated 10^5 mock quasars at $4.7 \leq z \leq 5.4$ based on the SED model, controlled by the QLF of M18 with the parameter ranges determined by previous studies (see details in Section 5.5.3), including photometric uncertainties of

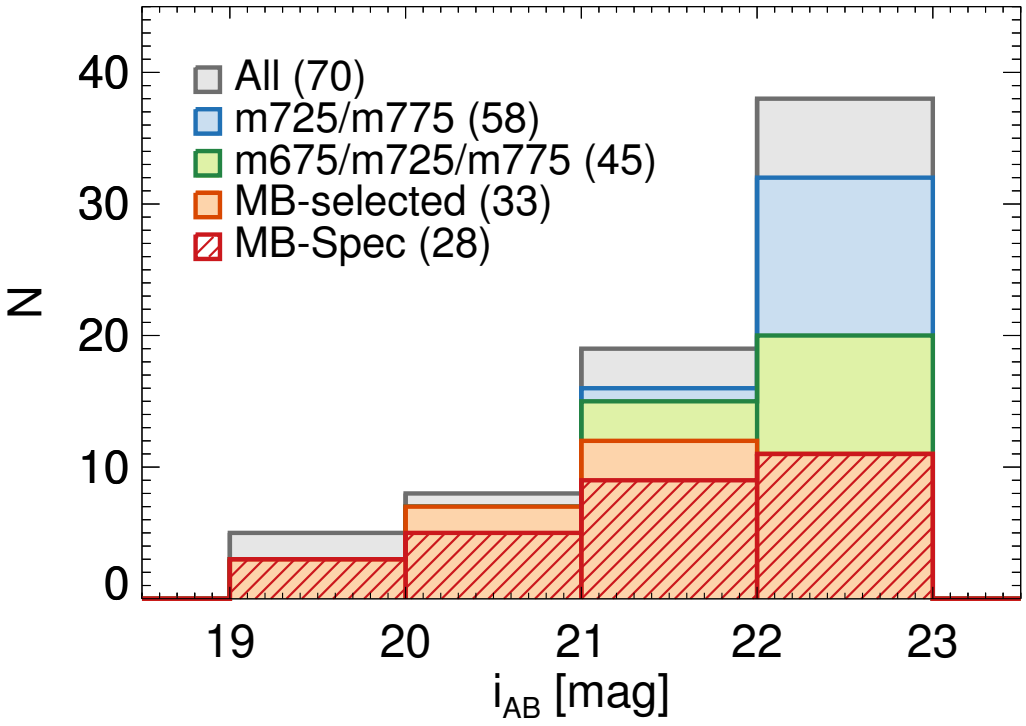

Figure 5.6. Histogram of our $z \sim 5$ quasar candidates along the i-band magnitude. While the 70 candidates for $z \sim 5$ quasar are shown as the gray histogram, the total 58 candidates with $m725$- and $m775$-band observations shown as the blue histogram, and 45 of them also have $m675$-band photometry (green histogram). Among the medium-band observed candidates, 33 candidates satisfy the medium-band color criteria given by Jeon et al. (2016; orange histogram), and 28 of them were spectroscopically identified as high redshift quasars by this work and previous works (M18; Ikeda et al. 2017). Note that the 28 candidates are given in the red hatched histogram for easy distinction from the orange histogram. There are seven quasars with spectroscopy, excluded from the red histogram owing to the lack of medium-band observations or the fact that their medium-band colors do not satisfy the color criteria.

0.1 mag. A total of 11.4% of the mock quasars are rejected by our criteria, corresponding to the fraction of the missed quasars. Thus, to have a highly complete sample, a rather generous broadband selection or a selection from a sample with higher photometry accuracy is desirable before applying the medium-band selection.

5.5.3 SED fitting and Redshift Measurements

The estimation of $z_{\rm spec}$ requires spectra with good S/N, which is usually expensive in observing time. As a good alternative, $z_{\rm phot}$ does not require observing time as extensive as spectroscopy, and it is still useful for deriving properties of high-redshift quasars. While $z_{\rm phot}$ of quasars can be determined by red colors from a sharp break at wavelength shorter than Lyα, their accuracy depends critically on how exactly one can sample the break in multiband photometry. In that regard, medium-band photometry can be useful since its dense wavelength sampling can improve the wavelength estimation of the break. We describe here our high-redshift quasar SED model for the better estimation of $z_{\rm phot}$ and $z_{\rm spec}$ of high-redshift quasars.

We generated an artificial quasar SED model based on the composite spectrum of SDSS quasars (Vanden Berk et al. 2001). Note that there is a more recent composite spectrum of SDSS quasars without the effect of host galaxy contamination (Selsing et al. 2016). But the rest-frame wavelength coverage is only $\lambda_{\rm rest} > 1000$ Å for that template ($\lambda_{\rm rest} > 800$ Å for Vanden Berk et al. 2001), and the host contamination is not a significant factor at rest-frame UV wavelengths for a quasar with $L_{\rm bol} \gtrsim 10^{46}$ erg s^{-1} (Shen et al. 2011), which is comparable to our quasars. Based on the spectra, we used spectral parameters described below to generate our quasar SED models for fitting.

The quasar continuum slope of the SDSS composite spectrum is $\alpha_\lambda = -1.54$ (Vanden Berk et al. 2001), where $F_\lambda \propto \lambda^{\alpha_\lambda}$. Note that, in a wavelength range of 1450–2200 Å, α_λ ranges from -2.5 to -0.5 (Davis et al. 2007; Shen et al. 2011; Mazzucchelli et al. 2017). To change the continuum slope of the composite spectrum for a given α_λ, we multiplied a factor of $(\lambda/1000\ \text{Å})^{\alpha_\lambda - \alpha_{\lambda,0}}$ by the composite spectrum, where

$\alpha_{\lambda,0} = -1.54$.

The equivalent width of Lyα and N V λ1240 (hereafter EW) is also important to determine the shape of the quasar SED model. For the EW estimation, we integrated the Lyα and N V fluxes over the continuum fluxes at the range of $1160 \leq \lambda_{\rm rest}$ (Å) ≤ 1290 ($f_{\rm Ly\alpha+NV}$). In order to adjust the EW value of the composite spectrum to an arbitrary EW value, we scaled the $f_{\rm Ly\alpha+NV}$ at that wavelength range by adjusting the power of p: $f_{\rm Ly\alpha+NV} = f_{\rm Ly\alpha+NV,V01} \times (\lambda_{\rm rest}/1290\ \text{Å})^p$, where $f_{\rm Ly\alpha+NV,V01}$ is the flux measured from the original spectrum of Vanden Berk et al. (2001).

After adjusting the α_λ and EW, we applied IGM attenuation to the composite spectra, using the polynomial approximation in Madau et al. (1996). The effective optical depth for the Lyα emission line at $4.5 < z < 5.5$ is in line with the values based on several observations (Songaila 2004; Fan et al. 2006) and other simulated templates for $z \sim 5$ quasars (McGreer et al. 2013; M18).

Including M_{1450} as a scaling factor, in summary, four parameters (z, M_{1450}, α_λ, and EW) are used to generate our quasar models for the fitting, as shown in Figure 5.7. Note that the M_{1450} and EW are left as independent parameters for the fitting instead of adopting the Baldwin effect, the correlation between EWs of quasar emission lines and the continuum luminosities (Baldwin 1977), considering the uncertainty of the Baldwin effect for Lyα at high redshift (Constantin et al. 2002; Dietrich et al. 2002). Several quasar model tracks from $z = 4.5$ to 5.5 are shown as the gray dots with solid lines in Figures 5.2 and 5.3, where we adopted $M_{1450} = -24$ mag, $\alpha_\lambda = -1.6$ and $\log(\text{EW/Å}) = 1.5$. Our simulated models also satisfy the criteria given by McGreer et al. (2013) and Jeon et al. (2016).

Based on the fluxes from the broad- and the medium-band observations, $z_{\rm phot}$ was determined by finding the minimum χ^2 value between the observed fluxes and the model fluxes, where χ^2 is defined as

$$\chi^2 = \sum_i \chi_i^2 + \sum_j \chi_j^2. \tag{5.2}$$

χ_i^2, the first term, is a standard form of χ^2 for the filters with detection,

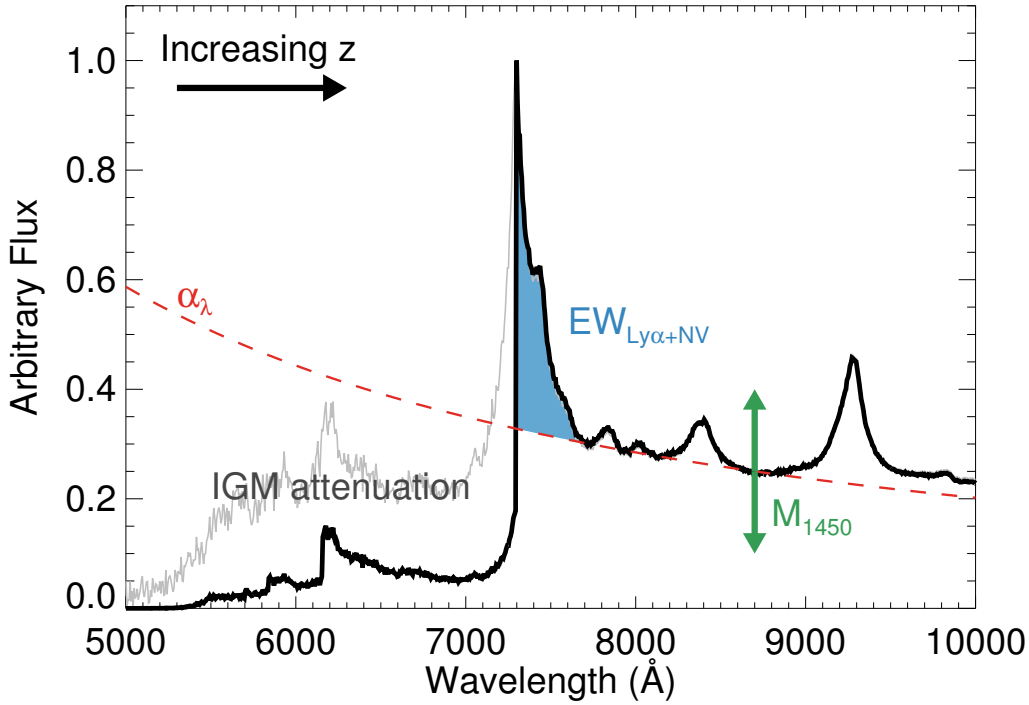

Figure 5.7. Quasar SED model with fitting parameters: z, M_{1450}, α_λ, and EW. The black solid line indicates our SED model for a high-redshift quasar at $z = 5$, while the gray solid line shows the SED model without IGM attenuation due to neutral hydrogen. The red dashed line shows a simple power law with a slope of α_λ, and the blue shaded region shows the EW defined in this work. See full details in Section 5.5.3.

$$\chi_i^2 = \left(\frac{f_{o,i} - f_{m,i}}{\sigma_i} \right)^2, \tag{5.3}$$

where $f_{o,i}$ is the observed flux in the ith band, σ_i is the standard deviation (or uncertainty) of the observed flux, and $f_{m,i}$ is the model flux in the same band, which is calculated by integrating the quasar model fluxes with the weight of the transmission curve of the band. For the case of the filters with the upper limit of fluxes, we refer to the χ^2 derivation by Sawicki (2012), which gives χ_j^2 of the second term of Eq. (5.2),

$$\begin{aligned} \chi_j^2 &= -2 \ln \int_{-\infty}^{f_{\rm lim,j}} \exp \left[-\frac{1}{2} \left(\frac{f_{o,j} - f_{m,j}}{\sigma_j} \right)^2 \right] df \\ &= -2 \ln \left\{ \sqrt{\frac{\pi}{2}}\, \sigma_j \left[1 + {\rm erf} \left(\frac{f_{\rm lim,j} - f_{m,j}}{\sqrt{2}\sigma_j} \right) \right] \right\} \end{aligned} \tag{5.4}$$

where $f_{\rm lim,j}$ is the upper limit of the flux in the jth band, $f_{m,j}$ is the model flux in the same band, σ_j is the sensitivity in the same band, and ${\rm erf}(x)$ is the error function for the numerical calculation: ${\rm erf}(x) = (2/\sqrt{\pi}) \int_0^x e^{-t^2} dt$. Note that we limited the χ_j^2 value to $\chi_j^2 \leq 0$ to restrict the χ^2 value being negative.

The minimum χ^2 was searched in the following parameter space of z, M_{1450}, α_λ, and EW: $4.5 \leq z \leq 5.5$ with a step size of 0.01, $-27.5 \leq M_{1450}$ (AB mag) ≤ -22.5 with a step size of 0.1 mag, $-3.6 \leq \alpha_\lambda \leq 0.4$ with a step size of 0.2, and $0.5 \leq \log({\rm EW/\AA}) \leq 2.5$ with a step size of 0.2. Note that the above ranges of α_λ and EW are chosen to cover the α_λ and EW values within about 2σ of the average values for high-redshift quasars, $\alpha_\lambda = -1.6 \pm 1.0$ (Mazzucchelli et al. 2017) and $\log({\rm EW/\AA})$ of $= 1.542 \pm 0.391$ in rest frame (Bañados et al. 2016). For each model, we estimated the model flux in each band by calculating the mean flux in each band, which was weighted by the filter transmission curve.

For each quasar, we calculated the $\chi_{\rm red}^2$ value (the reduced χ^2 value, defined as $\chi_{\rm red}^2 \equiv \chi^2/\nu_{\rm dof}$, where $\nu_{\rm dof}$ is the degree of freedom) for each model with broad ($grizJ$) and existing medium-band ($m675$-$m825$) fluxes. For the broadband photometry, we gave additional errors on the broadband magnitudes considering the possible variability

of quasars between the observing dates of the broad- and medium-band observations[5]. We found the minimum $\chi^2_{\rm red}$ value ($\chi^2_{\rm red,min}$) as the best-fit result and interpolated $\chi^2_{\rm red}$ values in the four parameter spaces to find points of $\chi^2_{\rm red} = \chi^2_{\rm red,min} + 1$, which are regarded as the marginal points for the errors of each parameter at the 1σ confidence level. Note that the interpolation may over/underestimate the 1σ errors by the bin size, but we expect that the effect is negligible. The best-fit results for 35 spectroscopically identified quasars are listed in Table 5.6, and Figure 5.8 shows the SEDs of the quasars with the best-fit models (blue solid lines).

Similarly to the broad- and medium-band SED fit, $z_{\rm spec}$ and the SED parameters of 13 quasars were also obtained by finding the minimum $\chi^2_{\rm red}$ with Eq. (5.2) and (5.3), but Eq. (5.4) for the upper limit case is not used. The wavelength range of the fitting was limited to $1100 \leq \lambda_{\rm obs}$ (Å)$/(1 + z_{\rm vis}) \leq 1600$, where $z_{\rm vis}$ is the redshift determined by visual inspection of the Lyα line on the spectra. It covers the Lyα line and the quasar continuum for the fitting. Among the SED parameters, α_λ was fixed to -1.54 since the wavelength coverage of our spectra is too narrow to reliably estimate the quasar continuum slope. In addition, the adopted parameter grid resolution is higher than the case of $z_{\rm phot}$ when estimating the best-fit parameters and their errors; the step sizes of $z_{\rm spec}$, M_{1450}, and $\log {\rm EW}$ were pushed down to 0.001, 0.01, and 0.1, respectively. Note that the systematic uncertainty in $z_{\rm spec}$ due to the adopted finite grid size is only ~ 0.002–0.004 for our binned spectra.

In Figure 5.4, the best-fit models are overplotted with the red lines, and we marked the wavelengths of possible emission lines, such as Lyβ λ1025, Lyα, N V λ1240, O I λ1304, Si IV λ1396, and C IV λ1549, with the blue vertical lines. In addition, the best-fit results are listed in Table 5.6.

[5]While the CFHTLS and the IMS data were obtained in 2003-2008 and 2009-2013, respectively, the medium-band observations were carried out in 2015-2018, corresponding to a term of 1-2 yr between the observations in the rest frame. The rest-frame far-UV variability of low-redshift quasars over a year scale is ~ 0.5 mag yr^{-1} for the most significant variable fraction of ~ 10 % (Welsh et al. 2011). Therefore, we gave an arbitrary error of 0.1 mag (1-2 yr $\times$ 0.5 mag yr^{-1} $\times$ 10 % $\sim$ 0.1 mag) to each broadband magnitude.

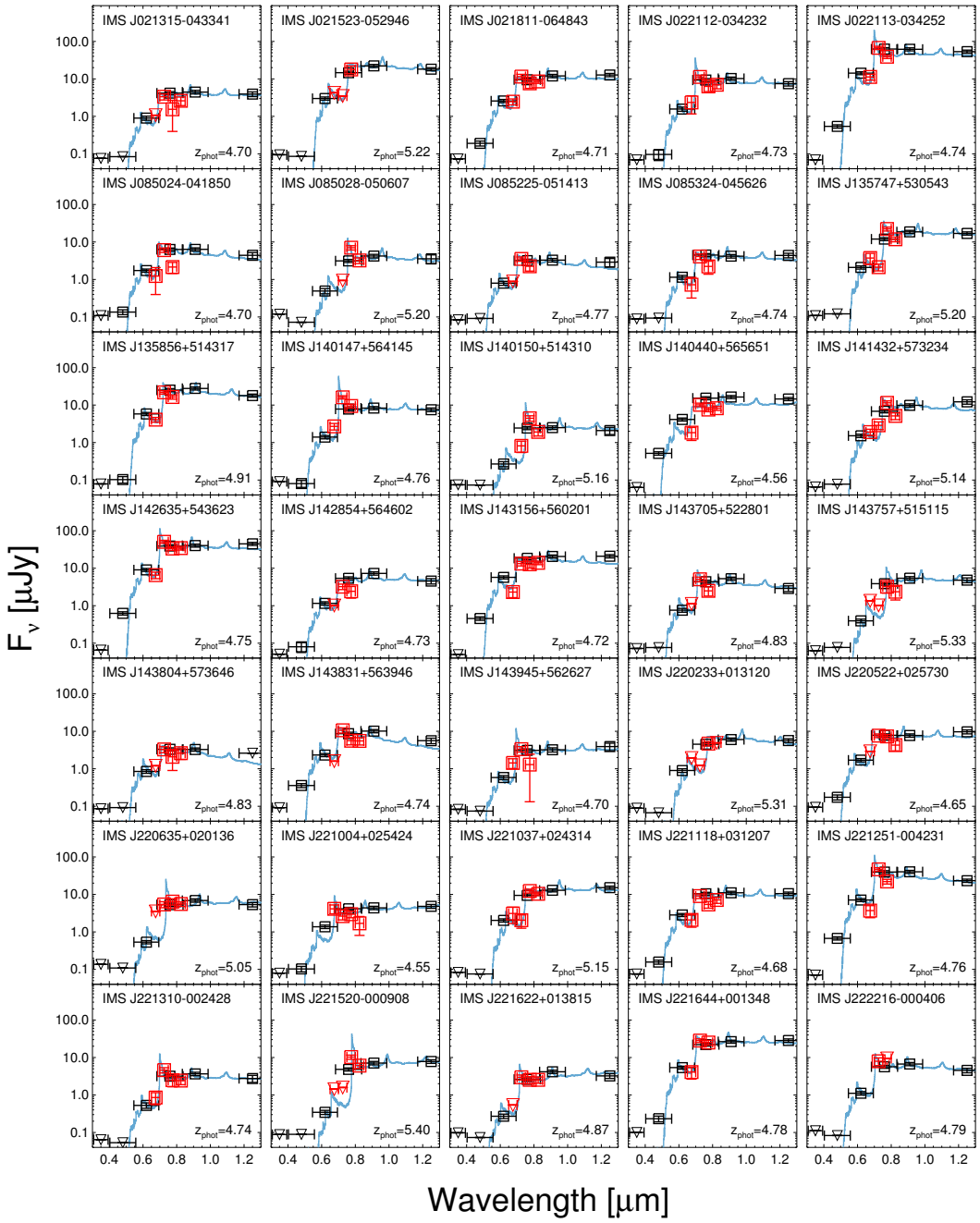

Figure 5.8. SEDs of quasars with broad- ($ugrizJ$) and medium-band ($m675$-$m825$) fluxes, which are shown as the black and red squares, respectively. Note that the downward-pointing triangles represent the 2.7σ upper limits. The best-fit model of each quasar is shown with the blue solid line, for which $\chi^2_{\rm red}$ and $z_{\rm phot}$ values are also indicated in each panel.

Table 5.6. Quantities of $z \sim 5$ Quasars from the Model Fitting

ID	Photometry				Spectroscopy			
	$z_{\rm phot}$	M_{1450} (mag)	α_λ	log EW (Å)	$z_{\rm spec}$	M_{1450} (mag)	log EW (Å)	References
IMS J021315−043341	$4.70^{+0.23}_{-0.10}$	$-23.7^{+0.1}_{-0.2}$	$-1.8^{+0.5}_{-0.9}$	$0.9^{+0.8}_{-0.3}$	$4.884^{+0.003}_{-0.035}$	$-23.65^{+0.73}_{-0.45}$	$1.9^{+0.3}_{-0.3}$	(1)
IMS J021523−052946	$5.22^{+0.17}_{-0.07}$	$-25.8^{+0.1}_{-0.1}$	$-2.6^{+0.4}_{-0.6}$	$\lesssim 0.5$	5.13	−25.6	-	(2)
IMS J021811−064843	$4.71^{+0.04}_{-0.07}$	$-24.8^{+0.1}_{-0.1}$	$-1.8^{+0.5}_{-0.5}$	$0.9^{+0.7}_{-0.3}$	$4.874^{+0.033}_{-0.028}$	$-24.66^{+0.23}_{-0.20}$	$1.6^{+0.2}_{-0.6}$	(1)
IMS J022112−034232	$4.73^{+0.17}_{-0.03}$	$-24.5^{+0.1}_{-0.2}$	$-1.8^{+0.4}_{-0.7}$	$1.9^{+0.2}_{-0.6}$	$4.976^{+0.003}_{-0.003}$	$-24.27^{+0.23}_{-0.14}$	$2.2^{+0.2}_{-0.2}$	(1)
IMS J022113−034252	$4.74^{+0.03}_{-0.01}$	$-26.4^{+0.1}_{-0.1}$	$-1.8^{+0.4}_{-0.2}$	$1.9^{+0.2}_{-0.2}$	5.02	−27.0	-	(2)
IMS J085024−041850	$4.70^{+0.07}_{-0.14}$	$-24.1^{+0.1}_{-0.1}$	$-2.8^{+1.0}_{-0.7}$	$1.3^{+0.4}_{-0.7}$	$4.799^{+0.003}_{-0.003}$	$-24.18^{+0.07}_{-0.08}$	$2.0^{+0.2}_{-0.2}$	(1)
IMS J085028−050607	$5.20^{+0.17}_{-0.04}$	$-23.9^{+0.2}_{-0.1}$	$-2.4^{+1.0}_{-1.1}$	$1.7^{+0.2}_{-0.2}$	$5.357^{+0.003}_{-0.008}$	$-23.47^{+0.22}_{-0.11}$	$2.2^{+0.2}_{-0.2}$	(1)
IMS J085225−051413	$4.77^{+0.20}_{-0.09}$	$-23.5^{+0.2}_{-0.1}$	$-2.8^{+1.0}_{-0.7}$	$1.1^{+0.6}_{-0.5}$	$4.819^{+0.003}_{-0.003}$	$-23.67^{+0.08}_{-0.08}$	$1.7^{+0.2}_{-0.2}$	(1)
IMS J085324−045626	$4.74^{+0.21}_{-0.10}$	$-23.8^{+0.1}_{-0.2}$	$-2.2^{+0.7}_{-0.8}$	$1.1^{+0.6}_{-0.5}$	$4.832^{+0.004}_{-0.004}$	$-23.89^{+0.04}_{-0.05}$	$1.8^{+0.2}_{-0.2}$	(1)
IMS J135747+530543	$5.20^{+0.10}_{-0.03}$	$-25.5^{+0.1}_{-0.1}$	$-2.0^{+0.4}_{-0.5}$	$1.5^{+0.2}_{-0.2}$	5.32	−25.5	-	(2)
IMS J135856+514317	$4.91^{+0.04}_{-0.04}$	$-25.7^{+0.1}_{-0.1}$	$-2.4^{+0.4}_{-0.3}$	$1.3^{+0.2}_{-0.2}$	4.97	−25.9	-	(2)
IMS J140147+564145	$4.76^{+0.06}_{-0.02}$	$-24.5^{+0.1}_{-0.1}$	$-1.8^{+0.2}_{-0.5}$	$2.1^{+0.2}_{-0.2}$	4.98	−24.7	-	(2)
IMS J140150+514310	$5.16^{+0.15}_{-0.01}$	$-23.4^{+0.2}_{-0.1}$	$-2.0^{+0.6}_{-0.9}$	$1.9^{+0.2}_{-0.2}$	5.17^{a}	-23.4^{a}	-	(2)
IMS J140440+565651	$4.56^{+0.09}_{-0.03}$	$-24.7^{+0.1}_{-0.1}$	$-1.6^{+0.4}_{-0.8}$	$\lesssim 0.5$	4.74	-	-	(2)
IMS J141432+573234	$5.14^{+0.04}_{-0.07}$	$-24.8^{+0.1}_{-0.1}$	$-2.4^{+0.9}_{-0.8}$	$1.3^{+0.3}_{-0.7}$	5.16	−24.7	-	(2)
IMS J142635+543623	$4.75^{+0.01}_{-0.01}$	$-26.2^{+0.1}_{-0.1}$	$-2.0^{+0.2}_{-0.5}$	$1.7^{+0.2}_{-0.2}$	4.76	−26.3	-	(2)
IMS J142854+564602	$4.73^{+0.27}_{-0.12}$	$-24.0^{+0.1}_{-0.3}$	$-1.8^{+0.5}_{-1.1}$	$\lesssim 0.5$	4.73	−24.0	-	(2)
IMS J143156+560201	$4.72^{+0.04}_{-0.04}$	$-25.3^{+0.1}_{-0.1}$	$-2.2^{+0.7}_{-0.6}$	$\lesssim 0.5$	4.75	-	-	(2)
IMS J143705+522801	$4.83^{+0.14}_{-0.11}$	$-23.8^{+0.2}_{-0.1}$	$-2.4^{+0.7}_{-0.5}$	$1.5^{+0.4}_{-0.5}$	4.78	-	-	(2)
IMS J143757+515115	$5.33^{+0.12}_{-0.24}$	$-24.2^{+0.3}_{-0.1}$	$-2.0^{+1.0}_{-0.7}$	$1.5^{+0.3}_{-0.9}$	5.17	−24.1	-	(2)
IMS J143804+573646	$4.83^{+0.20}_{-0.20}$	$-23.5^{+0.2}_{-0.2}$	$\lesssim -3.6$	$0.7^{+1.0}_{-0.2}$	4.84	−23.5	-	(2)

Table 5.6 (cont'd)

ID	Photometry				Spectroscopy			
	$z_{\rm phot}$	M_{1450} (mag)	α_λ	log EW (Å)	$z_{\rm spec}$	M_{1450} (mag)	log EW (Å)	References
IMS J143831+563946	$4.74^{+0.04}_{-0.07}$	$-24.5^{+0.1}_{-0.1}$	$\lesssim -3.6$	$1.1^{+0.5}_{-0.5}$	4.82	-	-	(2)
IMS J143945+562627	$4.70^{+0.03}_{-0.06}$	$-23.4^{+0.1}_{-0.1}$	$-1.4^{+0.8}_{-0.8}$	$1.9^{+0.2}_{-0.9}$	4.70	-23.2	-	(2)
IMS J220233+013120	$5.31^{+0.10}_{-0.23}$	$-24.5^{+0.2}_{-0.1}$	$-2.8^{+1.0}_{-0.7}$	$\lesssim 0.5$	$5.208^{+0.022}_{-0.003}$	$-23.85^{+0.10}_{-0.13}$	$2.0^{+0.2}_{-0.2}$	(1)
IMS J220522+025730	$4.65^{+0.07}_{-0.07}$	$-24.4^{+0.1}_{-0.1}$	$-1.8^{+0.5}_{-0.6}$	$1.3^{+0.4}_{-0.7}$	$4.743^{+0.004}_{-0.012}$	$-24.40^{+0.15}_{-0.12}$	$1.8^{+0.2}_{-0.2}$	(1)
IMS J220635+020136	$5.05^{+0.07}_{-0.15}$	$-24.2^{+0.1}_{-0.1}$	$-1.4^{+0.3}_{-0.5}$	$1.9^{+0.2}_{-0.3}$	$5.101^{+0.003}_{-0.003}$	$-24.41^{+0.11}_{-0.08}$	$1.9^{+0.2}_{-0.2}$	(1)
IMS J221004+025424	$4.55^{+0.07}_{-0.05}$	$-23.6^{+0.1}_{-0.1}$	$-1.2^{+0.4}_{-0.7}$	$1.7^{+0.4}_{-0.7}$	$4.638^{+0.003}_{-0.004}$	$-23.80^{+0.06}_{-0.05}$	$1.8^{+0.2}_{-0.2}$	(1)
IMS J221037+024314	$5.15^{+0.07}_{-0.06}$	$-25.2^{+0.1}_{-0.1}$	$-1.8^{+0.6}_{-0.7}$	$0.9^{+0.6}_{-0.3}$	$5.204^{+0.010}_{-0.012}$	$-25.23^{+0.03}_{-0.03}$	$1.4^{+0.2}_{-0.2}$	(1)
IMS J221118+031207	$4.68^{+0.06}_{-0.12}$	$-24.7^{+0.2}_{-0.1}$	$-1.8^{+0.6}_{-0.5}$	$0.7^{+0.8}_{-0.2}$	$4.821^{+0.003}_{-0.003}$	$-24.42^{+0.12}_{-0.13}$	$2.0^{+0.2}_{-0.2}$	(1)
IMS J221251−004231	$4.76^{+0.03}_{-0.01}$	$-26.0^{+0.1}_{-0.1}$	$-2.6^{+0.2}_{-0.3}$	$1.7^{+0.2}_{-0.2}$	4.95	-26.3	-	(3)
IMS J221310−002428	$4.74^{+0.20}_{-0.03}$	$-23.4^{+0.1}_{-0.2}$	$-1.8^{+0.8}_{-0.8}$	$1.9^{+0.3}_{-0.5}$	4.80	-23.5	-	(2)
IMS J221520−000908	$5.40^{+0.06}_{-0.20}$	$-24.5^{+0.1}_{-0.1}$	$-1.2^{+0.5}_{-0.5}$	$2.1^{+0.2}_{-0.2}$	5.28	-24.5	-	(2)
IMS J221622+013815	$4.87^{+0.20}_{-0.12}$	$-23.4^{+0.1}_{-0.2}$	$-0.8^{+0.3}_{-0.7}$	$1.7^{+0.2}_{-0.4}$	4.93	-23.3	-	(2)
IMS J221644+001348	$4.78^{+0.09}_{-0.04}$	$-25.8^{+0.1}_{-0.1}$	$-1.8^{+0.4}_{-0.4}$	$1.3^{+0.3}_{-0.7}$	5.01	-25.8	-	(2)
IMS J222216−000406	$4.79^{+0.24}_{-0.10}$	$-24.2^{+0.2}_{-0.2}$	$-2.2^{+0.5}_{-0.6}$	$1.5^{+0.6}_{-0.9}$	4.95	-24.3	-	(2)

Note. — The systematic uncertainty of the redshift determination with the Lyα fitting ($\Delta z \lesssim 0.1$; Kim et al. 2015a, 2018; M18) is not included in the uncertainties of $z_{\rm phot}$ and $z_{\rm spec}$. The spectral properties are from (1) this work, (2) M18, and (3) McGreer et al. (2013). For spectroscopic data in this work, we fixed α_λ to -1.54 when fitting our quasar SED model (see Section 5.5.3). Note that M_{1450} from (2) and (3) are determined by the i-band magnitudes and $z_{\rm spec}$, which are matched to model quasar spectra. The difference in cosmological parameters between the literature and this work is also concerned.

[a]For IMS J140150+514310, M18 provides $z_{\rm spec} = 4.20$. However, we revise it to be $z_{\rm spec} = 5.17$ from the Lyα break in the spectrum shown in Fig. 9 of M18 (see details in Section 5.4.3). M_{1450} is the value that assumes $z_{\rm spec} = 5.17$.

5.5.4 Medium-band Photometric Redshift Accuracy

In Table 5.6, the best-fit results of our $z \sim 5$ quasar sample are listed. The median uncertainty of $z_{\rm spec}$ is only 0.004, while that of the $z_{\rm phot}$ is 0.09. The left panel of Figure 5.9 shows the comparison of $z_{\rm spec}$ and $z_{\rm phot,BB}$, the photometric redshift determined with only broadband photometry, for 35 quasars. They show a loose correlation with a linear Pearson correlation coefficient of $r_c = 0.58$. If we introduce the additional medium-band photometry for the $z_{\rm phot}$ determination, there is a tight correlation between $z_{\rm spec}$ and $z_{\rm phot}$ with the improved r_c of 0.90 (right panel of Figure 5.9). For the two cases, the scatters of normalized median absolute deviations of $|\Delta z|/(1+z)$ ($\sigma_{\rm NMAD}$) are 0.029 and 0.016, respectively, where $\Delta z \equiv z_{\rm spec} - z_{\rm phot}$ and the $z_{\rm spec}$ are used for the reference redshifts.

Compared to the identical line (the black dashed line), there is a trend of $z_{\rm phot}$ slightly lower than $z_{\rm spec}$, which is described by the linear relation of $z_{\rm spec} = 1.087 \times z_{\rm phot} - 0.506$ (the red solid line in Figure 5.9). For a simple comparison, we plotted the distribution of $\Delta z/(1+z)$ in Figure 5.10. The median $\Delta z/(1+z)$ values for $z_{\rm phot}$ (red histogram) and $z_{\rm phot,BB}$ (blue histogram) are slightly biased toward lower redshift (-0.010 and -0.023, respectively). The small systematic bias in $\Delta z/(1+z)$ could be explained by the limitation in our quasar models and the filter system. A quasar model with a stronger Lyα emission can give a $z_{\rm phot}$ value that is slightly larger than a model with a weaker Lyα emission since both the models give the same amount of flux within a certain passband that samples the light above the sharp break at Lyα. For that reason, the $z_{\rm phot}$ probability distribution has a longer tail toward higher redshift. Since we adopt $z_{\rm phot}$ at the maximum probability (the best-fit value), this can result in a slight underestimation in $z_{\rm phot}$. In addition, the magnitudes at wavelengths longer than Lyα have smaller uncertainties than the wavelength below Lyα, and this can lead to a slight underestimation in in $z_{\rm phot}$ by giving more weight to the longer-wavelength magnitudes during the model fitting. Then, the fitting procedure tries to fit the longer-wavelength magnitudes better by adjusting the Lyα strength to preferentially allow a strong Lyα emission model with larger $z_{\rm phot}$ values. We confirm this by increasing the photometry

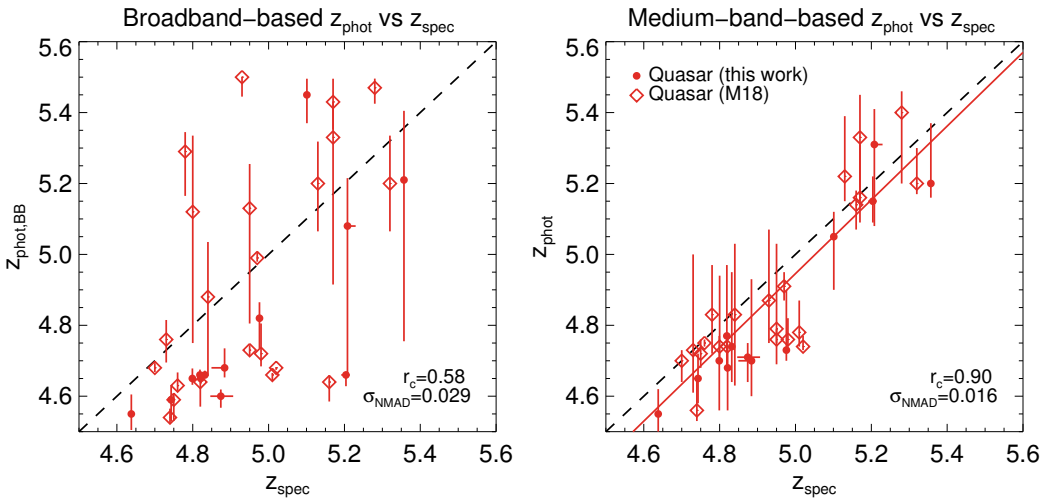

Figure 5.9. Comparison of $z_{\rm phot}$ versus $z_{\rm spec}$ of quasars at $z \sim 5$ for the $z_{\rm phot}$ values derived from broad band photometry only (left) and the $z_{\rm phot}$ values from the broad- and medium-band data (right). The symbols are the same as those in Figure 5.1. The black dotted line shows the case where $z_{\rm phot}$ is identical to $z_{\rm spec}$, and the red solid line indicates the best-fit result. The Pearson correlation coefficient (r_c) and the scatter of normalized median absolute deviation ($\sigma_{\rm NMAD}$) are noted in the lower right corner.

accuracy of a filter below Lyα of a $z_{\rm phot} = 4.7$ quasar from 0.05 to 0.5 mag. When the photometric error increases, the $z_{\rm phot}$ value drops by 0.1. Previous studies of quasar observations in medium bands also support this explanation. Jeon et al. (2016) used similar models that have a sharp break to measure $z_{\rm phot}$ of the bright quasar sample at $4.7 < z < 6.0$ with the SQUEAN medium-band observations, and the $\Delta z/(1+z)$ distribution is a Gaussian distribution of -0.010 ± 0.012 (Jeon et al. 2016). On the other hand, Wolf et al. (2003) used the SDSS quasar spectrum (Vanden Berk et al. 2001) without IGM attenuation for the $z_{\rm phot}$ determination of low-redshift quasars at $0.6 < z < 3.5$ with medium-band observations from the COMBO-17 survey. Their $z_{\rm phot}$ values are almost identical to $z_{\rm spec}$ with uncertainty of $\lesssim 0.05$, corresponding to the low IGM attenuation toward the lower-redshift quasars.

The standard deviation of the $z_{\rm phot}$ case (0.018) is smaller than that of the $z_{\rm phot,BB}$ case (0.043) by a factor of 2.4, in agreement with the previous suggestion that the $z_{\rm phot}$ determination could be improved with the inclusion of medium-band data. Our $z_{\rm phot}$ estimation method with the medium-band data opens up the possibility of constructing QLFs at redshift bins finer than previous attempts using broadband-based $z_{\rm phot}$ where they constructed QLFs with a coarse bin (e.g., $4.7 < z < 5.4$ in M18).

In summary, using the medium-band data, we can estimate the $z_{\rm phot}$ values of quasars accurately, comparable to the low-resolution spectroscopy. As we described above, the $z_{\rm phot}$ values of high-redshift quasars with $i < 23$ mag determined by the broad- and medium-band data are reasonably matched to $z_{\rm spec}$ by an uncertainty of $\langle|\Delta z|/(1+z)\rangle = 0.016$. Together with the low contamination rate of our medium-band-based approach, a percentage-level $z_{\rm phot}$ accuracy improves the LF and the number density estimation of $z \sim 5$ quasars and can even allow us to trace the large-scale distribution of quasars.

The amount of on-source integration we spent on each object ($i < 23$ mag) was about 2–3 hr. This was for using a 2.1 m telescope under the seeing of $1\farcs0$ to $1\farcs5$. In comparison, for the spectroscopic observations with Gemini or Magellan, we invested about 1–2 hr of time per target, including overheads. Considering that 1-2 m class telescope time is much more readily available, the medium-band-based approach is a very cost-effective way to identify high-redshift quasars and measure their redshifts to 1%–2% accuracy.

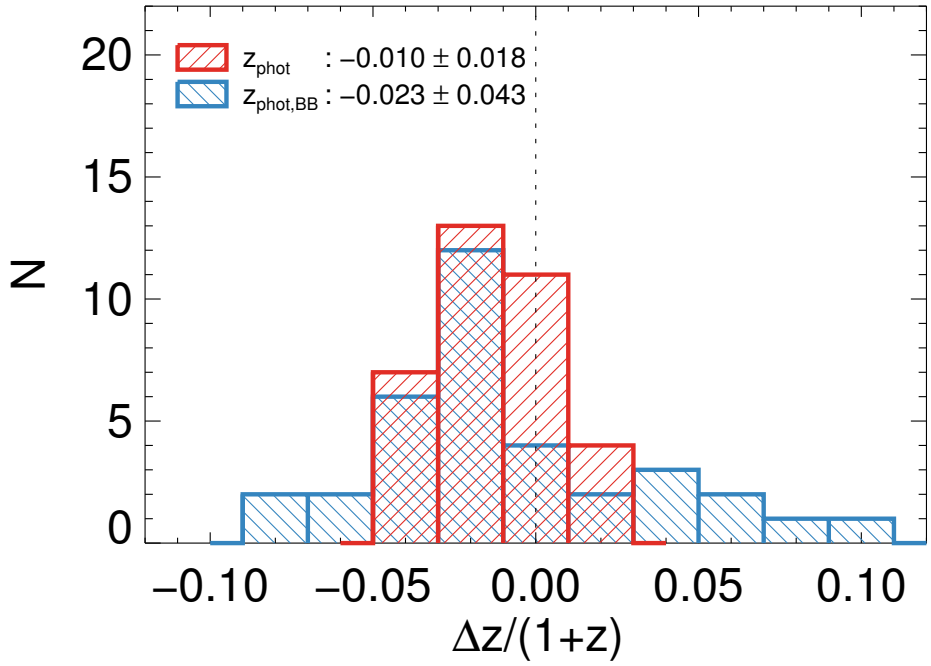

Figure 5.10. Histogram of $\Delta z/(1+z)$ of $z \sim 5$ quasars, where $\Delta z = z_{\rm phot} - z_{\rm spec}$. The red histogram represents the $\Delta z/(1+z)$ distribution based on $z_{\rm phot}$ including the medium-band photometry, while the blue one shows that of $z_{\rm phot,BB}$ with only the broadband photometry. Their median and standard deviation values are given in the legend. The vertical dotted line indicates $\Delta z/(1+z) = 0$.

5.6 Implication on the QLF at $z \sim 5$

Among the newly discovered 10 quasars, three quasars, IMS J021315−043341, IMS J021811−064843, and IMS J220635+020136, were not reported in the final sample of M18 even as quasar candidates, though these quasars are located in their survey area. The main difference in the broadband selection between ours and M18 is the presence of the NIR data from IMS, so this could be a reason for us picking up new quasars in the area already surveyed by M18. As shown in the middle panel of Figure 5.2 and Table 5.2, however, their *riz* colors (the colors used by M18 for quasar selection) are quite ordinary to be selected as quasar candidates. Also, they are not particularly faint ($i < 22.4$ mag) to be missed owing to large photometry uncertainties. Another possible reason for the rejection is the stellar source classification of M18 by using the difference of PSF-matched magnitude ($i_{\rm PSF}$) and AUTO magnitudes ($i_{\rm AUTO}$) in i band; $i_{\rm AUTO} - i_{\rm PSF} > -0.15$ mag, but the quasars also satisfy this criterion. Overall, the three quasars deserve to be selected by M18 even without the NIR data, but they are not. The differences in photometry between M18 and this work may be the reason, like the four M18 quasars excluded from our candidates (see Section 5.5.2), but we could not verify this because of the lack of the full catalog of M18 in our hand.

We estimated the chance of finding these quasars from the selection functions from M18. Based on the spectral properties (z, M_{1450}, α_λ, and EW in Table 5.6), the probabilities of finding the three quasars are as high as $\sim 95\%$, meaning that the quasars are not outliers. We can update the binned QLF of M18 by the three quasars in their sample. Assuming the same photometric (94%) and spectroscopic (86%) completeness of M18 for the three quasars (21.46 mag $< i <$ 22.35 mag), the number counts corrected by the incompleteness ($N_{\rm cor}$ in Table 1 in M18) in the magnitude bins of $M_{1450} = -24.35$ and -23.65 mag increase from 18.0 and 20.6 and from 7.8 to 9.1, respectively, corresponding to the increase in the binned QLF values at the faint end by 15%. This is a modest increase and is consistent with the results from M18 within the error. However, the discovery of the three new quasars in the previously surveyed area suggests the importance of independent surveys and applying different methods to gain a complete

sample of high-redshift quasars.

Our results of finding $z \sim 5$ quasars support the scenario of the minor contribution of quasars to the cosmic reionization, as the studies of high-redshift quasars have suggested so far (e.g., Willott et al. 2010b; Kashikawa et al. 2015; Kim et al. 2015a; Onoue et al. 2017; M18). Several tens of candidates remain to be observed with the medium bands, and the ionizing emissivity by quasars at the faint magnitude range of $M_{1450} \sim -23$ mag could change with our future sample with medium-band observations. However, even if we adopt a pessimistic identification rate of 53% (based on the 22 mag $< i <$ 23 mag quasar sample) for these remaining faint quasar candidates, the expected binned QLF at $z \sim 5$ is marginally in line with the 3σ upper limit by M18, meaning that faint quasars contribute to a minor fraction of UV photons to ionize IGM. The gap in the $z \sim 5$ quasar number density between optical and X-ray surveys would still remain unsolved.

5.7 Summary

We have performed a $z \sim 5$ quasar survey with a medium-band-based approach to improve faint quasar candidate selection based on the broadband colors. The follow-up imaging and spectroscopy allow us to find 10 new quasars at $z \sim 5$, among which 3 were missed in the surveys covering the same area. Using medium-band data of 35 spectroscopically identified quasars, we demonstrate that quasars can be distinguished effectively from other objects (e.g., brown dwarfs, galaxies) by imposing medium-band selection criteria on the broadband selected candidates ($\gtrsim$ 20 % of the broadband selected sample is ruled out). Furthermore, with the inclusion of the medium-band data, the $z_{\rm phot}$ accuracy improves by a factor of 2-3 in comparison to $z_{\rm phot,BB}$, producing a nearly 1% level accuracy of $\langle|\Delta z|/(1+z)\rangle = 0.016$ (or $\sigma_{\rm NMAD} = 0.016$). Despite our discovery of new faint quasars, the scarcity of $z \sim 5$ quasars is consistent with the recent suggestions that the high-redshift quasars are not main contributors to the cosmic reionization in the early universe. Based on the high accuracy of the $z_{\rm phot}$ determination, we expect that the completion of the medium-band survey will enable

us to improve the constraint on the faint-end slope of the QLF at $z \sim 5$ in the near future.

Chapter 6

Conclusion

Recent studies on high-redshift quasars suggest that (1) faint AGNs may be responsible for the cosmic reionization, (2) most of the luminous quasars known at $z \gtrsim 6$ have been found to grow rapidly with high accretion rates, and (3) the SMBH growth in the early universe may precede the prolonged intense star formation within its host galaxy, instead of quasars appearing after the obscured dusty star formation phase. In this thesis, we figure out these characteristics of high-redshift quasars, especially with the newly discovered faint quasars. As a result, we present their contribution to the cosmic reionization and the evolutionary scenario for the first SMBHs and their host galaxies.

First, we have performed the survey of faint quasars at $z \sim 6$, using the combination of the CFHTLS optical imaging data and the IMS NIR imaging data. IMS covers 86 deg^2 areas in J-band to the depths of $J_{\rm AB} \sim 23$ mag. Among the thirteen plausible quasar candidates that were selected by the color-selection technique, IMS J2204+0112 was newly identified as a faint quasar at $z \sim 6$. The spectrum of the quasar shows a sharp break at ~ 8422 Å, with emission lines redshifted to $z = 5.926 \pm 0.002$ and $M_{1450} = -23.99 \pm 0.11$ AB mag. Including the other quasars identified by other works, we derived the quasar luminosity function at $z \sim 6$, showing a flatten faint-end slope at $M_{1450} < -23$ mag. From these quasar luminosity functions, the ionizing photon density was calculated as $\dot{n}_{\rm ion} \sim 0.5$–$2.5 \times 10^{48}$ s^{-1} Mpc^{-3} that is significantly lower than the required value for the cosmic reionization; only $< 15\%$ of the amount required. This

result is in agreement with the previous observations of spectroscopically identified low-luminosity quasars, suggesting that the number of $M_{1450} \sim -23$ mag quasars at $z \sim 6$ may not be high enough to fully account for the reionization of the universe. In addition, our study demonstrates that faint quasars in the early universe can be identified effectively with a moderately wide and deep near-infrared survey such as the IMS.

Second, we estimate the $M_{\rm BH}$ of IMS J2204+0112, one of the faintest quasars that have been identified at $z \sim 6$. The suggestion of enhanced quasar activities in the early universe may not be the whole picture of SMBH growth since previous studies have not reached on faint quasars that are more likely to harbor SMBHs with low $\lambda_{\rm Edd}$. To gain a better understanding on the accretion activities in quasars in the early universe, we obtained a deep NIR spectrum of IMS J2204+0112 with a sensitive NIR spectrograph FIRE on the Magellan 6.5 m Telescope. From the redshifted C IV λ1549 emission line in the NIR spectrum, we find that IMS J2204+0112 harbors a SMBH with about a billion solar mass and $\lambda_{\rm Edd} \sim 0.1$, but with a large uncertainty in both quantities (0.41 dex). IMS J2204+0112 has one of the lowest Eddington ratios among quasars at $z \sim 6$, but a common value among quasars at $z \sim 2$. Its low $\lambda_{\rm Edd}$ can be explained with two scenarios; the SMBH growth from a stellar mass black hole through short-duration super-Eddington accretion events or from a massive black hole seed ($\sim 10^5\,M_{\odot}$) with Eddington-limited accretion. Also, we derived the intrinsic $\lambda_{\rm Edd}$ distribution of high-redshift quasars under the several assumptions, resulting that the $\lambda_{\rm Edd}$ values of high-redshift quasars are only slightly higher than those of $z \sim 2$ quasars. This result is consistent with the recent NIR observations of high-redshift quasars, requiring more extreme growth of the first SMBHs.

Third, we examine the SFRs of the low $\lambda_{\rm Edd}$ quasars at $z \sim 6$, including IMS J2204+0112. According to the recent simulation works on the first SMBHs and their host galaxies, high-redshift quasars with low $\lambda_{\rm Edd}$ would be found in actively star-forming hosts with a SFR of $> 100\ M_{\odot}\ {\rm yr}^{-1}$. We present the sub-mm observations of IMS J2204+0112, a faint quasar with a quasar bolometric luminosity of $L_{\rm bol} =$

4.24×10^{12} $L_\odot$ and a low $\lambda_{\rm Edd}$ of only 0.11 at $z \sim 6$, carried out with ALMA and SCUBA-2 on JCMT. From its sub-mm fluxes, we measure the rest-frame FIR luminosity of $L_{\rm FIR} = (3.30\text{–}4.30) \times 10^{12}$ $L_\odot$. Interestingly, the derived host galaxy's SFR is $\sim$ 560–731 $M_\odot$ yr^{-1}, an order of magnitude higher than those of the $L_{\rm bol}$-matched $z \gtrsim 6$ quasars with high $\lambda_{\rm Edd}$. Similar FIR excesses are also found for five $z \gtrsim 6$ low-$\lambda_{\rm Edd}$ quasars ($\lambda_{\rm Edd} < 0.2$) in the literature. We show that the overall SFR, $M_{\rm BH}$, and $\lambda_{\rm Edd}$ distributions of these and other sub-mm-detected quasars at $z \gtrsim 6$ can be explained with the evolutionary track of high-redshift quasars in a simulation study where the SMBH growth largely precedes the formation of the host galaxy. According to this picture, the nuclear activities of the low $\lambda_{\rm Edd}$, high $L_{\rm FIR}$ quasars are on the brink of being turned off, while their host galaxies continue to form the bulk of their stars at SFR > 100 $M_\odot$ yr^{-1}.

Fourth, we present the first results of the $z \sim 5$ faint quasar survey with IMS. To improve selection methods, the medium-band follow-up imaging has been carried out using the SQUEAN on the Otto Struve 2.1 m Telescope. The optical spectra of the candidates were obtained with 8-m class telescopes. We newly discovered 10 quasars with $-25 < M_{1450} < -23$ at $z \sim 5$, among which three have been missed in a previous survey using the same optical data over the same area, implying the necessity for improvements in high redshift faint quasars selection. We derived photometric redshifts from the medium-band data, and find that they have high accuracies of $\langle |\Delta z|/(1+z) \rangle = 0.016$. The medium-band-based approach allows us to rule out many of the interlopers that contaminate $\gtrsim 20\%$ of the broad-band-selected quasar candidates. These results suggest that the medium-band-based approach is a powerful way to identify $z \sim 5$ quasars and measure their redshifts at high accuracy (1–2%). It is also a cost-effective way to understand the contribution of quasars to the cosmic re-ionization history.

Bibliography

Aihara, H., Arimoto, N., Armstrong, R., et al. 2018, PASJ, 70, S4

Aihara, H., Armstrong, R., Bickerton, S., et al. 2018, PASJ, 70, S8

Alexander, D. M., & Hickox, R. C. 2012, New A Rev., 56, 93

Alvarez, M. A., Wise, J. H., & Abel, T. 2009, ApJ, 701, L133

Avni, Y., & Bahcall, J. N. 1980, ApJ, 235, 694.

Baldwin, J. A. 1977, ApJ, 214, 679

Bañados, E., Decarli, R., Walter, F., et al. 2015a, ApJ, 805, L8

Bañados, E., Venemans, B. P., Decarli, R., et al. 2016, ApJS, 227, 11

Bañados, E., Venemans, B. P., Mazzucchelli, C., et al. 2018, Nature, 553, 473

Bañados, E., Venemans, B. P., Morganson, E., et al. 2014, AJ, 148, 14

Bañados, E., Venemans, B. P., Morganson, E., et al. 2015b, ApJ, 804, 118.

Barai, P., Gallerani, S., Pallottini, A., et al. 2018, MNRAS, 473, 4003.

Becker, R. H., White, R. L., & Helfand, D. J. 1995, ApJ, 450, 559

Beckmann, V., & Shrader, C. R. 2012, Active Galactic Nuclei.

Beelen, A., Cox, P., Benford, D. J., et al. 2006, ApJ, 642, 694

Begelman, M. C., Volonteri, M., & Rees, M. J. 2006, MNRAS, 370, 289

Bentz, M. C., Peterson, B. M., Netzer, H., et al. 2009, ApJ, 697, 160.

Bertin, E., & Arnouts, S. 1996, A&AS, 117, 393

Bertin, E. 2010, SWarp: Resampling and Co-adding FITS Images Together, Astrophysics Source Code Library, ascl:1010.068

Bertoldi, F., Carilli, C. L., Cox, P., et al. 2003a, A&A, 406, L55.

Bertoldi, F., Cox, P., Neri, R., et al. 2003b, A&A, 409, L47.

Bolton, J. S., & Haehnelt, M. G. 2007, MNRAS, 382, 325.

Bouwens, R. J., Oesch, P. A., Illingworth, G. D., Ellis, R. S., & Stefanon, M. 2017, ApJ, 843, 129

Boyle, B. J., Shanks, T., Croom, S. M., et al. 2000, MNRAS,317, 1014

Bromm, V., & Loeb, A. 2003, ApJ, 596, L34

Burrows, A., Sudarsky, D., & Hubeny, I. 2006, ApJ, 640, 1063

Calzetti, D., Armus, L., Bohlin, R. C., et al. 2000, ApJ, 533, 682

Capak, P. L., Carilli, C., Jones, G., et al. 2015, Nature, 522, 455

Cardelli, J. A., Clayton, G. C., & Mathis, J. S. 1989, ApJ, 345, 245

Carilli, C. L., & Walter, F. 2013, ARA&A, 51, 105

Casali, M., Adamson, A., Alves de Oliveira, C., et al. 2007, A&A, 467, 777

Cavanagh, B., Jenness, T., Economou, F., & Currie, M. J. 2008, Astronomische Nachrichten, 329, 295

Chambers, K. C., Magnier, E. A., Metcalfe, N., et al. 2016, arXiv e-prints, arXiv:1612.05560.

Chiu, H.-Y. 1964, Physics Today, 17, 5, 21

Choi, N., Park, W.-K., Lee, H.-I., Ji, T.-G. J., Yiseul, & Im, M. P., Soojong 2015, Journal of Korean Astronomical Society, 48, 177

Coatman, L., Hewett, P. C., Banerji, M., & Richards, G. T. 2016, MNRAS, 461, 647

Coatman, L., Hewett, P. C., Banerji, M., et al. 2017, MNRAS, 465, 2120

Constantin, A., Shields, J. C., Hamann, F., Foltz, C. B., & Chaffee, F. H. 2002, ApJ, 565, 50

Covey, K. R., Ivezić, Ž., Schlegel, D., et al. 2007, AJ, 134, 2398

Davenport, J. R. A., Ivezić, Ž., Becker, A. C., et al. 2014, MNRAS, 440, 3430

Davis, S. W., Woo, J.-H., & Blaes, O. M. 2007, ApJ, 668, 682

Dayal, P., & Ferrara, A. 2018, Phys. Rep., 780, 1

Decarli, R., Falomo, R., Treves, A., et al. 2010, MNRAS, 402, 2453

Decarli, R., Walter, F., Venemans, B. P., et al. 2018, ApJ, 854, 97

DeGraf, C., Dekel, A., Gabor, J., & Bournaud, F. 2017, MNRAS, 466, 1462

DeGraf, C., Di Matteo, T., Khandai, N., et al. 2012, MNRAS, 424, 1892

Dempsey, J. T., Friberg, P., Jenness, T., et al. 2013, MNRAS, 430, 2534

Denney, K. D., Pogge, R. W., Assef, R. J., et al. 2013, ApJ, 775, 60

De Rosa, G., Decarli, R., Walter, F., et al. 2011, ApJ, 739, 56

De Rosa, G., Venemans, B. P., Decarli, R., et al. 2014, ApJ, 790, 145

Díaz-Santos, T., Assef, R. J., Blain, A. W., et al. 2018, Science, 362, 1034

Dietrich, M., Hamann, F., Appenzeller, I., & Vestergaard, M. 2003, ApJ, 596, 817

Dietrich, M., Hamann, F., Shields, J. C., et al. 2002, ApJ, 581, 912

Di Matteo, T., Khandai, N., DeGraf, C., et al. 2012, ApJ, 745, L29

Di Matteo, T., Springel, V., & Hernquist, L. 2005, Nature, 433, 604

Dressler, A., Bigelow, B., Hare, T., et al. 2011, PASP, 123, 288

Dunne, L., Eales, S., Edmunds, M., et al. 2000, MNRAS, 315, 115

Engel, H., Davies, R. I., Genzel, R., et al. 2011, ApJ, 729, 58

Eilers, A.-C., Davies, F. B., Hennawi, J. F., et al. 2017, ApJ, 840, 24

Eilers, A.-C., Hennawi, J. F., & Davies, F. B. 2018, ApJ, 867, 30

Fan, X., Hennawi, J. F., Richards, G. T., et al. 2004, AJ, 128, 515.

Fan, X., Narayanan, V. K., Lupton, R. H., et al. 2001, AJ, 122, 2833

Fan, X., Strauss, M. A., Becker, R. H., et al. 2006, AJ, 132, 117

Fan, X., Strauss, M. A., Schneider, D. P., et al. 2003, AJ, 125, 1649.

Fan, X., White, R. L., Davis, M., et al. 2000, AJ, 120, 1167

Ferrara, A., Salvadori, S., Yue, B., & Schleicher, D. 2014, MNRAS, 443, 2410

Ferrarese, L., & Merritt, D. 2000, ApJ, 539, L9.

Fleming, D. E. B., Harris, W. E., Pritchet, C. J., & Hanes, D. A. 1995, AJ, 109, 1044

Flesch, E. W. 2015, PASA, 32, 10

Flewelling, H. A., Magnier, E. A., Chambers, K. C., et al. 2016, arXiv e-prints, arXiv:1612.05243.

Fontanot, F., Cristiani, S., Monaco, P., et al. 2007, A&A, 461, 39

Fontanot, F., Cristiani, S., Pfrommer, C., Cupani, G., & Vanzella, E. 2014, MNRAS, 438, 2097

Fontanot, F., Cristiani, S., & Vanzella, E. 2012, MNRAS, 425, 1413

Gallerani, S., Fan, X., Maiolino, R., & Pacucci, F. 2017, PASA, 34, e022

García-Marín, M., Colina, L., & Arribas, S. 2009, A&A, 505, 1017

Gawiser, E., van Dokkum, P. G., Herrera, D., et al. 2006, ApJS, 162, 1

Gebhardt, K., Bender, R., Bower, G., et al. 2000, ApJ, 539, L13.

Georgakakis, A., Clements, D. L., Bendo, G., et al. 2009, MNRAS, 394, 533

Giallongo, E., Grazian, A., Fiore, F., et al. 2015, A&A, 578, A83

Glikman, E., Djorgovski, S. G., Stern, D., et al. 2011, ApJL, 728, L26

Glikman, E., Helfand, D. J., White, R. L., et al. 2007, ApJ, 667, 673

Goto, T. 2006, MNRAS, 371, 769

Grandi, S. A. 1982, ApJ, 255, 25

Grazian, A., Giallongo, E., Paris, D., et al. 2017, A&A, 602, A18

Gunn, J. E., & Peterson, B. A. 1965, ApJ, 142, 1633

Gunn, J. E., Siegmund, W. A., Mannery, E. J., et al. 2006, AJ, 131, 2332.

Gunn, J. E., & Stryker, L. L. 1983, ApJS, 52, 121

Gwyn, S. D. J. 2012, AJ, 143, 38

Haardt, F., & Madau, P. 2012, ApJ, 746, 125

Hao, C. N., Xia, X. Y., Mao, S., Wu, H., & Deng, Z. G. 2005, ApJ, 625, 78

Hao, C.-N., Xia, X.-Y., Shu-DeMao, Deng, Z.-G., & Wu, H. 2008, Chinese J. Astron. Astrophys., 8, 12

Harris, K., Farrah, D., Schulz, B., et al. 2016, MNRAS, 457, 4179

Hassan, S., Davé, R., Mitra, S., et al. 2018, MNRAS, 473, 227

Hewett, P. C., Foltz, C. B., & Chaffee, F. H. 1995, AJ, 109, 1498

Hewett, P. C., Warren, S. J., Leggett, S. K., & Hodgkin, S. T. 2006, MNRAS, 367, 454

Hickox, R. C., Jones, C., Forman, W. R., et al. 2009, ApJ, 696, 891

Ho, L. C., Goldoni, P., Dong, X.-B., Greene, J. E., & Ponti, G. 2012, ApJ, 754, 11

Hook, I. M., Jørgensen, I., Allington-Smith, J. R., et al. 2004, PASP, 116, 425

Hopkins, P. F., Hernquist, L., Cox, T. J., & Kereš, D. 2008, ApJS, 175, 356

Hudelot, P., Cuillandre, J.-C., Withington, K., et al. 2012, VizieR Online Data Catalog, 2317, 0

Ikeda, H., Nagao, T., Matsuoka, K., et al. 2017, ApJ, 846, 57

Ikeda, H., Nagao, T., Matsuoka, K., et al. 2012, ApJ, 756, 160

Im, M., Griffiths, R. E., & Ratnatunga, K. U. 1997, ApJ, 475, 457

Im, M., Lee, I., Cho, Y., et al. 2007, ApJ, 664, 64

Izumi, T., Onoue, M., Shirakata, H., et al. 2018, PASJ, 70, 36

Izumi, T., Onoue, M., Matsuoka, Y., et al. 2019, arXiv e-prints , arXiv:1904.07345.

Japelj, J., Vanzella, E., Fontanot, F., et al. 2017, MNRAS, 468, 389

Jenness, T., & Economou, F. 2015, Astronomy and Computing, 9, 40

Jeon, Y., Im, M., Ibrahimov, M., et al. 2010, ApJS, 190, 166

Jeon, Y., Im, M., Kim, D., et al. 2017, ApJS, 231, 16

Jeon, Y., Im, M., Pak, S., et al. 2016, Journal of Korean Astronomical Society, 49, 25

Jeon, M., Pawlik, A. H., Greif, T. H., et al. 2012, ApJ, 754, 34

Jiang, L., Fan, X., Bian, F., et al. 2009, AJ, 138, 305

Jiang, L., Fan, X., Annis, J., et al. 2008, AJ, 135, 1057.

Jiang, L., Fan, X., Brandt, W. N., et al. 2010, Natur, 464, 380

Jiang, L., Fan, X., Vestergaard, M., et al. 2007, AJ, 134, 1150

Jiang, L., McGreer, I. D., Fan, X., et al. 2015, AJ, 149, 188.

Jiang, L., McGreer, I. D., Fan, X., et al. 2016, ApJ, 833, 222

Johnson, J. L., Whalen, D. J., Li, H., & Holz, D. E. 2013, ApJ, 771, 116

Jun, H. D., & Im, M. 2013, ApJ, 779, 104

Jun, H. D., Im, M., Kim, D., & Stern, D. 2017, ApJ, 838, 41

Jun, H. D., Im, M., Lee, H. M., et al. 2015, ApJ, 806, 109

Karouzos, M., Im, M., Kim, J.-W., et al. 2014, ApJ, 797, 26

Karouzos, M., Woo, J.-H., Matsuoka, K., et al. 2015, ApJ, 815, 128

Kashikawa, N., Ishizaki, Y., Willott, C. J., et al. 2015, ApJ, 798, 28

Kaspi, S., Maoz, D., Netzer, H., et al. 2005, ApJ, 629, 61.

Kaspi, S., Smith, P. S., Netzer, H., et al. 2000, ApJ, 533, 631.

Khandai, N., Feng, Y., DeGraf, C., et al. 2012, MNRAS, 423, 2397.

Kim, D., & Im, M. 2018, A&A, 610, A31

Kim, Y., & Im, M. 2019, ApJ, 879, 117

Kim, Y., Im, M., Jeon, Y., et al. 2015a, ApJ, 813, L35

Kim, Y., Im, M., Jeon, Y., et al. 2018, ApJ, 855, 138

Kim, Y., Im, M., Jeon, Y., et al. 2019, ApJ, 870, 86.

Kim, D., Im, M., & Kim, M. 2010, ApJ, 724, 386

Kim, D., Im, M., Kim, J. H., et al. 2015b, ApJS, 216, 17

Kim, S., Jeon, Y., Lee, H.-I., et al. 2016, PASP, 128, 115004

Kim, E., Park, W.-K., Jeong, H., et al. 2011, Journal of Korean Astronomical Society, 44, 115

Kirkpatrick, A., Pope, A., Sajina, A., et al. 2015, ApJ, 814, 9

Kormendy, J., & Ho, L. C. 2013, ARA&A, 51, 511.

Kurk, J. D., Walter, F., Fan, X., et al. 2007, ApJ, 669, 32

Kurk, J. D., Walter, F., Fan, X., et al. 2009, ApJ, 702, 833

Lani, C., Netzer, H., & Lutz, D. 2017, MNRAS, 471, 59

Lapi, A., Mancuso, C., Bressan, A., & Danese, L. 2017, ApJ, 847, 13

Lapi, A., Raimundo, S., Aversa, R., et al. 2014, ApJ, 782, 69

Lawrence, A., Warren, S. J., Almaini, O., et al. 2007, MNRAS, 379, 1599

Lee, I., Im, M., Kim, M., et al. 2008, ApJS, 175, 116

Leipski, C., Meisenheimer, K., Walter, F., et al. 2014, ApJ, 785, 154

Li, L.-X. 2012, MNRAS, 424, 1461

Li, Y., Hernquist, L., Robertson, B., et al. 2007, ApJ, 665, 187

Lim, J., Chang, S., Pak, S., et al. 2013, Journal of Korean Astronomical Society, 46, 161

Lodato, G., & Natarajan, P. 2006, MNRAS, 371, 1813

Lusso, E., Comastri, A., Simmons, B. D., et al. 2012, MNRAS, 425, 623

Lusso, E., Worseck, G., Hennawi, J. F., et al. 2015, MNRAS, 449, 4204.

Lyu, J., & Rieke, G. H. 2017, ApJ, 841, 76

Lyu, J., & Rieke, G. H. 2018, ApJ, 866, 92

Lyu, J., Rieke, G. H., & Shi, Y. 2017, ApJ, 835, 257

Madau, P., Ferguson, H. C., Dickinson, M. E., et al. 1996, MNRAS, 283, 1388

Madau, P., & Haardt, F. 2015, ApJ, 813, L8

Madau, P., Haardt, F., & Dotti, M. 2014, ApJ, 784, L38

Madau, P., Haardt, F., & Rees, M. J. 1999, ApJ, 514, 648.

Magorrian, J., Tremaine, S., Richstone, D., et al. 1998, AJ, 115, 2285.

Maiolino, R., Cox, P., Caselli, P., et al. 2005, A&A, 440, L51.

Mancuso, C., Lapi, A., Prandoni, I., et al. 2017, ApJ, 842, 95

Markwardt, C. B. 2009, Astronomical Data Analysis Software and Systems XVIII, 411, 251

Mason, C. A., Treu, T., Dijkstra, M., et al. 2018, ApJ, 856, 2.

Matsuoka, Y., Iwasawa, K., Onoue, M., et al. 2018b, ApJS, 237, 5.

Matsuoka, Y., Onoue, M., Kashikawa, N., et al. 2016, ApJ, 828, 26

Matsuoka, Y., Onoue, M., Kashikawa, N., et al. 2018a, PASJ, 70, S35.

Matsuoka, Y., Onoue, M., Kashikawa, N., et al. 2019, ApJ, 872, L2.

Matsuoka, Y., Strauss, M. A., Kashikawa, N., et al. 2018c, ApJ, 869, 150.

Matthee, J., Sobral, D., Best, P., et al. 2017, MNRAS, 465, 3637

Matute, I., Márquez, I., Masegosa, J., et al. 2012, A&A, 542, A20

Matute, I., Masegosa, J., Márquez, I., et al. 2013, A&A, 557, A78

Mazzucchelli, C., Bañados, E., Venemans, B. P., et al. 2017, ApJ, 849, 91

McGreer, I. D., Fan, X., Jiang, L., & Cai, Z. 2018, AJ, 155, 131

McGreer, I. D., Jiang, L., Fan, X., et al. 2013, ApJ, 768, 105

McGreer, I. D., Mesinger, A., & D'Odorico, V. 2015, MNRAS, 447, 499.

McLure, R. J., & Dunlop, J. S. 2002, MNRAS, 331, 795.

McMullin, J. P., Waters, B., Schiebel, D., Young, W., & Golap, K. 2007, Astronomical Data Analysis Software and Systems XVI, 376, 127

Milosavljević, M., Couch, S. M., & Bromm, V. 2009, ApJ, 696, L146

Mineshige, S., Kawaguchi, T., Takeuchi, M., & Hayashida, K. 2000, PASJ, 52, 499

Moles, M., Benítez, N., Aguerri, J. A. L., et al. 2008, AJ, 136, 1325

Morganson, E., De Rosa, G., Decarli, R., et al. 2012, AJ, 143, 142.

Mortlock, D. J., Patel, M., Warren, S. J., et al. 2009, A&A, 505, 97.

Mortlock, D. J., Warren, S. J., Venemans, B. P., et al. 2011, Natur, 474, 616

Moutard, T., Arnouts, S., Ilbert, O., et al. 2016, A&A, 590, A102

Netzer, H. 2009, MNRAS, 399, 1907

Ohsuga, K., Mori, M., Nakamoto, T., & Mineshige, S. 2005, ApJ, 628, 368

Omont, A., Willott, C. J., Beelen, A., et al. 2013, A&A, 552, A43

Onoue, M., Kashikawa, N., Matsuoka, Y., et al. 2019, arXiv e-prints , arXiv:1904.07278.

Onoue, M., Kashikawa, N., Willott, C. J., et al. 2017, ApJ, 847, L15

Pacucci, F., Volonteri, M., & Ferrara, A. 2015, MNRAS, 452, 1922

Pâris, I., Petitjean, P., Aubourg, É., et al. 2018, A&A, 613, A51.

Pâris, I., Petitjean, P., Ross, N. P., et al. 2017, A&A, 597, A79

Park, W.-K., Pak, S., Im, M., et al. 2012, PASP, 124, 839

Park, K., & Ricotti, M. 2012, ApJ, 747, 9

Park, D., Barth, A. J., Woo, J.-H., et al. 2017, ApJ, 839, 93

Park, D., Woo, J.-H., Denney, K. D., & Shin, J. 2013, ApJ, 770, 87

Parsa, S., Dunlop, J. S., & McLure, R. J. 2018, MNRAS, 474, 2904

Pelupessy, F. I., Di Matteo, T., & Ciardi, B. 2007, ApJ, 665, 107

Pentericci, L., Carniani, S., Castellano, M., et al. 2016, ApJ, 829, L11

Peterson, B. M. 1993, PASP, 105, 247.

Petric, A. O., Carilli, C. L., Bertoldi, F., et al. 2003, AJ, 126, 15

Pezzulli, E., Valiante, R., & Schneider, R. 2016, MNRAS, 458, 3047

Pickles, A. J. 1998, PASP, 110, 863

Pitchford, L. K., Hatziminaoglou, E., Feltre, A., et al. 2016, MNRAS, 462, 4067

Planck Collaboration, Adam, R., Aghanim, N., et al. 2016, A&A, 596, A108

Reed, S. L., McMahon, R. G., Banerji, M., et al. 2015, MNRAS, 454, 3952.

Reed, S. L., McMahon, R. G., Martini, P., et al. 2017, MNRAS, 468, 4702

Regan, J. A., Visbal, E., Wise, J. H., et al. 2017, Nature Astronomy, 1, 0075

Ricci, F., Marchesi, S., Shankar, F., La Franca, F., & Civano, F. 2017, MNRAS, 465, 1915

Richards, G. T., Strauss, M. A., Fan, X., et al. 2006, AJ, 131, 2766

Robertson, B. E., Ellis, R. S., Dunlop, J. S., et al. 2010, Nature, 468, 49.

Robertson, B. E., Ellis, R. S., Furlanetto, S. R., & Dunlop, J. S. 2015, ApJ, 802, L19

Robertson, B. E., Furlanetto, S. R., Schneider, E., et al. 2013, ApJ, 768, 71

Runnoe, J. C., Brotherton, M. S., & Shang, Z. 2012, MNRAS, 422, 478

Runnoe, J. C., Brotherton, M. S., Shang, Z., & DiPompeo, M. A. 2013, MNRAS, 434, 848

Sakurai, Y., Inayoshi, K., & Haiman, Z., MNRAS, 461, 4496

Sawicki, M. 2012, PASP, 124, 1208

Schlafly, E. F., & Finkbeiner, D. P. 2011, ApJ, 737, 103

Schmidt, M., & Green, R. F. 1983, ApJ, 269, 352

Schulze, A., Bongiorno, A., Gavignaud, I., et al. 2015, MNRAS, 447, 2085

Selsing, J., Fynbo, J. P. U., Christensen, L., & Krogager, J.-K. 2016, A&A, 585, A87

Shen, Y., Greene, J. E., Strauss, M. A., Richards, G. T., & Schneider, D. P. 2008, ApJ, 680, 169-190

Shen, Y., Richards, G. T., Strauss, M. A., et al. 2011, ApJS, 194, 45

Shen, Y., Wu, J., Jiang, L., et al. 2019, ApJ, 873, 35.

Sijacki, D., Springel, V., & Haehnelt, M. G. 2009, MNRAS, 400, 100

Simpson, J. M., Smail, I., Swinbank, A. M., et al. 2015a, ApJ, 799, 81

Simpson, J. M., Smail, I., Swinbank, A. M., et al. 2015b, ApJ, 807, 128

Skrutskie, M. F., Cutri, R. M., Stiening, R., et al. 2006, AJ, 131, 1163

Smidt, J., Whalen, D. J., Johnson, J. L., Surace, M., & Li, H. 2018, ApJ, 865, 126

Smith, A., Bromm, V., & Loeb, A. 2017, Astronomy and Geophysics, 58, 3.22.

Smole, M., Micic, M., & Martinović, N. 2015, MNRAS, 451, 1964

Songaila, A. 2004, AJ, 127, 2598

Springel, V., Di Matteo, T., & Hernquist, L. 2005, MNRAS, 361, 776

Stach, S. M., Smail, I., Swinbank, A. M., et al. 2018, ApJ, 860, 161

Stanley, F., Alexander, D. M., Harrison, C. M., et al. 2017, MNRAS, 472, 2221

Tang, J.-J., Goto, T., Ohyama, Y., et al. 2017, MNRAS, 466, 4568.

Tang, B., Shang, Z., Gu, Q., Brotherton, M. S., & Runnoe, J. C. 2012, ApJS, 201, 38

Tody, D. 1993, Astronomical Data Analysis Software and Systems II, 52, 173

Trakhtenbrot, B. 2014, ApJ, 789, L9

Trakhtenbrot, B., Lira, P., Netzer, H., et al. 2017a, ApJ, 836, 8

Trakhtenbrot, B., & Netzer, H. 2012, MNRAS, 427, 3081

Trakhtenbrot, B., Volonteri, M., & Natarajan, P. 2017b, ApJ, 836, L1

Urry, C. M., & Padovani, P. 1995, PASP, 107, 803.

Vanden Berk, D. E., Richards, G. T., Bauer, A., et al. 2001, AJ, 122, 549

van Dokkum, P. G., Labbé, I., Marchesini, D., et al. 2009, PASP, 121, 2

Venemans, B. P., Bañados, E., Decarli, R., et al. 2015a, ApJ, 801, L11

Venemans, B. P., Decarli, R., Walter, F., et al. 2018, ApJ, 866, 159

Venemans, B. P., Findlay, J. R., Sutherland, W. J., et al. 2013, ApJ, 779, 24

Venemans, B. P., McMahon, R. G., Walter, F., et al. 2012, ApJ, 751, L25

Venemans, B. P., McMahon, R. G., Warren, S. J., et al. 2007, MNRAS, 376, L76.

Venemans, B. P., Verdoes Kleijn, G. A., Mwebaze, J., et al. 2015b, MNRAS, 453, 2259

Venemans, B. P., Walter, F., Decarli, R., et al. 2017a, ApJ, 837, 146

Venemans, B. P., Walter, F., Decarli, R., et al. 2017b, ApJ, 845, 154

Venemans, B. P., Walter, F., Decarli, R., et al. 2017c, ApJ, 851, L8

Venemans, B. P., Walter, F., Zschaechner, L., et al. 2016, ApJ, 816, 37

Vestergaard, M., & Osmer, P. S. 2009, ApJ, 699, 800

Vestergaard, M., & Peterson, B. M. 2006, ApJ, 641, 689

Volonteri, M. 2012, Science, 337, 544

Volonteri, M., Lodato, G., & Natarajan, P. 2008, MNRAS, 383, 1079

Volonteri, M., & Rees, M. J. 2005, ApJ, 633, 624

Volonteri, M., Silk, J., & Dubus, G. 2015, ApJ, 804, 148

Walter, F., Bertoldi, F., Carilli, C., et al. 2003, Nature, 424, 406.

Walter, F., Weiß, A., Riechers, D. A., et al. 2009, ApJ, 691, L1.

Wang, R., Carilli, C. L., Beelen, A., et al. 2007, AJ, 134, 617

Wang, R., Carilli, C. L., Neri, R., et al. 2010, ApJ, 714, 699

Wang, R., Carilli, C. L., Wagg, J., et al. 2008, ApJ, 687, 848

Wang, F., Fan, X., Yang, J., et al. 2017, ApJ, 839, 27.

Wang, J.-M., & Netzer, H. 2003, A&A, 398, 927

Wang, R., Wagg, J., Carilli, C. L., et al. 2011, AJ, 142, 101

Wang, R., Wagg, J., Carilli, C. L., et al. 2013, ApJ, 773, 44

Wang, R., Wu, X.-B., Neri, R., et al. 2016b, ApJ, 830, 53

Wang, F., Wu, X.-B., Fan, X., et al. 2016, ApJ, 819, 24

Wang, F., Yang, J., Fan, X., et al. 2018a, arXiv e-prints , arXiv:1810.11926.

Wang, F., Yang, J., Fan, X., et al. 2018b, ApJ, 869, L9

Watarai, K.-y., Mizuno, T., & Mineshige, S. 2001, ApJ, 549, L77

Welsh, B. Y., Wheatley, J. M., & Neil, J. D. 2011, A&A, 527, A15

Wethers, C. F., Banerji, M., Hewett, P. C., et al. 2018, MNRAS, 475, 3682

Willott, C. J., Albert, L., Arzoumanian, D., et al. 2010a, AJ, 140, 546

Willott, C. J., Bergeron, J., & Omont, A. 2015, ApJ, 801, 123

Willott, C. J., Bergeron, J., & Omont, A. 2017, ApJ, 850, 108

Willott, C. J., Delfosse, X., Forveille, T., Delorme, P., & Gwyn, S. D. J. 2005, ApJ, 633, 630

Willott, C. J., Delorme, P., Omont, A., et al. 2007, AJ, 134, 2435

Willott, C. J., Delorme, P., Reylé, C., et al. 2009, AJ, 137, 3541

Willott, C. J., Delorme, P., Reylé, C., et al. 2010b, AJ, 139, 906

Willott, C. J., McLure, R. J., & Jarvis, M. J. 2003, ApJ, 587, L15

Willott, C. J., Omont, A., & Bergeron, J. 2013, ApJ, 770, 13

Wolf, C., Wisotzki, L., Borch, A., et al. 2003, A&A, 408, 499

Woo, J.-H., Schulze, A., Park, D., et al. 2013, ApJ, 772, 49

Wright, E. L., Eisenhardt, P. R. M., Mainzer, A. K., et al. 2010, AJ, 140, 1868

Wu, X.-B., Wang, F., Fan, X., et al. 2015, Natur, 518, 512

Wyithe, J. S. B., & Loeb, A. 2012, MNRAS, 425, 2892

Yang, J., Fan, X., Wu, X.-B., et al. 2017, AJ, 153, 184

Yang, J., Wang, F., Fan, X., et al. 2018, arXiv:1811.11915

Yang, J., Wang, F., Wu, X.-B., et al. 2016, ApJ, 829, 33

York, D. G., Adelman, J., Anderson, J. E., et al. 2000, AJ, 120, 1579.

Zheng, X. Z., Xia, X. Y., Mao, S., Wu, H., & Deng, Z. G. 2002, AJ, 124, 18

요 약

고적색편이($z > 5$)의 초기 우주에서, 어두운 퀘이사는 전체 퀘이사의 대부분을 이루고 있다. 하지만 그들의 어두운 밝기 때문에, 관련 연구들은 제한된 범위에서 최근에서야 드물게 이루어졌다. 본 학위논문에서는 고적색편이의 어두운($M_{1450} > -24$ mag) 퀘이사에 대해 다양한 방면에서 연구를 진행했다.

첫째로, 적색편이 6에 있는 어두운 퀘이사를 찾기 위한 연구를 Infrared Medium-deep Survey (IMS) 근적외선 이미지 자료를 바탕으로 진행하였다. 총 86 deg^{2}의 영역에서 색 선택 방법을 이용해 25개의 퀘이사 후보를 선별하였고, 이번 연구에서 새롭게 발견된 IMS J2204+0112를 포함하여 그들 중 3개의 후보는 분광 관측을 통해 적색편이 6에 있는 퀘이사임이 확인되었다. 이러한 퀘이사 및 퀘이사 후보로부터 적색편이 6에서의 퀘이사 광도 곡선을 구했으며, 이 곡선으로부터 초기 우주의 중성 수소들을 모두 이온화시키는데 필요한 광자의 15% 미만이 퀘이사로부터 방출되는 것으로 계산되었다. 즉 초기 우주의 재이온화 과정에 퀘이사는 그리 많지 않은 기여를 한 것으로 확인되었다.

둘째로, 깊은 근적외선 분광 관측을 통해서 IMS J2204+0112의 중심부에 있는 초거대질량 블랙홀의 질량을 측정하였다. 블랙홀 주변의 가스들의 비리얼(Virial) 운동을 가정하여, 적색편이된 C IV λ1549 방출선을 통해 블랙홀 질량이 $M_{\rm BH} = 1.2 \times 10^9\ M_\odot$ 임을 측정하였고, 그 결과 에딩턴 비율이 $\lambda_{\rm Edd} \sim 0.1$임을 확인했다. 이 값은 지금까지 알려진 적색편이 6 퀘이사의 에딩턴 비율 중 가장 낮은 값들에 속하며, 초기 우주의 초거대질량 블랙홀은 모두 급격하게 성장한다고 알려진 사실의 반례가 되었다. 이렇게 낮은 에딩턴 비율을 가진 퀘이사는 100 $M_\odot$의 블랙홀이 슈퍼 에딩턴 강착을 겪거나 $10^5\ M_\odot$ 정도의 질량을 갖는 무거운 블랙홀이 에딩턴 제한적인 강착을 겪으면서 성장하는 것으로 설명될 수 있다. 또한 IMS J2204+0112를 포함하여, 적색편이 6 퀘이사의 본질적인 에딩턴 비율 분포를 계산하였고, 적색편이 2의 퀘이사와 비교했을 때 그 값이 0.35 dex 정도 약간 높은 것으로 확인됐으며, 이를 통해 초기 우주 초거대질량 블랙홀의 성장에 대해 제약을 주었다.

셋째로, Atacama Large Millimeter/submillimeter Array (ALMA)를 이용한 IMS J2204+0112의 sub-mm 영역 관측을 통하여, 해당 퀘이사의 모은하가 500–700 $M_\odot$ yr^{-1}의 별생성률을 갖는 것을 확인하였고, 이 값은 비슷한 밝기를 지닌 에딩턴 비율이 높은

퀘이사보다 10배 정도 높은 값이다. 흥미롭게도, IMS J2204+0112와 마찬가지로 낮은 에딩턴 비율($\lambda_{\rm Edd} < 0.2$)을 갖는 퀘이사가 모두 별생성률이 높은 은하들에 속해있는 것을 확인했고, 이는 먼저 빠르게 성장하는 초거대질량 블랙홀과 뒤따라 성장하는 모은하에 대한 최근 시뮬레이션과 일치하는 결과이다. 이에 따르면, 낮은 에딩턴 비율을 갖는 퀘이사의 초거대질량 블랙홀은 성장이 거의 끝나가는 단계에 있으며, 반면 그들의 모은하는 더 성장할 가능성이 있다.

마지막으로, 대역폭이 500 Å인 중대역 필터를 관측을 바탕으로한 색 선택 방법을 이용하여 적색편이 5의 어두운 퀘이사 탐사를 진행하였다. 가시광 영역의 분광 관측을 통해서 $-25 < M_{1450} < -23$의 밝기를 지닌 10개의 적색편이 5 퀘이사를 새롭게 발견했다. 이러한 발견은 퀘이사가 내뿜는 빛이 적색편이 5에서 수소들이 이온화 상태를 유지하기엔 충분하지 않다는 제안과 일치한다. 중대역 필터를 이용한 퀘이사 선별 방식을 이용하여, 우리는 광대역 색상을 통해 선별됐지만 퀘이사가 아닌 왜성과 같은 천체를 20% 이상 제외시킬 수 있었으며, 측광학적 적색편이를 $\langle|\Delta z|/(1+z)\rangle = 0.016$의 정확도로 결정할 수 있었다. 결론적으로, 이 방식은 퀘이사를 선별하고 그들의 측광학적 적색편이를 얻는데 매우 효율적인 방법임을 확인할 수 있었다.

주요어: cosmology: observations – galaxies: active – galaxies: high-redshift – quasars: emission lines – quasars: supermassive black holes – surveys

학 번: 2013-20389